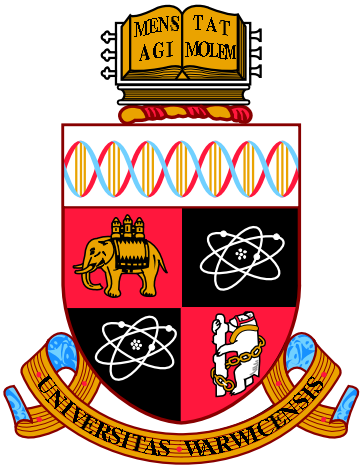

CP violation and neutrino mass ordering at the T2K experiment

by

Andrew Chappell

Thesis

Submitted to the University of Warwick

for the degree of

Doctor of Philosophy

Department of Physics

April 2019

THE UNIVERSITY OF WARWICK

Contents

List of Tables

List of Figures

Abbreviations

2p2h Two particles, two holes.

ANA Atmospheric Neutrino Anomaly.

BANFF Beam and ND280 Flux Extrapolation Task Force.

BF Best-fit.

C Charge conjugation (symmetry).

CC Charged-current.

CCnQE Charged-current non-quasi-elastic (interaction).

CCQE Charged-current quasi-elastic (interaction).

CERN European Organization for Nuclear Research.

CL Confidence Level.

CP Charge conjugation parity (symmetry).

CPT Charge, parity and time reversal (symmetry).

CPU Central Processing Unit.

DIS Deep Inelastic Scattering.

DOF Degrees of Freedom.

DUNE Deep Underground Neutrino Experiment.

ECal Electromagnetic calorimeter. A sub-detector in the ND280.

ERP East Rand Proprietary Gold Mine.

ES Elastic scattering.

FC Fully contained.

FGD Fine-Grained Detector. A sub-detector in the ND280.

FHC Forward Horn Current. The T2K beam mode that produces a beam predominantly composed of neutrinos.

FHC FLUktuierende KAskade.

FSI Final State Interaction.

FV Fiducial Volume.

GALLEX Gallium Experiment.

GCALOR An interface between GEANT and the CALOR89 calorimeter analysis system.

GEANT GEometry ANd Tracking (MC simulation package).

GNO Gallium Neutrino Observatory.

GPS Global Positioning System.

HK Hyper-Kamiokande (detector).

IMB Irvine-Michigan-Brookhaven (detector).

INGRID Interactive Neutrino Grid (detector). An on-axis near detector for T2K.

INO India-based Neutrino Observatory.

IO Inverted (mass) ordering.

JNUBEAM J-PARC Neutrino Beam.

JUNO Jiangmen Underground Neutrino Observatory.

J-PARC Japan Proton Accelerator Research Complex.

KGM Kolar Gold Mine.

LEP Large Electron-Positron (Collider experiment).

LE Low energy.

LFG Local Fermi Gas.

LINAC Linear accelerator. An accelerator at J-PARC.

MC Monte Carlo.

MiniBooNE Mini Booster Neutrino Experiment.

MINERvA Main Injector Experiment for ν-A

MINOS Main Injector Neutrino Oscillation Search.

MPPC Multi-Pixel Photon Counter.

MR Main Ring (Synchrotron). An accelerator at J-PARC.

NA61/SHINE North Area 61/SPS Heavy Ion and Neutrino Experiment.

NC Neutral-current.

NCQE Neutral-current quasi-elastic (interaction).

ND280 Near Detector (at) 280 m. An off-axis near detector for T2K.

NIWG Neutrino Interaction Working Group.

NN Nucleon-nucleon (correlations).

NO Normal (mass) ordering.

NOvA NuMI Off-Axis ν_e Appearance.

NuMI Neutrino at the Main Injector.

OD Outer detector.

ORCA Oscillation Research with Cosmics in the Abyss.

P Parity (symmetry).

PDD Pionless Delta Decay.

PID Particle Identification.

P0D π^0 detector. A sub-detector in the ND280.

PDG Particle Data Group.

PGoF Parameter Goodness of Fit.

PINGU Precision IceCube Next Generation Upgrade.

PMNS Pontecorvo-Maki-Nakagawa-Sakata.

PMT Photomultiplier Tube.

PN Photonuclear (effect).

POT Protons on Target.

QE Quasi-elastic.

RCS Rapidly Cycling Synchrotron. An accelerator at J-PARC.

RF Radio frequency.

RHC Reverse Horn Current. The T2K beam mode that produces a beam predominantly composed of antineutrinos.

RENO Reactor Experiment for Neutrino Oscillation.

RFG Relativistic Fermi Gas.

RMS Root mean square.

RPA Random Phase Approximation.

RPC Resistive Plate Chamber.

SAGE Soviet-American Gallium Experiment.

SF Spectral Function.

SI Secondary Interaction.

SK Super-Kamiokande (detector).

SKDETSIM Super-Kamiokande Detector Simulation.

SM Standard Model.

SMRD Side Muon Range Detector. A sub-detector in the ND280.

SNO Solar Neutrino Observatory.

SNP Solar Neutrino Problem.

SSM Standard Solar Model.

T2HK Tokai-to-Hyper-Kamiokande.

T2K Tokai-to-Kamioka.

TPC Time Projection Chamber. A sub-detector in the ND280.

UA1 Underground Area 1. T2K's magnet was originally deployed in the UA1 experiment at CERN.

V-A Vector minus axial vector.

WLS Wavelength Shifting (fibre).

Acknowledgments

I would like to thank my supervisors, Gary Barker and Steve Boyd for the support provided over these three-and-half years that has made this work possible.

Thank you to my fellow T2K collaborators for their hard work in producing the data used in my analyses and the valuable feedback provided. The collaboration provided an excellent environment in which to undertake this work.

I would particularly like to thank the *VALOR* group and the wider T2K oscillation analysis group, both for the opportunity to undertake this work and the invaluable feedback that aided the development of the analyses described in this document.

To my fellow physicists in office P450, thank you for your advice and assistance, and for providing an environment that's been a pleasure to work in during my time at Warwick.

To Alexandra Kviat and Georgia Karaiskou, thank you for being the best flatmates a person could hope for.

Finally, I would like to thank my parents, whose support has made this possible and worthwhile.

Declarations

This thesis is submitted to the University of Warwick in support of my application for the degree of Doctor of Philosophy. It has been composed by myself and has not been submitted in any previous application for any degree.

The work presented (including data generated and data analysis) was carried out by the author except in the cases outlined below:

- The T2K flux prediction (section 4.1), produced and validated by collaborators within T2K, supported by data from the NA61/SHINE collaboration
- The Super-Kamiokande MC templates (section 4.2 and 4.4), produced and validated by collaborators within T2K
- The near detector covariance matrix (section 4.3), produced and validated by collaborators within T2K
- The Super-Kamiokande detector covariance matrix (section 4.5), produced and validated by collaborators within T2K

Each of these components acted as inputs to my original work, which is presented in chapters five and six. This work was performed as part of the *VALOR* analysis group, making use of the *VALOR* software development kit, developed by myself, Costas Andreopoulos, Christopher Barry, Francis Bench, Thomas Dealtry, Steve Dennis, Davide Sgalaberna and Raj Shah.

The second chapter of this thesis provides the historical and theoretical background to neutrino physics. It is a review of the work undertaken by physicists that has made the work in this thesis possible.

Chapter three describes the T2K experiment itself, which provides the data for the analyses in this thesis. This chapter is derived from T2K documentation, including published literature and also internal technical notes produced by the T2K collaboration.

Abstract

T2K is a long baseline neutrino oscillation experiment studying the oscillation of ν_μ to ν_e over the 295 km baseline between the J-PARC accelerator and the Super-Kamiokande water Cherenkov detector.

A 3-flavour, 5 sample $\nu/\bar{\nu}$ joint analysis on the Run 1-9 dataset is performed to measure the neutrino CP phase, δ, where values other than zero and $n\pi$ imply a difference in the oscillation of neutrinos and antineutrinos. The 2σ confidence level allowed interval when applying the constraint on $\sin^2(\theta_{13})$ from reactors in normal mass ordering is $[-2.966, -0.628]$ and for inverted mass ordering is $[-1.799, -0.979]$. Thus, CP conservation is rejected at 2σ, a world leading measurement.

Differences in event rates are expected for different true values of the neutrino mass ordering and thus T2K has some sensitivity to the neutrino mass ordering. A 3-flavour, 5 sample $\nu/\bar{\nu}$ joint analysis on the Run 1-9 dataset is performed to measure the neutrino mass ordering. No strong evidence against either mass ordering hypothesis is observed.

Chapter 1

Introduction

The Standard Model, which first emerged in the 1960s, represents the best current understanding of particle physics. This model has been remarkably successful, correctly predicting the existence of the W and Z bosons, the gluon, the top and charm quarks and, most recently, the Higgs boson. Alongside these major achievements are precision predictions of physical observables that have been verified by experiment. Nonetheless, the Standard Model is known to be incomplete. Among the most significant open questions are the origin of gravity, the nature of dark matter and the very existence of a matter-dominated Universe.

The topics covered in this thesis are not part of the Standard Model. Neutrino oscillation, experimentally confirmed in the early 2000s, demonstrates that neutrinos have mass, while in the Standard Model neutrinos are massless particles. Neutrino oscillation provides the potential for CP violation in the lepton sector (which may explain the matter-dominated nature of the Universe) and it is this topic that forms one of the analyses in this thesis. The T2K neutrino oscillation experiment is used to constrain the value of the lepton CP phase, rejecting CP conservation at 2σ and thereby hinting at CP violation in the lepton sector.

The discovery that neutrinos have mass raises questions of the absolute mass scale and the ordering of the neutrino masses. While neutrino oscillation is unable to access the absolute mass scale of the neutrinos, it can measure the mass-squared differences between the mass states and thereby address the ordering of the masses. The order of the first two mass states is already known, but the relationship of the third mass state to these first two remains an open question; that is, is the third mass state heavier than the first two mass states, or lighter, the so called normal and inverted orderings respectively? It is this question that is tackled by the second analysis in this thesis. Using data from the T2K experiment, the mass ordering is

measured, finding no strong evidence against either mass ordering.

Chapter 2

History and theory of neutrino physics

2.1 History

2.1.1 Prediction and discovery of the neutrino

The story of the neutrino begins with the electron energy spectrum of β-decay in the early 20th century. At this time it was thought that in one form of β-decay an unstable atomic nucleus undergoes spontaneous decay, in which the atomic number, Z, of the nucleus, N, is increased by one, while the atomic mass, A, remains unchanged to produce a daughter nucleus N'

$$ {}^{A}_{Z}N \rightarrow {}^{A}_{Z+1}N' \tag{2.1} $$

Considering the nucleons involved in the process this is the decay of a neutron, n, to a proton, p, and an electron, e^-

$$ n \rightarrow p + e^- \tag{2.2} $$

There are however two significant problems with this view of β-decay. The first is with respect to conservation of angular momentum; the neutron is a spin-$\frac{1}{2}$ particle and therefore it cannot decay into exactly two spin-$\frac{1}{2}$ particles, as the proton and electron are, without violating this conservation law. The second problem concerns the conservation of energy and momentum; in 1914 Chadwick established that the electron energy spectrum was continuous (see [1]), a fact that was subsequently confirmed by Ellis and Wooster [2], however, with only two outgoing particles, energy

and momentum conservation requires that the electron energy spectrum take the form of a sharp peak, which for the β-decay of ^{210}Bi to ^{210}Po investigated by Ellis and Wooster would be found at $Q \approx 1.2\,\mathrm{MeV}$.

These problems led Pauli to propose, in 1930, that an undetected light, neutral, spin-$\frac{1}{2}$ particle [3] was emitted along with the neutron and electron, thus resolving the aforementioned conflicts with the conservation laws. Pauli's proposal was vindicated in 1956, when Reines and Cowan announced the discovery of the electron (anti)neutrino [4]. Reines and Cowan designed an experiment to make use of the substantial neutrino flux generated by nuclear reactors. In particular they situated large tanks containing a scintillating liquid solution doped with Cadmium and layers of scintillation counters to detect the inverse β-decay interaction

$$\bar{\nu}_e + p \rightarrow e^+ + n \tag{2.3}$$

The neutrinos from the Savannah River Plant reactor interacted with the protons in the scintillator to produce a positron and neutron, the positron detectable by the pair of photons produced upon annihilation and the subsequent capture of the neutron by the Cadmium solute produced a delayed gamma ray signal. The combination of the shielding around the tanks reduced the background from reactor neutrons, gamma rays and cosmic rays and the dependence of the signal magnitude on reactor power and proton concentration in the solution provided strong evidence that the signals originated from interactions occurring within the tanks and therefore provided the first conclusive proof of the existence of the neutrino.

Having taken 26 years between the prediction and detection of the neutrino, it took only 6 more years to discover a second flavour of neutrino. This experiment [5] used a particle accelerator at Brookhaven National Laboratory to produce pions by colliding protons with a Beryllium target to produce neutrinos via the decay

$$\pi^{\pm} \rightarrow \mu^{\pm} + (\nu_\mu/\bar{\nu}_\mu) \tag{2.4}$$

The neutrinos then travelled through an iron shield that attenuated the daughter muons and residual pions, to interact within a spark chamber where the resultant charged lepton tracks could be detected. The identification of these tracks only with muons rather than electrons demonstrated that these neutrinos must be of a different flavour to those produced in the experiment by Reines and Cowan.

With neutrinos now associated with both the electron and the muon, the discovery of the charged tau lepton in 1975 [6] raised the obvious question of whether there was an associated tau neutrino. A provisional answer was provided by the LEP

experiment [7], which measured the cross-section of the process

$$e^+ + e^- \rightarrow \nu + \bar{\nu} + \gamma \tag{2.5}$$

near the Z boson resonance. The single photon production cross-section is approximately proportional to the number of active, light neutrinos, which from the measurement was calculated to be 3, as would be expected if there is a single neutrino for each charged lepton. This picture was finally confirmed in 2000 at DONUT [8]. This experiment produced a neutrino beam through the collision of 800 GeV protons with a tungsten target, producing D_s mesons which then decayed via the process

$$D_s^- \rightarrow \tau^- + \bar{\nu}_\tau \tag{2.6}$$

The τ from this decay itself decayed producing a ν_τ as one of the daughter particles, before travelling 36 m to a shielded target composed of steel and emulsion plates, where a ν_τ interaction would register through the appearance of a track that would then display a kink after a few millimetres, representing the τ produced by the ν_τ interaction decaying into a μ (the visible kink) and $\bar{\nu}_\tau$ (invisible).

2.1.2 Solar Neutrino Problem

With the existence of the neutrino established, the particle provided an avenue to test the standard solar model (SSM), which predicted that the Sun would produce a flux of ν_e as a result of various reactions taking place during nuclear fusion within the Sun [9]. The long-running Homestake experiment [10] sought to measure part of this flux by looking for inverse β-decay in a tank filled with Chlorine, specifically through the interaction

$$\nu_e + {}^{37}\mathrm{Cl} \rightarrow {}^{37}\mathrm{Ar} + e^- \tag{2.7}$$

The resultant Argon atoms were periodically counted following chemical extraction from the tank (the period being determined by the time at which production of Argon reached approximate equilibrium with the Argon decay rate). The resultant measured neutrino capture rate was approximately one-third the expected value.

One of the drawbacks of the Homestake experiment was that the neutrino energy threshold of $\sim 0.8\,\mathrm{MeV}$ for the interaction was relatively high. Coupled with the fact that the cross-section increases with energy this meant that the principle contribution to the measured neutrino flux was from ^{8}B derived neutrinos, omitting the lower-energy region that actually provides the dominant component of the neutrino flux (see fig. 2.1). This short-coming could be overcome by using a different

target nucleus to provide the inverse β-decay reaction, specifically Gallium [11]:

$$\nu_e + {}^{71}\mathrm{Ga} \rightarrow {}^{71}\mathrm{Ge} + e^- \tag{2.8}$$

The energy threshold for this interaction, $E_\nu \sim 0.23$ MeV, is lower and therefore provides sensitivity to all sources of solar neutrinos, with the resultant Germanium atoms chemically extracted on a periodic basis for counting. This approach was

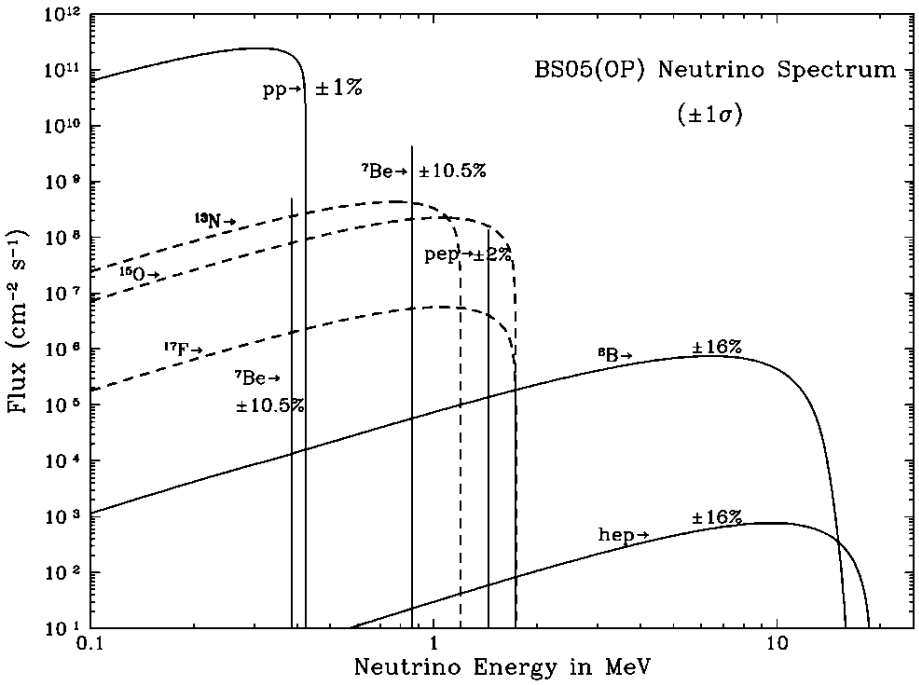

Figure 2.1: Solar neutrino energy spectrum. Reproduced from [12]

implemented by the GALLEX/GNO [13, 14] and SAGE experiments [15], measuring neutrino capture rates approximately half the value predicted on the basis of the SSM, thereby confirming the deficit discovered by the Homestake experiment. This deficit in the measured neutrino capture rate relative to that expected, given the predicted flux from the SSM, came to be known as the Solar Neutrino Problem (SNP).

2.1.3 Atmospheric Neutrino Anomaly

An additional natural source of neutrinos takes the form of atmospheric neutrinos. In particular, these neutrinos are produced by the interaction of cosmic rays (predominantly protons) with nuclei in the atmosphere, giving rise to hadrons, many of

which are charged pions, which in turn can decay to produce neutrinos supplemented by the additional processes

$$\mu^- \rightarrow e^- + \bar{\nu}_e + \nu_\mu \tag{2.9}$$

$$\mu^+ \rightarrow e^+ + \nu_e + \bar{\nu}_\mu \tag{2.10}$$

from the subsequent decay of a fraction of the daughter muons.

The first observations of atmospheric neutrinos were provided by plastic and liquid scintillator-based experiments in the Kolar Gold Mine (KGM) [16] and East Rand Proprietary Gold Mine (ERP) [17]. Both of these experiments measured muons traversing the detectors along a horizontal trajectory; with the rock surrounding the experiment providing target material for the atmospheric ν_μ interactions that would produce the muons to be detected, while acting as a shield against cosmic ray muons (vertical trajectories were still subject to a significant cosmic ray muon background). The KGM and ERP experiments each detected a number of events in excess of the expected background rate and interpreted the results as evidence for atmospheric neutrinos.

Precise measurements of atmospheric neutrinos became available with the advent of the Kamiokande and IMB water-Cherenkov experiments. Intended primarily as nucleon decay experiments, a precise understanding of the atmospheric neutrino background to the decay searches was necessary. However, Kamiokande measured [18, 19] the number of electrons and muons generated by ν_e and ν_μ particles present in the cosmic ray shower and found a deficit in the number of ν_μ associated events. A range of theoretical predictions of neutrino flux at the time meant that the deficit observed would have been unremarkable by itself, but the ratio of ν_μ/ν_e events was much more precisely established and the observed ratio was only ~ 0.6 of the predicted value. The IMB experiment similarly measured this ratio, finding a value ~ 0.7 of the predicted value [20]. This deficit came to be known as the Atmospheric Neutrino Anomaly (ANA).

2.1.4 Neutrino oscillation

The solution to the SNP and the ANA would be provided by the discovery of neutrino oscillation. In 1957 Bruno Pontecorvo produced the first papers [21, 22] proposing that neutrinos might oscillate to antineutrinos and vice versa, in analogy with the recently discovered $K^0 \leftrightarrow \bar{K}^0$ oscillations in the quark sector, with the neutrinos and antineutrinos observed being a mixed state of two underlying particles. While this mechanism for neutrino oscillation ultimately turned out to be

incorrect, the idea of oscillation itself remained, with a new mechanism proposed by Maki, Nakagawa and Sakata [23], which, rather than considering mixing between a neutrino and antineutrino, proposed mixing between a neutrino associated with the electron and a neutrino associated with the muon (the τ particle having not yet been discovered). These ideas were then developed [24, 25] by Pontecorvo and Gribov, with the latter paper focusing on the oscillation potential of neutrinos from the Sun, following the early results of the Homestake experiment, which had, at the time, failed to detect solar neutrinos despite theoretical predictions that such a detection should have been possible.

The resolution of the SNP was provided by the SNO experiment [26–28]. The key feature of SNO that allowed it to resolve the SNP was its ability to detect all three flavours of active neutrinos, rather than only ν_e, as in the case of the experiments discussed in section 2.1.2. As a (heavy) water-Cherenkov detector (see section 3.3), it could detect the charged-current (CC) and elastic scattering (ES) interactions

$$\text{CC: } \nu_e + d \rightarrow p + p + e^- \tag{2.11}$$

$$\text{ES: } \nu_\alpha + e^- \rightarrow \nu_\alpha + e^- \tag{2.12}$$

where $\alpha = e, \mu, \tau$. Thus the CC interaction provided the ability to detect the expected incident ν_e through the Cherenkov light produced by the outgoing electron, while the ES process provided the ability to detect interactions involving all active neutrino flavours through the same process, though with reduced sensitivity to incident ν_μ and ν_τ. Crucially however, the target nuclei in SNO (initially deuterium and subsequently also Chlorine following doping with salt) provided for neutron capture via the neutral-current (NC) process

$$\text{NC: } \nu_\alpha + d \rightarrow p + n + \nu_\alpha \tag{2.13}$$

This NC process is equally sensitive to all active neutrinos and can therefore measure the total flux of neutrinos coming from the Sun. Thus if some fraction of solar ν_e were oscillating en route to the detector, the oscillated neutrinos could be detected to confirm this (note that for all interactions the energy threshold was such that SNO was sensitive only to ^8B derived neutrinos). SNO found that the ratio of the ^8B flux from CC and NC interactions was about 0.3, not only confirming the ν_e deficit seen in earlier experiments, but further establishing that the missing ν_e had indeed oscillated to ν_μ and ν_τ en route from the Sun.

Resolution of the ANA would come from Kamiokande's successor, Super-

Kamiokande (SK) [29]. The goal of SK was to look for an asymmetry in events based on the trajectory of the detected particles. Given the weakly interacting nature of the neutrino (see section 2.2.1), a detected particle could just as easily travel up through the entire Earth on the way to the detector as travel down through only the atmosphere above the detector and therefore the flux of atmospheric neutrinos would be expected to be isotropic in the absence of neutrino oscillation. However, with neutrino oscillation hypothesised to depend upon the propagation distance of the neutrino (see section 2.2.2), these two scenarios represent propagation distances of ~ 15 km for downward going events and up to 13000 km for upward going events, allowing for a difference in event rates due to oscillation. This asymmetry was measured as

$$A = \frac{U - D}{U + D} \tag{2.14}$$

where U is the number of upward going events and D is the number of downward going events. In this way, an asymmetry close to zero would be consistent with no oscillation signal, while positive or negative values would provide evidence of oscillation. The result is shown in fig. 2.2, in which no significant asymmetry is observed for electron neutrinos, but a momentum-dependent asymmetry is observed for muon neutrinos, with events beyond ~ 1 GeV/c yielding an asymmetry of -0.3. This asymmetry was explained as resulting from $\nu_\mu \rightarrow \nu_\tau$ oscillations. Figure 2.3 shows the ratio of the number of events observed to the number of events predicted without oscillation, along with a similar ratio where observed events are replaced by an oscillation hypothesis using the SK best-fit, which clearly shows the deviation from the expected value of 1 in the absence of oscillation, along with a good fit to the oscillation hypothesis.

2.2 Theory

2.2.1 Weak interaction

The weak interaction is so named by virtue of the fact that, for small momentum transfer, electromagnetic and strong processes dominate over weak processes where such processes are allowed.

The weak interaction is mediated by three bosons; the charged W^- and W^+ bosons and the neutral Z boson. These give rise to two fundamental weak vertices, one neutral and one charged, which for the case of leptons can be seen in fig. 2.4. The neutral vertex has the property that the outgoing lepton is the same as the incident lepton, whereas the charged vertex does not respect flavour and therefore

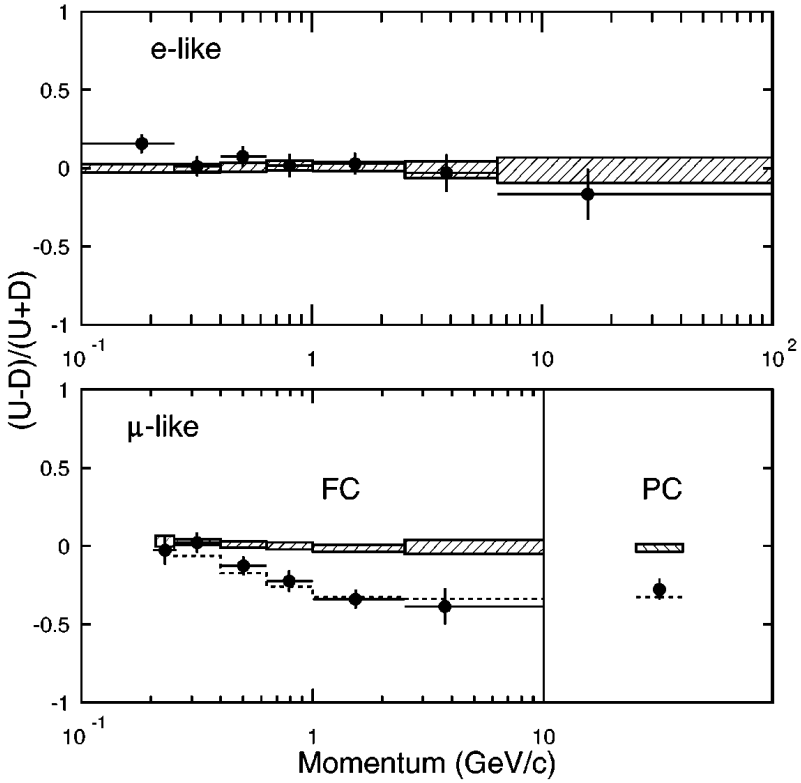

Figure 2.2: Asymmetry in upward and downward going events at SK. Shaded regions represent the predicted asymmetry in the absence of oscillation, while the dashed line represents $\nu_\mu \leftrightarrow \nu_\tau$ oscillations under the best-fit oscillation hypothesis. Fully contained (FC) events deposit all of their Cherenkov light in the inner detector. Partially contained (PC) events deposit some light in the outer detector. Reproduced from [29]

the outgoing and incident leptons are not the same. CC weak interactions are the only processes with this property and it is these interactions that provide the signal at T2K (see section 4.2.2).

Unlike the photon and gluons which act as mediators for the electromagnetic and strong interactions respectively, the weak mediators are (very) massive [30]:

$$M_W = 80.379 \pm 0.012 \text{ GeV}$$
$$M_Z = 91.1876 \pm 0.0021 \text{ GeV}$$

It is this fact that makes interactions mediated by these bosons weak. When considering energies well below the weak mediator masses, the amplitude of the process simplifies such that it can be expressed in terms of a ratio of the relevant weak

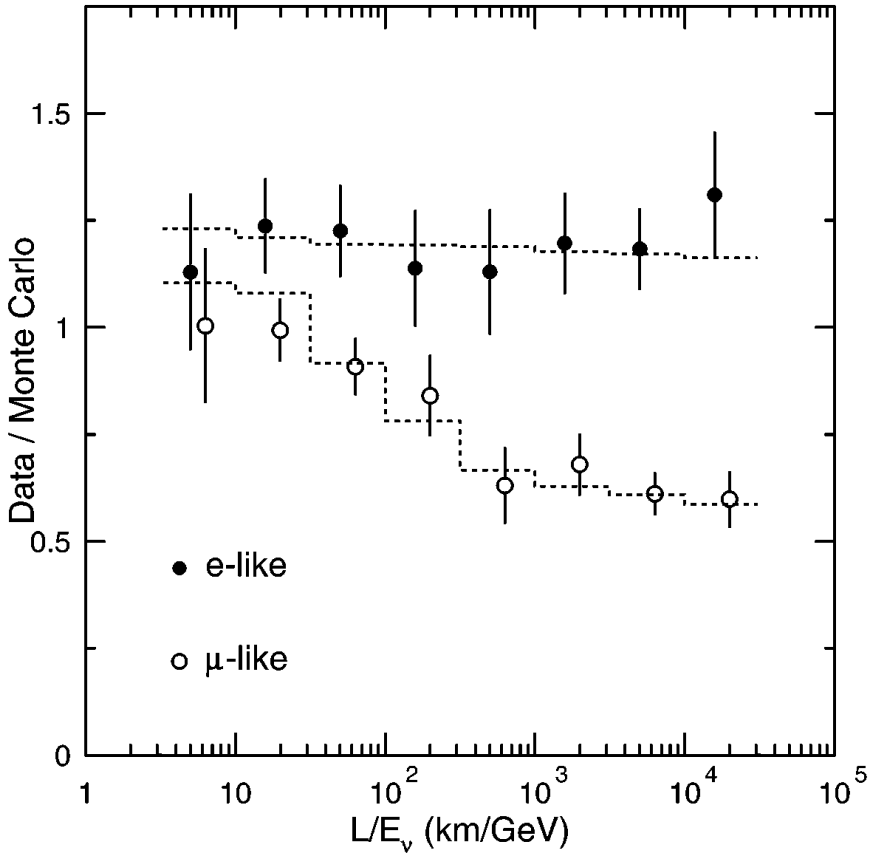

Figure 2.3: The ratio of observed events to predicted events in the absence of oscillation. Dashed lines represent the ratio of predicted events under the best-fit oscillation hypothesis to predicted events in the absence of oscillation. Reproduced from [29]

coupling constant, g_w or g_z and the mass of the relevant mediator, M_W or M_Z, $(g_w/M_W)^2$ [31]. From the Particle Data Group (PDG) [30] one can determine the values $g_w \simeq 0.653$ and $g_z \simeq 0.741$ and from there the corresponding fine structure constants ($\alpha = g_x^2/4\pi$), $\alpha_w \simeq 1/30$ and $\alpha_z \simeq 1/23$. This compares to the given value of the electromagnetic fine structure constant $\alpha \simeq 1/137$. It is clear that the weak nature of the interaction is not due to a small intrinsic coupling constant, as the weak constants are, in fact, larger than the electromagnetic equivalent, rather it is due to the massive nature of the mediator in the denominator.

The practical implication of the small interaction cross-sections of the neutrino due to its weak nature is that it is very difficult to detect and therefore experiments require both extremely large fluxes of neutrinos and large detector masses to accumulate sufficient numbers of events for useful study.

(a) Neutral current (b) Charged current

Figure 2.4: Fundamental weak vertices.

A notable property of weak interactions is that of chirality, which is related to the concept of helicity. Helicity is defined by

$$h \equiv \frac{\vec{s} \cdot \vec{p}}{p} \tag{2.15}$$

where $\vec{s}$ is the spin of the particle and $\vec{p}$ is its momentum. For massless spin-$\frac{1}{2}$ particles this quantity is well-defined; when the projection of spin onto momentum is parallel to momentum one has right-handed helicity ($h = \frac{1}{2}$) and when the projection of spin onto momentum is anti-parallel to momentum one has left-handed helicity ($h = -\frac{1}{2}$). However, neutrinos are massive particles and therefore a Lorentz boost can reverse the momentum without changing the spin, thereby changing the helicity[1]. The Lorentz invariant quantity for massive particles is provided by the concept of chirality. The chiral projection operators split a Dirac spinor into left- and right-handed components. In particular for a particle spinor, u, we have [33]

$$u_L = P_L u = \frac{1-\gamma^5}{2} u, \quad u_R = P_R u = \frac{1+\gamma^5}{2} u \tag{2.16}$$

with corresponding adjoint chiral spinors:

$$\overline{u_L} = \overline{u} P_R = \overline{u} \frac{1+\gamma^5}{2}, \quad \overline{u_R} = \overline{u} P_L = \overline{u} \frac{1-\gamma^5}{2} \tag{2.17}$$

where $\gamma^5 = i\gamma^0\gamma^1\gamma^2\gamma^3$ and γ^μ are the four gamma matrices of the Dirac equation. The antiparticle spinor, v, has chiral components [33]

$$v_L = P_R v = \frac{1+\gamma^5}{2} v, \quad v_R = P_L v = \frac{1-\gamma^5}{2} v \tag{2.18}$$

[1]Given that neutrinos are almost massless, experimentally we observe well-defined helicity in neutrinos [32]

with corresponding adjoint chiral spinors:

$$\overline{v_L} = \overline{v}P_L = \overline{v}\frac{1-\gamma^5}{2}, \quad \overline{v_R} = \overline{v}P_R = \overline{v}\frac{1+\gamma^5}{2} \tag{2.19}$$

In addition to the Lorentz invariance of these chiral quantities a second key property of weak interactions emerges if we look at the contribution, known as the weak current, j_μ, to the amplitude of the fundamental weak vertex in fig. 2.4b, which is given by [31]:

$$j_\mu = \overline{u_\nu}\gamma_\mu \left(\frac{1-\gamma^5}{2}\right) u_l \tag{2.20}$$

where u_ν and u_l are, respectively, the standard Dirac spinors for the neutrino and lepton associated with this fundamental vertex. Given that $(P_L)^2 = P_L$ and noting also that γ^5 anticommutes with γ_μ ($\gamma^5\gamma^\mu = -\gamma^\mu\gamma^5$) [34], the weak current can be rewritten as follows:

$$\begin{aligned} j_\mu &= \overline{u_\nu}\gamma_\mu \left(\frac{1-\gamma^5}{2}\right) u_l \\ &= \overline{u_\nu}\gamma_\mu \left(\frac{1-\gamma^5}{2}\right)\left(\frac{1-\gamma^5}{2}\right) u_l \quad \because P_L = (P_L)^2 \\ &= \overline{u_\nu}\left(\frac{1+\gamma^5}{2}\right)\gamma_\mu \left(\frac{1-\gamma^5}{2}\right) u_l \quad \because \gamma^5\gamma^\mu = -\gamma^\mu\gamma^5 \\ &= \overline{u_{\nu,L}}\gamma_\mu u_{l,L} \end{aligned} \tag{2.21}$$

Equation (2.21) shows that, in terms of chiral spinors, the fundamental weak vertex involves only the coupling of left-handed particles. If we now consider the fundamental vertex in which we exchange the particles for anti-particles we have the following weak current contribution:

$$\begin{aligned} j_\mu &= \overline{v_\nu}\gamma_\mu \left(\frac{1-\gamma^5}{2}\right) v_l \\ &= \overline{v_\nu}\gamma_\mu \left(\frac{1-\gamma^5}{2}\right)\left(\frac{1-\gamma^5}{2}\right) v_l \\ &= \overline{v_\nu}\left(\frac{1+\gamma^5}{2}\right)\gamma_\mu \left(\frac{1-\gamma^5}{2}\right) v_l \\ &= \overline{v_{\nu,R}}\gamma_\mu v_{l,R} \end{aligned} \tag{2.22}$$

Equation (2.22) shows that, in terms of chiral spinors, the fundamental weak vertex with particles exchanged for anti-particles involves only the coupling of right-handed anti-particles. We can therefore see that the weak force is a chiral interaction and

the Standard Model (SM) permits only the coupling of left-handed particles and right-handed antiparticles to the weak bosons.

2.2.2 Neutrino oscillation

In a three-flavour framework, neutrinos can be described in terms of flavour states $(\nu_e, \nu_\mu, \nu_\tau)$ and mass states (ν_1, ν_2, ν_3). The relationship between the flavour states and the mass states is given by [33]

$$|\nu_\alpha\rangle = \sum_{k=1}^{3} U^*_{\alpha k} |\nu_k\rangle \tag{2.23}$$

$$|\nu_k\rangle = \sum_{\beta=e,\mu,\tau} U_{\beta k} |\nu_\beta\rangle \tag{2.24}$$

From here on we'll assume that sums over flavour and mass states are over all possible flavour and mass states. Here, $U^*_{\alpha k}$ can be thought of as the amplitude for the ν_α created in a CC interaction being of mass state ν_i and $U_{\beta k}$ can be thought of as the amplitude for the lepton created by the propagating ν_i upon detection being of type β [35]. The mixing matrix, U, known as the Pontecorvo-Maki-Nakagawa-Sakata (PMNS) matrix, is [30]:

$$\begin{bmatrix} c_{12}c_{13} & s_{12}c_{13} & s_{13}e^{-i\delta} \\ -s_{12}c_{23} - c_{12}s_{23}s_{13}e^{i\delta} & c_{12}c_{23} - s_{12}s_{23}s_{13}e^{i\delta} & s_{23}c_{13} \\ s_{12}s_{23} - c_{12}c_{23}s_{13}e^{i\delta} & -c_{12}s_{23} - s_{12}c_{23}s_{13}e^{i\delta} & c_{23}c_{13} \end{bmatrix} \tag{2.25}$$

where $c_{ij} = \cos\theta_{ij}$, $s_{ij} = \sin\theta_{ij}$, θ_{ij} are the mixing angles and δ is the CP violating phase. It is clear that for non-zero mixing angles the flavour states are not the same as the mass states, but are, in fact, a superposition of the mass states and therefore, under these conditions, a neutrino with a well-defined flavour upon creation in a charged-current weak interaction is a superposition of three mass states.

One can then ask how the mass states evolve over time. The mass states are eigenstates of the Hamiltonian, H, [33]

$$H |\nu_k\rangle = E_k |\nu_k\rangle \tag{2.26}$$

where $E_k = \sqrt{\vec{p}^2 + m_k^2}$ is the energy eigenvalue. The time evolution is then given by the Schrödinger equation

$$i\frac{\mathrm{d}}{\mathrm{d}t} |\nu_k(t)\rangle = H |\nu_k(t)\rangle \tag{2.27}$$

with the plane wave solution [33]

$$|\nu_k(t)\rangle = e^{-iE_k t}\,|\nu_k\rangle \tag{2.28}$$

The factor $e^{-iE_k t}$ is the amplitude for ν_i to propagate for a time t. Substituting eq. (2.28) into eq. (2.23) then provides the time evolution of the flavour state $|\nu_\alpha\rangle = |\nu_\alpha(t=0)\rangle$ as

$$|\nu_\alpha(t)\rangle = \sum_k U^*_{\alpha k} e^{-iE_k t}\,|\nu_k\rangle \tag{2.29}$$

A further substitution of eq. (2.24) into eq. (2.29) yields

$$|\nu_\alpha(t)\rangle = \sum_\beta \left[\sum_k U^*_{\alpha k} U_{\beta k} e^{-iE_k t}\right] |\nu_\beta\rangle \tag{2.30}$$

and it can therefore be seen that if the PMNS matrix is not diagonal (i.e. it contains non-zero mixing angles), then a neutrino created with a well-defined flavour eigenstate can evolve in time to become a superposition of flavour eigenstates. The amplitude of the transition from $\nu_\alpha \to \nu_\beta$ is then given by [33]

$$A_{\nu_\alpha \to \nu_\beta}(t) \equiv \langle \nu_\beta | \nu_\alpha(t)\rangle = \sum_k U^*_{\alpha k} U_{\beta k} e^{-iE_k t} \tag{2.31}$$

with the corresponding probability [33]

$$P_{\nu_\alpha \to \nu_\beta}(t) \equiv \left|A_{\nu_\alpha \to \nu_\beta}(t)\right|^2 = \sum_k \sum_j U^*_{\alpha k} U_{\beta k} U_{\alpha j} U^*_{\beta j} e^{-i(E_k - E_j)t} \tag{2.32}$$

In the highly relativistic case of accelerator neutrinos, the binomial approximation can be used to express the energy eigenvalue, E_k, as

$$E_k \approx E + \frac{m_k^2}{2E} \tag{2.33}$$

where $E = |\vec{p}|$, i.e. the neutrino energy neglecting the mass contribution. This gives

$$E_k - E_j \approx \frac{m_k^2 - m_j^2}{2E} = \frac{\Delta m^2_{kj}}{2E} \tag{2.34}$$

and so the transition probability can be approximated in terms of this squared-mass

difference, Δm^2_{kj}:

$$P_{\nu_\alpha \to \nu_\beta}(t) = \sum_k \sum_j U^*_{\alpha k} U_{\beta k} U_{\alpha j} U^*_{\beta j} \exp\left\{ \frac{-i\Delta m^2_{kj} t}{2E} \right\} \tag{2.35}$$

In oscillation experiments, propagation time is not measured, but the distance L between the neutrino source and the detector is known. Using the fact that accelerator neutrinos are highly relativistic, the approximation $t = L$ can be used and so

$$P_{\nu_\alpha \to \nu_\beta}(L, E) = \sum_k \sum_j U^*_{\alpha k} U_{\beta k} U_{\alpha j} U^*_{\beta j} \exp\left\{ \frac{-i\Delta m^2_{kj} L}{2E} \right\} \tag{2.36}$$

We now have a transition probability specified in terms of the quantities U (and thereby the quantities $\theta_{12}, \theta_{13}, \theta_{23}$ and δ), $\Delta m^2_{21}, \Delta m^2_{32}$, L and E. L and E are set by the experiment, the elements of U determine the amplitude of the oscillations, while the squared-mass differences contribute to the phases of the neutrino oscillations (along with L and E).

A further useful step is to separate the oscillation probability into real and imaginary parts [33]:

$$\begin{aligned} P_{\nu_\alpha \to \nu_\beta}(L, E) = \delta_{\alpha\beta} &- 4 \sum_{k>j} \mathrm{Re}\left\{ U^*_{\alpha k} U_{\beta k} U_{\alpha j} U^*_{\beta j} \right\} \sin^2\left(\frac{\Delta m^2_{kj} L}{4E} \right) \\ &+ 2 \sum_{k>j} \mathrm{Im}\left\{ U^*_{\alpha k} U_{\beta k} U_{\alpha j} U^*_{\beta j} \right\} \sin\left(\frac{\Delta m^2_{kj} L}{2E} \right) \end{aligned} \tag{2.37}$$

where $\delta_{\alpha\beta}$ is the Kronecker delta. Such a separation makes it immediately clear that neutrino oscillation will only occur if at least one neutrino has mass and that, furthermore, at least one of those neutrinos has a mass that is different from the others, so observation of neutrino oscillation implies neutrino mass.

The separation into real and imaginary parts also allows for a simplified expression for the probability that a neutrino survives in its original flavour, because for $\alpha = \beta$, we have $U^*_{\alpha k} U_{\beta k} U_{\alpha j} U^*_{\beta j} = |U_{\alpha k}|^2 |U_{\alpha j}|^2$, which is real, therefore

$$P_{\nu_\alpha \to \nu_\alpha}(L, E) = 1 - 4 \sum_{k>j} |U_{\alpha k}|^2 |U_{\alpha j}|^2 \sin^2\left(\frac{\Delta m^2_{kj} L}{4E} \right) \tag{2.38}$$

In addition, for the anti-neutrino transition, $\bar{\nu}_\alpha \to \bar{\nu}_\beta$, the sign of the imaginary part

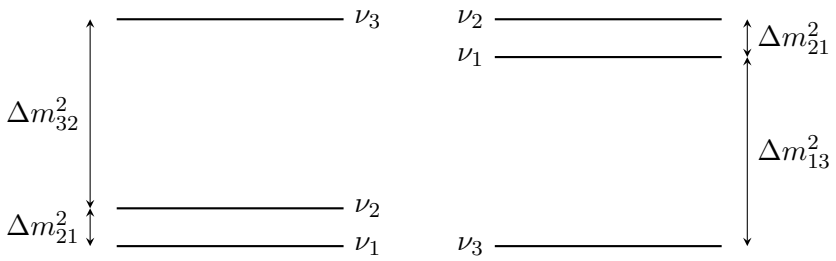

Figure 2.5: Normal (left) and inverted (right) mass orderings.

of eq. (2.37) flips, giving [35]

$$P_{\nu_\alpha \to \nu_\beta}(L,E) = \delta_{\alpha\beta} - 4\sum_{k>j} \mathrm{Re}\{U^*_{\alpha k}U_{\beta k}U_{\alpha j}U^*_{\beta j}\} \sin^2\left(\frac{\Delta m^2_{kj}L}{4E}\right) - 2\sum_{k>j} \mathrm{Im}\{U^*_{\alpha k}U_{\beta k}U_{\alpha j}U^*_{\beta j}\} \sin\left(\frac{\Delta m^2_{kj}L}{2E}\right) \tag{2.39}$$

This change of sign is significant, because it follows that if U is complex, i.e. $\delta \neq 0, \pi$, then $P_{\nu_\alpha \to \nu_\beta} \neq P_{\bar{\nu}_\alpha \to \bar{\nu}_\beta}$, implying leptonic CP violation.

2.2.3 Neutrino mass

Though the observation of neutrino oscillation has established that neutrinos have mass, the absolute scale remains unknown and furthermore, despite measurements of the mass-squared differences, the ordering of the neutrino masses is not fully established, with two possibilities remaining. The allowed mass orderings are known as normal ordering, for which $m_1 < m_2 < m_3$ and inverted ordering, for which $m_3 < m_1 < m_2$, as shown in fig. 2.5. The confirmation that neutrinos have mass also presents another complication. In the SM fermion masses arise from the Higgs mechanism [33] and involve the coupling of left-handed and right-handed fields, such that for neutrinos the Dirac mass term is [34]

$$\mathcal{L}_D = -m_D \overline{\nu}\nu = -m_D\left(\overline{\nu_R}\nu_L + \overline{\nu_L}\nu_R\right) \tag{2.40}$$

The implication of the existence of a right-handed neutrino field is problematic, given that there is no evidence for such a field. Without a right-handed neutrino field, the Dirac mass term is zero and the SM therefore predicts massless neutrinos. An alternative to the Dirac mass term is the Majorana mass term. The idea is to construct a mass-term using the left-handed neutrino field only, by finding a right-handed function of ν_L that can be substituted in place of ν_R. The solution

proposed by Majorana was to apply the charge conjugation operator to the adjoint left-handed spinor

$$\nu_L^C = \hat{C}\overline{\nu_L} \tag{2.41}$$

where the anti-particle is indicated by the superscript C to avoid notational confusion between adjoint spinors and antiparticles. To see that this is a right-handed function we can simply apply the chiral projection operators. Starting with P_R

$$\begin{aligned} P_R\left(\nu_L^C\right) &= P_R\left[\left(\frac{1+\gamma^5}{2}\right)\nu^C\right] \\ &= \left(\frac{1+\gamma^5}{2}\right)\left(\frac{1+\gamma^5}{2}\right)\nu^C \\ &= \left(\frac{1+\gamma^5}{2}\right)\nu^C \\ &= \nu_L^C \end{aligned} \tag{2.42}$$

we retrieve our starting field and when applying P_L

$$\begin{aligned} P_L\left(\nu_L^C\right) &= P_L\left[\left(\frac{1+\gamma^5}{2}\right)\nu^C\right] \\ &= \left(\frac{1-\gamma^5}{2}\right)\left(\frac{1+\gamma^5}{2}\right)\nu^C \\ &= \left(\frac{1-\gamma^5+\gamma^5-1}{4}\right)\nu^C \\ &= 0 \end{aligned} \tag{2.43}$$

the field vanishes. This allows the mass term to be rewritten as [33]

$$\mathcal{L}_M = -\tfrac{1}{2} m_M \left(\overline{\nu_L^C}\nu_L + \overline{\nu_L}\nu_L^C\right) \tag{2.44}$$

where the factor 1/2 is introduced to avoid double-counting because ν_L^C and $\overline{\nu_L}$ are not independent. The coupling of the particle and antiparticle via the Majorana mass, m_M, does not violate charge conservation for the neutral neutrino as it would for charged leptons, but it does imply that the neutrino and antineutrino are the same particle.

2.2.4 Neutrino oscillation in matter

All of the preceding discussion has assumed neutrinos propagating in a vacuum. For T2K, however, the neutrinos propagate through Earth's crust, which is composed

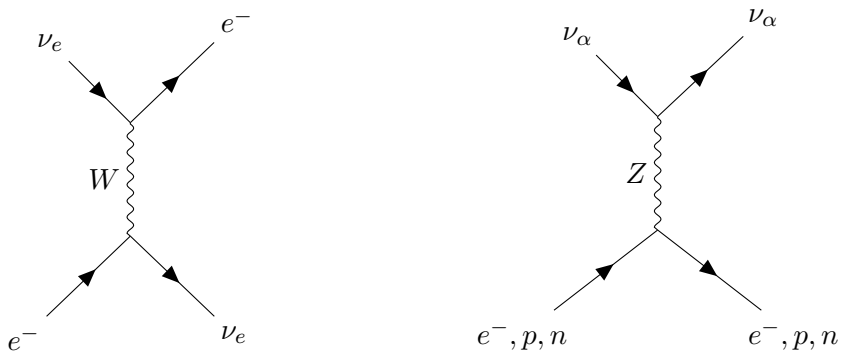

(a) CC (b) NC

Figure 2.6: Coherent forward scattering processes.

of matter with an approximately constant density. Wolfenstein showed [36] that transit through matter introduced a potential due to coherent forward scattering (see fig. 2.6) with particles in the medium. The potential resulting from the CC interactions is given by [33]

$$V_{CC} = \sqrt{2} G_F N_e \tag{2.45}$$

where G_F is the Fermi constant and N_e is the number density of electrons in the medium. The corresponding NC potential is given by [33]

$$V_{NC} = -\tfrac{1}{2}\sqrt{2} G_F N_n \tag{2.46}$$

where N_n is the number density of neutrons in the medium; in the NC case the effects of protons and electrons cancel for neutral matter. All flavours have the same contribution from the NC potential and so this has no effect on neutrino oscillation for a three-flavour framework. The result of the potential due to matter is a modification to the flavour Hamiltonian [33]

$$\mathcal{H} = -\frac{1}{2E}\left(U M^2 U^\dagger + A\right) \tag{2.47}$$

where

$$M^2 = \begin{bmatrix} 0 & 0 & 0 \\ 0 & \Delta m^2_{21} & 0 \\ 0 & 0 & \Delta m^2_{31} \end{bmatrix}, \qquad A = 2EV_{CC} \begin{bmatrix} 1 & 0 & 0 \\ 0 & 0 & 0 \\ 0 & 0 & 0 \end{bmatrix}$$

The implications of the matter effect for neutrino oscillation probabilities can be determined in a two-flavour approximation. In a two-flavour approximation the

vacuum mixing matrix is described with a single mixing angle, θ, as

$$U = \begin{bmatrix} \cos\theta & \sin\theta \\ -\sin\theta & \cos\theta \end{bmatrix} \tag{2.48}$$

and the single mass-squared difference is $\Delta m^2 = m_2^2 - m_1^2$, defined to be positive for convenience. The transition probability, $P_{\nu_\alpha \to \nu_\beta}$, for $\alpha \neq \beta$ is then [33]

$$P_{\nu_\alpha \to \nu_\beta}(L, E) = \sin^2(2\theta) \sin^2\left(\frac{\Delta m^2 L}{4E}\right) \tag{2.49}$$

Introducing matter effects yields an effective Hamiltonian in the flavour basis with the form [33]

$$\mathcal{H}_F = \frac{1}{4E} \begin{bmatrix} -\Delta m^2 \cos 2\theta + A_{CC} & \Delta m^2 \sin 2\theta \\ \Delta m^2 \sin 2\theta & \Delta m^2 \cos 2\theta - A_{CC} \end{bmatrix}$$

where $A_{CC} = 2EV_{CC}$. An effective Hamiltonian in the mass basis can be found by diagonalisation using the matrix U_M [33]

$$U_M = \begin{bmatrix} \cos\theta_M & \sin\theta_M \\ -\sin\theta_M & \cos\theta_M \end{bmatrix} \tag{2.50}$$

which is the effective mixing matrix in matter, such that

$$\mathcal{H}_M = U_M^T \mathcal{H}_F U_M = \frac{1}{4E} \begin{bmatrix} -\Delta m_M^2 & 0 \\ 0 & \Delta m_M^2 \end{bmatrix} \tag{2.51}$$

We've moved from a two-parameter description in a vacuum with mixing angle θ and mass-squared difference Δm^2, to a two-parameter description in matter with an effective mixing angle θ_M and effective mass-squared difference Δm_M^2, given by [33]

$$\Delta m_M^2 = \sqrt{\left(\Delta m^2 \cos 2\theta - A_{CC}\right)^2 + \left(\Delta m^2 \sin 2\theta\right)^2} \tag{2.52}$$

$$\sin 2\theta_M = \frac{\Delta m^2 \sin 2\theta}{\Delta m_M^2} \tag{2.53}$$

For constant density matter the transition probability becomes [33]

$$P_{\nu_\alpha \to \nu_\beta}(L, E) = \sin^2(2\theta_M) \sin^2\left(\frac{\Delta m_M^2 L}{4E}\right) \tag{2.54}$$

which has the same structure as the two-neutrino vacuum case eq. (2.49), but with the mixing angle and mass-squared difference replaced by their corresponding effective values in matter. The electron number density relevant to T2K is $N_e \sim 1.7 \times 10^{30}\,\mathrm{m}^{-3}$ [33], yielding $A_{CC} \approx 1.5 \times 10^{-4}\,\mathrm{eV}^2$ when $E = 600\,\mathrm{MeV}$. Setting $\Delta m^2 = 2.463 \times 10^{-3}\,\mathrm{eV}^2$ and $\theta = 46.5°$ [37] the effective parameters are found to be

$$\Delta m^2_M \approx 2.5 \times 10^{-3}\,\mathrm{eV}^2 \tag{2.55}$$

$$\theta_M \approx 42° \tag{2.56}$$

and so the effective parameters relevant for T2K are barely modified by the matter effect.

2.2.5 CP violation

During the high-energy phase of the early Universe the processes

$$\gamma + \gamma \leftrightarrow p + \bar{p} \tag{2.57}$$

occurred with equal probability. However, as the Universe expanded and temperature decreased, so did the mean energy of photons, which dropped out of thermal equilibrium with the baryons and antibaryons and thus the forward process was suppressed, leaving only the reverse process

$$p + \bar{p} \rightarrow \gamma + \gamma \tag{2.58}$$

Additionally, the expansion of the Universe reduced the number density of baryons and antibaryons, such that this process also became very rare, effectively fixing the number of baryons and antibaryons. The predicted number density of baryons, n_B and antibaryons, $n_{\bar{B}}$, relative to the number density of photons, n_γ, is [34]

$$n_B = n_{\bar{B}} \approx 10^{-18} n_\gamma \tag{2.59}$$

However, observation does not agree with this prediction, finding a difference in the number densities of baryons and antibaryons [34]

$$n_B - n_{\bar{B}} \approx 10^{-9} n_\gamma \tag{2.60}$$

That we exist in a matter-dominated Universe despite the expectation that the early Universe would have been composed of equal parts matter and antimatter is an observation in need of an explanation. According to Sakharov [38], three conditions must be met to explain the asymmetry:

1. Baryon number is not conserved (so processes exist that can preferentially create baryons (antibaryons) over antibaryons (baryons))
2. C and CP are not conserved (so processes that preferentially create baryons are not balanced by processes preferentially creating antibaryons)
3. Departure from thermal equilibrium (so baryon number violating processes are not balanced by their inverse reactions)

while CP violation has been demonstrated in the quark sector, it is of insufficient magnitude to explain the asymmetry and so an additional source of CP violation is required and this is a key motivation in searching for CP violation in the lepton sector.

Before discussing CP, it is worthwhile to introduce the component parts; charge conjugation (C) and parity (P). The operation of charge conjugation converts a particle, $|p\rangle$, into its antiparticle, $|\bar{p}\rangle$:

$$\hat{C}\,|p\rangle = |\bar{p}\rangle \tag{2.61}$$

For Dirac spinors the particular form of the charge conjugation operator is $\hat{C}\psi = i\gamma^2\psi^*$ [34] and a second application of $\hat{C}$ gives us the original particle:

$$\hat{C}^2\,|p\rangle = |p\rangle \tag{2.62}$$

and so it is clear that the eigenvalues of this operator are ± 1. Furthermore, charge conjugation is multiplicative, so the eigenvalue for a system is the product of the eigenvalues of its components. Charge conjugation is not a symmetry of weak interactions, because the application of $\hat{C}$ to a left-handed neutrino would result in a left-handed antineutrino, which does not exist, as established in section 2.2.1.

The operation of parity takes a particle $\psi(t, \vec{x})$ and inverts its spatial components to give $\psi(t, -\vec{x})$: [34]

$$\hat{P}\psi(t, \vec{x}) = \psi(t, -\vec{x}) \tag{2.63}$$

For Dirac spinors, this operator takes the form $\hat{P} = \gamma^0$ [34]. It should be noted that when applied to a standard vector, $\vec{x}$, we have $\hat{P}\vec{x} = -\vec{x}$, but when applied to the

cross-product of two vectors, $\vec{z} = \vec{x} \times \vec{y}$, the application of the parity operator to each of $\vec{x}$ and $\vec{y}$ results in $\hat{P}\vec{z} = \vec{z}$. Clearly, $\hat{P}$ acts differently on ordinary vectors and these latter, so called axial vectors, a point we will return to below. As with charge conjugation, a second application of $\hat{P}$ returns us to the original state

$$\hat{P}^2\psi(t,\vec{x}) = \psi(t,\vec{x}) \tag{2.64}$$

giving us an eigenvalue of $+1$ for axial vectors and -1 for vectors. The parity of fermions and antifermions is required to be opposite in quantum field theory [31] and are arbitrarily chosen to be $+1$ and -1 respectively [2], while the weak bosons possess negative parity [34]. As with charge conjugation, the parity of a composite system is the product of the parities of its constituents.

While parity is respected in strong and electromagnetic interactions [31], the V-A structure of the weak interactions results in the violation of parity in weak interactions [39] due to the different behaviour of the vector and axial vector parts noted here. This can be seen by an application of the parity operation to the weak current introduced in section 2.2.1:

$$j_\mu = \overline{u_\nu}\gamma_\mu \left(\frac{1-\gamma^5}{2}\right) u_l \tag{2.65}$$

Application of the parity operator and noting that $(\gamma_0 u_\nu)^\dagger = u_\nu^\dagger \gamma_0 = \overline{u_\nu}$ [34] yields

$$\overline{u_\nu}\gamma_0 \frac{\gamma_\mu}{2}\gamma_0 u_l - \overline{u_\nu}\gamma_0 \frac{\gamma_\mu}{2}\gamma_5\gamma_0 u_l \tag{2.66}$$

Splitting eq. (2.66) into its time-like and space-like components, we find the time-like component is

$$\begin{aligned}
& \overline{u_\nu}\gamma_0 \frac{\gamma_0}{2}\gamma_0 u_l - \overline{u_\nu}\gamma_0 \frac{\gamma_0}{2}\gamma_5\gamma_0 u_l \\
\Rightarrow\quad & \overline{u_\nu}\gamma_0 \frac{\gamma_0}{2}\gamma_0 u_l + \overline{u_\nu}\gamma_0 \frac{\gamma_0}{2}\gamma_0\gamma_5 u_l \qquad \because \gamma^0\gamma^5 = -\gamma^5\gamma^0 \\
\Rightarrow\quad & \overline{u_\nu}\frac{\gamma_0}{2} u_l + \overline{u_\nu}\frac{\gamma_0}{2}\gamma_5 u_l \\
\Rightarrow\quad & \overline{u_\nu}\gamma_0 \left(\frac{1+\gamma_5}{2}\right) u_l
\end{aligned} \tag{2.67}$$

We can see that the vector part is unchanged by the parity operator, whereas the

[2] this choice is relevant to the definition $\hat{P} = \gamma^0$; the opposite convention $\hat{P} = -\gamma^0$ would work equally well [34]

axial vector part swaps sign. In a similar fashion, the space-like components produce

$$\begin{aligned}
& \overline{u_\nu}\gamma_0\frac{\gamma_k}{2}\gamma_0 u_l - \overline{u_\nu}\gamma_0\frac{\gamma_k}{2}\gamma_5\gamma_0 u_l \\
\Rightarrow \quad & -\overline{u_\nu}\gamma_0\gamma_0\frac{\gamma_k}{2}u_l - \overline{u_\nu}\gamma_0\gamma_0\frac{\gamma_k}{2}\gamma_5 u_l \qquad \because \gamma^\mu\gamma^\nu = -\gamma^\nu\gamma^\mu \\
\Rightarrow \quad & -\overline{u_\nu}\frac{\gamma_k}{2}u_l - \overline{u_\nu}\frac{\gamma_k}{2}\gamma_5 u_l \\
\Rightarrow \quad & -\overline{u_\nu}\gamma_k\left(\frac{1+\gamma_5}{2}\right)u_l
\end{aligned} \tag{2.68}$$

Here, the vector part swaps sign due to the parity operation, but the axial vector part remains unchanged. Combining eq. (2.67) and eq. (2.68) yields the weak current under a parity operation

$$\begin{aligned}
j_\mu &= \overline{u_\nu}\gamma_0\left(\frac{1+\gamma_5}{2}\right)u_l - \overline{u_\nu}\gamma_k\left(\frac{1+\gamma_5}{2}\right)u_l \\
&= \overline{u_\nu}\gamma^0\left(\frac{1+\gamma_5}{2}\right)u_l + \overline{u_\nu}\gamma^k\left(\frac{1+\gamma_5}{2}\right)u_l \qquad \because \gamma_k = -\gamma^k \\
&= \overline{u_\nu}\gamma^\mu\left(\frac{1+\gamma_5}{2}\right)u_l
\end{aligned} \tag{2.69}$$

Proceeding in the manner introduced in section 2.2.1, we find

$$\begin{aligned}
j_\mu &= \overline{u_\nu}\gamma^\mu\left(\frac{1+\gamma_5}{2}\right)u_l \\
&= \overline{u_\nu}\gamma^\mu\left(\frac{1+\gamma_5}{2}\right)\left(\frac{1+\gamma_5}{2}\right)u_l \qquad \because P_R = (P_R)^2 \\
&= \overline{u_\nu}\left(\frac{1-\gamma_5}{2}\right)\gamma^\mu\left(\frac{1+\gamma_5}{2}\right)u_l \qquad \because \gamma^5\gamma^\mu = -\gamma^5\gamma^\mu \\
&= \overline{u_{\nu,R}}\gamma_\mu u_{l,R}
\end{aligned} \tag{2.70}$$

To summarise, under a parity operation the weak current transforms left-handed particles (see eq. (2.21)) to right-handed particles

$$\overline{u_{\nu,L}}\gamma_\mu\left(\frac{1-\gamma^5}{2}\right)u_{l,L} \xrightarrow{\hat{P}} \overline{u_{\nu,R}}\gamma^\mu\left(\frac{1+\gamma_5}{2}\right)u_{l,R} \tag{2.71}$$

which, as with charge conjugation, encounters a difficulty in that right-handed neutrinos do not exist, as established in section section 2.2.1. The CP operation is the combination of both the charge conjugation and parity operations. Starting from eq. (2.70), applying the charge conjugation operator and using $\gamma^5\gamma^\mu = -\gamma^5\gamma^\mu$,

$\gamma^0\gamma^2 = -\gamma^2\gamma^0$ and $\left(\gamma^k\right)^2 = -1$

$$\begin{aligned} j_\mu &= \overline{u_\nu}\left(\frac{1-\gamma_5}{2}\right)\gamma^\mu\left(\frac{1+\gamma_5}{2}\right)u_l \\ &= i\gamma_2\overline{v_\nu}\left(\frac{1-\gamma_5}{2}\right)\gamma^\mu\left(\frac{1+\gamma_5}{2}\right)i\gamma_2 v_l \\ &= -i^2\gamma_2\gamma_2\overline{v_\nu}\left(\frac{1+\gamma_5}{2}\right)\gamma^\mu\left(\frac{1-\gamma_5}{2}\right)i\gamma_2 v_l \\ &= -\overline{v_\nu}\left(\frac{1+\gamma_5}{2}\right)\gamma^\mu\left(\frac{1-\gamma_5}{2}\right)i\gamma_2 v_l \\ &= -\overline{v_{\nu,R}}\gamma_\mu v_{l,R} \end{aligned} \tag{2.72}$$

Thus, the parity operation takes a left-handed neutrino to a right-handed neutrino (note the overall change in sign is irrelevant), with the charge conjugation operation producing a right-handed antineutrino and so the combined operator is consistent with what we observe in nature; left-handed neutrinos and right-handed antineutrinos:

$$\overline{u_{\nu,L}}\gamma_\mu\left(\frac{1-\gamma^5}{2}\right)u_{l,L} \xrightarrow{\hat{CP}} -\overline{v_{\nu,R}}\gamma^\mu\left(\frac{1+\gamma_5}{2}\right)v_{l,R} \tag{2.73}$$

Any potential for CP violation is therefore not a result of the V - A structure of the weak interaction, rather it comes in the form of the physical phase, δ, in the mixing matrix, U [33]. If it is found that $U = U^*$, that is, U is real, then CP is conserved.

However, in the quark sector it was first demonstrated that not even CP provided a conserved quantity of weak interactions by measuring the decay of long-lived neutral kaons, K_L [40]. This long-lived kaon has CP = -1 and therefore should decay to three π, a composite system also possessing CP = -1 if CP is conserved. The observation of a two π decay, with CP = 1 conclusively demonstrated CP violation.

What is the magnitude of CP violation in the quark sector? This can be expressed in a manner that is independent of the chosen parametrisation of the mixing matrix by means of the Jarlskog invariant [41], which, in the quark sector is found to be $J_q = (3.15 \pm 0.15) \times 10^{-5}$ [30]. The Jarlskog invariant also offers the benefit that a maximum amount of CP violation can be defined [33]

$$|J|_{\max} = \frac{1}{6\sqrt{3}} \tag{2.74}$$

Clearly, $|J_q| \ll |J|_{\max}$ and this small effect means that quark sector CP violation is insufficient to explain the baryon asymmetry [42]. In the neutrino sector, the

Jarlskog invariant can be specified in terms of the standard parametrisation as: [33]

$$J_\nu = c_{12}s_{12}c_{23}s_{23}c_{13}^2 s_{13}\sin\delta \tag{2.75}$$

2.3 Current status of research

This section presents a brief overview of the current status of efforts to measure neutrino oscillation parameters (no consideration will be given to the Dirac or Majorana character of neutrinos, the absolute mass scale, or sterile neutrinos). While many experiments have contributed to the current state of our knowledge, a number being highlighted in section 2.1, this section will focus on contemporary and recently completed experiments.

2.3.1 $|\Delta m^2_{32}|$, θ_{23} and the mass ordering

Access to the so called atmospheric parameters and the mass ordering is provided principally by atmospheric-neutrino experiments and accelerator experiments. The MINOS (Main Injector Neutrino Oscillation Search) experiment [43] was a long-baseline accelerator experiment with a neutrino beam produced at the NuMI facility at Fermilab and plastic scintillator detectors on 1.04 km and 735 km baselines (the far detector having a 5.4 kton mass), but also took measurements of atmospheric neutrinos. MINOS had little sensitivity to the mass ordering, finding best-fits [43] for the atmospheric parameters in the inverted mass ordering

$$\begin{aligned} |\Delta m^2_{32}| &= 2.41^{+0.11}_{-0.09} \times 10^{-3}\ \text{eV}^2 \\ \sin^2(\theta_{23}) &= 0.41^{+0.26}_{-0.07} \end{aligned}$$

however, normal ordering intervals were not excluded at 1σ

$$\begin{aligned} |\Delta m^2_{32}| &= 2.37^{+0.09}_{-0.09} \times 10^{-3}\ \text{eV}^2 \\ \sin^2(\theta_{23}) &= 0.41^{+0.24}_{-0.06} \end{aligned}$$

More recent results from SK [44] prefer normal mass ordering over inverted mass ordering at between 81.9% and 96.7% probability when considering the range of oscillation parameters allowed at SK's 90% confidence level, with the normal mass

ordering best-fit of atmospheric parameters found to be

$$\begin{aligned} \left|\Delta m^2_{32}\right| &= 2.50^{+0.13}_{-0.31} \times 10^{-3}\ \text{eV}^2 \\ \sin^2(\theta_{23}) &= 0.587^{+0.036}_{-0.069} \end{aligned}$$

In addition to the preference for normal mass ordering, SK has a weak preference for the upper octant ($\sin^2(\theta_{23}) > 0.5$) at around 1σ.

T2K's latest result [37] is consistent with the SK result, finding

$$\begin{aligned} \left|\Delta m^2_{32}\right| &= 2.463^{+0.071}_{-0.070} \times 10^{-3}\ \text{eV}^2 \\ \sin^2(\theta_{23}) &= 0.526^{+0.032}_{-0.036} \end{aligned}$$

While T2K's fit of $\sin^2(\theta_{23})$ does not exclude maximal mixing, the Bayesian analysis also reported in [37] prefers the upper octant with a 78% posterior probability, along with an 87% posterior probability for the normal mass ordering.

NOvA (NuMI Off-Axis ν_e Appearance) is another long-baseline accelerator experiment [45], which, like MINOS, uses a neutrino beam from Fermilab's NuMI facility, but employing liquid-scintillator-based detectors at 1 km and 810 km baselines, with a 14 kton far detector. NOvA's latest results [45] find

$$\begin{aligned} \left|\Delta m^2_{32}\right| &= 2.44^{+0.08}_{-0.070} \times 10^{-3}\ \text{eV}^2 \\ \sin^2(\theta_{23}) &= 0.56^{+0.04}_{-0.04} \end{aligned}$$

with the inverted mass ordering rejected at the 95% confidence level. Though NOvA's best-fit is within the upper octant, maximal mixing is still allowed at the 1σ level, with a second, local minimum

$$\sin^2(\theta_{23}) = 0.47^{+0.04}_{-0.04}$$

The IceCube experiment [46] is an ice Cherenkov neutrino detector located within the ice of Antarctica, measuring both cosmic and atmospheric neutrinos. Within IceCube is the DeepCore detector [47], a more densely instrumented region located in the bottom centre region of IceCube's 1 km^3 volume. The latest result [47] from IceCube-DeepCore finds normal mass ordering best-fits (though current data has low sensitivity to the mass ordering)

$$\begin{aligned} \left|\Delta m^2_{32}\right| &= 2.31^{+0.11}_{-0.13} \times 10^{-3}\ \text{eV}^2 \\ \sin^2(\theta_{23}) &= 0.51^{+0.07}_{-0.09} \end{aligned}$$

It can be seen that the results from these various experiments are generally consistent and also provide similar precision, particularly for the contemporary experiments, with a general preference for the normal mass ordering and best-fits preferring the upper octant, though with maximal mixing still allowed. The most notable difference is the low value of $\left|\Delta m^2_{32}\right|$ at IceCube relative to T2K and NOvA, but this represents little more than a 1σ discrepancy.

2.3.2 Mixing angle θ_{13}

The mixing angle θ_{13} is accessible to accelerator experiments and reactor experiments. T2K's latest measurement [48] finds[3]

$$\sin^2(2\theta_{13}) = 0.105^{+0.027}_{-0.024}$$

The Double Chooz experiment [49] employs a liquid scintillator detector to measure the flux of $\bar{\nu}_e$ at a baseline of 1050 m from two nuclear reactor cores in France (the experiment has since added an identical near detector at 400 m [50]). Its latest published results [49] find

$$\sin^2(2\theta_{13}) = 0.090^{+0.032}_{-0.029}$$

RENO (Reactor Experiment for Neutrino Oscillation) [51] uses two 16 ton liquid scintillator targets to measure the $\bar{\nu}_e$ flux from 6 nuclear reactor cores at baselines of 290 m and 1380 m in South Korea. The latest results [51] from RENO report[4]

$$\sin^2(2\theta_{13}) = 0.086 \pm 0.008$$

Finally, the Daya Bay experiment [52] employs eight identical 20 ton fiducial mass liquid scintillator detectors measuring the $\bar{\nu}_e$ flux from six nuclear reactors. Four of the detectors act as near detectors on ~ 500 m baselines, while the remaining four act as far detectors on baselines of ~ 1.6 km. Daya Bay's latest result [52] provides the most precise of the current measurements of θ_{13}, finding[5]

$$\sin^2(2\theta_{13}) = 0.0841 \pm 0.0033$$

[3] T2K actually reports $\sin^2(\theta_{13})$, but here the result has been converted to $\sin^2(2\theta_{13})$ for ease of comparison with the reactor measurements.

[4] RENO's reported statistical and systematic errors have been added in quadrature.

[5] Daya Bay's reported statistical and systematic errors have been added in quadrature.

The various reported measurements of θ_{13} show good agreement, with the greatest precision currently provided by RENO and, in particular, Daya Bay.

2.3.3 CP violating phase, δ

The non-zero value of θ_{13} has made measurements of the CP violating phase, δ, accessible to the appearance channel of long-baseline neutrino oscillation experiments. T2K and NOvA provide the most precise constraints to date on the value of the CP violating phase. In particular, the latest result from T2K [37, 53] finds

$$\delta_{bestfit} = -1.87 \qquad \delta \in [-2.41, -1.17]$$

disfavouring the inverted mass ordering at almost the 2σ level and further excluding the CP conserving values of 0 and π at more than 2σ ($[-2.99, -0.59]$). NOvA's latest result [45] finds[6]

$$\delta = -2.48 \qquad \delta \in [-\pi, +0.38] \cup [+2.86, +\pi]$$

The current measurements of the two experiments are consistent (though uncertainties remain large), with best fits near the maximally CP violating value $-\pi/2$, though NOvA does not exclude CP conserving values at 1σ.

2.3.4 Global fits

Establishing the values for the various neutrino oscillation parameters that represent a reference set for our best knowledge of the sector is determined by global fits combining the different measurements from an array of neutrino experiments. The PDG reviews global analyses and selects one to use for the reference values, with the latest instantiation of the PDG [30] using the global fit performed by Capozzi *et al.* [54], incorporating data from T2K, NOvA, Daya Bay and Super-Kamiokande as of mid-2017 (note that more recent results are reported in the preceding sections). The best-fit parameters from this analysis can be seen in table 2.1[7].

2.3.5 Future plans

In addition to the continuing operation of a number of the aforementioned experiments in an effort to further refine our knowledge of the oscillation parameters, a

[6] NOvA reports the CP phase on the interval $[0, 2\pi]$, but here the result is shifted to the interval $-\pi, +\pi$ for easier comparison with T2K.

[7] In inverted ordering $\sin^2(\theta_{23})$ also has an allowed 1σ region in the lower octant; $[0.417, 0.448]$

Parameter	Best-fit and uncertainty	
Δm^2_{21}	$7.37^{+0.17}_{-0.16} \times 10^{-5}$ eV^2	
$\lvert\Delta m^2_{32}\rvert$	$2.49^{+0.04}_{-0.03} \times 10^{-3}$ eV^2	$\left(2.54 \pm 0.03 \times 10^{-3}\text{ eV}^2\right)$
$\sin^2(\theta_{12})$	$0.297^{+0.017}_{-0.016}$	
$\sin^2(\theta_{13})$	0.0215 ± 0.0007	$\left(0.0216^{+0.008}_{-0.009}\right)$
$\sin^2(\theta_{23})$	$0.425^{+0.021}_{-0.015}$	$\left(0.589^{+0.016}_{-0.022}\right)$
δ	$-1.95^{+0.72}_{-0.60}$	$\left(-2.17^{+0.97}_{-0.60}\right)$

Table 2.1: Neutrino oscillation parameter best-fits and 1σ uncertainties from a global fit. Values are for normal (inverted) ordering, or independent of mass ordering if only a single value is quoted. Reproduced from [54], with $|\Delta m^2_{32}|$ computed from the given value of $m^2_3 - (m^2_1 + m^2_2)/2$ and δ adjusted to fit the range $[-\pi, +\pi]$.

number of new experiments are planned to attempt to definitively determine if CP symmetry is violated in the lepton sector, what the mass ordering is and the octant of θ_{23}.

Atmospheric neutrinos

PINGU (Precision IceCube Next Generation Upgrade) [55] is a proposed addition to the IceCube experiment that will improve IceCube's sensitivity to low energy atmospheric neutrinos by further increasing the instrumentation density within a sub-region of DeepCore. The resultant improved ν_μ disappearance measurement will allow determination, within 4 years of operation, of the octant at the 3σ confidence level in normal mass ordering if $\sin^2(\theta_{23}) < 0.44$ or $\sin^2(\theta_{23}) > 0.58$ and further allow a 3σ determination of the mass ordering.

A conceptually similar experiment is ORCA (Oscillation Research with Cosmics in the Abyss) [56], also using a dense array of instrumentation to measure atmospheric neutrinos, but anchored in the deep ocean, rather than ice. ORCA's 1.8 Mton detector will have the sensitivity to determine the mass ordering at between $3\sigma - 5\sigma$ within ~ 10 years of operation.

INO (India-based Neutrino Observatory) [57] is a proposed atmospheric neutrino detector, based in India, that will employ a 50 kton magnetized iron calorimeter using resistive plate chamber (RPC) active detector elements (neutrino interactions in the iron targets produce charged particles which ionize the gas in the RPCs, with the resultant electrons read out when they traverse the chamber). The magnetic field allows discrimination of neutrinos and antineutrinos and INO expects to

achieve $\sim 3\sigma$ determination of the mass ordering with 10 years of operation.

Finally, Hyper-Kamiokande (HK) is a next generation water Cherenkov detector, based on SK. The current design proposal [58] is for a 258 kton detector with around eight times the fiducial mass of SK and with the potential for a second tank to be added. HK should be able to resolve the mass ordering at more than 3σ for $\sin^2(\theta_{23}) > 0.53$.

Accelerator neutrinos

DUNE (Deep Underground Neutrino Experiment) is a next generation long-baseline neutrino oscillation experiment [59] based in the US, employing liquid argon based detector technology, with a total fiducial mass of ~ 40 kton on a 1300 km baseline relative to the source at Fermilab. DUNE's very long baseline will enable a 5σ discovery [60] of the mass ordering with 400 kt $\cdot$ MW $\cdot$ year exposure[8], as well as establish 3σ evidence for CP violation for 75% of true values of δ with 1320 kt $\cdot$ MW $\cdot$ year exposure and 5σ discovery of CP violation for 50% of true values of δ with 810 kt $\cdot$ MW $\cdot$ year exposure. DUNE also represents the experiment with the greatest sensitivity to the octant of θ_{23}, for which it can achieve $\sim 5\sigma$ confidence level for true $\sin^2(\theta_{23}) = 0.45$.

Alongside the future HK detector is a corresponding long-baseline neutrino oscillation experiment intended to succeed T2K. T2HK [61] will use an upgraded J-PARC neutrino beam over the same baseline as T2K, with HK acting as the far detector. T2HK provides the greatest sensitivity to CP violation, expecting confirmation of CP violation at the 3σ (5σ) confidence level for 76% (57%) of true values of δ. T2HK also has sensitivity to the octant of θ_{23}, for which it can achieve $> 3\sigma$ evidence for true $\sin^2(\theta_{23}) \leq 0.46$ and $\sin^2(\theta_{23}) \geq 0.57$ for the normal mass ordering.

Reactor neutrinos

Finally, the JUNO (Jiangmen Underground Neutrino Observatory) experiment [62] in China is currently under construction, with a primary goal to measure the neutrino mass ordering. The 20 kton liquid scintillator detector will measure reactor antineutrinos from two reactor complexes at a 53 km baseline and is expected to achieve $> 3\sigma$ evidence for the mass ordering.

[8] All sensitivity figures are based on the CDR reference design

Chapter 3

The T2K experiment

The T2K (Tokai-to-Kamioka) experiment is a long baseline neutrino oscillation experiment designed with the primary goals of measuring the oscillation parameter θ_{13} and δ via the appearance of ν_e in a ν_μ beam and improving the precision of the measurement of the oscillation parameters θ_{13} and Δm^2_{32} via the disappearance of ν_μ from the ν_μ beam. Secondary goals include neutrino cross-section measurements and sterile neutrino searches. The experiment is composed of a neutrino beamline, near detector complex and the Super Kamiokande (SK) far detector, with neutrinos derived from a beam of protons produced by the J-PARC proton synchrotron, based in Tokai (see fig. 3.1). The following sections will describe each of these components of the experiment.

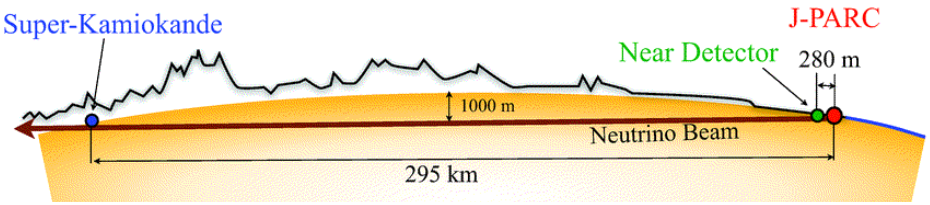

Figure 3.1: The T2K experiment. Reproduced from [63]

3.1 Neutrino beam

T2K's beam is composed predominantly of neutrinos from the decay of secondary pions where the pion momenta are mostly less than 10 GeV [64]. The resultant energy of daughter neutrinos in the small angle approximation [65] can be expressed as

$$E_\nu \approx \frac{0.43 E_\pi}{1 + \gamma^2 \theta^2} \tag{3.1}$$

where E_ν is neutrino energy, E_π is pion energy, $\gamma = E_\pi/m_\pi$, m_π is pion mass and θ is the angle between the pion and daughter neutrino. Figure 3.2 shows how E_ν varies with E_π for a number of different values of θ and it can be seen that as the angle between the neutrino and pion moves away from zero the resultant neutrino energy becomes relatively insensitive to the parent pion energy.

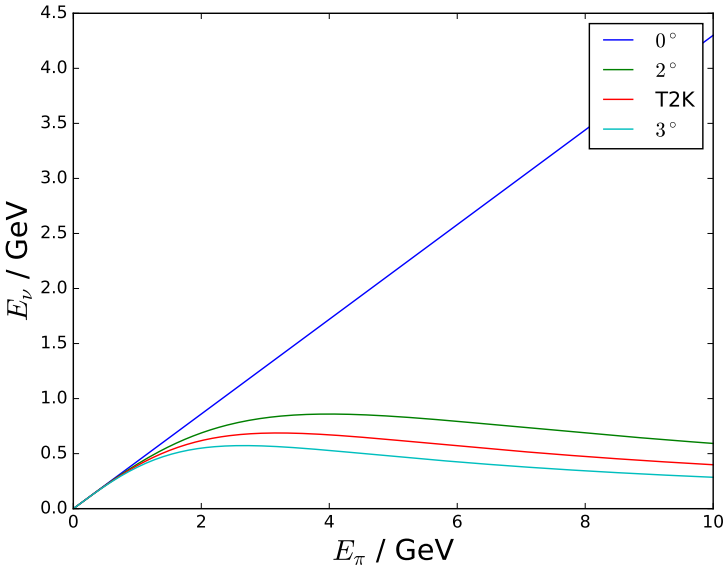

Figure 3.2: Neutrino energy by parent pion energy

For a fixed baseline, the neutrino oscillation probability depends upon the neutrino energy and for T2K's 295 km baseline the oscillation probability reaches a maximum at around 600 MeV. As such, T2K deploys an off-axis beam methodology, such that the neutrinos propagate at an angle offset from the baseline that connects the proton target and SK [63] by 2.5°, producing a narrow-band beam peaked around 600 MeV at SK. The use of the off-axis methodology also has the effect of reducing the intrinsic ν_e background to the appearance experiment, by reducing the flux of high-energy kaons (which decay to ν_e). The angle can be tuned to between 2.0° and 2.5° to alter the peak neutrino energy if needed; this angle is constrained by the need for the beam to pass through the central area of the INGRID detector (see section 3.2).

The proton beam is produced at J-PARC by a combination of 3 accelerators (see fig. 3.3); a linear accelerator (LINAC), a rapidly cycling synchrotron (RCS) and a main ring synchrotron (MR). The LINAC accelerates H^- ions to 400 MeV, which are then stripped of their electrons upon injection into the RCS to produce an H^+ beam. The RCS has a circumference, L, of 348.33 m [66], combined with the RF

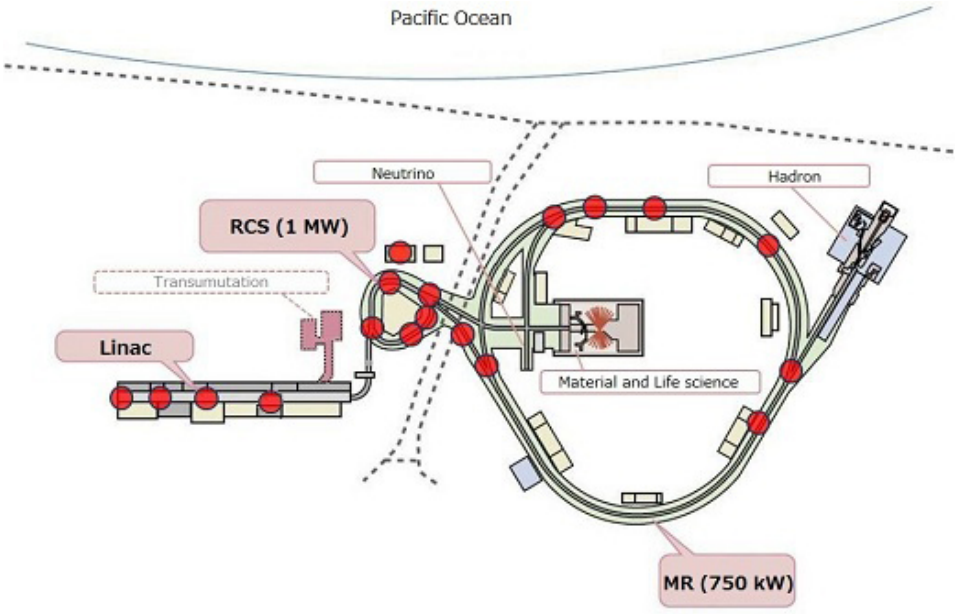

Figure 3.3: The J-PARC accelerator complex. Reproduced from the J-PARC public website

frequency, f_{RF}, of $1.67 - 1.72\,\mathrm{MHz}$, the harmonic number can be calculated as

$$h = \frac{L f_{RF}}{c} \tag{3.2}$$

yielding a value of 2 and 2 bunches are used in each cycle.

The RCS accelerates the beam to 3 GeV with a 25 Hz cycle, with around 5% of the bunches being injected into the MR, the remainder going to the Material and Life Science Facility. The MR accelerates the proton beam to 30 GeV, with a circumference of 1567.5 m, 4.5 times that of the RCS and therefore has a harmonic number of 9. However, only 8 bunches are used in each spill, with all 8 bunches being extracted in a single turn (MR cycles are 2.48 s for fast extraction to the neutrino beamline) by 5 kicker magnets, yielding a 4.1 μsec spill width, composed of 58 ns wide bunches, separated by 581 ns. This timing structure of the beam is important in reducing the cosmic muon induced background.

The extracted bunches then propagate through the neutrino beamline (see fig. 3.4). In the first instance the protons enter the primary beamline, evacuated to $\sim 3 \times 10^{-6}$ Pa to allow connection with the MR beam pipe, where, during the 54 m preparation section 11 normal conducting magnets are used to steer and focus the beam so that it can be accepted into the 147 m arc section, that employs a further 14 pairs of superconducting magnets to steer the beam through $\sim 81^{\circ}$ to point in

the direction of Kamioka, before the final stage of steering and focusing is applied by 10 normal conducting magnets in the 37 m focusing section, which also directs the beam downwards by $\sim 3.6°$. Various systems, which will not be discussed here, monitor the intensity, position, profile and loss of the proton beam.

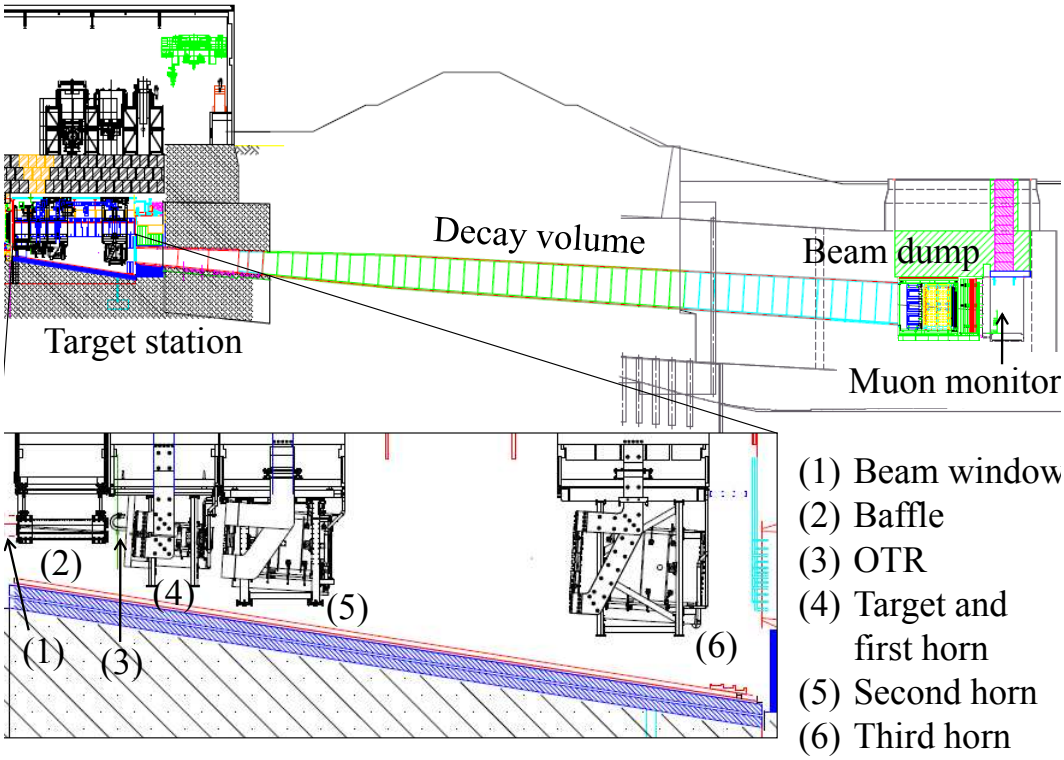

Figure 3.4: T2K neutrino beamline. Reproduced from [63]

From the focusing section, the beam enters the secondary beamline, composed of the target station, decay volume and beam dump. The target station, residing inside a helium vessel at 1 atmosphere, contains the target and three magnetic horns. The core of the target is a 91.4 cm (1.9 interaction lengths) graphite rod, with a 2.6 cm diameter. Graphite was chosen as materials with a significantly higher density would be melted by the beam. The core is further contained within a 2 mm thick graphite tube and 0.3 mm thick titanium casing and cooled via helium gas flowing through the gaps between core, tube and casing. The accumulation of POT over the course of Run 1-9 is shown in fig. 3.5. The interaction between the protons and the target results in the production of secondary pions, which are then collected by the first horn magnet, within which the target resides, with the toroidal magnetic fields of the second and third horn magnets focusing the pions. When the horns are operating with a current of 320 kA the maximum field is 2.1 T, sufficient

to increase the neutrino flux at peak energy at SK by a factor of ~ 16 relative to 0 kA.

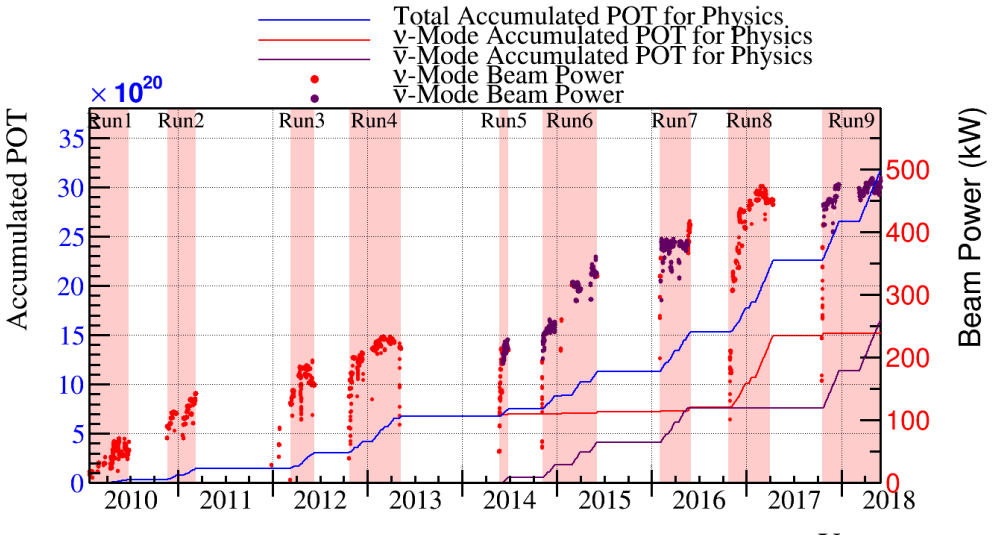

Figure 3.5: T2K POT by run period.

The focussed pions then enter a 96 m decay volume, where the pions decay, primarily to muons and muon neutrinos (see fig. 3.6), before reaching the beam dump. The beam dump is composed of ~ 3.2 m of graphite, followed by a further 2.4 m of iron, such that only neutrinos and muons with an energy greater than ~ 5 GeV pass through.

The distribution of those muons passing through the beam dump is measured by a muon monitor [67], located just behind the beam dump, to a precision of better than 0.25 mrad (required precision is 1 mrad), corresponding to ~ 3 cm at the 118 m distance of the muon monitor from the target and further measures the beam

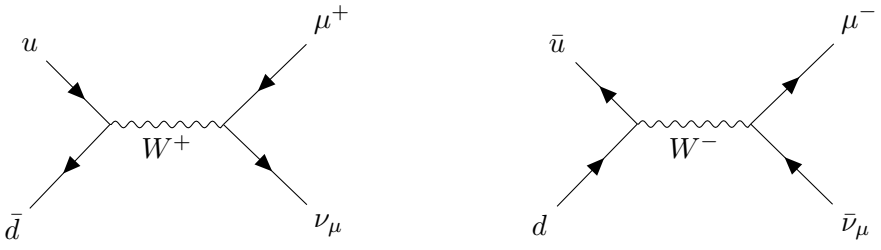

(a) π^+ (b) π^-

Figure 3.6: Pion decay.

intensity to a precision of 2.9%. The direction of the neutrino beam is then taken to be the direction from the target to the centre of the muon profile.

3.2 Near detectors

The near detector complex comprises a set of detectors 280 m from the proton target whose function is to measure neutrino interactions and thereby predict the neutrino interactions at the far detector.

The ND280 detector is the primary detector and positioned off-axis, in line with the target-to-far detector baseline and positioned on a floor about 24 m below the surface within a pit. It measures the neutrino flux, energy spectrum, ν_e contamination and rates for neutrino interactions. This permits prediction of the ν_μ flux at SK along with the intrinsic ν_e contamination, and the measurement of ν_μ interactions allows measurement of backgrounds to the ν_e appearance search, most particularly the dominant NC1π^0 background. The capability to measure various different interactions led to a multi-component detector (see fig. 3.7, composed of a π^0 detector (P0D), two fine grained detectors (FGDs), three time projection chambers (TPCs), an electromagnetic calorimeter (ECal), contained within a magnet (previously part of the UA1 experiment) instrumented with a muon range detector (SMRD).

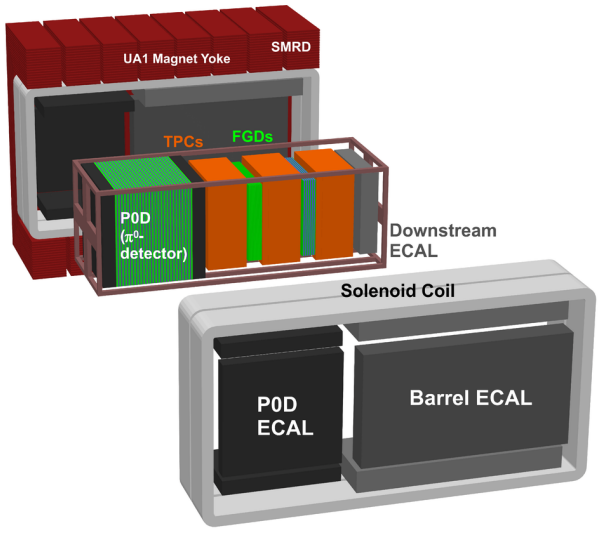

Figure 3.7: Schematic of the ND280 showing the sub-detectors situated within the UA1 magnet. Reproduced from [63]

The key detection technologies used at the near detectors are TPCs and

plastic scintillators. Prior to describing the individual detector components, a brief introduction to the concept behind the technologies will be given. A TPC is a gas-filled detector permeated by a uniform electric field parallel to a magnetic field [68]. As charged particles pass through the detector volume they ionize the gas and the resulting ions drift towards the end caps due to the presence of the electric field, while the presence of the magnetic field acts to correct any drift perpendicular to the electric field, causing the ions to spiral tightly around the electric field lines until reaching the end caps, thus maintaining the radial and azimuthal position information about the field line. Timing information can then be used to determine the longitudinal distance of the interaction vertex (i.e. how long the ions take to drift to the end caps). A scintillator operates via incident particles exciting free valence electrons into higher energy states, whose subsequent decay to the ground state results in the emission of scintillation photons, which can be detected by photon counting detectors. The bars showing hit activity can then be used to establish the location of the particle interaction and thereby determine the incident particle trajectory. Due to the presence of a 0.2 T magnetic field at the ND280, PMTs are not a suitable choice of photon detector [69] and thus multi-pixel photon counters (MPPC) were chosen, being insensitive to magnetic fields. The peak of the scintillation light from the bars is at 420 nm, whereas the MPPCs operate with longer wavelengths and thus wavelength shifting (WLS) fibres, running along the length of each scintillator bar, are employed, absorbing light centred on 430 nm and re-emitting light centred on 476 nm [63] to better match the requirements of the MPPCs attached to the WLS fibre.

The most upstream of the detectors is the P0D, designed to measure the cross-sections of neutrino interactions on water that generate π^0s [70], particularly neutral current (NC) π^0 interactions

$$\nu_\mu + N \rightarrow \nu_\mu + N + \pi^0 + X \tag{3.3}$$

and also to measure the intrinsic ν_e component of the beam. To achieve this the P0D is comprised of interleaved water target and plastic scintillator layers (fig. 3.8) to measure the resultant charged particles from interactions, sandwiched between two ECals that are composed of interleaved sheets of lead and plastic scintillator layers. The P0D allows for running without water between the scintillators and therefore the interaction rate on water can be determined by comparing the interaction rate during data taking with and without the water. The P0D contains 40 scintillator modules (7 in each of the ECals and 26 within the water target region), each with

134 horizontal bars and 126 vertical bars containing scintillating fibre arranged to form a plane, allowing three-dimensional resolution of a charged particle trajectory according to which fibres are activated in a given module.

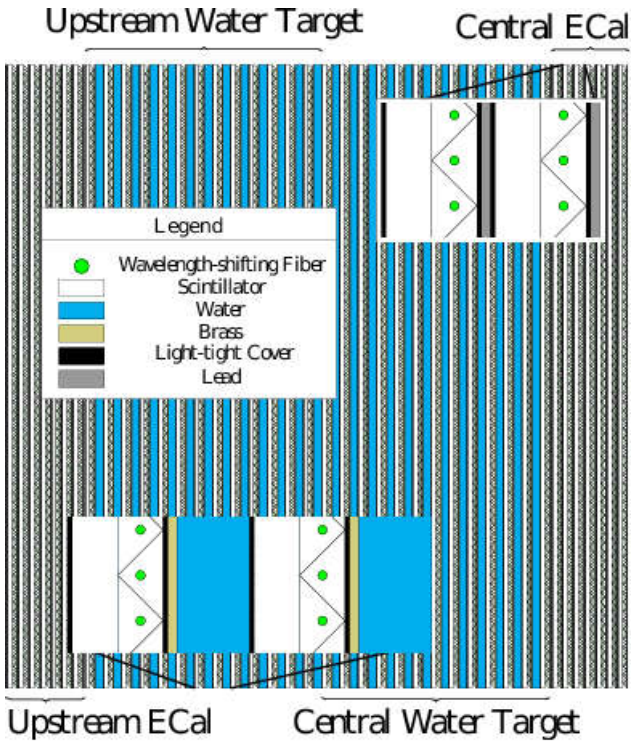

Figure 3.8: Schematic of the P0D. Reproduced from [70]

Downstream of the P0D are the TPCs and FGDs, collectively known as the tracker. These detectors are interleaved such that two FGDs act as active targets [71] between three TPCs. The FGDs are relatively short ($\sim 30\,\text{cm}$) such that most particles from neutrino interactions will exit the FGDs to be measured in the TPCs, but short-range particles, such as recoil protons, are measured by the FGD, therefore requiring fine granularity of detection to resolve the direction of these short tracks. The most important interaction to measure is the CCQE interaction

$$\nu_l + N \rightarrow l^- + p \tag{3.4}$$

which is the most common interaction at T2K's beam energy. The incident neutrino energy can be inferred from the energy and momentum of the outgoing lepton, with a precision limited (to around 10%) by the Fermi momentum of the neutron in the target nucleus. CCQE interactions can be used to measure the neutrino beam flux

and energy spectrum at the near detector and thereby predict the flux and energy spectrum at SK.

An important background to the CCQE interaction at SK is CC1π^+ production,

$$\nu_l + N \rightarrow l^- + N' + \pi^+ \tag{3.5}$$

which can often result in only the π^+ being below the Cherenkov threshold, making the process an irreducible background to the CCQE process at SK and thus assessing the size of this background is an important measurement at the near detector. With the tracker able to see all charged particles in an interaction, CCQE events can be selected from those events containing only a lepton and recoil proton, with events containing additional charged tracks being rejected. Events fitting this profile can then additionally be checked for consistency of charge deposition and momentum with the CCQE hypothesis.

As for the P0D, the FGD uses plastic (polystyrene) scintillators for particle detection, however, there are no interleaved lead sheets and whereas the scintillators have a triangular cross-section of 17 mm $\times$ 33 mm in the P0D, the scintillators in the FGD have finer granularity and a square cross-section of 9.6 mm on a side. The FGD scintillator bars have a hit efficiency [71] by track angle, θ, in excess of 99% for $|\theta| > 12°$, falling smoothly to 93% at $\theta = 0°$, while the hit efficiency by distance, d, from the bar centre exceeds 99% for $d < 0.35$ cm, falling smoothly to 88% at the edge of the bar. These again adopt horizontal and vertical orientation, with 15 layers in FGD1 and 7 layers in FGD2. The reason for the lower scintillator layer count in FGD2 is that FGD2 also contains 6 water targets interleaved between the scintillator layers, as in the P0D. Comparing the interaction rates of the two FGDs allows for determination of cross-sections on both carbon and water.

In T2K, each TPC is designed as a two chamber, Argon gas-filled field cage (see fig. 3.9) with a central cathode at -25 kV separating the two chambers, which in turn are contained within a box whose outer walls are at ground potential. The field cage is instrumented at each end with micromegas modules at -350 V parallel to the cathode plane. The maximum drift distance is 897 mm, thereby yielding a drift field of ~ 275 V/cm, close to the saturation point of the Argon gas mixture (the point at which the maximum drift speed of charged particles in an electric field is achieved). Achieving good CCQE neutrino energy resolution depends upon the TPC momentum resolution, with the T2K goal set to a resolution of approximately $0.1p_\perp$. Figure 3.10 compares the simulated TPC momentum resolution against that goal. For the purposes of ν_e beam contamination, the important consideration is the fact that ionization energy loss for electrons is around 45% larger than that for muons in

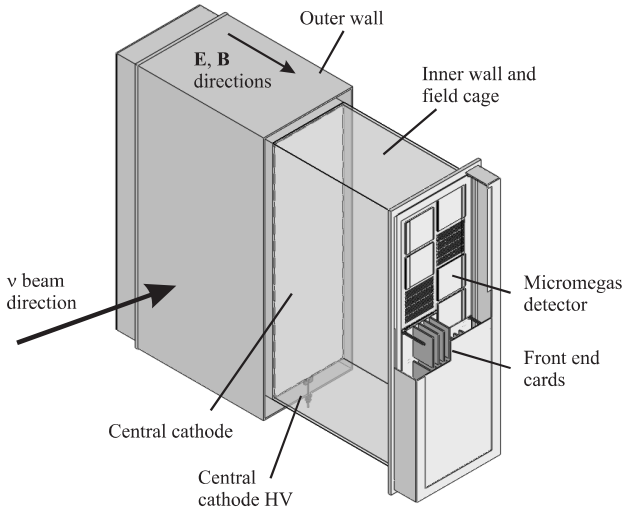

Figure 3.9: Schematic of a TPC. Reproduced from [72]

the momentum range of interest (see fig. 3.11) and therefore resolution in ionization energy loss needs to be better than 10% to distinguish the two particles effectively. The deposited energy resolution is $7.8 \pm 0.2\%$ [72] for minimum ionizing particles, compared to a 10% requirement, which leads to a probability of misidentifying a muon as an electron of just 0.2% for tracks with a momentum less than 1 GeV/c.

As with the P0D and FGD, the active component of the ECal [69] uses plastic scintillators, in this case interleaved between lead sheets. The ECal is composed of 13 detectors; 6 surrounding the P0D, known as the P0D ECal; 6 surrounding the tracker, known as the barrel ECal; and a further detector downstream of the most downstream TPC, known as the downstream ECal. The P0D and barrel ECals feature 6 detectors because the top and bottom components must be split in two to allow for opening of the magnet, to which they are attached, whereas the side detectors are each single units.

The scintillator bars have a cross-section of $40\,\text{mm} \times 10\,\text{mm}$, the 10 mm depth was chosen to minimise the effect on the size of the inner detectors given the constraint of residing within the UA1 magnet, whilst having a thickness sufficient to produce enough light for a reliable signal. The 40 mm width was a compromise between superior reconstruction efficiency for smaller bar widths and reduced channel costs of larger bar widths. The hit efficiency of the downstream ECal is $\sim 99\%$, while the barrel ECal has hit efficiencies of $\sim 99\%$ for bars with readouts at both ends and $\sim 97\%$ for bars with readouts only at one end. In addition the number of layers was determined by a need to contain electromagnetic showers of up to

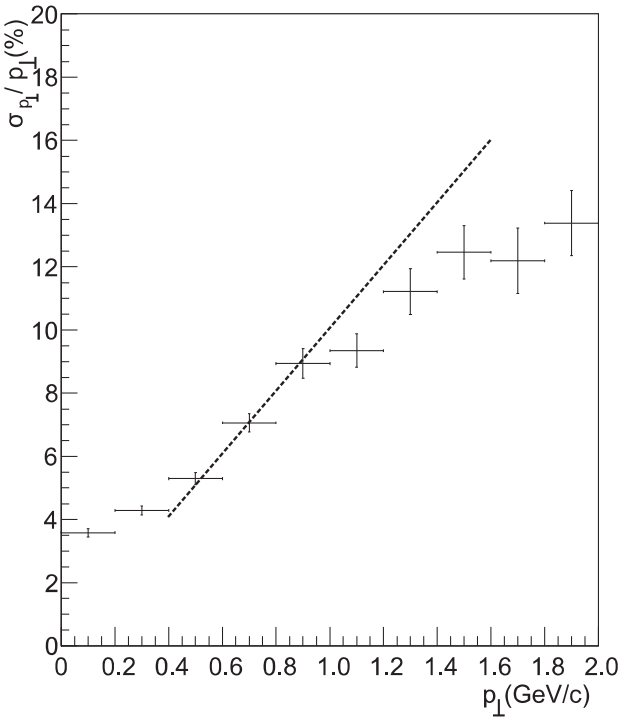

Figure 3.10: TPC momentum resolution from MC simulation (points) and the corresponding goal (dashed line). Reproduced from [72]

3 GeV, with 10 electron radiation lengths being required to ensure at least 50% of the energy resulting from photon showers associated with π^0 decay. The goal of the tracker ECal is to measure neutral particle energy and aid the tracker in particle identification. The ECal PID performance can be seen in fig. 3.12, showing the excellent separation between muons and electrons, particularly in the downstream ECal. The scintillator bar orientation varies between the different components of the tracker ECal, with the downstream ECal adopting the same horizontally and vertically oriented bars as the FGD and P0D, while the barrel ECal has scintillator bars that run parallel to the beam in all components. The P0D ECal meanwhile is designed to tag escaping energy and distinguish between photons and muons, the P0D itself providing shower reconstruction. Unlike the other active scintillator-based detectors, the P0D ECal scintillators all run parallel to the beam and requires a smaller number of interaction lengths (~ 4.3) to ensure shower containment and photon/muon separation.

The INGRID (Interactive Neutrino Grid) detector [63] is an on-axis detector measuring the neutrino beam profile at the near detector complex, sharing the same pit as the ND280, but with the horizontal detectors located on a floor 33 m below the

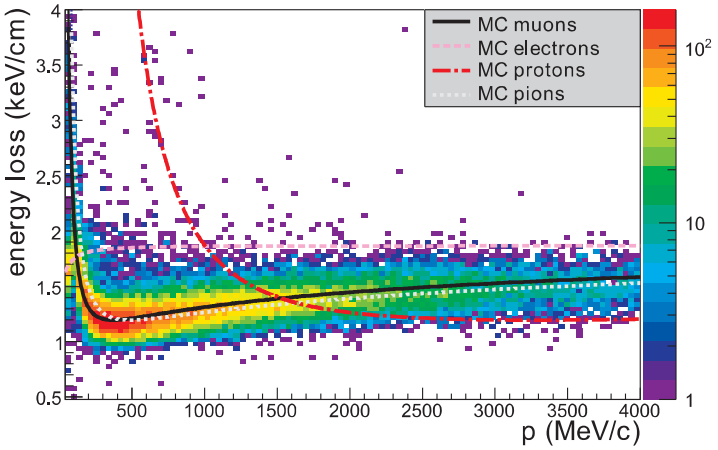

Figure 3.11: Distribution of energy loss as a function of momentum for negatively charged particles. Reproduced from [72]

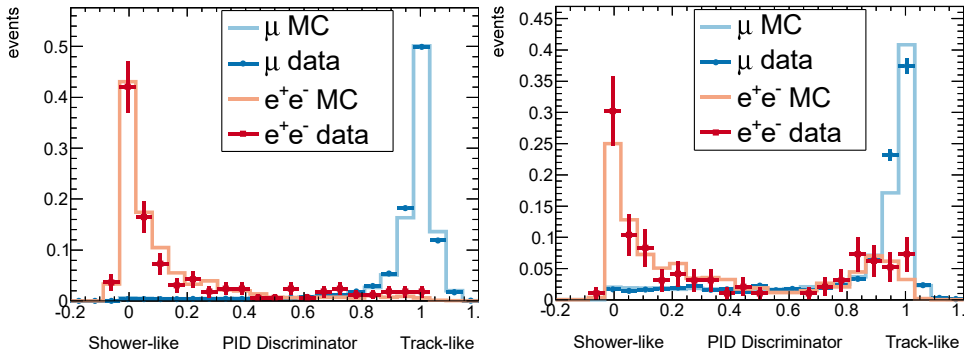

Figure 3.12: PID statistic for the downstream (left) and barrel (right) ECals. Reproduced from [69].

surface and the bottom modules located on a floor 37 m below the surface. The beam direction and intensity is measured based on neutrino interactions on iron, with an interaction rate sufficient to provide a daily measurement of the beam profile. The detector, shown in fig. 3.13, is constructed from 16 identical modules, 7 vertically aligned modules and 7 horizontally aligned modules arranged in a cross, along with 2 additional modules outside the main cross. The centre of the cross corresponds to the defined neutrino beam centre, and the measured beam centre is determined to a precision of better than 0.4 mrad by measuring event rates in each module. The two off-cross modules are used to assess beam asymmetry. Each module is composed of layers of active scintillator interleaved with iron plates, with the bars having a cross-section of 10 mm × 50 mm, oriented vertically and horizontally to provide full

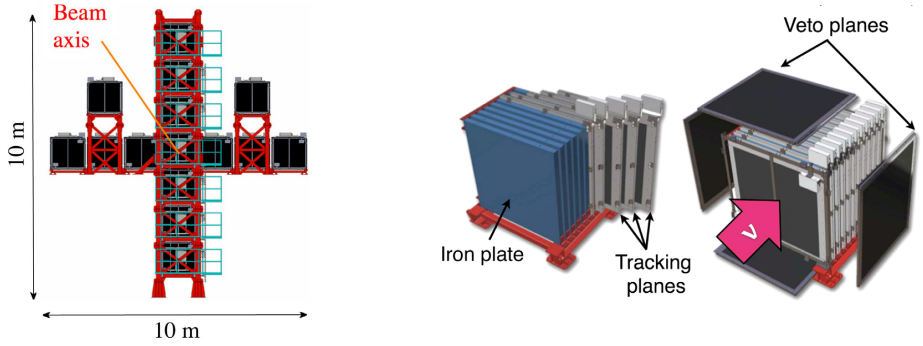

Figure 3.13: The INGRID detector (left) and a single module (right). Reproduced from [73]

3D position resolution.

3.2.1 Simulation

Interactions at the Near Detector complex are simulated using the NEUT [74] Monte Carlo generator, with the resultant energy deposition from final state particles within the detectors simulated using GEANT4 [75], before simulation of active detector response (including scintillation light produced by scintillator bars and electron drift in the TPCs) is provided by a custom electronics simulation (elecSim) package. The event information produced by elecSim is equivalent to that produced by real data processing, and thereafter follows the same calibration and reconstruction process as real data [63].

3.3 Far detector

The Super-Kamiokande water Cherenkov detector acts as T2K's far detector. The detector is 295 km from the target in Tokai, situated 2.5° off-axis and measures the flavour composition of the neutrino beam, looking for ν_e appearance and ν_μ disappearance. The detector is located 1 km deep within Mount Ikenoyama to reduce the cosmic muon flux (by 5 orders of magnitude [76]).

SK is a stainless steel cylindrical tank (see fig. 3.14) of height 41 m and diameter 39 m containing 50 kton of pure water acting as the target. SK's volume is split into 2 main volumes; an inner detector having a 33.8 m diameter and 36.2 m height and instrumented with 11129 inward facing photomultiplier tubes (PMTs) providing 40% coverage of the detector area, and an outer detector extending about 50 cm beyond the inner detector region and instrumented with 1885 outward facing

PMTs. The two regions are separated by a stainless steel scaffold covered by plastic sheets that act both to optically isolate the two regions and, within the inner detector region reduce scattering of photons back into the inner detector volume, while maximising reflection within the outer detector volume to maximise signal detection despite the relatively sparse instrumentation. The outer detector is used to veto activity in the inner detector resulting from interactions outside the inner detector volume.

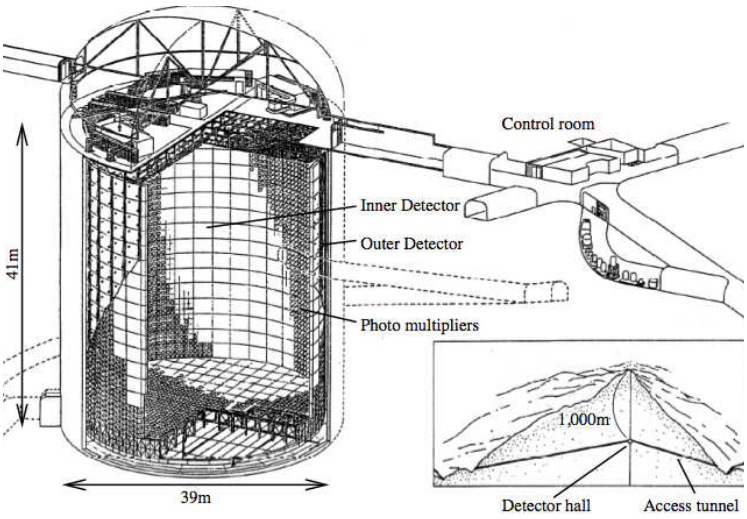

Figure 3.14: Super-Kamiokande detector. Reproduced from [63]

When neutrino interactions produce charged particles above a particular energy threshold, those particles can propagate with a speed greater than that of light in water, resulting in the emission of Cherenkov light, which in turn is detected by the PMTs, producing a characteristic ring-shaped pattern on the walls of the SK tank. The resultant pattern can be analysed to determine momenta and interaction vertices of the particles as well as determine the particle identification. SK's particle discrimination is excellent at T2K energies, with the probability to misidentify an electron as a muon at 0.7%, while the probability to misidentify a muon as an electron is 0.8% [77] (see fig. 4.22). Furthermore, SK's momentum resolution for muons (electrons) is $1.7\% + 0.7\%/\sqrt{p\ (\mathrm{GeV}\,/\,\mathrm{c})}$ ($0.6\% + 2.6\%/\sqrt{p\ (\mathrm{GeV}\,/\,\mathrm{c})}$), with corresponding angular resolution of 1.8° (3.0°) [77].

Consider fig. 3.15, where a charged particle travels from point A to point B at a fraction, β, of the speed of light in a vacuum, c, for a time, t. As the particle emits light at points along its path, it continues to travel with speed βc and thus covers a distance βct en route from A to B. Meanwhile, the light emitted from each

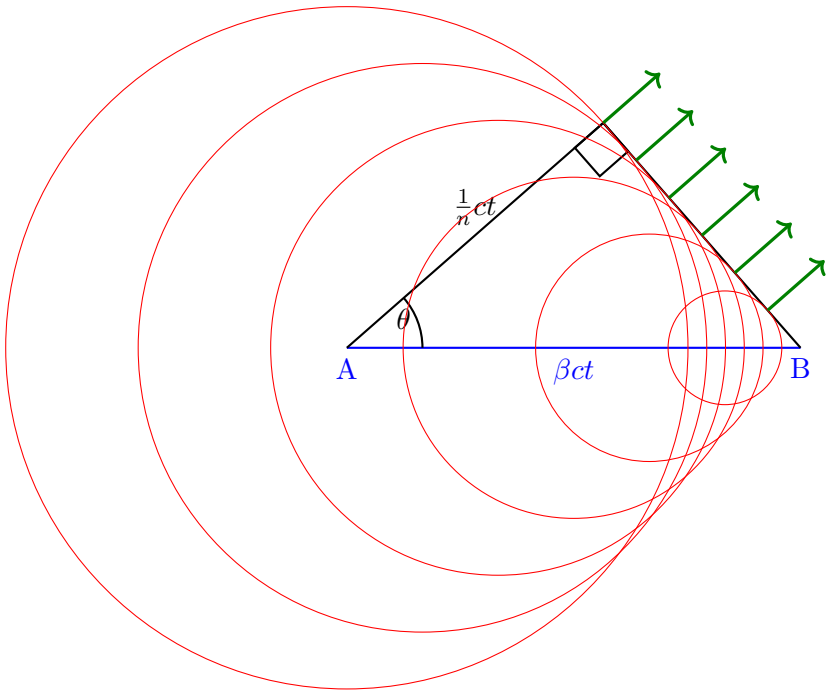

Figure 3.15: Structure of Cherenkov light. Adapted from [78].

point along the path AB travels at a speed c/n, where n is the refractive index of the medium, approximately 1.33 for water and thereby covers a distance ct/n, as indicated by the red circles. With $\beta c > c/n$ one can see that the light produces a wavefront as indicated by the green arrows, with an opening angle given by

$$\cos\theta = \frac{1}{\beta n} \tag{3.6}$$

and it is this opening angle that gives rise to the Cherenkov rings in the detector.

3.3.1 Simulation

Interactions in the far detector are simulated, based upon input neutrino flux and energy spectrum, using the NEUT [74] Monte Carlo generator, with simulation of particle propagation through the detector volume and the resultant detector response provided by a custom detector simulation software package, SKDETSIM.

3.3.2 Event reconstruction

The events identified either from simulation or real data are reduced and categorized; in particular, events are restricted to those coincident with the beam trigger window

and then classified as:

- Fully contained (FC): Events above a particular energy threshold and originating and terminating in the inner detector.
- Outer detector (OD): Events above a particular energy threshold with more than 15 hits in an outer detector cluster.
- Low energy (LE): Events below the energy threshold that are still indicative of neutrino interactions.

Each category is subject to selection cuts to reduce backgrounds and it is the resultant set of events that are passed to the physics analyses.

Event reconstruction proceeds by determining the initial interaction vertex and track direction based on the timing of PMT hits and from a well-defined edge in the PMT charge pattern. A Hough transform [79] is then applied iteratively to identify rings in the distribution of PMT hits, with candidate rings then being classified as either electron-like or muon-like according to comparison of the reconstructed ring to an analytically computed ring for muons and an MC calculated ring for electrons. CCQE interactions involving ν_μ and ν_e produce leptons of their respective flavours. Muons, by virtue of their relatively large mass undergo little scattering and therefore produce sharp rings of PMT hits. By contrast, electrons scatter more easily due to their low mass and therefore produce electromagnetic showers that produce fuzzy rings of PMT hits from the overlap of multiple Cherenkov rings. These characteristics of the hit patterns produced by electron and muons allow flavour to be inferred for the incident neutrino, with example patterns shown in fig. 3.16. Finally, the momentum of the reconstructed particle can be calculated from the distribution of charge within the corresponding ring.

3.4 Physics results

As noted at the beginning of this section, among T2K's primary goals were a first observation of non-zero $\sin^2\theta_{13}$ and improved precision in the measurements of $\sin^2\theta_{23}$ and Δm^2_{32}. These goals were achieved with the discovery of ν_e appearance [80] and world-leading disappearance parameter measurements [48].

Among other important goals for the T2K experiment was the measurement of neutrino interaction cross-sections. T2K now has numerous such publications; ν_μ, ν_e and $\bar{\nu}_\mu$ CC inclusive cross-sections on carbon [81–83], ν_μ CC inclusive cross-sections on iron [73, 84], the ν_μ CC1π^+ cross-section on water [85], ν_μ CCQE cross-sections on carbon [86–88], ν_e CCQE and ν_μ CC0π cross-sections on water [89, 90]

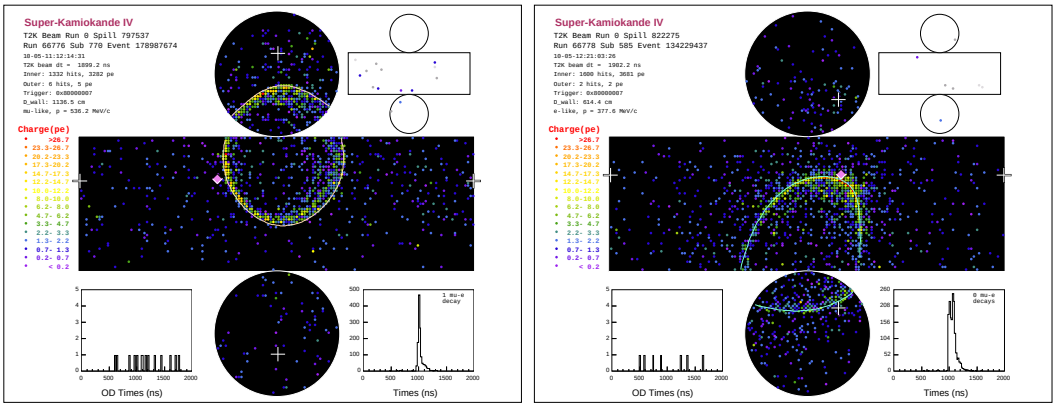

(a) muon-like event

(b) electron-like event

Figure 3.16: Reconstructed events in Super-Kamiokande. Reproduced from [63].

and NCQE cross-sections on oxygen and coherent pion production cross-section on carbon [91].

In addition to these studies, T2K has also performed searches for sterile neutrinos [92] by looking for ν_e disappearance in the ND280 detector, Lorentz and CPT violation [93] by looking for ν_μ disappearance at the INGRID detector and use time of flight information to compute an upper bound for neutrino mass [94].

As of Run 1-9 (May 2018) T2K achieved a total integrated POT in Forward Horn Current (FHC)[1] mode of 1.4938×10^{21} and in Reverse Horn Current (RHC) mode of 1.6346×10^{21}. Run 9 has moved the ratio of FHC to RHC POT close to 1, which will help to improve the constraint on δ and help the experiment to publish more antineutrino results.

[1]FHC refers to the horn magnet configuration that preferentially focuses π^+ and thereby produces a neutrino-dominated beam, while RHC refers to the horn magnet configuration that preferentially focuses π^- and thereby produces an antineutrino-dominated beam.

Chapter 4

Inputs to the analysis

The analysis in this thesis depends upon a number of inputs. The simulation of the beamline and resulting flux prediction is described in section 4.1, whilst the subsequent simulation of neutrino interactions at the ND280 and SK is discussed in section 4.2. Tuning of predicted spectra at SK using data from T2K's near detector is described in section 4.3, along with details relating to the production of a covariance matrix for flux and cross-section parameters. The SK data selection methodology is outlined in section 4.4 and finally determination of the systematic uncertainties at SK are covered in section 4.5. Figure 4.1 provides a high-level overview of how the inputs into the analysis fit into the analysis procedure.

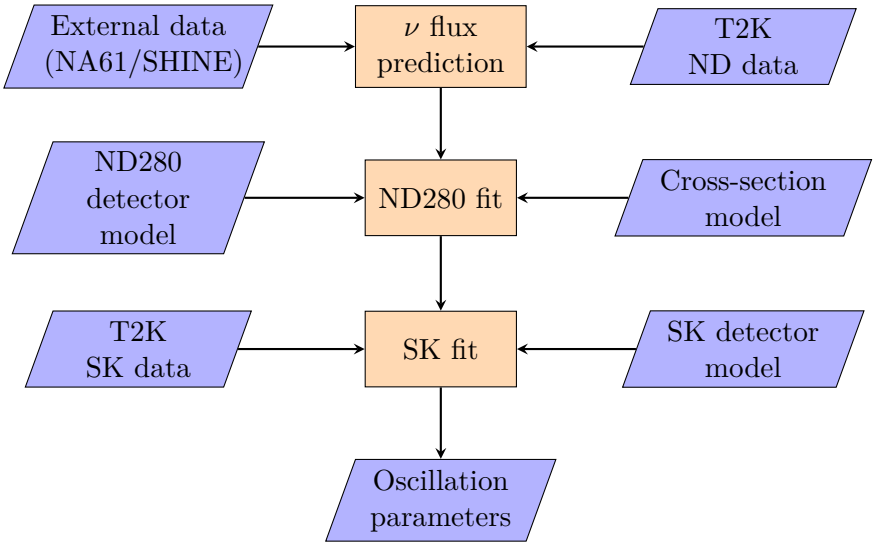

Figure 4.1: High-level overview of analysis procedure.

4.1 Flux prediction

The T2K beam simulation is used to predict the neutrino flux at the T2K near and far detectors. Interaction of the incident protons with the carbon target and baffle is simulated in FLUKA (version 2011.2c.6) [95] and interactions outside the target/baffle are simulated by GCALOR (version 1.05/04) [96], with the flight and subsequent decay of the secondary pions and kaons throughout the beamline (see section 3.1) simulated in JNUBEAM (a bespoke package based on GEANT3) [97]. These predictions are then tuned on external data sources, as well as T2K data. The NA61/SHINE experiment (hereafter NA61), uses the interaction of 30 GeV protons with a thin (2cm long, about 4% of the nuclear interaction length) graphite target [64, 98, 99] and a replica of the T2K target [100] to measure the distribution of hadrons produced in proton-graphite interactions. These data are then used to tune the beam simulation such that it can reproduce the hadron production distribution when predicting the neutrino flux. The pion and kaon phase space relevant to T2K that is covered by these data are shown in figs. 4.2 to 4.3, with a large fraction of the phase space covered.

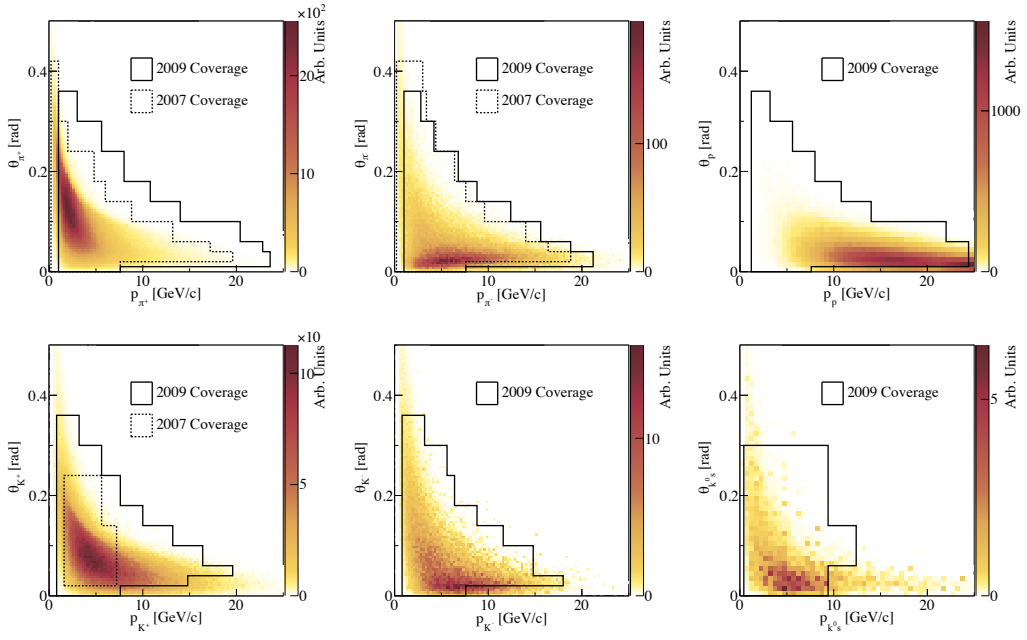

Figure 4.2: The predicted (shaded) phase space of π^+, π^-, p, K^+, K^-, K^0_S (top-left to bottom-right) contributing to the neutrino flux at SK along with the regions covered by NA61 data (outlines) for a neutrino beam. Reproduced from [101]

The final tuned T2K flux at SK, under a no oscillation hypothesis and with-

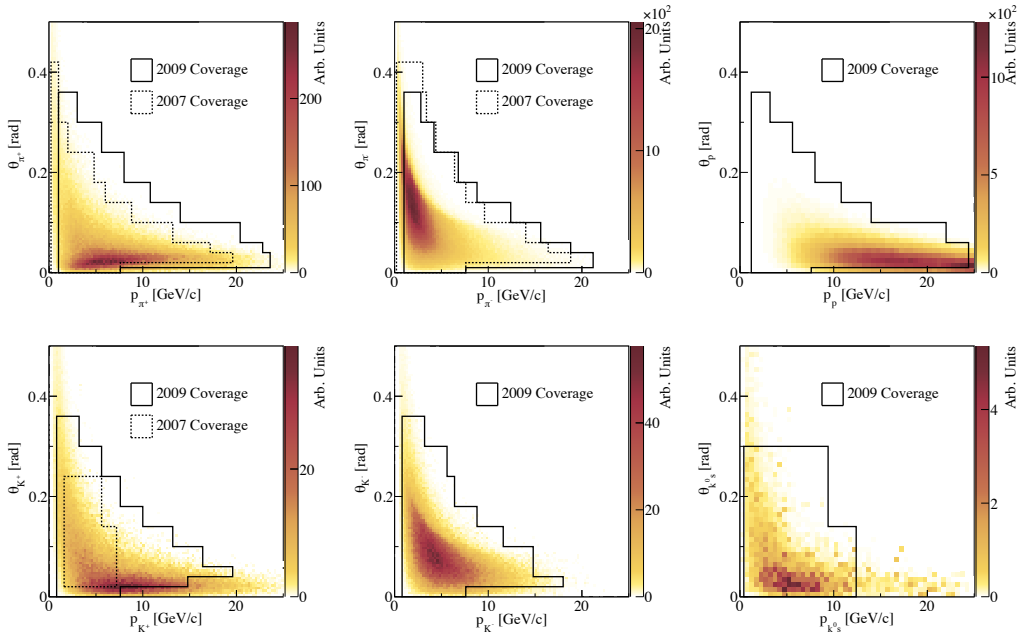

Figure 4.3: The predicted (shaded) phase space of π^+, π^-, p, K^+, K^-, K^0_S (top-left to bottom-right) contributing to the neutrino flux at SK along with the regions covered by NA61 data (outlines) for an antineutrino beam. Reproduced from [101]

out SK detector effects is shown in fig. 4.4.

Figures 4.5 to 4.7 show the pion, kaon and proton multiplicities observed by NA61 overlaying the prediction from FLUKA. The agreement between observation and prediction is good for both pions and kaons, but the prediction for protons is generally biased towards larger values. This information can be used to compute weights to tune the MC prediction. This is performed in two steps [97, 101]; first a weight is applied based on the interaction probability (the probability that an incident proton interacts in the target and produces a particular daughter particle that then escapes the target without undergoing another interaction) by calculating the ratio of the interaction probabilities assuming the cross-sections from data and assuming the cross-sections from the model. A second weight is computed from the ratio of observed and predicted particle multiplicities.

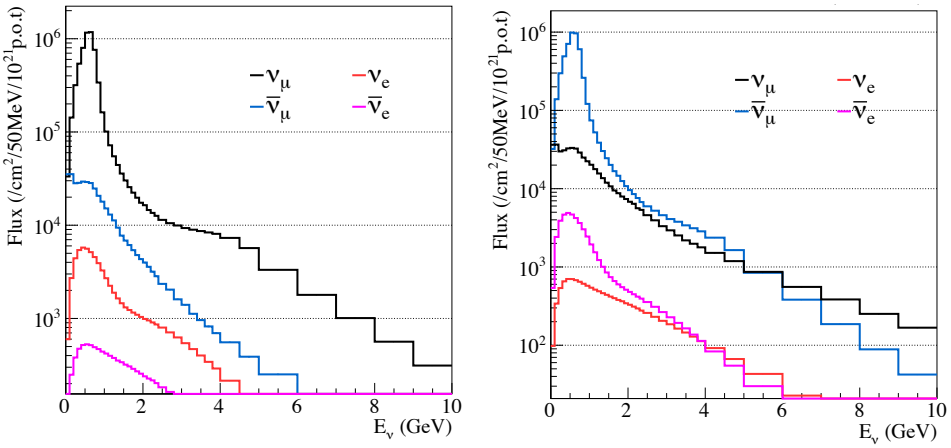

(a) FHC (b) RHC

Figure 4.4: T2K flux prediction at SK. Reproduced from [101]

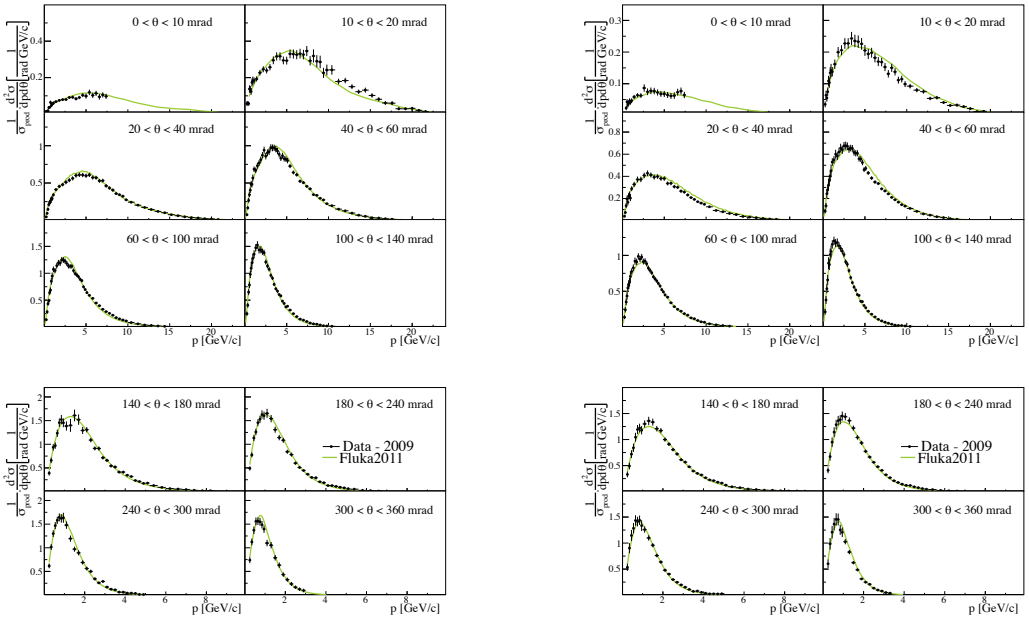

Figure 4.5: Observed multiplicities of π^+ (left) and π^- (right) using the NA61 thin target. The FLUKA prediction is shown in green. Reproduced from [101].

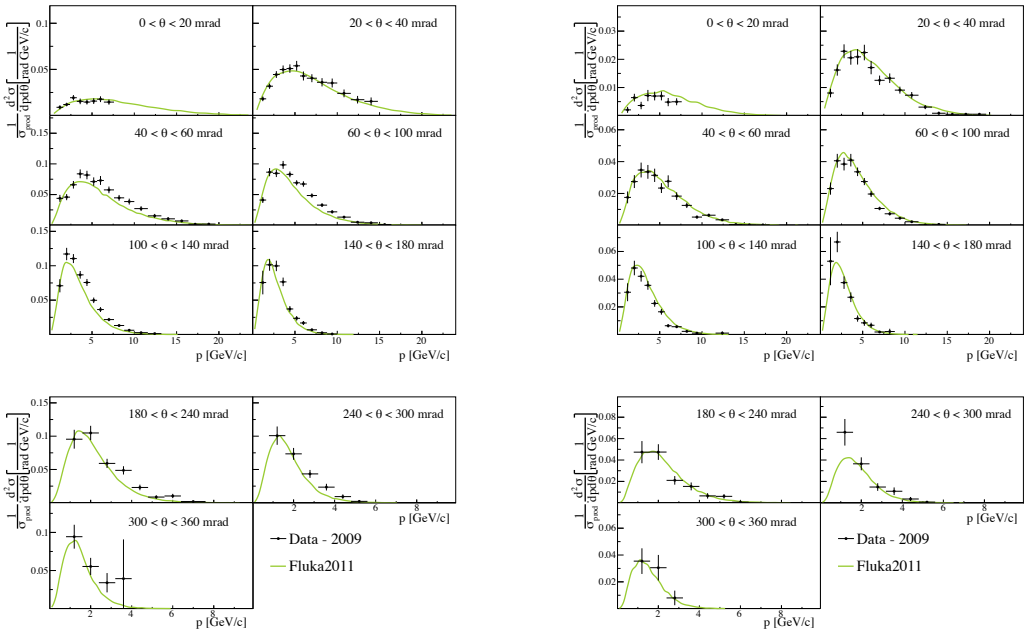

Figure 4.6: Observed multiplicities of K^+ (left) and K^- (right) using the NA61 thin target. The FLUKA prediction is shown in green. Reproduced from [101].

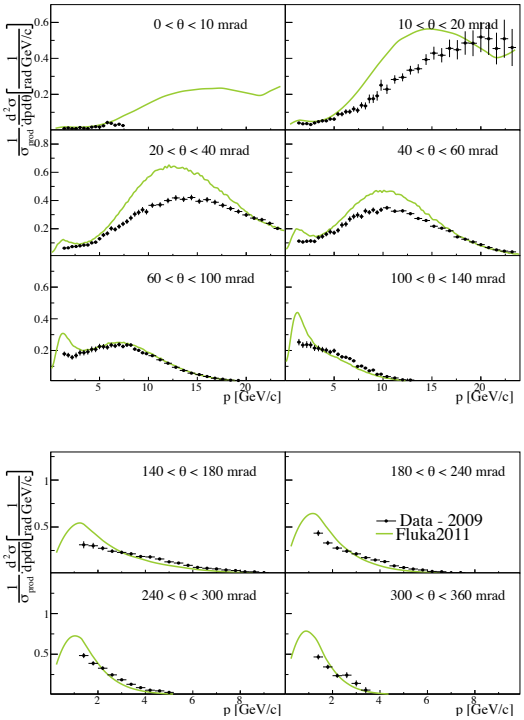

Figure 4.7: Observed proton multiplicities using the NA61 thin target. The FLUKA prediction is shown in green. Reproduced from [101]

The application of these weights yields the final tuned/untuned flux ratios shown in fig. 4.8. The tune has the effect of increasing the rate of ν_μ and ν_e events in both FHC and RHC beam modes, while the $\bar{\nu}_\mu$ and $\bar{\nu}_e$ events are enhanced at low energies and suppressed at high energies in both beam modes.

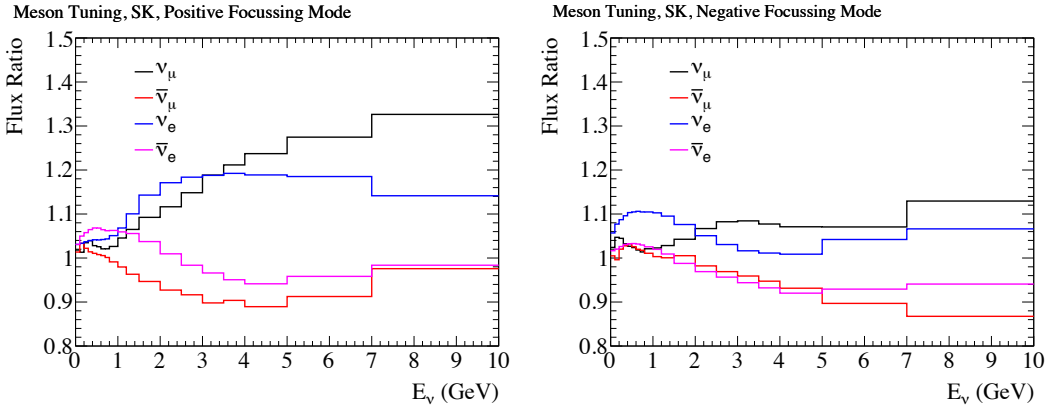

Figure 4.8: Ratio of tuned and untuned SK flux for FHC (left) and RHC (right) beam modes. Reproduced from [101]

4.2 The neutrino event generator

The simulation of neutrino interactions is implemented in the NEUT (version 5.3.2) MC generator [102]. Detection of neutrino interactions must proceed indirectly given that neutrinos carry no charge, and thus we study the products of neutrino interactions. This section will discuss the different stages involved in calculating the interaction cross-sections.

T2K uses water and hydrocarbon targets for neutrino interactions and therefore interactions with multiple nucleons within each nucleus must be considered. In this analysis, ν-nucleus interactions are modelled, using the 'impulse approximation', as the incoherent sum of the cross-section of the neutrino with each nucleon (or pair of nucleons for 2p2h) [102] based on the initial momentum of the nucleon:

$$\sigma_{\nu A} = \sum_{i=1}^{Z} \sigma_p\left(p_i\right) + \sum_{j=1}^{A-Z} \sigma_n\left(p_j\right) + \sigma\left(\text{2p2h}\right) \tag{4.1}$$

where A and Z are respectively the atomic mass number and atomic number of the target nucleus, $\sigma_p\left(p_i\right)$ is the interaction cross-section associated with the proton having momentum p_i, $\sigma_n\left(p_j\right)$ is the interaction cross-section associated with the

neutron having momentum p_j and σ (2p2h) is the interaction cross-section associated with two-body current interactions (see section 4.2.2).

4.2.1 Nuclear model

Modelling of the nuclear effects depends upon the kinematics of the initial nucleus, the energy needed to remove a nucleon from the nucleus, re-interaction of outgoing hadrons with the remaining nucleons and any screening or enhancement of the cross-section due to the nuclear potential.

A number of different nuclear models have been considered for T2K [103]; the Relativistic Fermi Gas (RFG), the Local Fermi Gas (LFG) and the Spectral Function (SF). The RFG assumes a uniform distribution of nucleon momenta in the space of energy, momentum and radial position up to the Fermi momentum, p_F, which depends upon the size of the nucleus and models the density of nuclear matter as being constant, which is valid for an infinite system. The LFG includes the effect of the finite nucleus size, modifying the density and momentum distributions, while the SF models nuclear matter based on a two-dimensional distribution of momentum and removal energy.

The choice of nuclear model used in T2K was informed by data from the MiniBooNE [104, 105] and MINERvA [106] experiments. In particular, the T2K Neutrino Interaction Working Group (NIWG) undertook fits [107] of these data. In addition, two possibilities exist for handling the nuclear potential (see below) in the RFG models; relativistic Random Phase Approximation (RPA) and non-relativistic RPA [108] and thus fits were undertaken for three nuclear models:

1. SF
2. RFG with relativistic RPA
3. RFG with non-relativistic RPA

Implementation of the LFG model is ongoing within the T2K collaboration and will be included in future fits. The best-fits of the SF and RFG with relativistic RPA are shown in figs. 4.9 to 4.10 and show small differences. RFG with non-relativistic RPA is not shown in these plots, being disfavoured in the fits.

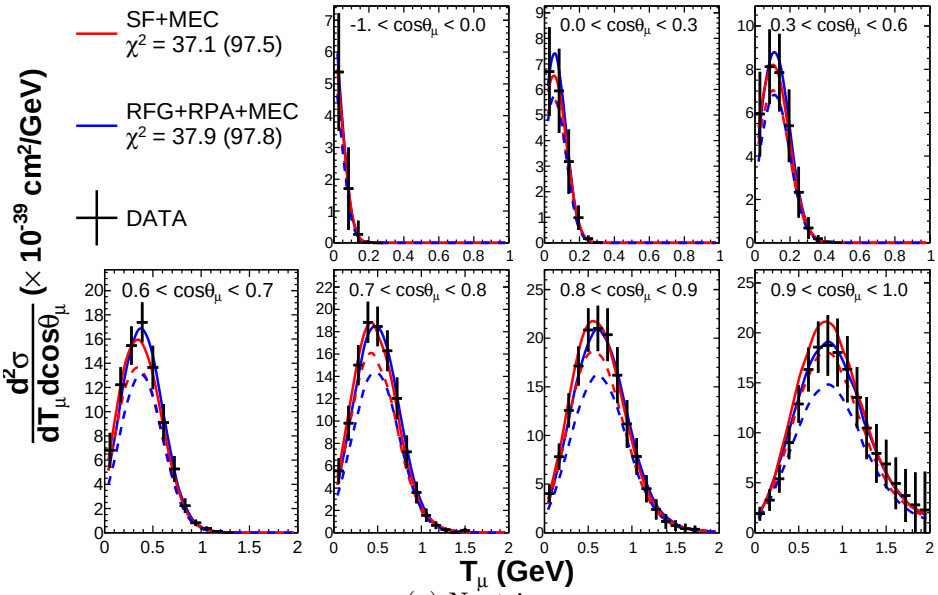

(a) Neutrino

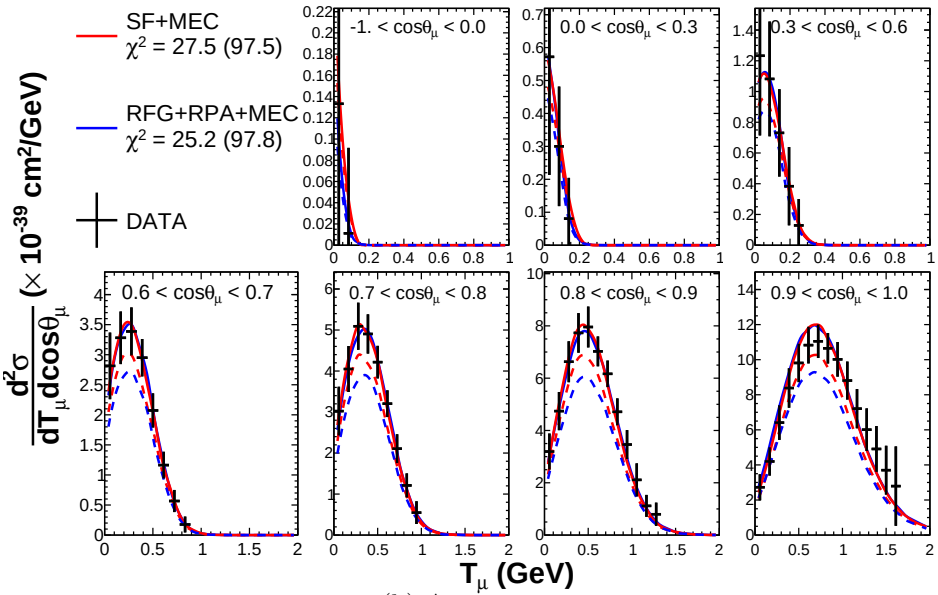

(b) Antineutrino

Figure 4.9: Comparison of nuclear model best-fits to MiniBooNE data (solid lines include MiniBooNE flux normalisation parameters as fit parameters, dashed lines do not fit the flux normalisation parameters). Neutrino interactions on multiple nucleons (MEC) are included. θ_μ is the angle between the incoming neutrino and outgoing muon. Reproduced from [107].

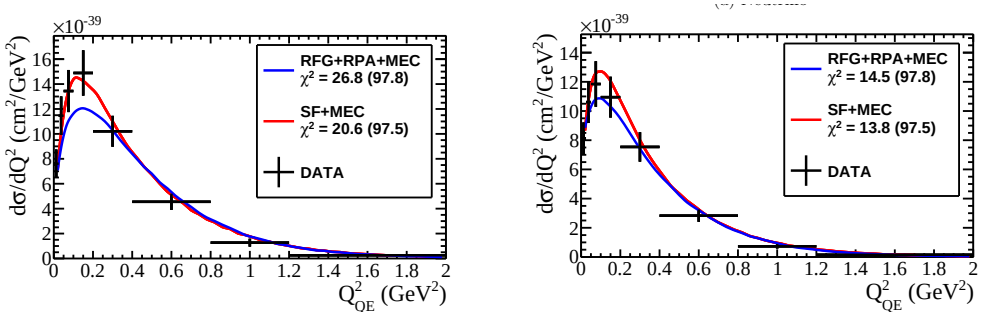

(a) Neutrino (b) Antineutrino

Figure 4.10: Comparison of nuclear model best-fits to MINERvA data. Neutrino interactions on multiple nucleons (MEC) are included. θ_μ is the angle between the incoming neutrino and outgoing muon. Reproduced from [109].

While SF is the nominal model used in NEUT 5.3.2, disagreements between this model and data were observed. In particular, using the Parameter Goodness of Fit (PGoF) test [109], it was found that the SF model joint fits of MINERvA and MiniBooNE data sets were returning very different parameters when compared to separate fits of the data sets, while the RFG model showed greater compatibility between joint and separate fits. When considering all data and the number of degrees of freedom (DOF), the χ^2_{PGoF}/DOF statistic was found to be 25.3 / 6 for RFG with non-relativistic RPA, 17.9 / 6 for RFG with relativistic RPA and 41.1 / 4 for SF. As a result of these findings, T2K adopts the RFG nuclear model with relativistic RPA, requiring the application of two weights to the MC, one to reweight from the default SF model to RFG for QE processes (NC and pion production processes are simulated directly in RFG [110]) and a second to reweight from RFG to RFG with relativistic RPA.

Once the primary ν-nucleon interaction has been handled, one must check for the exit of the nucleon from the nucleus based on the value of the removal energy, subtracting the removal energy from the exiting nucleon if this happens. The value of the removal energy, E_b, is constrained by electron scattering data [111], where its value can be determined based on the location of the CCQE peak (see section 4.2.2).

The next stage is to simulate the interaction of daughter particles from the primary interaction with the remaining nucleons (the so-called 'final state interaction' (FSI)) through a cascade model that treats hadrons as moving classically within the nucleus and undergoing independent collisions, where energy and momentum are conserved and the mean free path calculation takes into account medium effects and is tuned by free particle nucleon scattering data.

The nuclear potential is accounted for by the Random Phase Approximation

(RPA) [108, 112], which attempts to describe the collective effects of nucleon-nucleon interactions and correlations as a function of q^2, where q is the four-momentum transferred to the nucleon, constrained by π-nucleus scattering data [113]. However, as theoretical uncertainties remain large, an alternative parameterisation using Bernstein polynomials [114] attempts to reproduce the q^2 dependence of the Nieves model [108] while covering larger uncertainties (see fig. 4.11). These effects are applied only in CCQE processes because, while such effects are expected in pion-production, no calculation exists for pion-production and therefore they are accommodated as part of the tuning of pion-production parameters on external data.

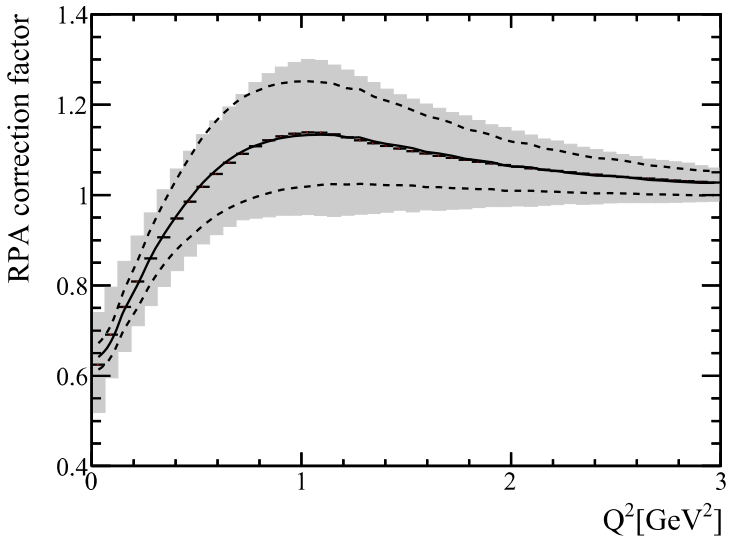

Figure 4.11: Nominal Nieves RPA correction factor (solid black line) and uncertainties (dashed black lines) and the corresponding nominal BeRPA correction (black data points) and uncertainties (grey band). Reproduced from [103].

4.2.2 Neutrino scattering

Neutrino scattering processes implemented in NEUT include quasi-elastic, resonance production and decay, two-body current interactions, coherent pion production and deep inelastic scattering.

CCQE

The CCQE process is the most important scattering process for T2K, being the dominant ν-nucleon interaction at energies below $\sim$ 1 GeV. The process involves the interaction of a neutrino (antineutrino) with a neutron (proton) to produce a negatively (positively) charged lepton and a proton (neutron), as shown in fig. 4.12. The cross-section is calculated under the Llewellyn-Smith [115] model. However, this model calculates cross-sections under an assumption that the nucleons are free, which is not the case for T2K and therefore in-medium effects are accommodated using the RFG model described in the previous section.

The CCQE cross-section is very sensitive to the shape of the weak axial form factor, $F_A(q^2)$, of the nucleon [116], which T2K assumes to be modelled by a dipole of the form

$$F_A(q^2) = \frac{F_A(0)}{\left[1 + q^2 / \left(M_A^{QE}\right)^2\right]^2} \tag{4.2}$$

While the value of $F_A(0)$ can be determined from beta-decay experiments and is known quite well, the value of the axial mass, M_A^{QE} is constrained only by neutrino-deuterium scattering in bubble chambers [117] and remains a significant source of uncertainty [116]. In this analysis the form factor uncertainty is included within the ν_μ/ν_e cross-section systematic [103].

The energy of the incident neutrino in a CCQE interaction can be reconstructed from the outgoing lepton energy, E_l, momentum, p_l and angle, θ_l, assuming the target nucleon is initially at rest, as

$$E_r = \frac{M_p^2 - (M_n - E_b)^2 - M_l^2 + 2E_l(M_n - E_b)}{2(M_n - E_b - E_l + p_l \cos\theta_l)} \tag{4.3}$$

where M_p, M_n and M_l are the proton, neutron and outgoing lepton masses respectively and E_b is the removal energy. Strictly, eq. (4.3) is the reconstructed neutrino energy for the neutrino CCQE process, with the neutron and proton mass terms exchanged for the antineutrino CCQE case. However, the difference between the two versions is negligible, so T2K uses only the neutrino CCQE version when computing reconstructed energy. It should also be noted that for the purposes of computing reconstructed energy, events are assumed to be CCQE (though see the comment on single pion production below).

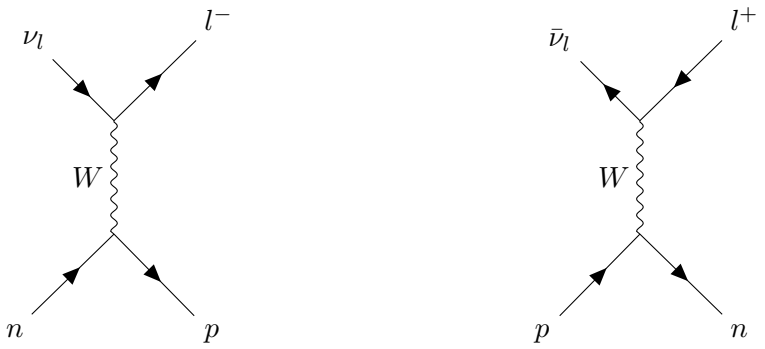

(a) ν (b) $\bar{\nu}$

Figure 4.12: CCQE processes.

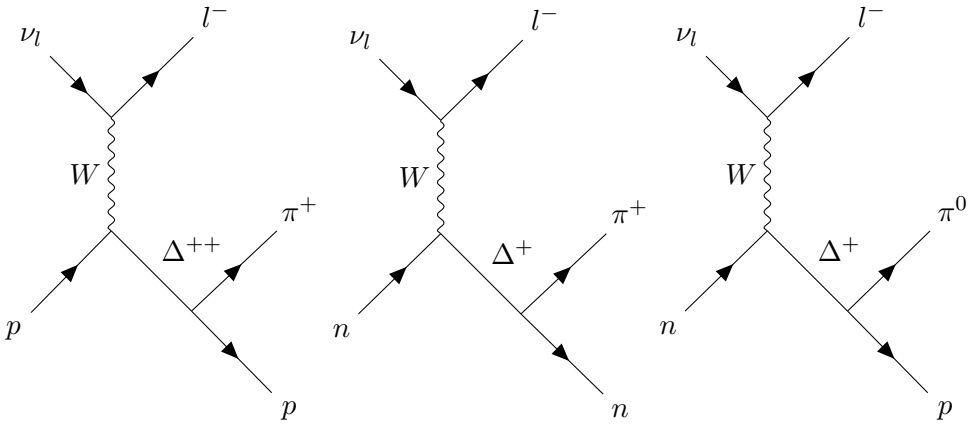

Figure 4.13: Charged current single pion production processes via $\Delta(1232)$ resonances.

Resonances

At sufficiently high energies charged current neutrino interactions can result in the production of heavier intermediate baryons along with the outgoing lepton. This baryon can then undergo decay into a nucleon and another particle, either a photon or meson, typically a pion, as shown in fig. 4.13.

Single pion production is modelled using the Rein-Sehgal formalism [118], with the cross-section of each process computed in two steps; the amplitude of the resonance is determined and then multiplied by the decay probability of the resonance into (in this case) one pion and one nucleon. A total of 18 resonances below 2 GeV are considered [102]. For this analysis, the single pion production processes have individual interaction modes for charged current (CC1π) and neutral current (NC1π) processes, while all other resonances are grouped together in combined

interaction modes for each of charged current ('CC other') and neutral current ('NC other').

The Rein-Sehgal model depends upon the axial mass constant (M_A^{RES}), axial form factor (C_5^A) and the non-resonant background scaling (BgRes). The non-resonant background scaling factor is included because single pion production is not adequately described solely in terms of resonances [118], so an additional energy-dependent contribution (rising with energy) to the cross-section is included.

It should also be noted that single pion production (specifically π^+ production) has its own sample at SK (see section 4.4), for which an alternative reconstructed energy formula is used

$$E_r = \frac{M_p E_l + \frac{1}{2}(M_d^2 - M_l^2 - M_p^2)}{M_p - E_l + p_l \cos\theta_l} \tag{4.4}$$

where M_d is the mass associated with the Δ resonance.

2p2h

2p2h (2 particles, 2 holes) processes involve the interaction of a neutrino with two nucleons (see fig. 4.15). The total cross-section is a combination of three contributions; meson exchange currents, which are dominated by pionless Δ decay (PDD), nucleon-nucleon correlations (NN) and an interference term between PDD and NN [103]. In this scenario, both nucleons can be ejected from the nucleus, leaving behind two holes, hence 2 particles, 2 holes. Electron scattering data [111, 119] demonstrates that 2p2h processes contribute substantially to the cross-section between CCQE and resonance regions; that is, the dip in the region between the CCQE and resonance peaks (see fig. 4.14) is shallower than expected and 2p2h interactions are believed to explain this. These processes are important in ν-nucleus interactions because the signal can be misidentified as quasi-elastic and therefore result in a biased energy reconstruction. NEUT simulates 2p2h using the Nieves model [108].

There are four systematic parameters governing uncertainties in 2p2h processes; two concern the overall normalisation, one for each of ν and $\bar{\nu}$, the uncertainty on the propagation of the normalisation from Carbon to Oxygen, and an uncertainty on the 2p2h shape on Oxygen.

Coherent pion production

Rather than interacting with an individual nucleon in the target nucleus, neutrinos can interact with the nucleus as a whole, leaving the nucleus unchanged and creating

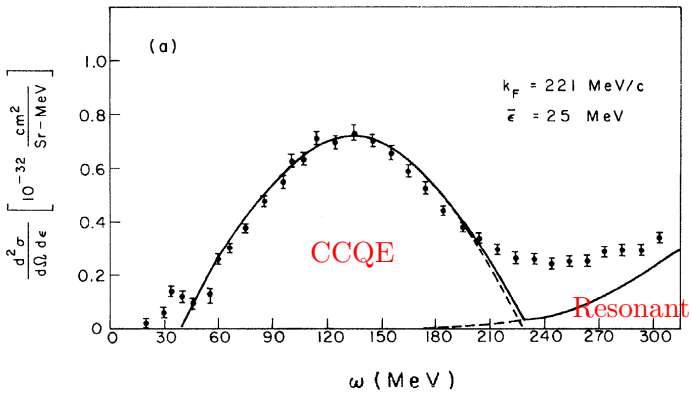

Figure 4.14: Cross-sections from electron scattering data on carbon showing the observed excess between the CCQE and resonance regions, which is described by 2p2h processes. Reproduced from [111].

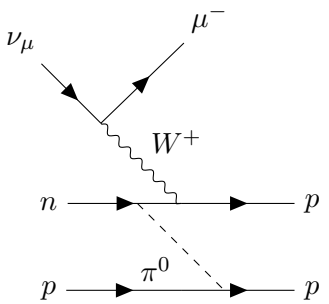

Figure 4.15: An example 2p2h process.

a pion (see fig. 4.16). This process has been observed at energies above 2 GeV and is modelled in NEUT using the Rein-Sehgal model [120]. At energies below 1 GeV this model over-estimates the cross-section and so a reweighting based on comparison to the Berger-Sehgal model [121] is used to correct this over-estimation.

In this analysis there are also systematic parameters describing the normalisation uncertainty associated with the CC and NC coherent pion production processes (uncorrelated).

Deep inelastic scattering and multiple pion production

At sufficiently high energies ($E_\nu \gg m_N$), neutrino-nucleon interactions are dominated by deep inelastic scattering (DIS), where the nucleon in the interaction is broken up and hadronisation occurs. DIS is simulated for hadronic invariant mass above 1.3 GeV [102]. The distribution of nucleons is determined from the method of

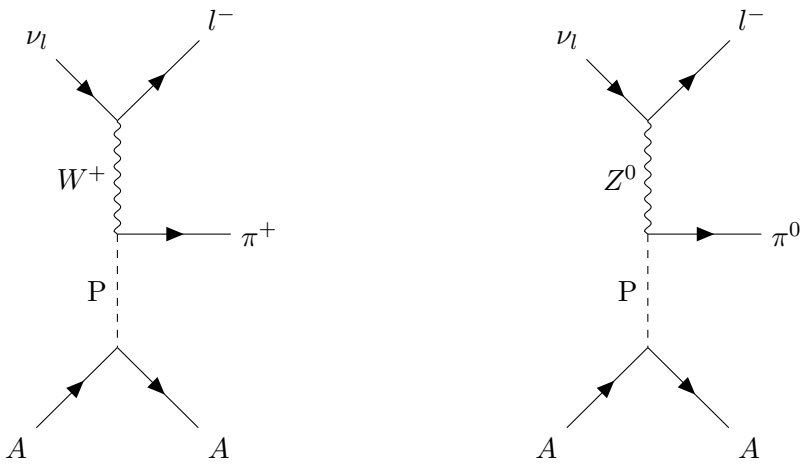

(a) CC (b) NC

Figure 4.16: Coherent pion production. A represents the entire atomic nucleus, while P is a Pomeron carrying 4-momentum to that nucleus.

Glück, Reya and Vogt [122], with corrections applied to improve the agreement with data at low q^2 [123] and neutral current cross-sections for DIS processes come from [124, 125]. Due to the overlap in the range of hadronic invariant masses with the single pion production processes below 2 GeV, a pion multiplicity probability function is used to cut out single pion events in this region to avoid double counting, with the pion multiplicities being tuned on hydrogen bubble chamber data [126]. Systematic parameters associated with DIS describe the uncertainty on the charged current pion multiplicity and the uncertainty on the neutral current event normalisation.

Final state, secondary and photo-nuclear interactions

As previously noted, daughter particles in neutrino-nucleon interactions must pass through the nuclear medium before exiting the nucleus and therefore there is the opportunity for those particles to undergo interactions within the nucleus prior to observation. In particular, absorption, scattering and particle production can affect the observed final state. Such interactions are referred to as final state interactions (FSI). While daughter leptons can undergo FSI, because these interactions are electromagnetic the interactions are not strong enough to warrant consideration, whereas daughter hadrons undergo strong interactions and therefore must be accounted for.

FSI are relevant to T2K because changes to the observable particles and kinematics of those particles can lead to biases in the reconstructed neutrino energy. For

example, at T2K the main channel for neutrino interactions is the CCQE channel, which is assumed to be a two body interaction, where the daughter particles are an observable charged lepton and a (typically) unobservable nucleon, with the energy reconstruction being based on the observed lepton energy, momentum and angle (see eq. (4.3)). However, if a single pion production interaction was to take place, with daughter charged lepton, nucleon and pion and the daughter pion were to be absorbed, the event would look like a CCQE event, leading to an incorrect neutrino energy reconstruction from a failure to account for the third daughter particle. Even (quasi-)elastic scattering of pions, that don't change the observable particles can have an effect, as changes to the kinematics can affect both the pion identification efficiency and reduce the visible energy of an interaction as the pion loses energy with each scattering event. In addition, charge exchange interactions (e.g. $\pi^+ \rightarrow \pi^0$) change the rate of π^0 production, which is an important background for ν_e appearance. With these various channels allowing for misidentification of events and incorrect energy reconstruction, accurate modelling of FSI and SI processes is very important.

NEUT implements a cascade model for FSI and SI, tuned to external data sets. Whilst FSI affects all final state particles, the pion is most significant at T2K energies and so pion re-interaction is given special consideration for FSI and SI in NEUT. It should be noted that the π^0 lifetime outside of the nucleus is extremely short and therefore π^0 does not undergo secondary interactions [127]. The FSI model is tuned to external pion scattering data [113]; while this external data has a beam of pions incident on a target nucleus, rather than a pion created within the nucleus, as is the case for T2K, the physics of pion-nucleus interaction should be the same in each case. This also motivates the use of the same cascade model for SI once a pion has left the nucleus.

In the NEUT cascade model [127] the starting position for a pion produced within an Oxygen nucleus is determined based on a Woods-Saxon potential describing the nuclear density:

$$\frac{\rho(r)}{\rho_0} = \frac{1}{1 + \exp\left(\frac{r-c}{\alpha}\right)} \tag{4.5}$$

where r is the distance from the centre of the nucleus, while c and α are the nuclear radius and surface thickness respectively, whose values are determined from electron scattering data [128]. The initial pion kinematics are determined from the ν-nucleus interaction model described previously, and the pion is then classically propagated through the nuclear medium in a sequence of steps until it is either absorbed, or leaves the nucleus. A pion is determined to have left the nucleus once its distance

from the centre exceeds a value R_N, which is determined such that $\rho(R_N)/\rho_0 \simeq 10^{-4}$, ensuring that most of the nuclear medium is encompassed without wasting computational time in the low density region. Interaction probabilities are calculated at each step according to the model of Salcedo et al [129] for pion momenta below 500 MeV and are taken from pion scattering data on free protons and deuterons [130] for pion momenta above 500 MeV, with the two regions blended over 400-500 MeV to prevent discontinuities. At each step the pion travels a distance dx, where dx is chosen so that the probability of two or more interactions in a single step is negligible ($dx = R_N/100$).

In the cascade model five parameters control pion interaction probability at each step; at low momenta (< 500 MeV) there are parameters for pion absorption and QE scattering along with a sixth parameter that controls the fraction of charge exchange in QE scattering; while at higher momenta there are parameters governing QE scattering, single charge exchange and inelastic scattering. However, these parameters are not implemented as response functions at SK. Rather a covariance matrix is constructed relating the number of events in bin i to bin j from a reweighting of each SK sample according to a set of 16 variations of the aforementioned parameters, selected to conservatively cover external data. The binning is the same as used for the SK detector matrix (see section 4.5) and as such the FSI+SI errors are added in quadrature with the SK detector errors (see section 4.5).

A simple model for photo-nuclear effects, in which one of the photons from $\pi^0 \to \gamma\gamma$ is absorbed by a nucleon (reducing the efficiency of π^0 rejection), is implemented in SKDETSIM [131]. In this model propagation of photons with an energy below 150 MeV is stopped according to the measured photo-nuclear cross section. The uncertainty in the photo-nuclear interactions is also added in quadrature to the SK detector matrix (see section 4.5).

4.3 Near detector constraints

The predicted spectra at SK are tuned based on a fit of data collected from neutrino interactions in ND280 (see fig. 4.1). This fit is performed using two different frameworks [132]; one frequentist framework, known as the BANFF fit (Beam and ND280 Flux Extrapolation Task Force) and a Bayesian Markov Chain Monte Carlo fitter called MaCh3. These two fitters provided cross-validation of the near detector fit, but for the purpose of this analysis the input is provided by the frequentist framework and so the discussion of the near detector constraint will be undertaken in the context of the BANFF fit. This input takes the form of a vector of tuned

central values for systematic parameters, along with a covariance matrix describing the uncertainties and correlations between the various parameters.

4.3.1 Near detector samples

The BANFF fit adopts a binned likelihood fit for selected event samples, with systematic weights applied on an event-by-event basis and with penalty terms applied for selected systematic parameters. Data from T2K runs 2-6 are used in the near detector fit, with 3 FHC samples and 4 RHC samples being fit simultaneously. In particular:

- FHC: ν_μ CC0π, ν_μ CC1π^+ and ν_μ CC-other
- RHC: $\bar{\nu}_\mu$ CC 1-Track, $\bar{\nu}_\mu$ CC N-Track, ν_μ CC 1-Track and ν_μ CC N-Track

with each sample binned in p_μ and $\cos\theta_\mu$, where p_μ is the observed muon momentum and θ_μ is the opening angle of the muon with respect to the nominal beam direction. As is the case for the SK MC, the MC at the ND280 is reweighted from an SF nuclear model to RFG with an RPA correction applied to CCQE events and coherent pion production events reweighted based on MINERvA data to correct from the Rein-Sehgal to Berger-Sehgal model [133].

Inclusive selection

Each of the 7 samples undergoes a common set of pre-selection cuts to extract CC events before a final set of cuts selects 1 of the 7 samples for each event. The cuts for the pre-selection are [134]:

1. Data quality cut: This requires events to arrive within the beam time window (events in different bunches within the same spill are treated independently) and a good global ND280 data quality flag.
2. Track multiplicity cut: There must be at least 1 track crossing a TPC.
3. Track quality cut: To improve the reliability of track reconstruction the highest momentum track in the event is selected and this track must be of sufficient length (more than 18 hit clusters in the TPC). Furthermore, there must be a corresponding segment of the track in an FGD (FGD1 + TPC2 or FGD2 + TPC3), with the vertex for the track within the FGD fiducial volume (at least 5 scintillator bars away from the edge of an XY module and not in the first XY module in the z-direction).

4. Upstream background veto: Tracks originating in the P0D and undergoing scattering in an FGD can be reconstructed as two tracks (P0D + TPC1 + FGD1 and FGD1 + TPC2). If the second highest momentum track starts 150mm upstream of the primary track the event is excluded. Additionally, if the primary track starts in FGD2 then the event is excluded if the secondary track starts in FGD1.

5. Broken track cut: Muon tracks can be broken such that one track is fully contained in an FGD, with a second track starting in the last layers of the FGD and then propagating to the TPC. If an FGD-only track is present, the FGD + TPC track must start more than 425mm away from the most downstream edge of the FGD.

6. Muon PID: The primary track is a muon according to a dE/dx measurement PID hypothesis.

FHC CC selections

Having performed the pre-selection, the allocation of an event to 1 of the 3 FHC CC selections is based on the content of any secondary tracks accompanying the primary muon candidate. The selection can follow 1 of 2 paths depending on the availability of TPC PID and is undertaken as follows [134]:

1. Coincidence cut: Any secondary track must exist in the same bunch and FGD fiducial volume as the muon candidate.

2. Track quality cut: The secondary track must enter a TPC and deposit more than 18 hit clusters in that TPC.

3. PID cut: If the secondary track is positive, select either π^+, e^+, or p based on TPC PID hypothesis. If the secondary track is negative, select either π^-, or e^- based on TPC PID hypothesis.

The second path where TPC PID is not available, due to momentum being too low or track angle too high[1] is:

1. Coincidence cut: Any secondary track must exist in the same bunch and FGD fiducial volume as the muon candidate.

[1]In this instance it is also possible that a secondary track is not evident in the same bunch as the primary track due to low π momentum, but that a Michel electron is observed outside of the bunch time window ($\pi^{\pm} \rightarrow \mu^{\pm} \rightarrow e^{\pm}$) due to the 2.19$\mu$s decay time of the muon, in which case the π antecedent can be identified by the presence of a Michel electron

2. PID cut: If the secondary track is positive, select π^+ based on FGD PID hypothesis or Michel electron tag. If the secondary track is negative, select π^- based on FGD PID hypothesis or Michel electron tag.

Finally, with secondary tracks identified and classified the event is allocated to an FHC sample as:

- If no $\pi^\pm$ or $e^\pm$ are identified, the event is assigned to the FHC CC0π sample.
- If the sum of TPC π^+, FGD π^+ and FGD Michel electrons is 1, then the event is allocated to the FHC CC1π sample.
- Events with one or more π^-, or π^0 and more than 1 π^+ form the CC-Other sample.

RHC CC selections

The RHC CC selections allocate events to 1 of 4 samples based on the number of tracks in the sample and whether or not the primary muon candidate is a 'right-sign' μ^+ or 'wrong-sign' μ^-. Having performed the pre-selection cuts, the final cut to allocate an event to a particular sample is trivial [135, 136]:

- Events with 1 track and a right-sign primary muon candidate are allocated to the RHC $\bar{\nu}_\mu$ CC 1-Track sample.
- Events with more than 1 track and a right-sign primary muon candidate are assigned to the RHC $\bar{\nu}_\mu$ CC N-Track sample.
- Events with 1 track and a wrong-sign primary muon candidate are added to the RHC ν_μ CC 1-Track sample.
- Events with more than 1 track and a wrong-sign primary muon candidate form the RHC ν_μ CC N-Track sample.

4.3.2 Fit methodology

The BANFF fit minimises the chi2 function, which is defined as [137]:

$$\Delta\chi^2 = 2\sum_{i=1}^{N_{bins}} N_i^p(\vec{b},\vec{x},\vec{d}) - N_i^d + N_i^d \ln\left[N_i^d/N_i^p(\vec{b},\vec{x},\vec{d})\right] \tag{4.6}$$
$$+ \sum_{i=1}^{N_{flux}}\sum_{j=1}^{N_{flux}} \Delta b_i (V_b^{-1})_{i,j} \Delta b_j$$
$$+ \sum_{i=1}^{N_{xsec}}\sum_{j=1}^{N_{xsec}} \Delta x_i (V_x^{-1})_{i,j} \Delta x_j$$
$$+ \sum_{i=1}^{N_{det}}\sum_{j=1}^{N_{det}} \Delta d_i (V_d^{-1})_{i,j} \Delta d_j$$

where N_i^d is the observed number of events in each analysis bin i, with i ranging over all p_μ and $\cos\theta_\mu$ bins in each sample and N_i^p is the corresponding predicted number of events, which depends upon the flux, $\vec{b}$, cross-section, $\vec{x}$ and detector, $\vec{d}$, systematic parameters. V_b, V_x and V_d are the covariance matrices for the flux, cross-section and detector systematic parameters respectively and Δb, Δx and Δd are variations away from the nominal values of the beam, cross-section and detector systematic parameter nominal values respectively.

The vector $\vec{d}$ and its associated covariance matrix V_d are first determined by computing the mean and variance of the number of events in each bin from 2000 throws of the detector systematic parameters. These parameters can modify event weights and observed quantities, such as momentum, allowing events to migrate between samples and bins in addition to altering the normalisation.

4.3.3 Fit result

The resultant covariance from the BANFF fit is shown in figs. 4.17 to 4.18, with central values and pre- and post-fit errors presented in Appendix A.

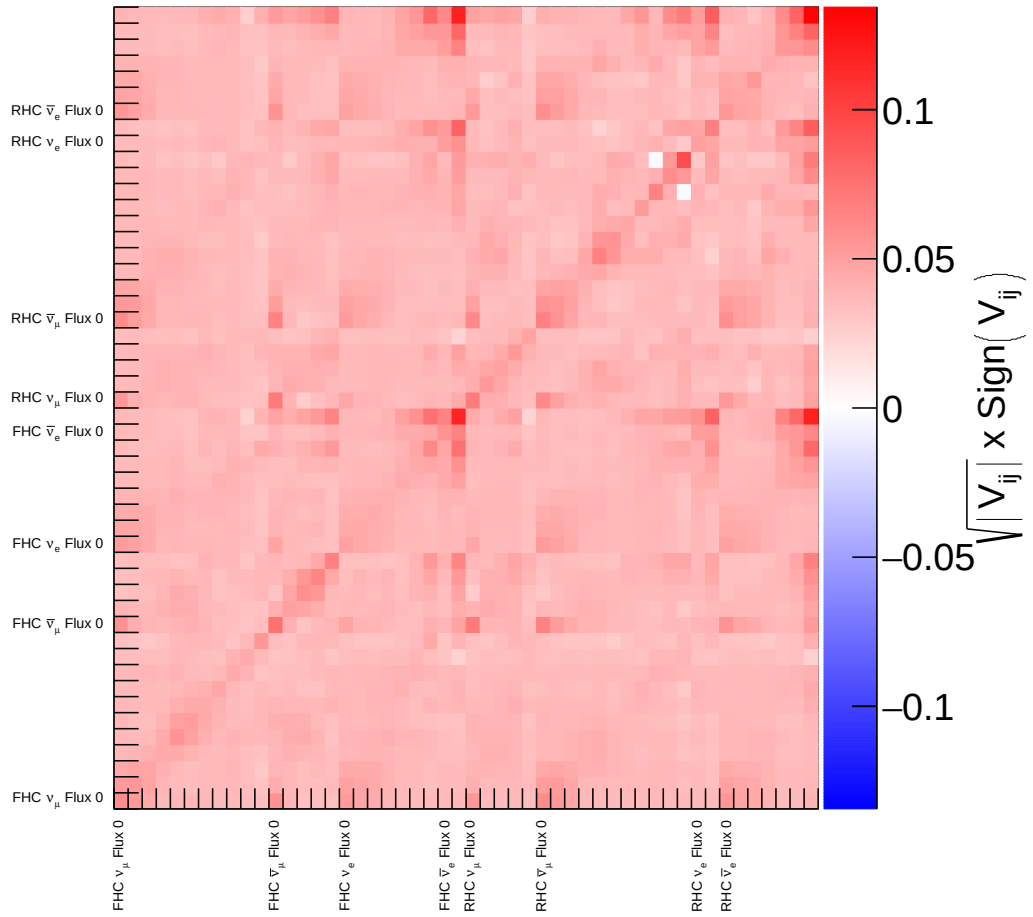

Figure 4.17: The flux covariance matrix from the BANFF fit. The parameters in the flux covariance matrix are presented from bottom-to-top and left-to-right in the order specified in tables A.1 to A.2.

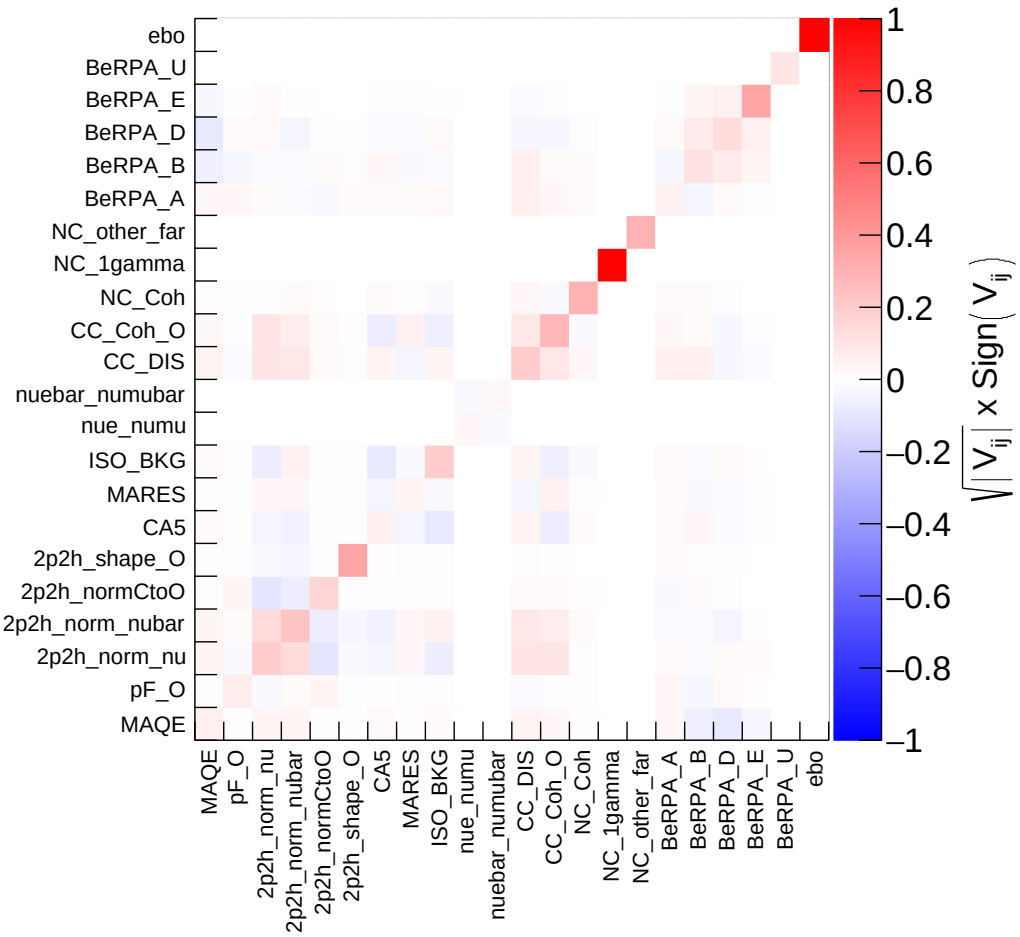

Figure 4.18: The cross-section covariance matrix from the BANFF fit.

4.4 SK samples

Events at SK are split into five different categories; 1-ring ν_μ-like, 1-ring ν_e-like and 1-ring ν_e CC1π^+-like in FHC and 1-ring ν_μ-like and 1-ring ν_e-like in RHC. The aim is to achieve a high purity of the desired type of event whilst retaining the largest possible sample and as such, the event selection procedure is designed to achieve these goals.

4.4.1 Common cuts

In the first step, a set of cuts common to all five samples are applied to the SK data to ensure that only high-quality data are retained in each sample [138–140]:

1. Good beam spill: A set of cuts applied based on parameters such as beam direction and horn current.

2. SK data quality: The SK data quality depends upon a variety of different factors, with cuts applied to exclude events taken when the data acquisition program was not working correctly, when bad subruns[2] occur (for example a subrun coincident with blasting in Kamioka mine), when parts of the detector cease to function correctly, when errors occur in both sets of GPS data, when special data blocks[3] are taken and when there is activity in the detector in the 100μs before beam arrival to avoid contamination of the event sample due to cosmic ray muons.

3. Timing cut: A cut is applied to retain only those events occurring in the interval $[-2, +10]$ μs of the arrival time of the leading edge of a beam spill.

4. Containment cut: Events that originate outside the inner detector and then enter are rejected by looking for activity in the outer detector. In particular, if 16 or more PMT hits are observed in the highest charge outer detector hit cluster the event is rejected, otherwise it is classified as fully contained (FC).

4.4.2 Fiducial volume definitions

Discrimination between e-like and μ-like events depends upon features of the Cherenkov rings and thus it is important to have well imaged rings. Events that are close to the inner detector wall and point towards the wall will typically hit too few PMTs to generate well imaged Cherenkov rings, whereas those that are close to the inner

[2] A subrun is approximately 1 minute of real-time observation

[3] special data blocks periodically replace PMT hit signal data with other information

detector wall, but point inwards, towards the opposite wall will typically hit enough PMTs to produce well imaged Cherenkov rings. As such, the fiducial volume (FV) within the inner detector is defined in terms of the minimum distance from the event vertex to the inner detector wall (*wall*) and the distance from the event vertex to the inner detector wall along the direction of the particle track (*towall*) [141]. While all samples apply an FV cut, the FV itself has a different definition for the case of 1-ring ν_e-like, 1-ring ν_μ-like and 1-ring ν_e CC1π^+-like samples, with the respective definitions applying in both FHC and RHC samples where relevant.

4.4.3 1-ring ν_e-like selection

This section details the cuts that are applied to the SK events to produce the FHC and RHC 1-ring ν_e-like samples. The cut descriptions refer to the conditions under which an event is retained.

1. FV cut: $wall > 80$ cm and $towall > 170$ cm
2. Ring counting cut: 1 Cherenkov ring
3. PID cut: Cherenkov ring identified as 1-ring ν_e-like over 1-ring ν_μ-like
4. Visible energy cut: $E_r > 100$ MeV (in practice reconstructed momentum is used)
5. Decay electron cut: 0 decay electrons
6. Reconstructed energy cut: $E_r < 1250$ MeV
7. π^0 rejection cut: Cherenkov ring identified as 1-ring ν_e-like over π^0-like

Figures 4.19 to 4.26 show the selection effect as each cut is applied in sequence. One can see that very few oscillated ν_e are found within bins of higher ring multiplicity and thus this cut eliminates a large fraction of the dominant ν_μ CC and NC backgrounds. The PID cut then eliminates much of the remaining ν_μ CC background, leaving predominantly NC and intrinsic ν_e backgrounds. Most of the remaining ν_μ CC background and a large fraction of the NC background is eliminated by requiring a minimum visible energy. The decay electron cut has the largest effect on the RHC sample, where the sample is dominated by background where decay electrons are found, while in FHC it serves to split the sample into the 1-ring ν_e-like and 1-ring ν_e CC1π^+-like samples. The reconstructed energy cut has the principal effect of eliminating the intrinsic ν_e background that

exists at higher energies where few oscillated ν_e are found. Finally the π^0 rejection cut serves to reduce much of the remaining NC background while retaining most of the CC events, producing the final, high purity selections shown in fig. 4.27.

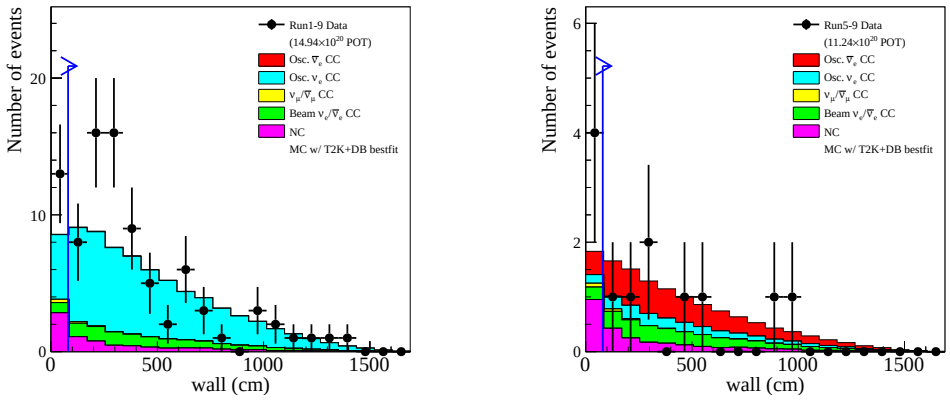

Figure 4.19: Distribution of events by the shortest distance to the inner detector wall in the 1-ring ν_e-like sample in FHC (left) and RHC (right). Reproduced from [138].

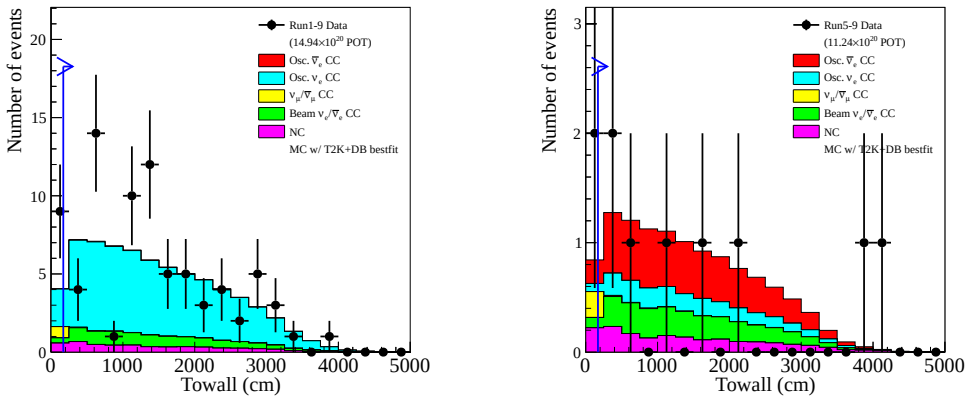

Figure 4.20: Distribution of events by the distance to the inner detector wall along the direction of particle momentum in the 1-ring ν_e-like sample in FHC (left) and RHC (right). Reproduced from [138].

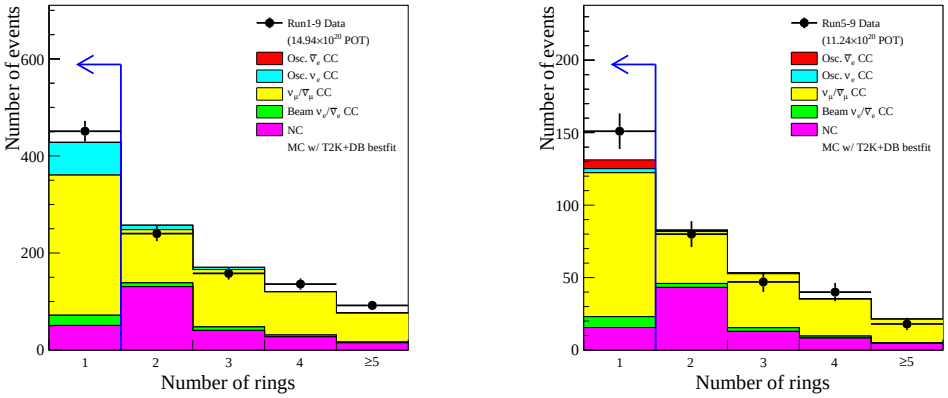

Figure 4.21: Distribution of events by the number of Cherenkov rings in the 1-ring ν_e-like sample in FHC (left) and RHC (right). Reproduced from [138].

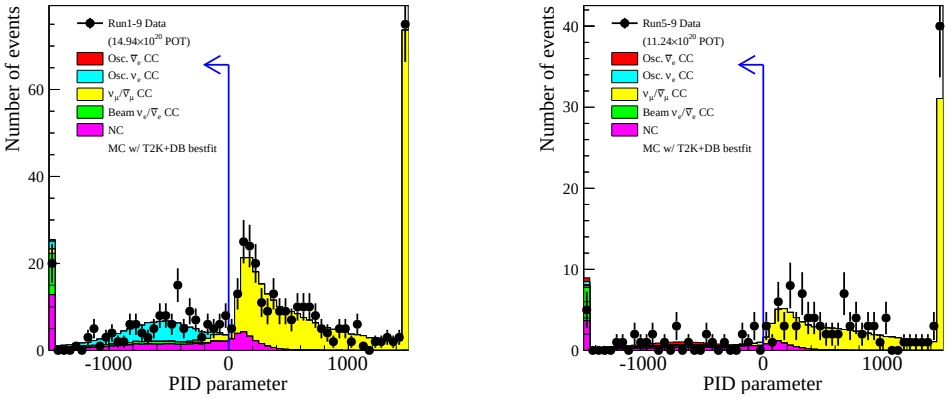

Figure 4.22: Distribution of events by the PID parameter in the 1-ring ν_e-like sample in FHC (left) and RHC (right). Reproduced from [138].

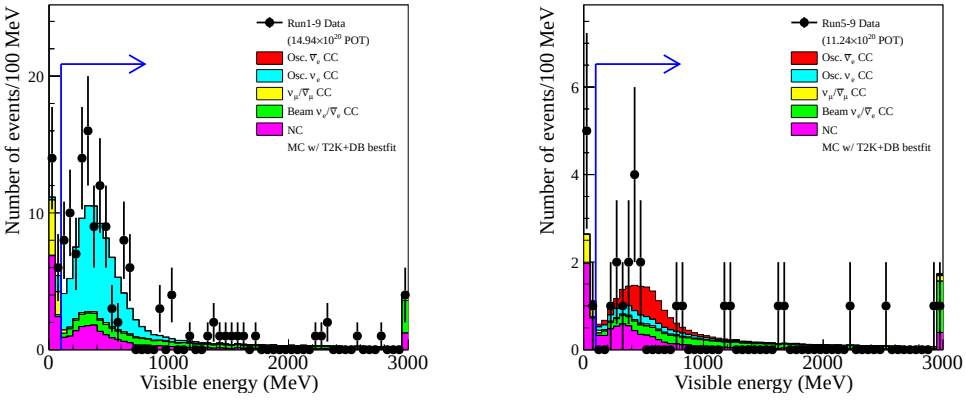

Figure 4.23: Distribution of events by visible energy in the 1-ring ν_e-like sample in FHC (left) and RHC (right). Reproduced from [138].

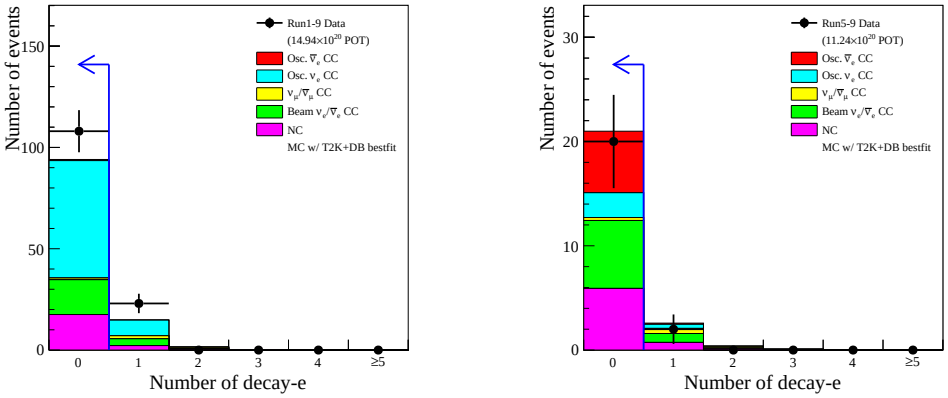

Figure 4.24: Distribution of events by the number of decay electrons in the 1-ring ν_e-like sample in FHC (left) and RHC (right). Reproduced from [138].

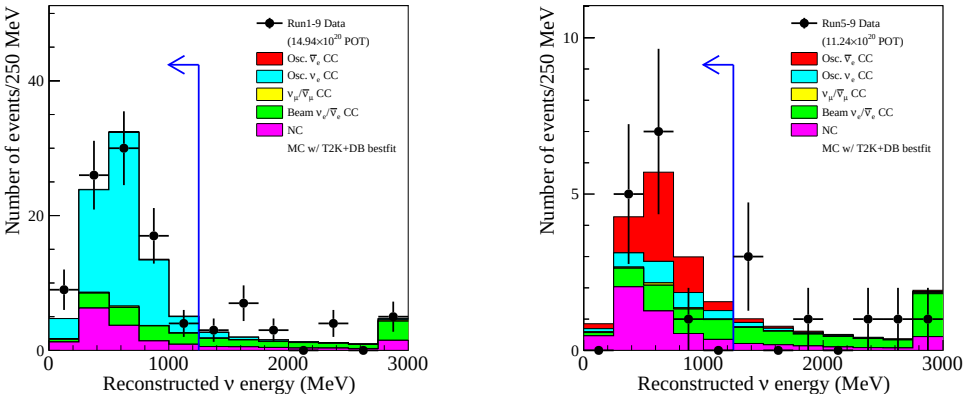

Figure 4.25: Distribution of events by reconstructed neutrino energy in the 1-ring ν_e-like sample in FHC (left) and RHC (right). Reproduced from [138].

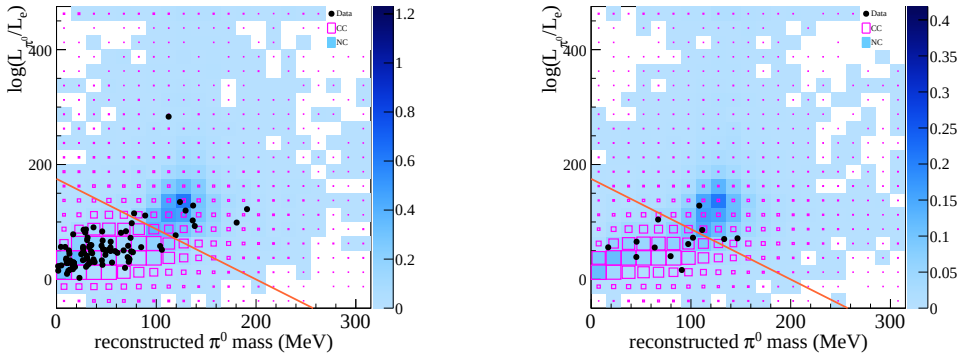

Figure 4.26: Distribution of events in PID parameter and reconstructed π^0 mass in the 1-ring ν_e-like sample in FHC (left) and RHC (right). The size of the magenta boxes indicates the number of CC events, while the blue shading indicates NC events. Reproduced from [138].

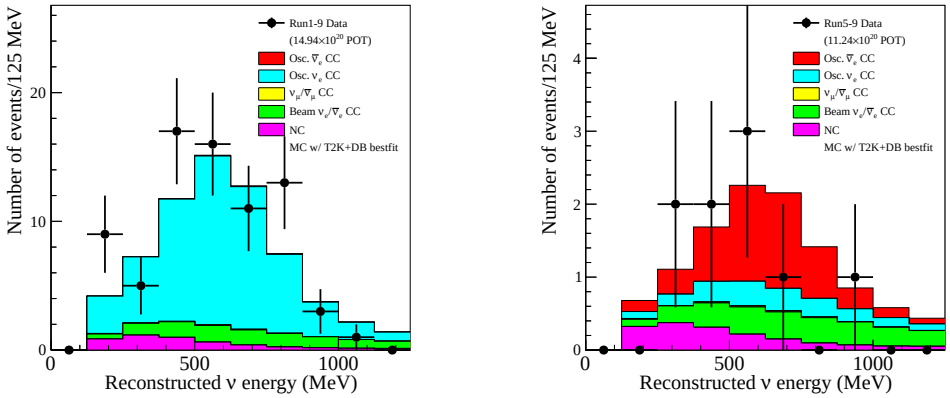

Figure 4.27: Final selection after all cuts are applied in the 1-ring ν_e-like sample in FHC (left) and RHC (right). Reproduced from [138].

4.4.4 1-ring ν_e CC1π^+-like selection

This section details the cuts that are applied to the SK events to produce the FHC 1-ring ν_e CC1π^+-like sample. The cut descriptions refer to the conditions under which an event is retained.

1. FV cut: *wall* $>$ 50 cm and *towall* $>$ 270 cm
2. Ring counting cut: 1 Cherenkov ring
3. PID cut: Cherenkov ring identified as 1-ring ν_e-like over 1-ring ν_μ-like
4. Visible energy cut: $E_r > 100$ MeV (in practice reconstructed momentum is used)
5. Decay electron cut: 1 decay electron
6. Reconstructed energy cut: $E_r < 1250$ MeV
7. π^0 rejection cut: Cherenkov ring identified as 1-ring ν_e-like over π^0-like

Figures 4.28 to 4.31 show the selection effect as each cut is applied in sequence, with the effect of each cut behaving, unsurprisingly, much like the 1-ring ν_e-like sample and producing the final selection shown in fig. 4.32.

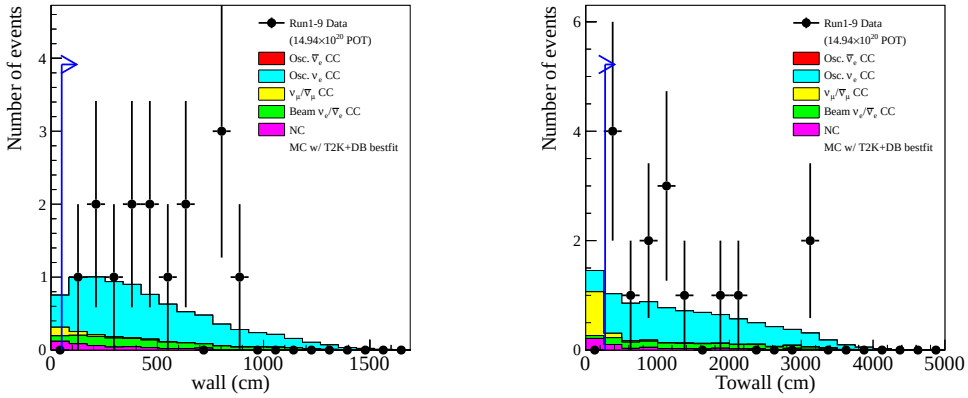

Figure 4.28: Distribution of events by the shortest distance to the inner detector wall (left) and the distance to the inner detector wall along the direction of particle momentum (right) in the 1-ring ν_e CC1π^+-like sample. Reproduced from [138].

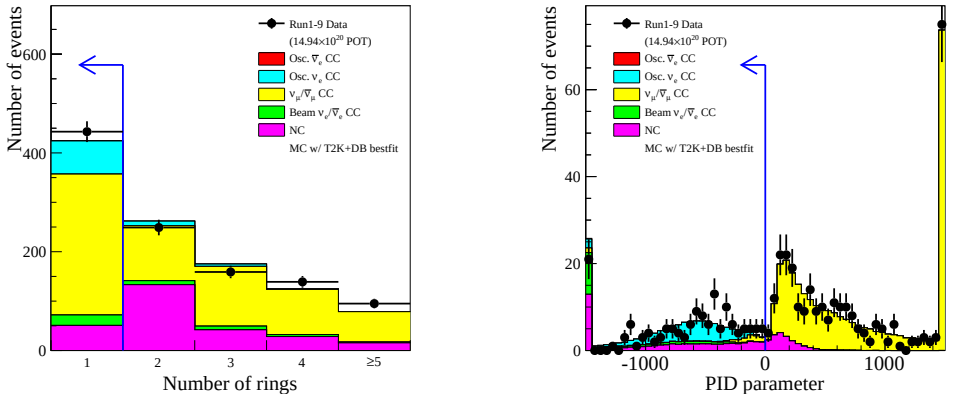

Figure 4.29: Distribution of events by the number of Cherenkov rings (left) and by PID parameter (right) in the 1-ring ν_e CC1π^+-like sample in FHC (left) and RHC (right). Reproduced from [138].

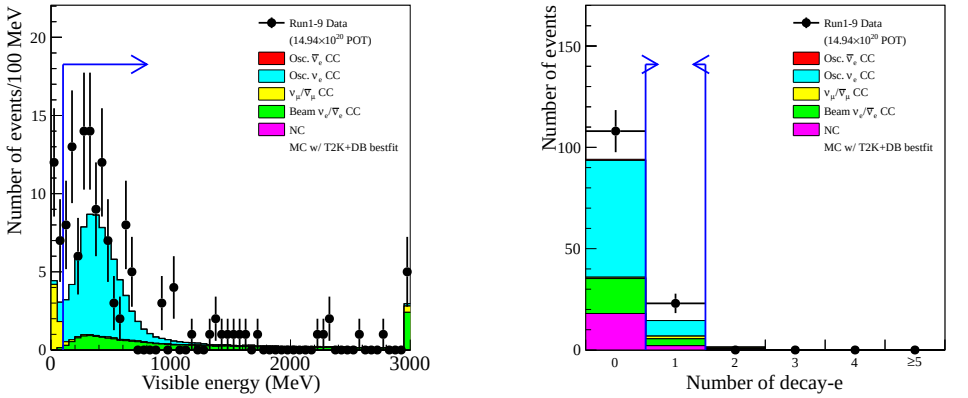

Figure 4.30: Distribution of events by visible energy (left) and number of decay electrons (right) in the 1-ring ν_e CC1π^+-like sample. Reproduced from [138].

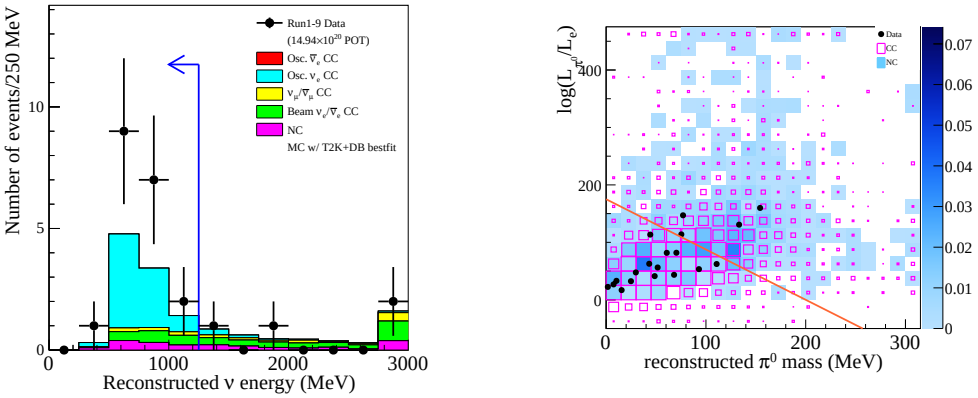

Figure 4.31: Distribution of events by reconstructed neutrino energy (left) and in PID parameter and reconstructed π^0 mass in the 1-ring ν_e CC1π^+-like sample. The size of the magenta boxes indicates the number of CC events, while the blue shading indicates NC events. Reproduced from [138].

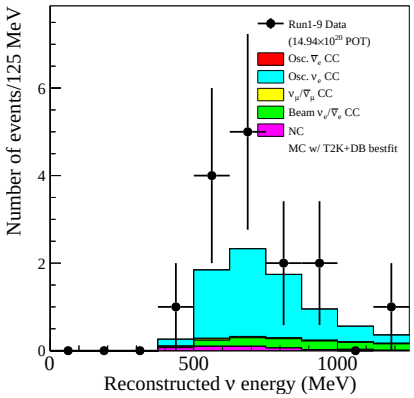

Figure 4.32: Final selection after all cuts are applied in the 1-ring ν_e CC1π^+-like sample. Reproduced from [138].

4.4.5 1-ring ν_μ-like selection

This section details the cuts that are applied to the SK events to produce the FHC and RHC 1-ring ν_μ-like samples. The cut descriptions refer to the conditions under which an event is retained.

1. FV cut: *wall* $>$ 50 cm and *towall* $>$ 250 cm
2. Ring counting cut: 1 Cherenkov ring
3. PID cut: Cherenkov ring identified as 1-ring ν_μ-like over 1-ring ν_e-like
4. μ momentum cut: $p_\mu > 200$ MeV

5. Decay electron cut: < 2 decay electrons

6. π^+ rejection cut: Cherenkov ring identified as 1-ring ν_μ-like over π^+-like

Figures 4.33 to 4.39 show the selection effect as each cut is applied in sequence. Similarly to the 1-ring ν_e-like samples, few CC events are observed at higher ring multiplicities and therefore the ring counting cut eliminates much of the NC and CCnQE background, while the PID cut eliminates ν_e events. The decay electron cut reduces the CCnQE background while having little effect on the CCQE events, while the π^+ rejection cut removes much of the NC background to produce the final selections shown in fig. 4.40, where the principal remaining background is from CCnQE events in FHC and both CCnQE and wrong-sign muon events in the RHC sample.

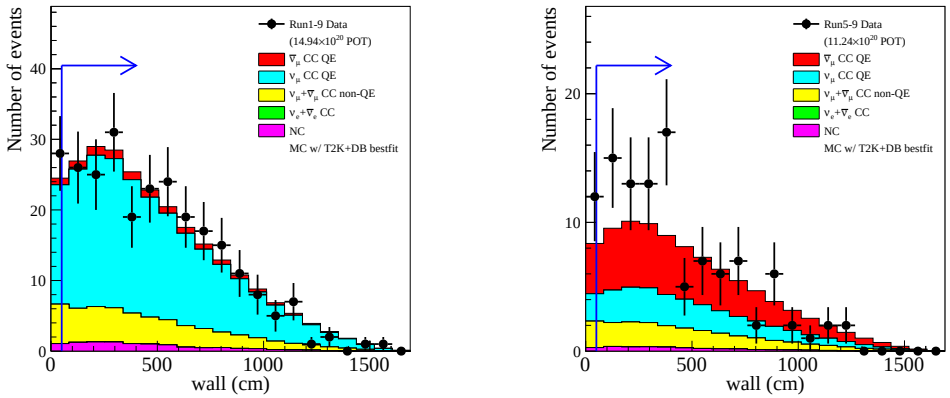

Figure 4.33: Distribution of events by the shortest distance to the inner detector wall in the 1-ring ν_μ-like sample in FHC (left) and RHC (right). Reproduced from [138].

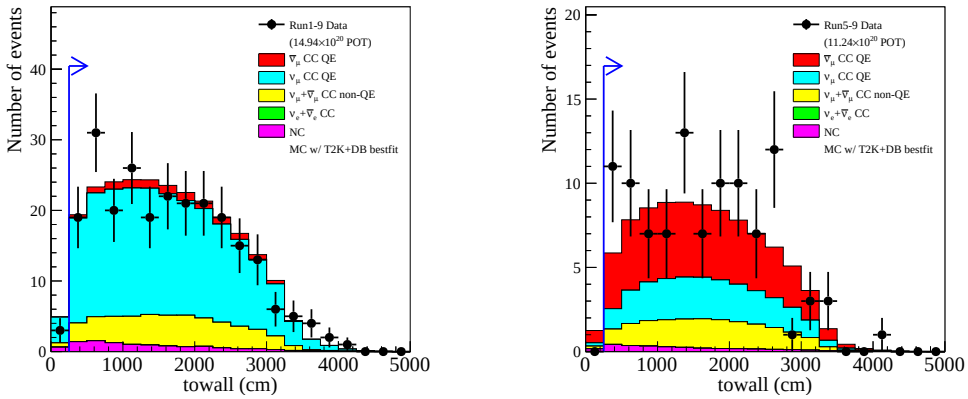

Figure 4.34: Distribution of events by the distance to the inner detector wall along the direction of particle momentum in the 1-ring ν_μ-like sample in FHC (left) and RHC (right). Reproduced from [138].

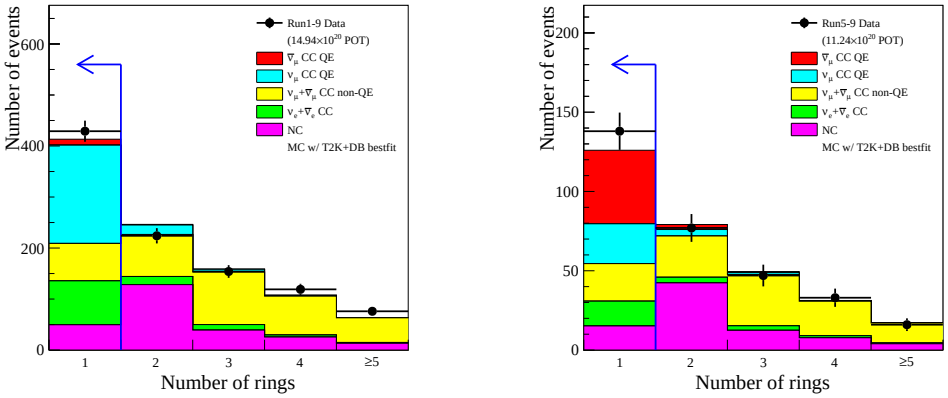

Figure 4.35: Distribution of events by the number of Cherenkov rings in the 1-ring ν_μ-like sample in FHC (left) and RHC (right). Reproduced from [138].

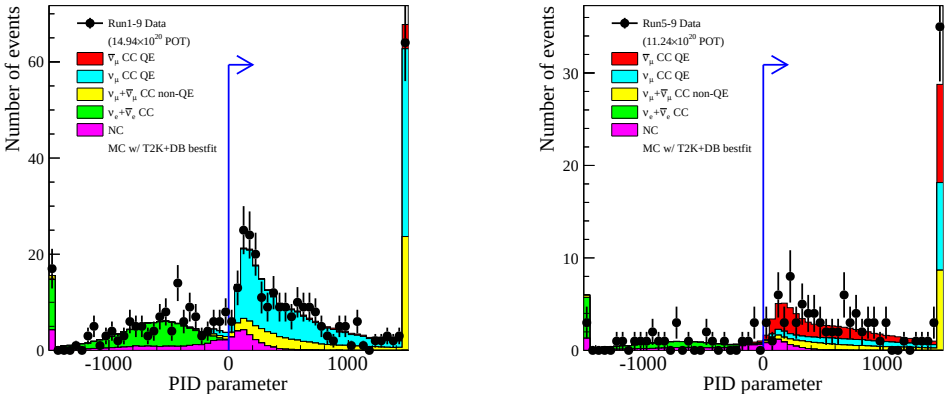

Figure 4.36: Distribution of events by the PID parameter in the 1-ring ν_μ-like sample in FHC (left) and RHC (right). Reproduced from [138].

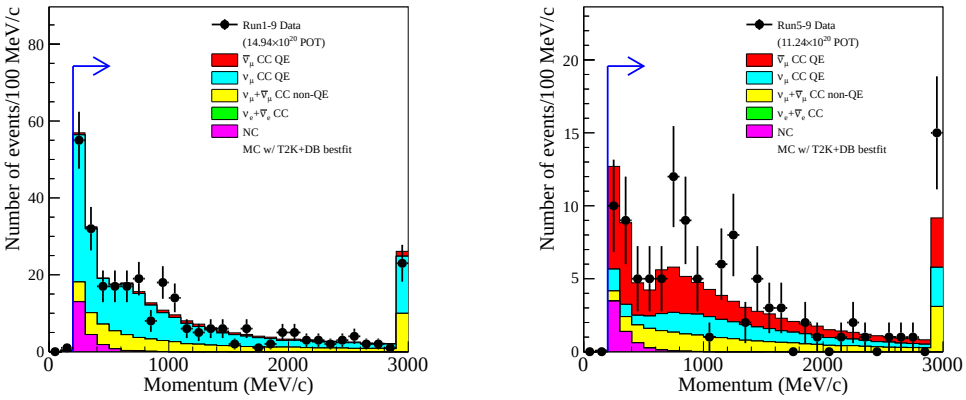

Figure 4.37: Distribution of events by visible energy in the 1-ring ν_μ-like sample in FHC (left) and RHC (right). Reproduced from [138].

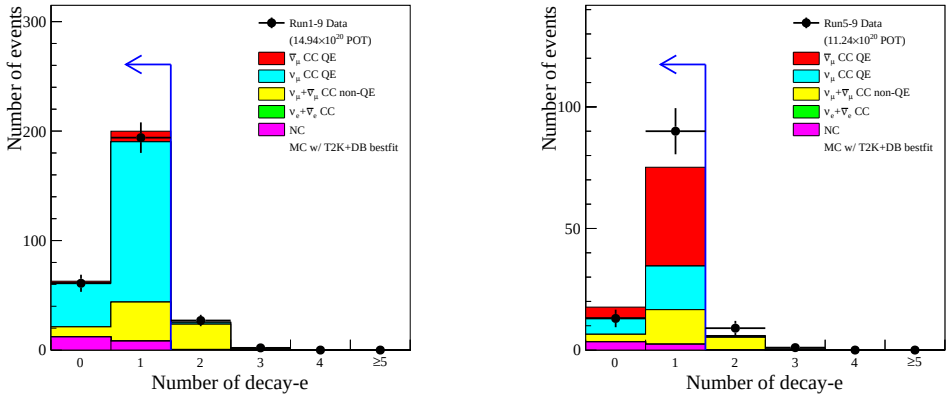

Figure 4.38: Distribution of events by the number of decay electrons in the 1-ring ν_μ-like sample in FHC (left) and RHC (right). Reproduced from [138].

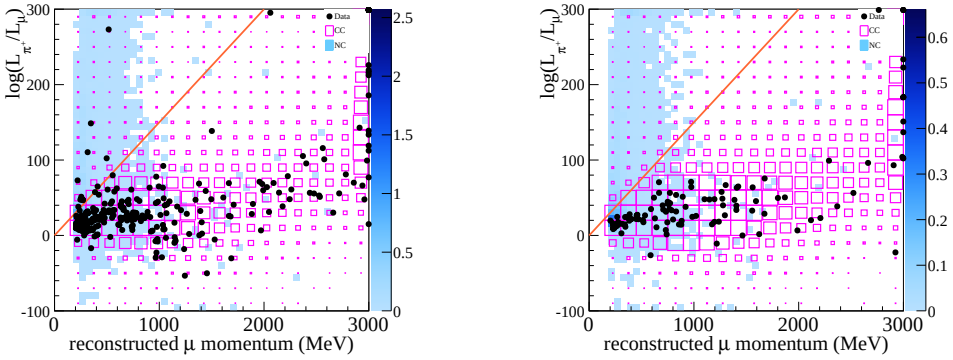

Figure 4.39: Distribution of events in PID parameter and reconstructed muon momentum in the 1-ring ν_μ-like sample in FHC (left) and RHC (right). The size of the magenta boxes indicates the number of CC events, while the blue shading indicates NC events. Reproduced from [138].

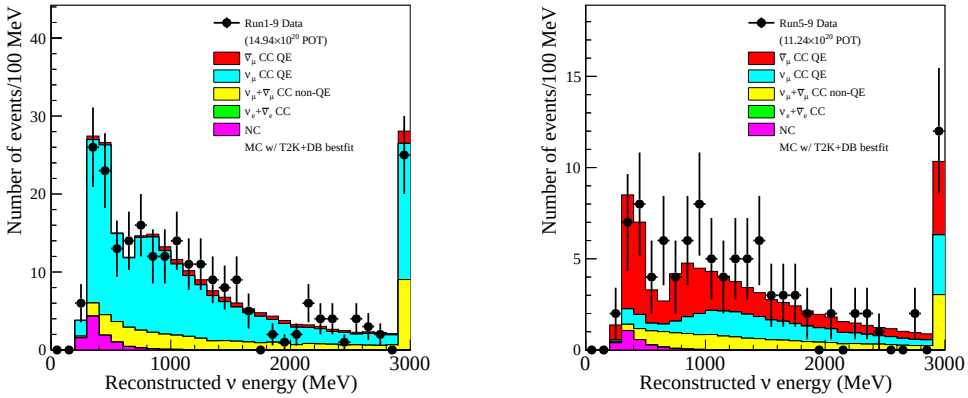

Figure 4.40: Final selection after all cuts are applied in the 1-ring ν_μ-like sample in FHC (left) and RHC (right). Reproduced from [138].

4.5 SK detector systematics

SK detector systematics describe the uncertainties associated with the efficiency with which SK characterises the different event topologies described in the preceding sections. In order to categorize each event a number of (sample-dependent) cuts are applied to SK events by the fiTQun reconstruction algorithm [141]:

- Fiducial volume cut: Event vertices must be within the inner detector volume and a sufficient distance from the detector wall
- Outer detector activity cut: Reject tracks that might have originated outside the inner detector
- Ring counting cut: Classify events according to the number of Cherenkov rings produced
- Particle identification cut: Classify the particle species
- Momentum cut: Reject events with insufficiently high momentum
- Decay electron cut: Identify events that produce decay electrons in addition to a main ring
- π^0 rejection cut: Identify Cherenkov rings arising from π^0 decay

As a result the number of events corresponding to each observable topology depends upon the choices made for the cuts and the uncertainties associated with the cut variables. A covariance matrix is produced to quantify the uncertainties associated with the SK detector efficiencies, using the following binning (which applies to both FHC and RHC configurations):

1-ring ν_e-like sample

For each of 3 reconstructed neutrino energy bins in the range (0, 0.35) GeV, [0.35, 0.8) GeV and [0.8, 1.25) GeV:

- Oscillated ν_e CCQE-like
- $\nu_\mu/\bar{\nu}_\mu$ CCQE-like
- Intrinsic ν_e CCQE-like
- All NC

1-ring ν_μ-like sample

For each of 3 reconstructed neutrino energy bins in the range (0, 0.4) GeV, [0.4, 1.1) GeV and [1.1, 30) GeV:

- $\nu_\mu/\bar{\nu}_\mu$ CCQE-like

For all reconstructed neutrino energies:

- $\nu_\mu/\bar{\nu}_\mu$ CCnQE-like
- Oscillated and intrinsic ν_e CCQE-like
- All NC

1-ring ν_e CC$1\pi^+$-like sample

For each of 2 reconstructed neutrino energy bins in the range (0.3, 0.8) GeV and [0.8, 1.25) GeV:

- Oscillated ν_e CCQE-like
- $\nu_\mu/\bar{\nu}_\mu$ CCQE-like
- Intrinsic ν_e CCQE-like
- All NC

Note that the CCQE-like reconstructed energy binning is designed to provide a single bin covering the region of maximal oscillation and then bins above and below this region. Uncertainties are computed for each of the cuts outlined above (also for vertex position and track direction are also calculated, as the fiducial volume cut depends upon these values) before being combined to give a single uncertainty in each of the bins defined above [142]. The data used to evaluate the systematic uncertainties come from SK atmospheric fits [143] and from hybrid π^0 samples [144] (in which the data sample is constructed by combining e-like rings from SK data with simulated γ-ray events to create composite π^0-like events). Control samples are produced from these data sets where the cut of interest has not been applied, with the distribution of the cut variable compared between data and MC and the difference is taken to be the 1σ error. The cut value is then varied by this amount and the resultant effect on the number of events passing the cuts for each sample is evaluated to determine a systematic error for the cut variable [142]. The resultant SK detector covariance matrix is shown in fig. 4.41.

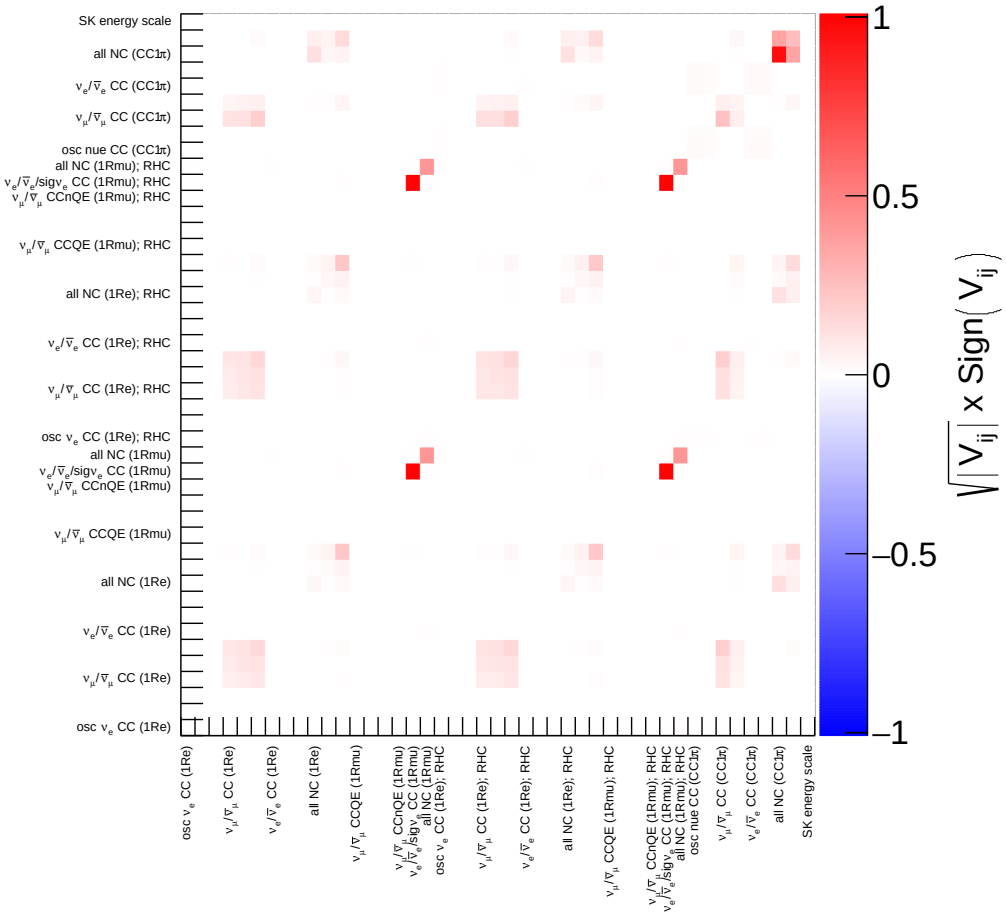

Figure 4.41: The SK detector covariance matrix.

In addition to the SK detector systematics outlined above, there is an additional uncertainty on the SK energy scale, which is not correlated with the other parameters. The error in the absolute energy scale is calculated from four SK Run IV control samples [138]; decay electrons from stopping cosmic ray muons; π^0s from atmospheric neutrino interactions; sub-GeV stopping cosmic ray muons; and multi-GeV stopping cosmic ray muons. These four samples provide coverage over a momentum range of about 30 MeV to 10 GeV. This uncertainty is computed as the difference between the positions of the peaks of the energy distributions in data and MC, with the largest uncertainty among the four samples representing the absolute energy scale error. Finally, the total energy scale uncertainty is computed as the sum, in quadrature, of the absolute energy scale uncertainty and the variation in

time of the light attenuation length in SK.

As noted in section 4.2.2, the final SK matrix is the result of a sum in quadrature of the detector errors and the FSI, SI and PN errors. The covariance matrix associated with the FSI, SI and PN effects is presented in fig. 4.42, while the associated table of errors due to the sum in quadrature of all SK-related uncertainties can be found in Appendix B.

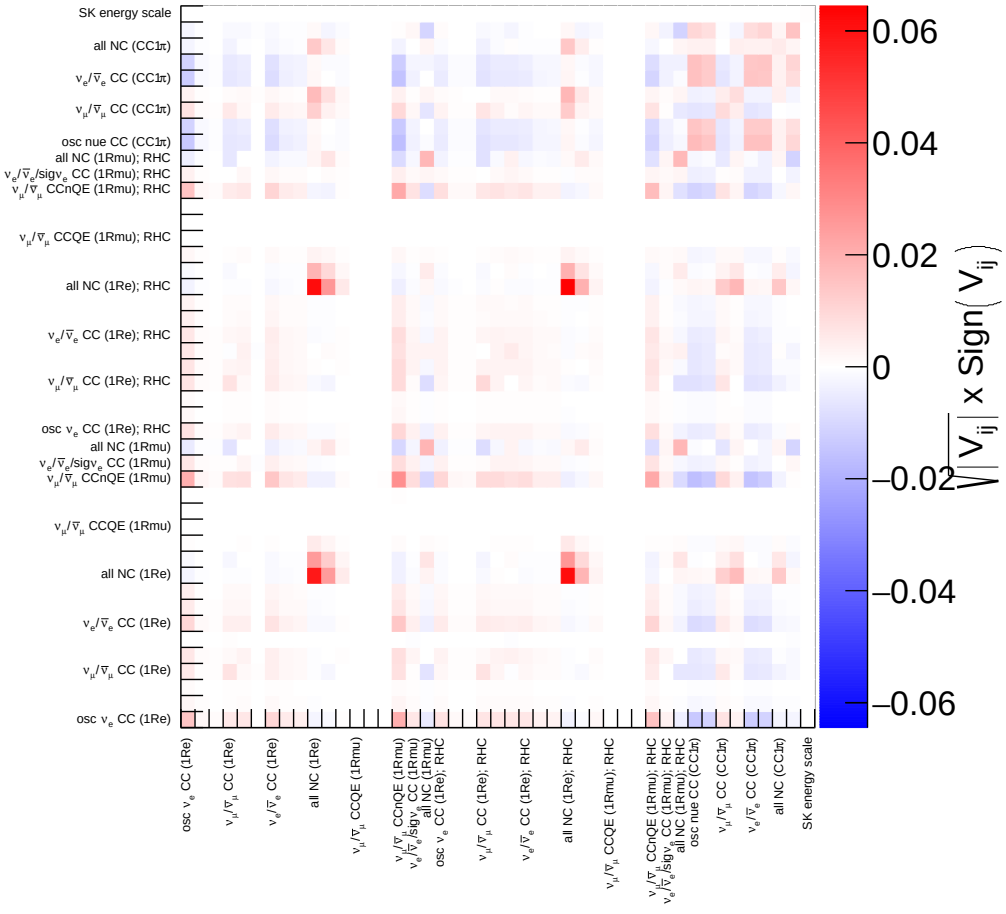

Figure 4.42: The SK FSI, SI and PN covariance matrix.

Chapter 5

CP phase measurement

T2K began collecting data on 23 January 2010 and currently has data processed up to 31 May 2018. This chapter describes the measurement of the neutrino CP phase performed with this data. This dataset was collected over the course of nine distinct run periods, incorporating a mixture of FHC and RHC running, such that a similar amount of POT is now observed in each configuration; in particular 1.4938×10^{21} in FHC and 1.6346×10^{21} in RHC. Figure 3.5 shows the pattern of POT accumulation for the entire T2K run history. Section 5.1 describes the hypothesis being tested, in which the δ parameter is fitted, section 5.2 describes the so called Asimov simulated data sets, used for sensitivity studies, while section 5.3 describes the fitting methodology. Section 5.4 presents the predicted event rates and associated spectra, while the effects of systematics on these spectra are documented in section 5.5. The method for constructing confidence regions is described in section 5.6. The expected sensitivity of the analysis is determined for different true oscillation parameter values in section 5.7. Observed event rates and spectra are shown in section 5.8.1. Confidence intervals produced using the constant-$\Delta\chi^2$ method and Feldman-Cousins method are presented in section 5.8.2 and section 5.8.3 respectively.

5.1 Hypothesis

The goal of this analysis is to provide a T2K measurement of the neutrino CP phase, δ and evaluate whether or not there is any indication of leptonic CP violation. From

eq. (2.38), the survival probability, $\mathrm{P}_{\nu_\mu \to \nu_\mu}$, is given by

$$\begin{aligned}\mathrm{P}_{\nu_\mu \to \nu_\mu} = 1 &- 4\left(c_{12}^2 c_{13}^2 c_{23}^2 s_{23}^2 + c_{13}^2 s_{12}^2 s_{13}^2 s_{23}^4 - 2c_{12}c_{13}^2 c_{23} s_{12} s_{13} s_{23}^4 \cos\delta\right) \sin^2\left(\frac{\Delta m_{32}^2 L}{4E}\right) \\ &- 4\left(c_{13}^2 c_{23}^2 s_{12}^2 s_{23}^2 + c_{12}^2 c_{13}^2 s_{13}^2 s_{23}^4 + 2c_{12}c_{13}^2 c_{23} s_{12} s_{13} s_{23}^2 \cos\delta\right) \sin^2\left(\frac{\Delta m_{31}^2 L}{4E}\right)\end{aligned} \tag{5.1}$$

where terms involving Δm_{21}^2 are omitted given that for T2K's baseline and energy $\sin^2\left(\Delta m_{3k}^2 L/4E\right) \gg \sin^2\left(\Delta m_{21}^2 L/4E\right)$. The corresponding ν_e appearance probability (eq. (2.37)), $\mathrm{P}_{\nu_\mu \to \nu_e}$, is given by

$$\begin{aligned}\mathrm{P}_{\nu_\mu \to \nu_e} = &- 4c_{13}s_{13}s_{23}\left[c_{23}s_{13}s_{23}\left(s_{12}^2 - c_{12}^2\right) - c_{12}s_{12}c_{23}^2 \cos\delta\right] \sin^2\left(\frac{\Delta m_{32}^2 L}{4E}\right) \\ &- 4c_{12}c_{13}s_{13}\left[c_{12}^2 s_{13} s_{23}^2 + c_{12}c_{23}s_{12}s_{23}\cos\delta + c_{23}^2 s_{12}^2 s_{13}\cos 2\delta\right] \sin^2\left(\frac{\Delta m_{31}^2 L}{4E}\right) \\ &+ 2c_{13}s_{13}s_{23}c_{12}s_{12}c_{23}^2 \sin\delta \sin^2\left(\frac{\Delta m_{32}^2 L}{4E}\right) \\ &- 2c_{12}c_{13}s_{13}\left[c_{12}c_{23}s_{12}s_{23}\sin\delta + c_{23}^2 s_{12}^2 s_{13}\sin 2\delta\right] \sin^2\left(\frac{\Delta m_{31}^2 L}{4E}\right)\end{aligned} \tag{5.2}$$

where terms involving Δm_{21}^2 are again omitted, along with terms including a factor $\sin^3(\theta_{13})$). It can be seen in eq. (5.1) that the terms involving δ are equal and opposite apart from the factor of $\sin^2\left(\Delta m_{3k}^2 L/4E\right)$. Given that $\sin^2\left(\Delta m_{3k}^2 L/4E\right) \gg \sin^2\left(\Delta m_{21}^2 L/4E\right)$, it follows that $\sin^2\left(\Delta m_{32}^2 L/4E\right)$ and $\sin^2\left(\Delta m_{31}^2 L/4E\right)$ are approximately equal and therefore the terms involving δ largely cancel, leaving the disappearance channel relatively insensitive to the value of δ. As a result, the key channel is the appearance channel. The oscillation parameters have effects that are at least of similar magnitude to that of δ. For this reason, in this analysis, variations in the other oscillation parameters will be taken into account (see section 5.3).

Fits are performed separately for the case of normal and inverted mass ordering and thus the prior is specified in terms of Δm_{32}^2 in normal ordering and Δm_{13}^2 in inverted ordering.

5.2 Asimov data sets

Throughout this chapter references will be made to the 'Asimov data sets'. These are simulated data sets that are generated according to different oscillation hypotheses and are used as representative data sets to determine T2K's sensitivity (see sec-

tion 5.7) without the need to generate large numbers of toy experiments[1]. The oscillation parameter values corresponding to each Asimov data set are provided in table 5.1.

Parameter(s)	Asimov A	Asimov B	Asimov FC NO	Asimov FC IO
$\sin^2\theta_{23}$	0.528	0.450	0.535	0.530
$\sin^2\theta_{13}$ reactors	0.0212	0.0212	0.0216	0.0216
$\sin^2\theta_{12}$	0.307	0.307	0.307	0.307
$\lvert\Delta m^2_{32}\rvert$ (NH) / $\lvert\Delta m^2_{31}\rvert$ (IH)	2.509×10^{-3} eV^2/c^4	2.509×10^{-3} eV^2/c^4	2.452×10^{-3} eV^2/c^4	2.404×10^{-3} eV^2/c^4
Δm^2_{21}	7.53×10^{-5} eV^2/c^4	7.53×10^{-5} eV^2/c^4	7.53×10^{-5} eV^2/c^4	7.53×10^{-5} eV^2/c^4
δ_{CP}	-1.601	0	-1.885	-1.382
Mass Ordering	Normal	Normal	Normal	Inverted

Table 5.1: Values of oscillation parameters for the Asimov data sets. In the Asimov A data set the nominal values of $\sin^2 2\theta_{13}$, $\sin^2 2\theta_{12}$ and Δm^2_{21} are from the PDG global fit [30], while all the other oscillation parameter values correspond to the most probable values obtained by the Bayesian analysis on the T2K run 1-4 neutrino mode data [77]. The Asimov FC values for non-solar parameters are based on the best-fits obtained using T2K Run 1-9 data with the reactor constraint [146].

5.3 Fit Method

The nominal SK MC templates (templates specify neutrino event rates from simulation and are described below) are constructed by applying the 1-ring ν_e-like cuts, 1-ring ν_μ-like cuts and 1-ring ν_e CC1π^+-like cuts (see section 4.4) to the official SK MC templates constructed during the full SK simulation to produce five distinct samples at SK; the 1-ring ν_e-like and 1-ring ν_μ-like samples in FHC and RHC, and the 1-ring ν_e CC1π^+-like sample in FHC. Then, for a given set of input parameters predictions are made for the spectra of each of the five samples based upon the application of weights for POT, oscillation probabilities and systematic parameters to the nominal templates

The templates are constructed for a variety of true interaction modes and binned in true neutrino energy (E_t), reconstructed neutrino energy (E_r) and for the three ν_e-like samples, in the angle between the lepton and beam directions (θ).

Oscillation probabilities are calculated for the E_t bin, using the energy at the centre of the bin and applied to the CC templates, with $\mathrm{P}(\nu_\mu \to \nu_\mu)$ applied to the $\nu_\mu \to \nu_\mu$ template, $\mathrm{P}(\nu_\mu \to \nu_e)$ applied to the $\nu_\mu \to \nu_e$ template and so on. Oscillation probabilities are not applied to the NC templates, since these already represent the mixture of $\nu_e + \nu_\mu + \nu_\tau$ (and their antineutrino counterparts), which are unchanged under 3 flavour oscillations.

[1]The name 'Asimov' is a reference to Isaac Asimov's short story, *Franchise* [145], in which a supercomputer selects a single individual considered to be representative of the whole population to determine what the outcome of an election would have been without the need to hold one.

In this analysis, each of the five SK samples uses 50 templates, covering the range of interaction modes. In particular

- 6 CCQE (ν_μ, $\bar{\nu}_\mu$, ν_e, $\bar{\nu}_e$, $\nu_\mu \to \nu_e$, $\bar{\nu}_\mu \to \bar{\nu}_e$)
- 6 CC1π (ν_μ, $\bar{\nu}_\mu$, ν_e, $\bar{\nu}_e$, $\nu_\mu \to \nu_e$, $\bar{\nu}_\mu \to \bar{\nu}_e$)
- 6 CC coherent (ν_μ, $\bar{\nu}_\mu$, ν_e, $\bar{\nu}_e$, $\nu_\mu \to \nu_e$, $\bar{\nu}_\mu \to \bar{\nu}_e$)
- 6 CC 2p-2h (ν_μ, $\bar{\nu}_\mu$., ν_e, $\bar{\nu}_e$, $\nu_\mu \to \nu_e$, $\bar{\nu}_\mu \to \bar{\nu}_e$)
- 6 CC other (ν_μ, $\bar{\nu}_\mu$, ν_e, $\bar{\nu}_e$, $\nu_\mu \to \nu_e$, $\bar{\nu}_\mu \to \bar{\nu}_e$)
- 4 NC1π^0 (ν_μ, $\bar{\nu}_\mu$, ν_e, $\bar{\nu}_e$)
- 4 NC1$\pi^\pm$ (ν_μ, $\bar{\nu}_\mu$, ν_e, $\bar{\nu}_e$)
- 4 NC coherent (ν_μ, $\bar{\nu}_\mu$, ν_e, $\bar{\nu}_e$)
- 4 NC other (ν_μ, $\bar{\nu}_\mu$, ν_e, $\bar{\nu}_e$)
- 4 NC 1γ (ν_μ, $\bar{\nu}_\mu$, ν_e, $\bar{\nu}_e$)

Note that for the NC templates ν_μ is a proxy for the mixture of $\nu_\mu + \nu_e + \nu_\tau$ as a result of oscillations and similarly for the other flavours, with no corresponding oscillated templates to avoid double-counting.

The binning scheme for the templates was optimised to balance the goal of maximum sensitivity to oscillation parameters with the need to ensure a reasonable number of events in each reconstructed bin, with the finest binning occurring in the region of the oscillation maximum around 600 MeV. For ν_μ-like samples the templates have 84 bins in E_t and 73 bins in E_r. ν_e-like templates have 84 bins in E_t, 25 bins in E_r and 15 bins in θ.

The two-dimensional binning scheme used for the e-like samples is to improve the separation of the different interaction/flavour components, in particular $\nu_\mu \to \nu_e$ and $\bar{\nu}_\mu \to \bar{\nu}_e$, which is fundamental to a measurement of δ. The improved separation becomes possible as a result of events populating slightly different regions of the phase space; it can be seen in fig. 5.1 that the E_r spectra are rather similar in both FHC and RHC, while the θ spectra show clear shape differences. For all templates the E_t binning is:

- 6 50-MeV bins from 0-0.3 GeV,
- 28 25-MeV bins from 0.3-1 GeV,

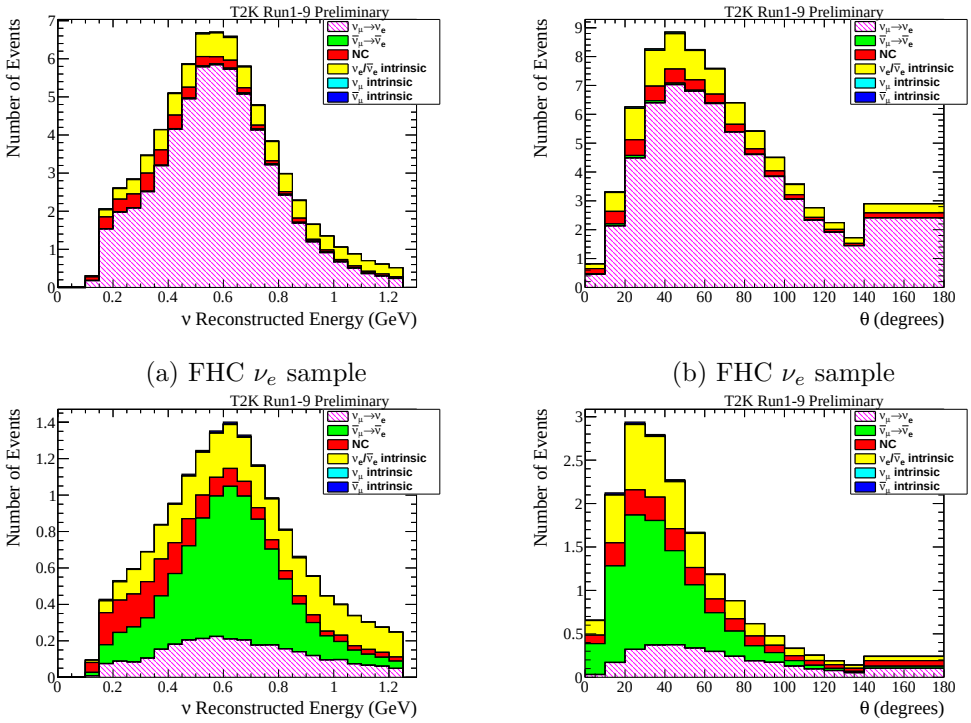

(a) FHC ν_e sample

(b) FHC ν_e sample

(c) RHC $\bar{\nu}_e$ sample

(d) RHC $\bar{\nu}_e$ sample

Figure 5.1: Predicted Asimov A spectra. Distributions are a function of the reconstructed neutrino energy (left) and reconstructed angle (right). The distributions correspond to the statistics collected in the full Run 1-9 data set. The spectra are generated with the nominal values of the systematic parameters.

- 40 50-MeV bins from 1-3 GeV,
- 5 100-MeV bin from 3-3.5 GeV,
- 1 bin from 3.5-4 GeV,
- 1 bin from 4-5 GeV,
- 1 bin from 5-7 GeV,
- 1 bin from 7-10 GeV and
- 1 bin from 10-30 GeV

For ν_μ-like samples the E_r binning is:

- 60 50-MeV bins from 0-3 GeV,
- 4 250-MeV bins from 3-4 GeV,

- 4 500-MeV bins from 4-6 GeV,
- 4 1000-MeV bins from 6-10 GeV and
- 1 bin from 10-30 GeV.

For ν_e-like samples the E_r binning is:

- 25 50-MeV bins from 0-1.25 GeV.

The θ binning used for ν_e-like samples is

- 14 10° bins from 0° to 140°,
- 1 bin for the range $140° - 180°$.

The nominal SK MC templates are constructed by applying the 1-ring ν_e-like, 1-ring ν_μ-like and 1-ring ν_e CC1π^+-like selection cuts to the official SK MC samples [138].

The normalisation of each event sample is calculated from the number of events with a MC truth interaction vertex within the fiducial volume

$$N = \int dSdIdE \cdot \frac{d^3\Phi_{SK}}{dSdIdE_\nu} \cdot \sigma_{H_2O} \cdot \frac{N_A}{A} \cdot \rho \cdot L \tag{5.3}$$

where $d^3\Phi_{SK}/dSdIdE$ is the number of flux particles for the given neutrino species per neutrino energy bin dE_ν, per unit area dS, per POT. The total interaction cross-section on water for the given neutrino species is given by σ_{H_2O}, I is the beam exposure in terms of POT, N_A is Avogadro's number, A is the mass number for water, ρ is the water density and L is the neutrino path length in the water volume.

The SK MC samples are normalised to the Run 1-9 POT. Each sample is first normalised to 1 POT by weighting it with the ratio of the number of events per 22.5 kt per POT to the number of generated events in the true fiducial volume in all available MC. Each sample is then normalised to the Run 1-9 exposure according to whether the sample is FHC or RHC, by weighting the result respectively by 1.4938×10^{21} and 1.6346×10^{21} .

The test statistic used to quote confidence intervals for δ is based on a comparison of the observed and predicted spectra at SK. The predicted number $N_{r,\theta}$ of single ring events in the r-th and θ-th bin (treating the ν_μ-like samples as having a single bin in θ) is computed for each sample as follows:

$$N_{r,\theta} = \sum_m \sum_t \sum_{r\prime} P_{m;t} \cdot T_{r;r\prime;f^{SK}_{E;r}} \cdot S_{m;t;r\prime,\theta;\vec{f}} \cdot N^{MC}_{m;r\prime,\theta;t} \tag{5.4}$$

where $N^{MC}_{m;r\prime,\theta;t}$ is the input SK MC template containing the number of events in the MC sample with true reaction mode, m, in the true energy bin, t, reconstructed energy bin, $r\prime$, and reconstructed lepton angle bin, θ. $S_{m;t;r\prime,\theta;\vec{f}}$ is an overall, multiplicative, systematic error factor depending on a vector of systematic parameters $\vec{f}$, which is a function of m, t, $r\prime$ and θ. $T_{r;r\prime;f^{SK}_{E;r}}$ is a transfer function describing the migration of events between the reconstructed energy bins r and $r\prime$ due to uncertainty in the SK reconstructed energy scale, $f^{SK}_{E;r}$. Finally, $P_{m;t}$ is the 3-flavour oscillation probability applied to the true energy bin of the SK MC template corresponding to mode m. Oscillations are applied as a function of true energy to the MC templates for all CC interactions.

The MC templates calculated from the 1-ring ν_μ-like and 1-ring $\bar{\nu}_\mu$-like MC samples are weighted with $\mathrm{P}(\nu_\mu \to \nu_\mu)$ and $\mathrm{P}(\bar{\nu}_\mu \to \bar{\nu}_\mu)$ respectively, while those from the 1-ring ν_e-like and 1-ring ν_e CC1π^+-like MC samples are weighted via $\mathrm{P}(\nu_\mu \to \nu_e)$, with the 1-ring $\bar{\nu}_e$-like MC samples weighted by $\mathrm{P}(\bar{\nu}_\mu \to \bar{\nu}_e)$. Oscillation probabilities are computed in a 3-flavour framework that includes matter effects from constant-density matter, where Earth's crust is assumed to have a density of 2.6 g/cm^3. While oscillations of ν_e and ν_μ to ν_τ are possible, their effect is negligible ($\ll 1\%$) [147] because their energy threshold is around 3.5 GeV and therefore no ν_τ nor $\bar{\nu}_\tau$ samples or templates are used.

The likelihood function used for this analysis is:

$$-2\ln\lambda(\overline{\delta};\vec{a}) = 2\sum_{i=0}^{N-1}\left[n_i^{obs}\ln\left(\frac{n_i^{obs}}{n_i^{exp}}\right) + n_i^{exp} - n_i^{obs}\right] \tag{5.5}$$

where $\overline{\delta}$ is the estimated value of δ, $\vec{a}$ is the vector of systematic parameter values (including the oscillation parameters that are not being fitted), N is the number of reconstructed energy and lepton angle bins, n_i^{obs} is the number of events observed in bin i and $n_i^{exp} = n_i^{exp}(\overline{\delta};\vec{a})$ is the corresponding expected number of events. The total likelihood is then the product of the likelihoods of each SK sample

$$\lambda(\overline{\delta};\vec{a}) = \prod_{s=1}^{N_s}\lambda_s(\overline{\delta};\vec{a}) \tag{5.6}$$

where s is the sample from N_s samples, which in turn can be expressed as the sum

$$-2\ln\lambda(\overline{\delta};\vec{a}) = \sum_{s=1}^{N_s} -2\ln\lambda_s(\overline{\delta};\vec{a}) \tag{5.7}$$

Rather than allowing all parameters to float and applying a penalty term for

parameters that deviate from their prior, the systematic parameters are marginalised while δ is maximised with respect to the likelihood distribution, eliminating the nuisance parameters. This involves generating toy spectra in which each systematic parameter is thrown from a Gaussian distribution with a mean and standard deviation determined by the BANFF fit (see section 4.3), which acts to weight throws according to prior information, eliminating the need for a penalty term for the systematic parameters. The likelihoods for each toy are then averaged to yield a marginal likelihood, $\lambda_{marg}(\delta)$ that only depends on δ:

$$\lambda_{marg}(\delta) = \int_{\Phi} \lambda(\delta;\vec{\phi})\pi(\vec{\phi})\,\mathrm{d}\vec{\phi} = \frac{1}{n}\sum_{1}^{n}\lambda(\delta;\vec{\phi}_i) \tag{5.8}$$

where $\vec{\phi}$ is the set of nuisance parameters in the parameter space Φ, $\pi(\vec{\phi})$ is the prior of the nuisance parameters, n is the number of toys used for marginalisation and $\vec{\phi}_i$ is the single set of nuisance parameters extracted for the i-th toy. In order to effectively sample the parameter space, Φ, many $\vec{\phi}$ are needed, with this analysis using 40 000 toys for marginalisation when the reactor constraint is applied and 80 000 toys for marginalisation when the reactor constraint is not applied. An alternative approach to eliminating nuisance parameters is the profile likelihood, which follows a similar approach to marginalisation, but takes the maximum likelihood from the toys at each point of interest, rather than the average likelihood. However, the profile likelihood is known to produce intervals that do not have correct coverage for all values of the nuisance parameters and can also produce biased estimates [148].

For this analysis, the marginal log-likelihood, is used, because it follows a χ^2 distribution in the large sample limit (Wilks' theorem [149]):

$$\chi^2 = -2\ln\lambda_{marg}(\delta) = -2\ln\left[\frac{1}{n}\sum_{1}^{n}\lambda(\delta;\vec{\phi}_i)\right] \tag{5.9}$$

Correlations between systematic variations are taken into account for the marginalisation toys through Cholesky decomposition [150], though no statistical fluctuations are applied. It should be noted that if throws of the systematic parameters result in a predicted number of events that is negative, or a systematic parameter is thrown outside of its physical range, the toy is rejected and parameters re-thrown.

According to whether the fit is to be performed with or without the reactor constraint, the appropriate number of E_r-θ spectra are generated and stored for each sample at each point of interest for δ and in each mass ordering. The points of interest for δ are defined as the centres of 101 bins on the interval $[-\pi, +\pi]$. The

Sample	Not Osc	Asimov A
FHC ν_μ	1226.6 ± 71.9	272.4 ± 21.6
FHC ν_e	15.6 ± 4.2	72.8 ± 10.8
RHC ν_μ	459.1 ± 29.6	139.5 ± 13.4
RHC ν_e	7.0 ± 2.7	16.8 ± 4.3
FHC ν_e CC1π^+	2.6 ± 1.7	6.9 ± 2.9

Table 5.2: The expected number of events in Run 1-9 data set for each selected sample. Statistical and systematic (see table 5.4) errors are added in quadrature.

set of systematic parameter throws, $\vec{a}$, is the same at each point of interest. For a given data set and a single point of interest of δ and mass ordering, the procedure for calculating the marginal log-likelihood is:

- Retrieve the marginalised spectra for the point of interest
- For each marginalisation toy:
  - Use eq. (5.5) to retrieve the log-likelihood
  - Compute the likelihood as $\lambda(\overline{\delta};\vec{a}) = e^{-(-2\ln\lambda(\overline{\delta};\vec{a}))/2}$
- Compute the marginal log-likelihood, χ^2, from eq. (5.9)

Finally, the best-fit value, δ_{bf}, is found by looking for the minimum value of χ^2 across all points of interest.

5.4 Predicted spectra

In this section, expected spectra at SK are presented. Unoscillated and oscillated spectra assuming Asimov A (table 5.1) oscillation parameters are considered. All plots are generated for an integrated exposure corresponding to Run 1-9. The per-sample event rates, with all selections applied, for the no-oscillation hypothesis and the Asimov A oscillation hypothesis are given in table 5.2. The corresponding predicted spectra can be seen in figs. 5.2 to 5.3, with comparisons of the FHC ν_e sample and RHC $\bar{\nu}_e$ sample spectra showing that θ vs E_r distributions are populated differently by $\nu_\mu \to \nu_e$ and $\bar{\nu}_\mu \to \bar{\nu}_e$ events.

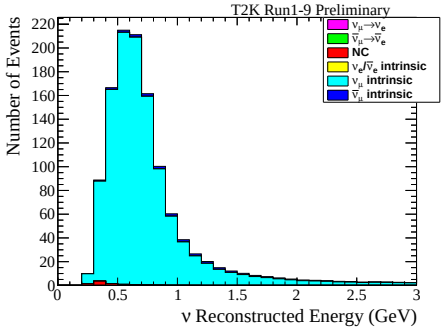

(a) FHC ν_μ sample

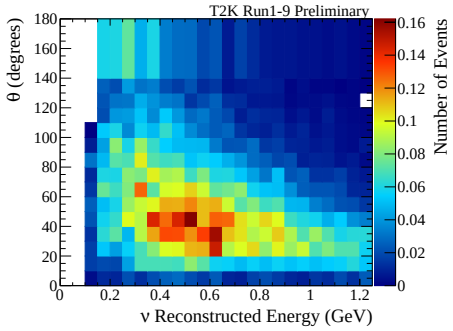

(b) FHC ν_e sample

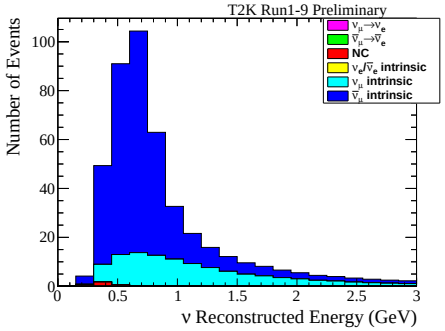

(c) RHC $\bar{\nu}_\mu$ sample

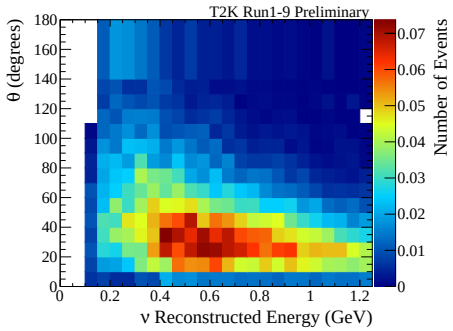

(d) RHC $\bar{\nu}_e$ sample

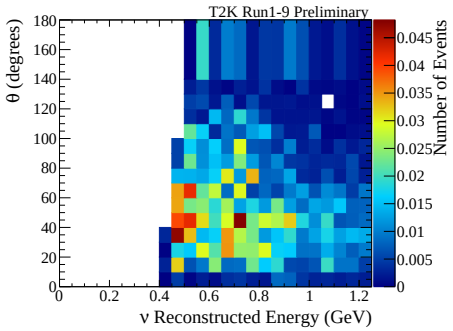

(e) FHC ν_e CC1π^+ sample

Figure 5.2: Predicted unoscillated spectra. μ-like distributions are a function of the reconstructed neutrino energy, while the e-like distributions are functions of both the reconstructed neutrino energy and the reconstructed angle between the outgoing lepton and the neutrino direction. The distributions correspond to the statistics collected in the full Run 1-9 data set. The spectra are generated with the nominal values of the systematic parameters.

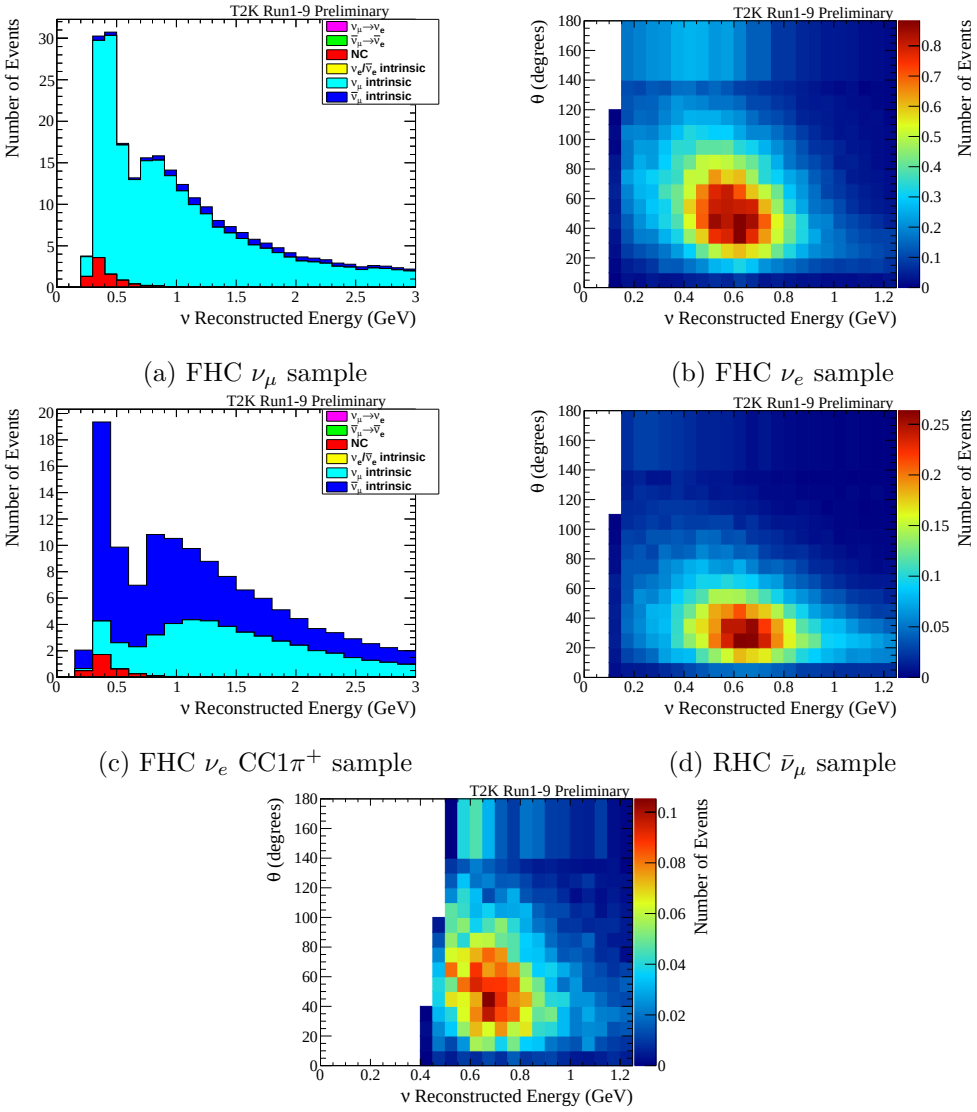

(a) FHC ν_μ sample

(b) FHC ν_e sample

(c) FHC ν_e CC1π^+ sample

(d) RHC $\bar{\nu}_\mu$ sample

(e) RHC $\bar{\nu}_e$ sample

Figure 5.3: Predicted Asimov A spectra. μ-like distributions are a function of the reconstructed neutrino energy, while the e-like distributions are functions of both the reconstructed neutrino energy and the reconstructed angle between the outgoing lepton and the neutrino direction. The distributions correspond to the statistics collected in the full Run 1-9 data set. The spectra are generated with the nominal values of the systematic parameters and the oscillation parameters corresponding to the Asimov A data set.

5.5 Effect of systematics on predicted spectra

It is important to understand the effect of the 119 systematic parameters used in this analysis on the SK spectra. Of particular importance for a measurement of the neutrino CP phase is the effect of the systematic uncertainties on the ratio of the number of events between FHC and RHC samples. If correlations do not reproduce the physics correctly, a fake asymmetry between neutrino and antineutrino oscillations could be observed. Furthermore, if correlations exist but are not taken into account, the measurement of δ could be biased. The true value of δ determines whether correlations or anti-correlations between systematic parameters have the greatest effect in hiding any oscillation asymmetry. In particular, if true δ is equal to $\pm\pi/2$ then anti-correlation in the e-like samples could hide any oscillation asymmetry. Alternatively, in the case that true $\delta \sim 0$, it is uncorrelated parameters that reduce the sensitivity to δ. Particularly important individual parameters in this regard are those representing the uncertainties on the ν_e/ν_μ and $\bar{\nu}_e/\bar{\nu}_\mu$ CC cross-section ratios, σ_{ν_e} and $\sigma_{\bar{\nu}_e}$, which are applied respectively to ν_e and $\bar{\nu}_e$ events. Their fractional error from the near detector fit is $\sim 2.8\%$ and they are partially anti-correlated with non-diagonal elements in the covariance matrix of -0.0004. The binding energy parameter, E_b, also produces a large uncertainty on the ratio of events between FHC and RHC samples, though this parameter is uncorrelated with the other systematic parameters.

Parameter(s)	Prior	Range
$\sin^2\theta_{23}$	uniform	$[0.3; 0.7]$
$\sin^2 2\theta_{13}$ reactors	gaussian	0.0857 ± 0.0046
$\sin^2 2\theta_{13}$ T2K only	uniform	$[0.03; 0.2]$
$\sin^2 2\theta_{12}$	gaussian	0.846 ± 0.021
Δm^2_{32} (NH) / Δm^2_{13} (IH)	uniform	$[2.3; 2.7] \times 10^{-3}$ eV^2/c^4
Δm^2_{21}	gaussian	$(7.53 \pm 0.18) \times 10^{-5}$ eV^2/c^4
δ_{CP}	uniform	$[-\pi; +\pi]$
Mass Hierarchy	fixed	NH or IH

Table 5.3: Treatment of the oscillation parameters in the $\nu/\bar{\nu}$ joint analysis. All the gaussian priors are from [30]. The parameter $\sin^2 2\theta_{13}$ is constrained using the gaussian prior when the reactor constraint is applied and the uniform prior when it is not. The mass hierarchy is not marginalised but fixed to either normal, or inverted hierarchy.

The effect of each category of systematic parameter on the expected event rate for each SK sample is given in table 5.4. The mean and RMS of 10 000 throws of the respective systematics, with all correlations taken into account using Cholesky

decomposition [150] is computed for each sample, both without and with the near detector constraint applied (see Appendix C). Oscillation parameters are fixed at Asimov A values when not varied and varied according to the priors defined in table 5.3 (reactor constraint applied) when they are varied. Table 5.4 summarizes the errors with the near detector constraint applied.

	1-Ring μ		**1-Ring e**			
Error source	FHC	RHC	FHC	RHC	FHC CC1π^+	FHC/RHC
SK Detector	2.40	2.01	2.83	3.80	13.15	1.47
SK FSI+SI+PN	2.21	1.98	3.00	2.31	11.43	1.57
Flux + Xsec constrained	3.27	2.94	3.24	3.10	4.09	2.67
E_b	2.38	1.72	7.13	3.66	2.95	3.62
$\sigma(\nu_e)/\sigma(\bar{\nu}_e)$	0.00	0.00	2.63	1.46	2.61	3.03
NC1γ	0.00	0.00	1.09	2.60	0.33	1.50
NC Other	0.25	0.25	0.15	0.33	0.99	0.18
Osc	0.03	0.03	2.69	2.49	2.63	0.77
All Systematics	5.12	4.45	8.81	7.13	18.38	5.96
All with osc	5.12	4.45	9.19	7.57	18.51	6.03

Table 5.4: Percentage error on event rate by error source and sample. Final column is the percentage error on the ratio of FHC/RHC events in the one-ring e sample.

Figures 5.4 to 5.5 show the error envelopes and fractional errors by E_r for the case where all systematic errors (including marginalised oscillation parameters) are applied. In the error envelope plots (left), the solid blue line represents the event rate by reconstructed energy with all systematic parameters set to their nominal prior values, with the solid black line representing the corresponding event rate with all systematic parameters set to the best-fit determined by the near detector constraint. The envelopes defined by the dashed blue lines represent the 1σ intervals determined from 10000 throws of the systematic parameters according to the prior uncertainties, while the envelopes defined by the red regions are the corresponding 1σ intervals based on throws of the systematic parameters using post-near detector fit uncertainties. The fractional error plots (right) are then defined as the respective ratios of the event rates at $\pm 1\sigma$ to those at nominal for pre- and post-near detector fit systematic parameter values and uncertainties.

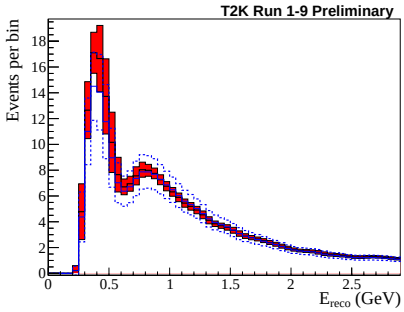

(a) 1-ring ν_μ-like

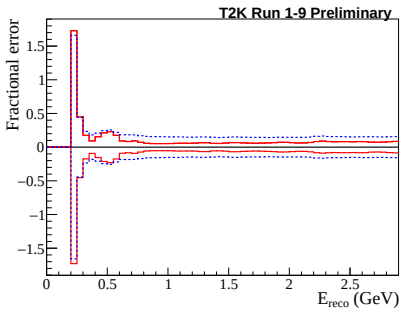

(b) 1-ring ν_μ-like

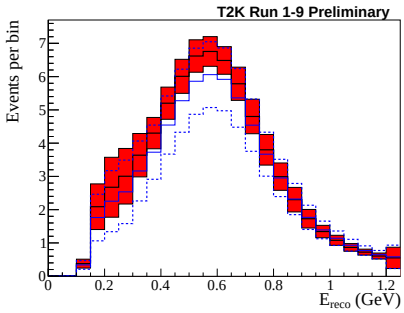

(c) 1-ring ν_e-like

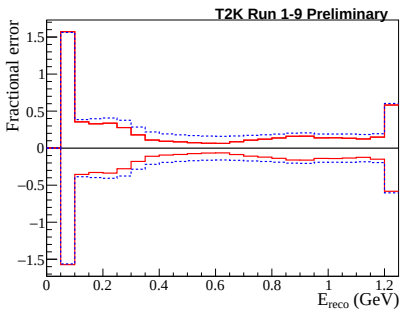

(d) 1-ring ν_e-like

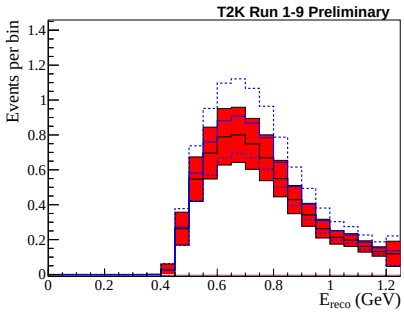

(e) 1-ring ν_e CC1π^+-like

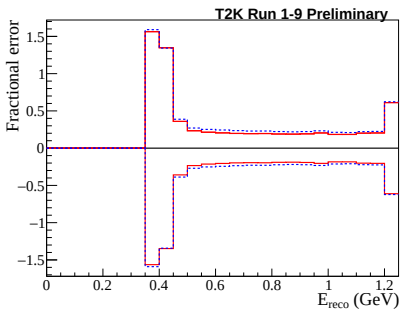

(f) 1-ring ν_e CC1π^+-like

Figure 5.4: Error envelopes (left) showing the post-BANFF fit nominal event rates (black line) and RMS errors (red band), and the pre-BANFF fit nominal event rates (solid blue line) and RMS errors (dashed blue line) in each reconstructed energy bin for each FHC sample at SK. The corresponding fractional errors (right) are shown for the post-BANFF fit event rates (red lines) and pre-BANFF fit event rates (blue lines).

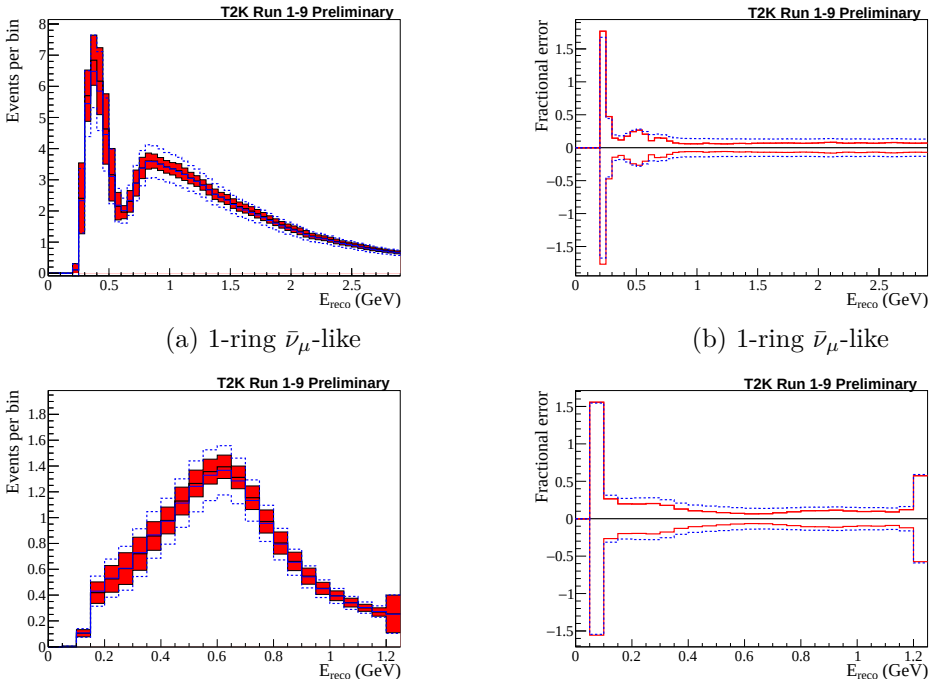

(a) 1-ring $\bar{\nu}_\mu$-like

(b) 1-ring $\bar{\nu}_\mu$-like

(c) 1-ring $\bar{\nu}_e$-like

(d) 1-ring $\bar{\nu}_e$-like

Figure 5.5: Error envelopes (left) showing the post-BANFF fit nominal event rates (black line) and RMS errors (red band), and the pre-BANFF fit nominal event rates (solid blue line) and RMS errors (dashed blue line) in each reconstructed energy bin for each RHC sample at SK. The corresponding fractional errors (right) are shown for the post-BANFF fit event rates (red lines) and pre-BANFF fit event rates (blue lines).

5.6 Construction of confidence intervals

Following the fit procedure described in section 5.3, the χ^2 distribution is shifted with respect to the χ^2 value at the best-fit value of δ, $\chi^2(\delta_{bf})$

$$\Delta\chi^2(\delta) = \chi^2(\delta) - \chi^2(\delta_{bf}) \tag{5.10}$$

A confidence interval can then be set according to the inequality

$$\Delta\chi^2(\delta) > \Delta\chi^2_{crit} \tag{5.11}$$

where $\Delta\chi^2_{crit}$ is the critical value for a given confidence level (CL), X%. If the inequality in eq. (5.11) holds, then the given value of δ can be said to be excluded at the X% CL. In the Gaussian approximation, constant values of $\Delta\chi^2_{crit}$ can be used and this approach is referred to as the constant-$\Delta\chi^2$ method.

However, the oscillation probability is not linear in oscillation parameters and this can result in unreliable confidence intervals when using the constant-$\Delta\chi^2$ method. To address this problem, confidence intervals are also computed using the Feldman-Cousins method [151]. In this method, rather than having a single critical value for a given CL, a critical value is computed for each point of interest in δ and both mass orderings. Given that the Feldman-Cousins procedure is highly computationally intensive, requiring thousands of CPU hours of computation for each point of interest, critical values for nine points of interest of δ are computed for each mass ordering, which includes the CP conserving and maximally CP violating points 0, $\pm\pi$ and $\pm\pi/2$ (given the equivalence of δ at $-\pi$ and $+\pi$, the critical value is calculated for only one of these points and copied for the other) and linearly interpolated between these values. Furthermore, the method is only undertaken for the case in which the reactor constraint is applied. The procedure consists of the following steps:

1. At least 2×10^4 simulated data sets are produced assuming true δ takes on the value of the grid point and taking into account both statistical and systematic uncertainties (i.e. systematic parameters, including the remaining oscillation parameters, are thrown from the standard analysis priors).

2. For each simulated data set:

   (a) $\chi^2(\delta_{true})$ is obtained by computing $\chi^2(\delta)$ with respect to the marginalisation toys produced for the data fit, with δ fixed to the true value corresponding to the grid point.

   (b) $\chi^2(\delta_{bf})$ is obtained by minimizing $\chi^2(\delta)$ with respect to the marginalisation toys produced for the data fit, leaving δ free.

   (c) The test statistic is then calculated as

$$\Delta\chi^2 = \chi^2(\delta_{true}) - \chi^2(\delta_{bf}) \tag{5.12}$$

3. This results in a distribution of $\Delta\chi^2(\delta)$, $f(\Delta\chi^2)$.

4. Several critical values for $X\%$ CL (68.27%, 90%, 95.45%), $\Delta\chi^2(\delta)_{crit}$, are then defined as:

$$\Delta\chi^2_{crit} : \int_0^{\Delta\chi^2_{crit}} f(\Delta\chi^2) d(\Delta\chi^2) = X\% \tag{5.13}$$

5. This procedure is repeated to produce critical values for all of the points of interest of δ in each mass ordering.

Throws of the non-δ oscillation parameters use the priors defined in table 5.3, with the exception of the atmospheric parameters, $\sin^2\theta_{23}$ and Δm^2_{32} (Δm^2_{13}). The atmospheric parameters are thrown from the likelihood surface (see fig. 5.6) that is the result of a simultaneous fit of the atmospheric parameters to a simulated data set. The simulated data set is generated assuming true atmospheric parameters equal to those found in a simultaneous fit of the atmospheric parameters using the Run 1-9 data, with remaining oscillation and systematic parameters set according to the Asimov FC simulated data sets defined in table 5.1. The fit method is the same as for δ, with the reactor constraint applied, appropriate substitution of fit variables and δ thrown from a uniform prior. The reason to avoid using the likelihood surface from the data fit directly is because this approach causes the critical values to become smaller in the vicinity of the best-fit for δ because the generated simulated data sets more closely correspond to the real data, artificially shrinking the confidence interval.

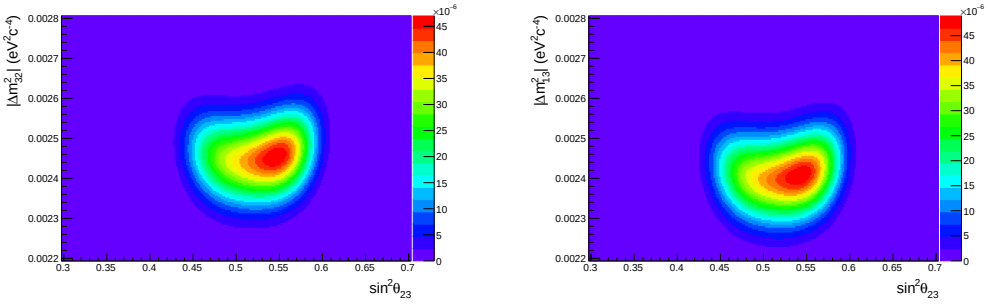

(a) Normal ordering (b) Inverted ordering

Figure 5.6: Distribution of atmospheric parameter throws for calculating Feldman-Cousins critical values.

5.7 Sensitivity studies

One approach to determining the sensitivity of an analysis is to produce and fit a large number of toy experiments. However, such an approach incurs a high computational cost and therefore this analysis defines two 'Asimov' data sets, for which fits are performed to provide a representative median sensitivity without the need to fit very large numbers of toys (such an approach is used for the single case of the best-fit value of δ in section 5.9). In particular, the Asimov data set A uses oscillation parameter values near existing best-fit values to provide the 'most representative' sensitivities, whereas the Asimov data set B is similar to Asimov A, but assumes CP

is conserved and has a value for $\sin^2\theta_{23}$ in the lower octant (see table 5.1). Thus, the resultant sensitivity contours indicate the ability of the analysis to measure δ in the absence of statistical fluctuations, under the assumption that true values of the oscillation parameters correspond to the Asimov values and with all systematic parameters fixed at their central values. Fits are performed for each of normal and inverted mass ordering, and also with and without the reactor constraint on $\sin^2\theta_{13}$. Sensitivity is determined with respect to the constant-$\Delta\chi^2$ method.

5.7.1 Sensitivity to δ

The sensitivity to δ with and without reactor constraint is shown for the Asimov data sets A and B in fig. 5.7.

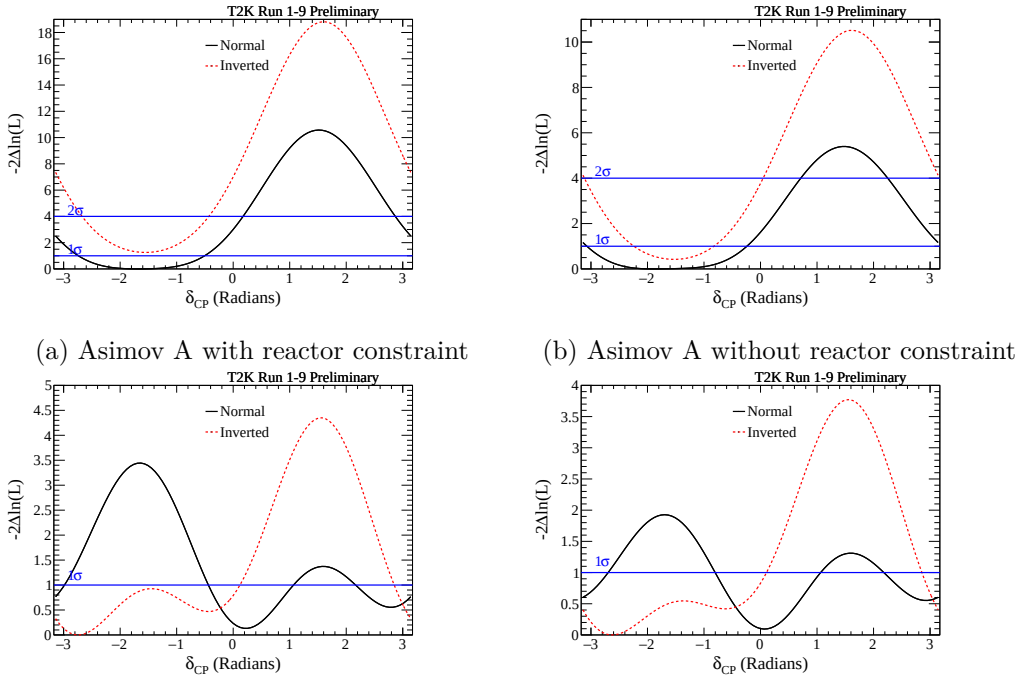

(a) Asimov A with reactor constraint

(b) Asimov A without reactor constraint

(c) Asimov B with reactor constraint

(d) Asimov B without reactor constraint

Figure 5.7: The expected $\Delta\chi^2$ distribution as a function of δ with and without reactor constraint for Asimov data sets A and B. The normal and inverted mass ordering $\Delta\chi^2$ distributions are shifted to reflect the global best-fit χ^2 value, which is taken to be the minimum between normal and inverted mass ordering for the given Asimov set.

One can see from fig. 5.7 that for Asimov A a broad range of positive values of δ can be excluded at 2σ if the reactor constraint is applied to $\sin^2\theta_{13}$, but CP conserving values are only excluded at 1σ. If the reactor constraint is not applied,

a small range of values of δ around $+\pi/2$ are excluded at 2σ, while CP conserving values are again excluded at 1σ. The Asimov B case demonstrates little sensitivity to δ. Furthermore, for Asimov A it can be seen that the inverted mass ordering is disfavoured relative to the true normal mass ordering, whereas for Asimov B the best-fit value of δ near $-\pi$ in the inverted mass ordering is narrowly preferred over the true value of $\delta = 0$ in normal mass ordering. This is the result of a lack of sensitivity to distinguish $\delta = 0$ in normal mass ordering from $\delta = \pi$ in inverted mass ordering, as demonstrated by fig. 5.8, which shows normalised one-ring e-like spectra for Asimov data set B with different values of δ. It is clear from the plots that the spectrum for $\delta = 0$ in normal mass ordering is similar in shape to the spectrum for $\delta = \pi$ in inverted mass ordering and vice versa.

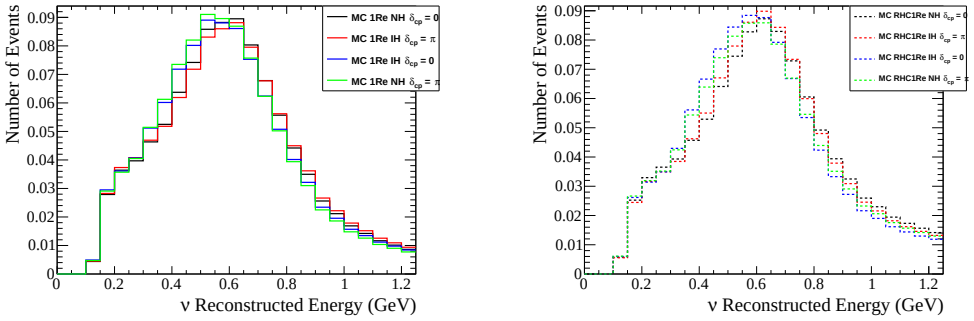

(a) MC one-ring FHC e-like spectra

(b) MC one-ring RHC e-like spectra

Figure 5.8: Normalised spectra for one-ring e-like samples showing the effect of changing the mass hierarchy and true value of δ for the Asimov B data set.

5.8 Results

The results of the Run 1-9 data set fit, for an exposure of 1.4938×10^{21} POT in neutrino mode and of 1.6346×10^{21} POT in antineutrino mode, are shown in this section.

5.8.1 Predicted and observed spectra

The expected number of events in the Run 1-9 data set are shown in table 5.5 for oscillation parameters as defined for Asimov A and B, Asimov A with δ at zero, for the case of no oscillation and also Asimov FC NO (i.e. T2K's best-fit with Run 1-9 data applying the reactor constraint). The observed number of events is also shown in Table 5.5. The predicted and observed spectra are shown for each of the

Sample	Asimov A	Asimov A ($\delta = 0$)	Asimov B	Asimov BF	Not Osc	Observed
FHC ν_μ	272.4	272.1	285.0	276.7	1226.6	243
FHC ν_e	72.8	60.8	54.2	73.7	15.6	75
RHC ν_μ	139.5	139.2	143.2	141.9	459.1	140
RHC ν_e	16.8	19.2	17.4	17.2	7.0	15
FHC ν_e CC1π^+	6.9	6.0	5.4	6.9	2.6	15

Table 5.5: The observed, expected and best-fit number of events in Run 1-9 data set for an FHC exposure of 1.4938×10^{21} POT and an RHC exposure of 1.6346×10^{21} POT are shown for each selected sample. The prediction is produced using the BANFF tuning and the oscillation parameters shown in table 5.1.

samples in fig. 5.9. The e-like samples are broken down into E_r and θ projections in fig. 5.10. While a deficit in observed events in the FHC ν_μ sample relative to the best-fit prediction is evident, one can also see from the spectra that shape and normalisation are described rather well within the errors and the discrepancy between the observed and predicted sample event rate is approximately 1.5σ when adding systematic (5.1%) and statistical (6.0%) errors in quadrature. For the RHC $\bar{\nu}_\mu$ sample one can see that predicted event rates are in excellent agreement with observation both in terms of normalisation and shape. A similar picture can be seen for the FHC ν_e sample and RHC $\bar{\nu}_e$ sample, though the pattern of excess and deficit in observation relative to prediction is interesting here for reasons to be discussed in later sections. The FHC ν_e CC1π^+ sample stands out for an observed event rate that is more than double the best-fit prediction, albeit on a small event rate, which is consequential for the fit of δ, as shall be discussed later.

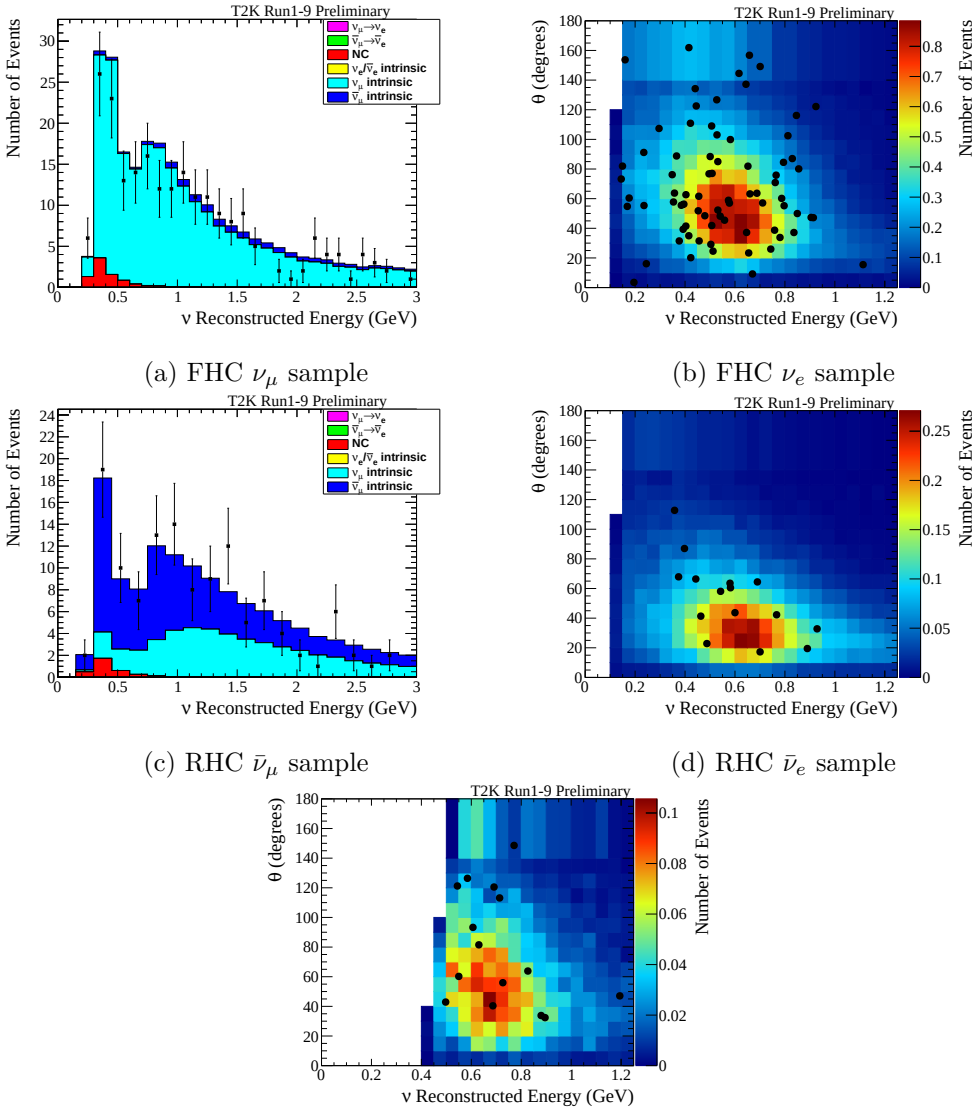

(a) FHC ν_μ sample

(b) FHC ν_e sample

(c) RHC $\bar{\nu}_\mu$ sample

(d) RHC $\bar{\nu}_e$ sample

(e) FHC ν_e CC1π^+ sample

Figure 5.9: Predicted spectra and observed events (points). μ-like distributions are a function of the reconstructed neutrino energy, while the e-like distributions are functions of both the reconstructed neutrino energy and the reconstructed angle between the outgoing lepton and the neutrino direction. The distributions correspond to the statistics collected in the full Run 1-9 data set. The spectra are generated with the systematic parameters at nominal and the oscillation parameters corresponding to the best-fit values from the data fit (solar parameters at PDG 2018).

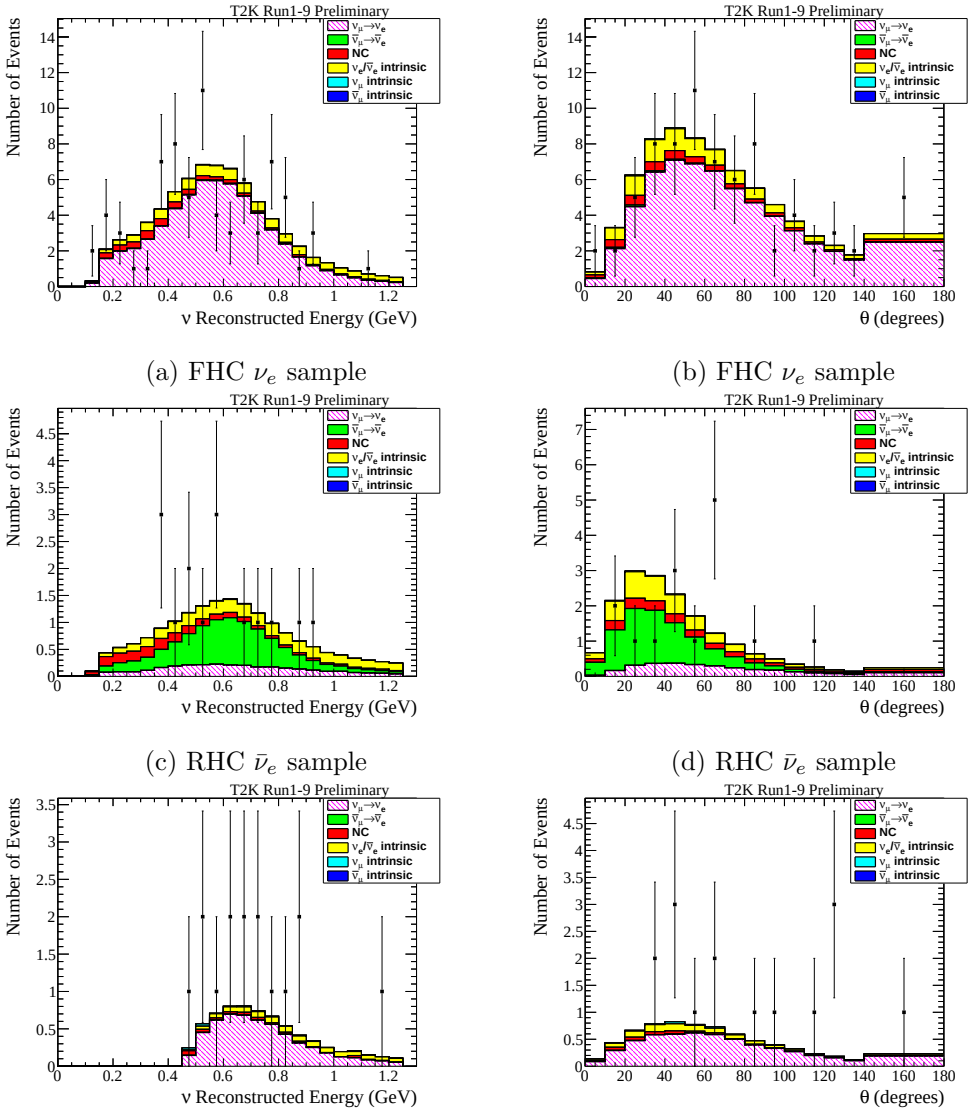

(a) FHC ν_e sample

(b) FHC ν_e sample

(c) RHC $\bar{\nu}_e$ sample

(d) RHC $\bar{\nu}_e$ sample

(e) FHC ν_e CC1π^+ sample

(f) FHC ν_e CC1π^+ sample

Figure 5.10: Predicted spectra and observed events (points). The e-like distributions are functions of both the reconstructed neutrino energy and the reconstructed angle between the outgoing lepton and the neutrino direction, with the projections in each variable shown here. The distributions correspond to the statistics collected in the full Run 1-9 data set. The spectra are generated with the systematic parameters at nominal and the oscillation parameters corresponding to the best-fit values from the data fit (solar parameters at PDG 2018).

5.8.2 Constant $\Delta\chi^2$ confidence intervals

The result for δ with and without reactor constraint is shown in fig. 5.11.

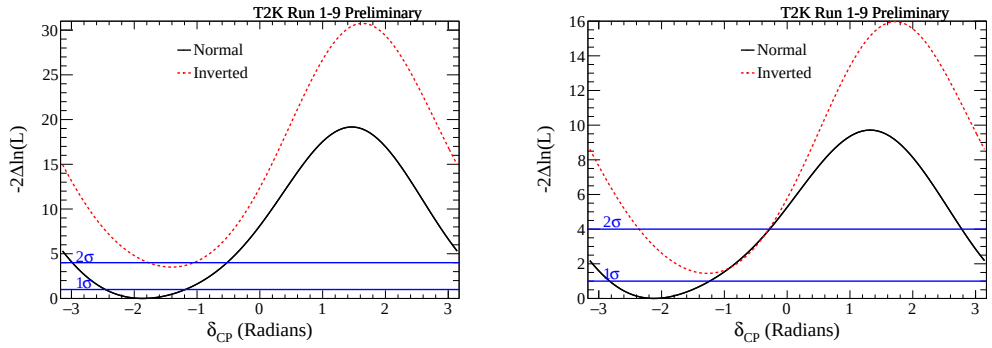

(a) δ with reactor constraint

(b) δ without reactor constraint

Figure 5.11: The observed $\Delta\chi^2$ distribution as a function of δ with and without reactor constraint. Normal and inverted mass ordering $\Delta\chi^2$ distributions shifted to the same global best-fit χ^2 value, which is taken to be the minimum between normal and inverted ordering.

The most notable feature of each fit is the stronger contour relative to the Asimov A sensitivity study, for which a direct comparison can be seen in fig. 5.12. This feature can be explained with reference to table 5.6, which presents expected event rates for Asimov A oscillation parameters, but with varying values of δ. From

Sample	$\delta = -\pi/2$	$\delta = 0$	$\delta = \pi/2$	$\delta = \pi$	Observed
FHC ν_μ	272.4	272.1	272.4	272.8	243
FHC ν_e	72.8	60.8	49.3	61.3	75
RHC ν_μ	139.5	139.2	139.5	139.9	140
RHC ν_e	16.8	19.2	21.3	18.9	15
FHC ν_e CC1π^+	6.9	6.0	4.8	5.7	15

Table 5.6: Predicted total number of events in each SK sample for an FHC exposure of 1.4938×10^{21} and an RHC exposure of 1.6346×10^{21} POT, for Asimov data set A oscillation parameters, but with varying δ.

this it can be seen that expected FHC ν_e event rates (including the FHC ν_e CC1π^+ sample) reach a maximum value for $\delta = -\pi/2$, which is exceeded by the observed event rate, particularly for the FHC ν_e CC1π^+ sample. Considering the RHC ν_e event rate, it can be seen that the expected event rate reaches a minimum value for $\delta = -\pi/2$ and that the observed event rate is lower than this value. Observed event rates that are somewhat more extreme than those expected for maximal CP violation results in stronger exclusion of values of δ away from this region. The

observed contour will be compared to the expected sensitivity in section 5.9. With the reactor constraint applied the fit excludes CP conservation in normal ordering at 2σ and inverted ordering is almost excluded entirely at 2σ. Table 5.7 shows the best-fit values and confidence intervals on δ based on the constant-$\Delta\chi^2$ method.

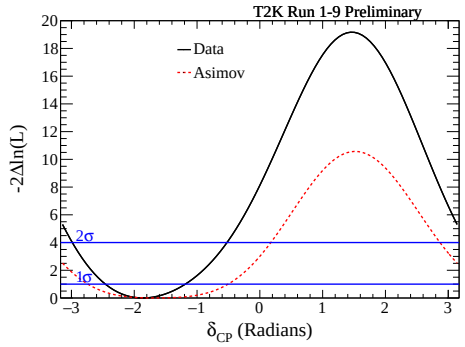

(a) Normal ordering with reactor constraint

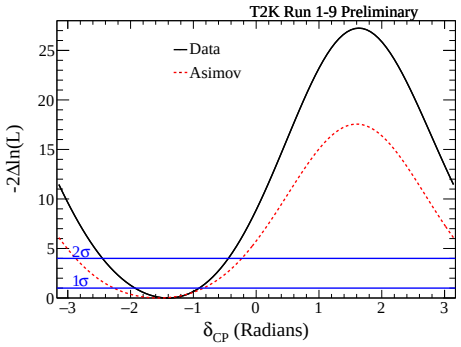

(b) Inverted ordering with reactor constraint

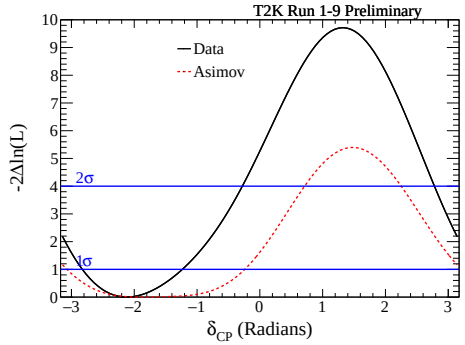

(c) Normal ordering without reactor constraint

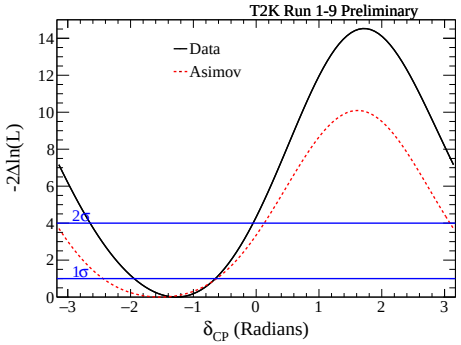

(d) Inverted ordering without reactor constraint

Figure 5.12: The observed $\Delta\chi^2$ distribution as a function of δ with and without reactor constraint, compared to expected $\Delta\chi^2$ distributions for Asimov A.

Reactor	Best-fit (NH)	$\pm1\sigma$ (NH)	Best-fit (IH)	$\pm1\sigma$ (IH)
Yes	-1.885	[-2.460,-1.187]	-1.382	-
No	-2.136	[-2.827,-1.234]	-1.257	-

Table 5.7: The best-fit and confidence intervals at 1σ CL obtained with the constant-$\Delta\chi^2$ method for the measurement of δ versus mass ordering.

5.8.3 Feldman-Cousins critical values

The Feldman-Cousins critical values, computed using the method described in section 5.6 are shown in fig. 5.13. The critical values at 1σ, 90% and 2σ CL are com-

puted for both true mass orderings at the following true values of δ; $-\pi$, $-3\pi/4$, $-\pi/2$, $-\pi/4$, 0, $+\pi/4$, $+\pi/2$, $+3\pi/4$, and $+\pi$. As previously noted, the reason for

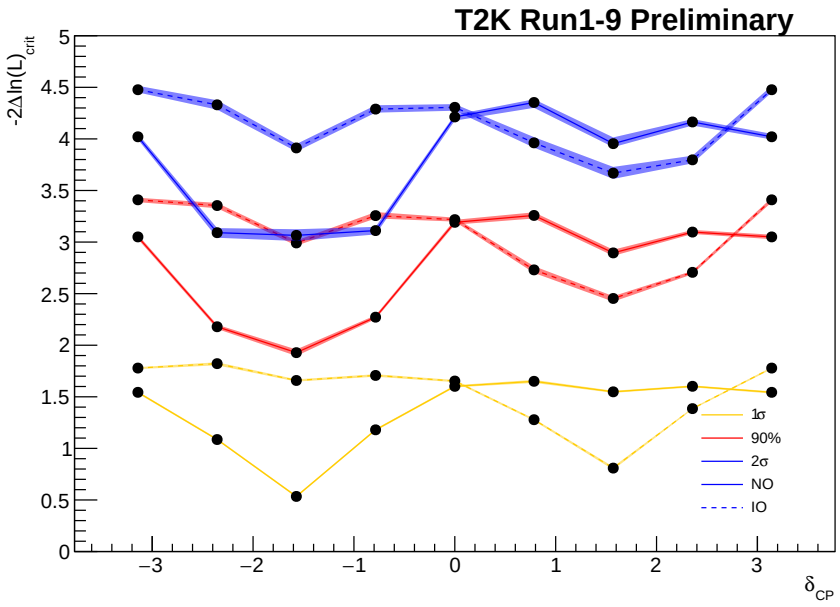

Figure 5.13: Feldman-Cousins $\Delta\chi^2$ critical values for Run 1-9. Critical values are shown for 1σ, 90% and 2σ confidence levels for 9 evenly spaced values on the range $[-\pi, \pi]$ and linearly interpolated between these points. Critical values are determined true normal hierarchy (solid lines) and true inverted hierarchy (dashed lines). The $\pm 1\sigma$ uncertainty on the critical values for each confidence level is also shown as a shaded band.

undertaking the Feldman-Cousins method is that critical $\Delta\chi^2$ values are not expected to follow the Gaussian approximation and the deviation from the Gaussian approximation is evident at most values of δ. The largest deviations are seen in the regions around maximal CP violation, where, for example the 2σ critical value in normal ordering at $\delta = -\pi/2$ is around 3.1, rather than the value of 4 that one would find for the Gaussian case. This section will discuss the reasons for the particular pattern of behaviour observed in the Feldman-Cousins critical values; in particular, fig. 5.13 shows that the critical values typically exceed the Gaussian value for a single degree of freedom at low confidence levels, but are generally lower than the Gaussian value at higher confidence levels. Furthermore, within a fixed confidence level and mass ordering, the Feldman-Cousins critical value decreases as the maximally CP-violating points are approached, with the magnitude of this effect at each point depending upon the true mass ordering.

As an aid to discussion the bi-event plot in fig. 5.14 shows how the event

rate in the ν_e-like (the FHC ν_e sample and FHC ν_e CC1π^+ sample are combined for the purpose of this plot) and $\bar{\nu}_e$-like samples varies as oscillation parameters are varied. In this plot those oscillation parameters that are not varied take on Asimov data set A values, systematic parameters are fixed at nominal values, while $\sin^2(\theta_{23})$ variously takes on values of 0.45 (red), 0.5 (black) and 0.55 (blue), Δm^2_{32} (Δm^2_{31}) is set to values constituting normal (solid) and inverted (dashed) ordering, while δ is varied between $-\pi/2$, 0, $+\pi/2$ and π, denoted by the points on the ellipses formed by interpolating between these values. T2K's observation is also presented on the plot.

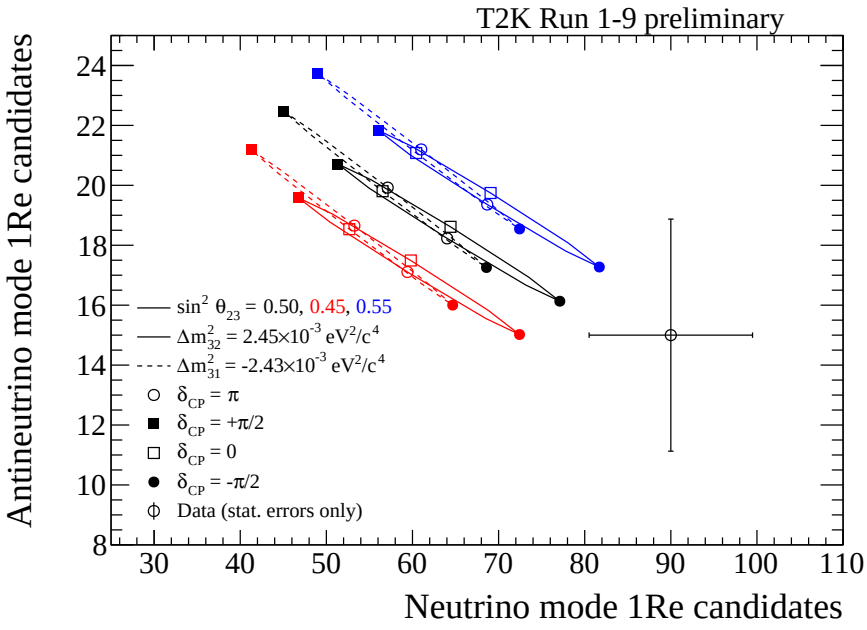

Figure 5.14: This plot shows the candidate RHC ν_e-like event rate vs the candidate FHC ν_e-like event rate (combining the two FHC ν_e-like samples) for a variety of different oscillation parameter values. Predictions are generated for the given values of δ and $\sin^2(\theta_{23})$ for normal mass ordering (solid lines) and inverted mass ordering (dashed lines), with remaining oscillation parameters fixed at the central values defined in table 5.1 and systematics at nominal. T2K's observation is also shown along with statistical errors.

Mass ordering effect

Mass ordering is a discrete, non-nested parameter [152] and there is significant degeneracy between the two mass orderings, as evidenced by the bi-event plot, where, for a broad range of values of δ, a given value of δ in the normal ordering (for exam-

ple) produces an event rate prediction that is very similar to an inverted ordering prediction for a different value of δ. As a result of this degeneracy it is possible to

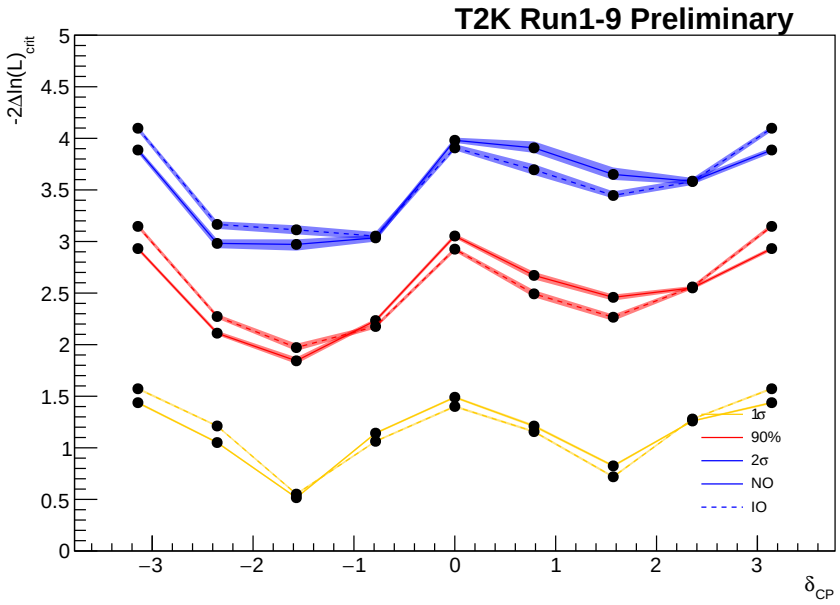

Figure 5.15: Critical $\Delta\chi^2$ values for fixed mass order

find a best-fit for a given toy in the wrong mass ordering. Given the definition (see section 5.6) of $\Delta\chi^2$ is

$$\Delta\chi^2 = \chi^2_{\text{true}} - \chi^2_{\text{bf}}$$

it follows that finding a best-fit in the incorrect mass ordering leads to a higher value of $\Delta\chi^2$ than would be the case for a fit in the true mass ordering, because finding a minimum in the wrong mass ordering necessarily implies that the minimum χ^2 value in that mass ordering is lower than the minimum χ^2 value in the true mass ordering. This effect can be clearly demonstrated by recomputing the critical $\Delta\chi^2$ values while prohibiting fits to the wrong mass ordering (fig. 5.15); the critical values largely converge for the two true mass orderings and shift to lower values of $\Delta\chi^2$. Furthermore, fig. 5.16 shows, for true $\delta = -\pi/2$ and true normal ordering, how best-fits from the wrong mass ordering provide global best-fits, with the region $-\pi < \delta < 0$ being populated almost exclusively by best-fits from the wrong mass ordering for higher values of $\Delta\chi^2$. The ability to fit the wrong mass ordering is particularly relevant near physical boundaries. Consider the black ellipses in fig. 5.14; the ν_e event rate for true δ equal to $+\pi/2$ in true normal ordering is approximately 51, but there are no variations in δ within this mass ordering that

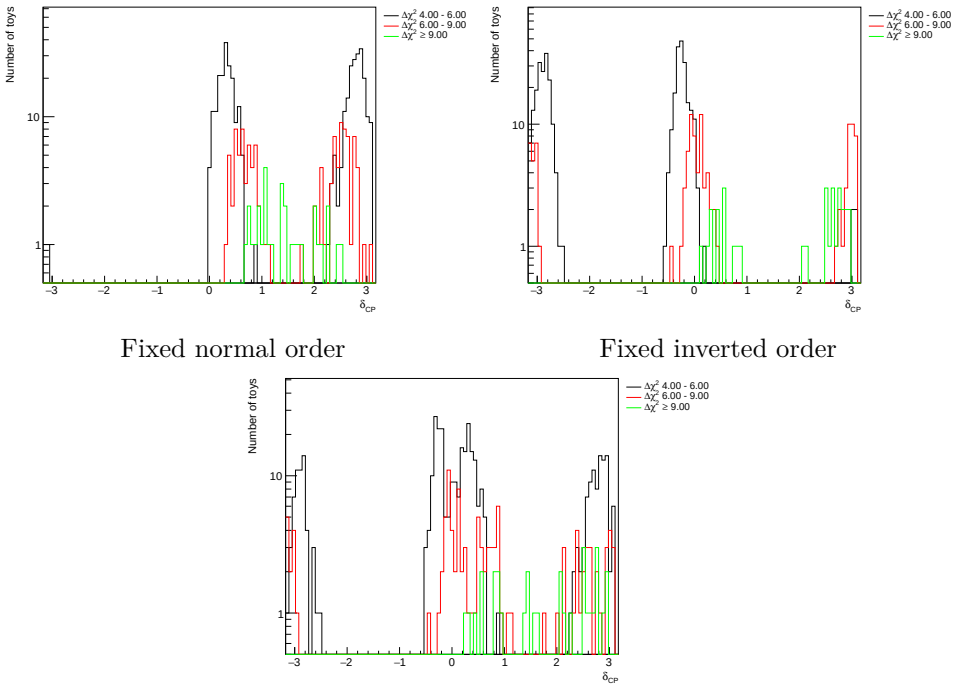

Fixed normal order

Fixed inverted order

Global

Figure 5.16: Distribution of best-fit values in δ_{CP} for true $\delta_{CP} = -\pi/2$ for the specified ranges of $\Delta\chi^2$.

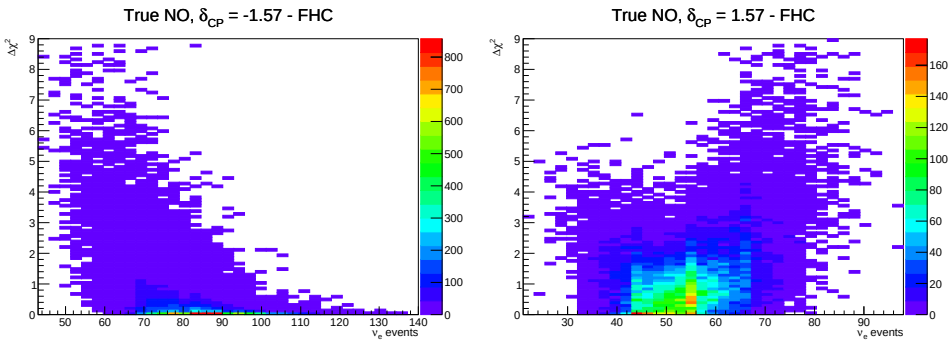

(a) True $\delta = -\pi/2$.

(b) True $\delta = +\pi/2$.

Figure 5.17: $\Delta\chi^2$ vs ν_e event rate for true normal ordering

produce a lower ν_e event rate. Thus, even a small downward fluctuation in the ν_e event rate goes beyond this physical boundary. However, the inverted ordering toys can still cover such a fluctuation, where the physical boundary at true δ equal to $+\pi/2$ predicts approximately 45 ν_e events, providing a range of values of δ able to cover fluctuations below 51 events. Such fluctuations result in an increase in the the $\Delta\chi^2$ values. This effect can be observed in fig. 5.17b. If the inverted ordering was unavailable to fit fluctuations below the physical boundary we would expect to see a narrowing of the $\Delta\chi^2$ distribution as the rate of ν_e events decreases due to the inability to fluctuate to lower values of χ^2 within the normal ordering, much as is seen for upward fluctuations with true $\delta = -\pi/2$ (fig. 5.17a), where inverted ordering toys do not cover such fluctuations. Instead we see the width of the $\Delta\chi^2$ distribution is maintained below the physical boundary. As a result, it is reasonable to expect lower critical $\Delta\chi^2$ values for true $\delta < 0$ than for true $\delta > 0$ in true normal ordering and vice versa for true inverted ordering.

Effect of the physical boundaries

For a given set of true oscillation parameters the ν_e event rate reaches a maximum for $\delta = -\pi/2$ and a minimum for $\delta = +\pi/2$ (see fig. 5.14). Considering $\delta = -\pi/2$ in true normal ordering, fluctuations above this maximum are therefore unable to produce downward fluctuations in $\Delta\chi^2$, as can be seen in fig. 5.18a, where, as noted above, best-fits pile up at the physical boundary and the $\Delta\chi^2$ distribution narrows as the event rate increases, because a more extreme statistical fluctuation cannot be accommodated by a more extreme value of δ or mass ordering.

Considering in turn $\delta = +\pi/2$ (figs. 5.17b and 5.18b), downward fluctuations still hit the physical boundary, but with two additional effects; the previously noted ability to fit in the wrong mass ordering, which causes some pileup at nearby non-maximal values of δ (as confirmed by the disappearance of this pileup when disallowing fits to the wrong mass ordering in fig. 5.19b), along with a lower ν_e event rate in the region of $\delta = +\pi/2$ leading to lower sensitivity and therefore producing a more even spread of best-fits in the region around the true value within the normal ordering (fig. 5.19b). It should be noted that effects from the opposite physical boundary (e.g. $\delta = +\pi/2$ for true $\delta = -\pi/2$) are more common for higher values of $\Delta\chi^2$, since this naturally corresponds to larger fluctuations in the event rate.

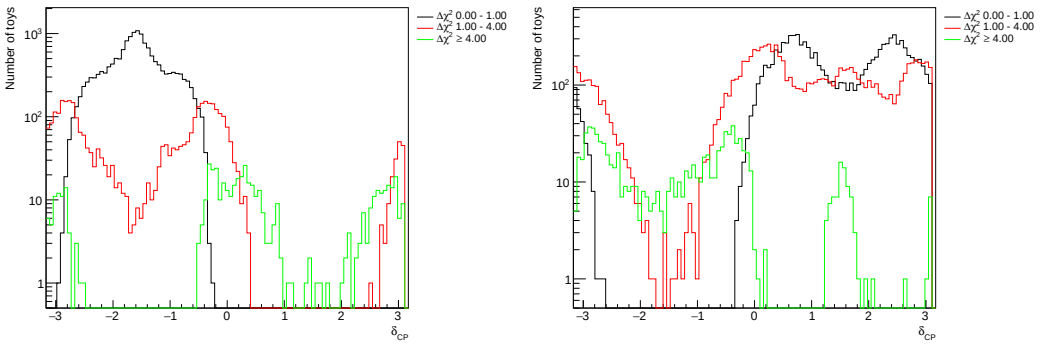

(a) True $\delta = -\pi/2$ (b) True $\delta = +\pi/2$

Figure 5.18: Distributions of best-fit values for different ranges of $\Delta\chi^2$ in true normal ordering.

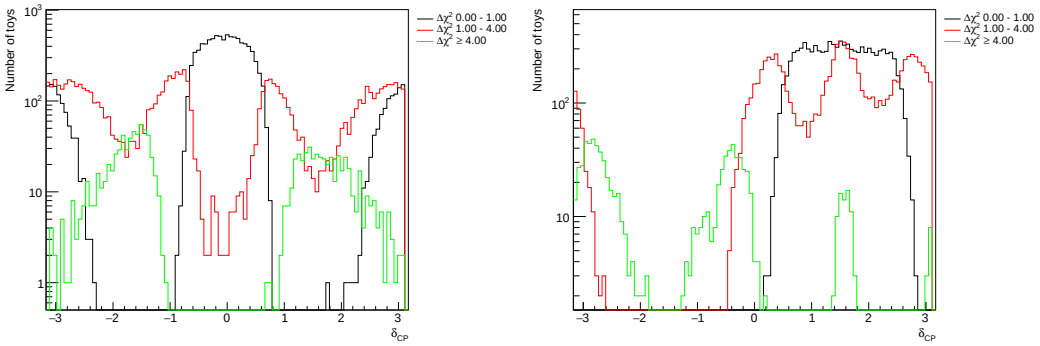

(a) True $\delta = 0$ (b) True $\delta = +\pi/2$

Figure 5.19: Distributions of best-fit values for different ranges of $\Delta\chi^2$ in fixed normal ordering.

Degeneracy in δ

It remains to consider one additional feature in the pattern of critical $\Delta\chi^2$ values; the elevated critical values for true $\delta = 0$ at only 1σ confidence levels (even for fixed mass ordering) relative to the Gaussian approximation. Figure 5.19a highlights that for fixed normal ordering, the degeneracy between 0 and π pushes up the critical value for lower confidence levels, with this effect being absent at higher confidence levels due to a lack of sensitivity to separate 0 and π, meaning $\Delta\chi^2 = \chi^2_0 - \chi^2_\pi$ is not large enough to populate the tail of the $\Delta\chi^2$ distribution.

Summary

The behaviour observed in the critical $\Delta\chi^2$ values relative to that expected in the Gaussian approximation can be explained by the following factors:

1. The physical boundaries in δ act to bias critical values away from their Gaussian approximation.

2. Mass ordering is a discrete, non-nested parameter and works as an additional degree of freedom, though without sufficient freedom to make the critical values behave as if the problem has two degrees of freedom.

3. The mass ordering can help to keep the best-fit value of δ away from the physical boundary when fluctuations in the number of events are modest, broadening the $\Delta\chi^2$ distributions and thereby increasing the critical values, most notably at the 1σ level.

4. The physical boundary effect is increasingly evident at higher confidence levels, since these confidence levels correspond to more extreme statistical fluctuations that favour best-fit δ-mass order values far from the true point and more frequently beyond the physical boundaries and therefore we continue to see lower critical values at greater distances from the physical boundaries.

5.8.4 Feldman-Cousins confidence intervals

In figs. 5.20a to 5.20c the confidence intervals obtained with the Feldman-Cousins method are shown for δ and mass ordering with the reactor constraint for the Run 1-9 data set. Inverted ordering is almost excluded at 2σ, except for a small interval around $\delta = -\pi/2$, while inverted ordering is excluded altogether at 90% CL. In normal ordering, which corresponds to the best-fit mass ordering, the CP conserving values of $\delta = 0$ and $\delta = \pi$ are excluded at 2σ.

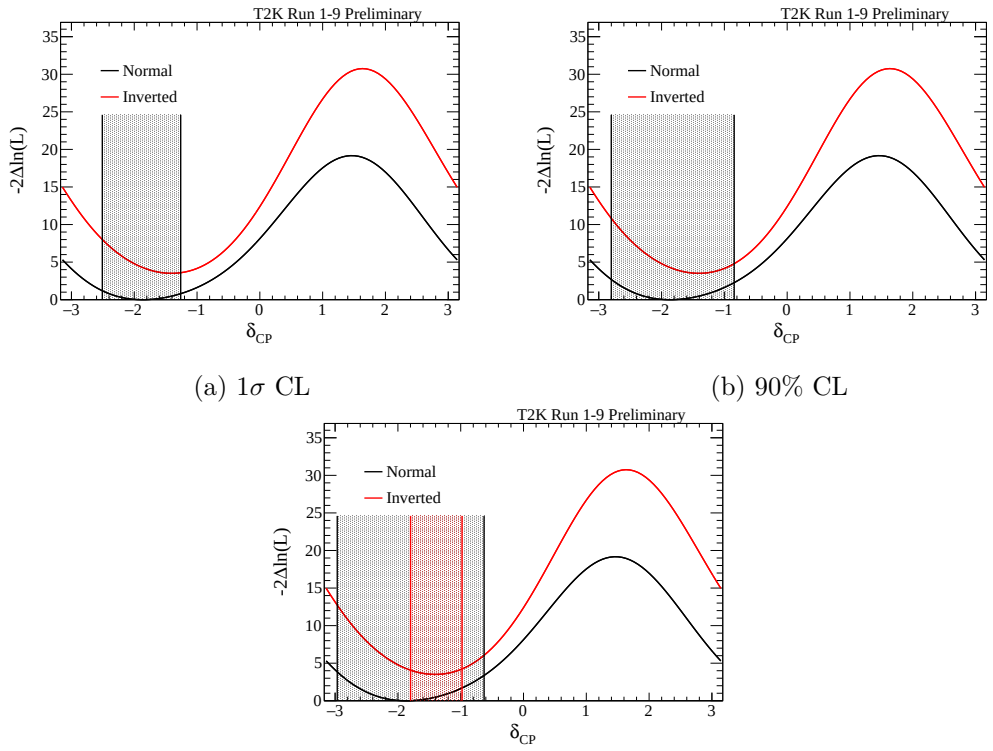

(a) 1σ CL

(b) 90% CL

(c) 2σ CL

Figure 5.20: Feldman-Cousins confidence intervals for the observed $\Delta\chi^2$ distributions for Run 1-9. Observed $\Delta\chi^2$ distributions are shifted with respect to the global minimum.

The corresponding Feldman-Cousins confidence intervals are shown in table 5.8. Comparing the intervals in the constant-$\Delta\chi^2$ and Feldman-Cousins methods it can be seen that the 1σ intervals in normal ordering are similar (the constant-$\Delta\chi^2$ interval being $\sim 2\%$ wider), which is not surprising, given that the Feldman-Cousins critical values are quite close to 1 in the relevant regions (slightly higher than 1 at the lower limit of the interval, slightly lower than 1 at the upper limit). In both cases, the 1σ interval for inverted ordering is empty. As we consider the higher confidence levels more notable differences begin to emerge, for the 90% CL the constant-$\Delta\chi^2$ interval in normal ordering is $[-2.804, -0.750]$, while for the 2σ CL, the constant-$\Delta\chi^2$ interval in normal ordering is $[-2.986, -0.523]$ and in inverted ordering is $[-1.773, -1.051]$. The net result is that the normal ordering contours are around 5% wider using the constant-$\Delta\chi^2$ method, while the inverted ordering interval is 14% narrower. This is consistent with the behaviour of the Feldman-Cousins critical values, where the critical values in normal ordering are less than the Gaussian value of 4 in the region around the best-fit due to the physical boundary,

whereas the inverted ordering critical values are greater than the Gaussian value due to the mass ordering degeneracy.

Reactor	CL	Normal ordering	Inverted ordering
Yes	1σ	$[-2.509, -1.260]$	-
Yes	90%	$[-2.801, -0.844]$	-
Yes	2σ	$[-2.966, -0.628]$	$[-1.799, -0.979]$

Table 5.8: The confidence intervals at 1σ, 90% and 2σ CL obtained with the Feldman-Cousins method for the Run 1-9 data set is shown for the measurement of δ versus mass ordering.

5.8.5 Jarlskog invariant

Having established a best-fit value for δ we can now compute the Jarlskog invariant to determine a parametrisation-independent measure of CP violation. The oscillation parameter values used are those for T2K's best-fit, defined in table 5.1. From this the Jarlskog invariant is found to be

$$J = -3.15 \times 10^{-2} \tag{5.14}$$

which is approximately 11% of the maximum allowed value and three orders of magnitude larger than the value in the quark sector.

5.9 Expected sensitivity

In section 5.7 it was noted that sensitivity was determined based on the results of fits of a representative simulated data set, rather than based on the distribution of many toy experiments for computational reasons. However, in light of the observed constraints being rather stronger than those expected based on Asimov A fits, further consideration of how the observed result compares to the sensitivity of the experiment is warranted.

5.9.1 Expected sensitivity method

This section outlines the procedure to produce the expected sensitivity comparison plots, in particular, the description assumes true normal ordering and $\delta = -1.885$.

- 2×10^4 simulated data sets are generated following the Feldman-Cousins method for a true value of δ and mass ordering, in this case $\delta = -1.885$ and normal ordering.

- A χ^2 distribution is computed with respect to the marginalisation toys as a function of δ and mass ordering.
- For each simulated data set, the minimum value of χ^2 for each bin of δ, $\chi^2_{bin,min}$ is found with respect to both normal and inverted ordering.
- The test statistic is then computed as $\Delta\chi^2_{bin} = \chi^2_{bin} - \chi^2_{bin,min}$, which is slightly different to the Feldman-Cousins method, where $\Delta\chi^2_{FC} = \chi^2_{true} - \chi^2_{bf}$. The distributions of $\Delta\chi^2_{bin}$ and $\Delta\chi^2_{FC}$ coincide if the bin centre is equal to the true value of δ and normal ordering.
- This results in a $\Delta\chi^2$ distribution from which we can draw conclusions about the expected $\Delta\chi^2$ for each value of δ given a hypothesised true value and mass ordering.
- The spread of the $\Delta\chi^2$ distribution for each point of δ and mass ordering is obtained as the range of the $\Delta\chi^2_{bin}$ distribution that contains respectively the 68.27% and 95.45% of the toy experiments on its left side. The test statistic $\Delta\chi^2_{bin}$ is assumed to be one-sided by construction, because $\chi^2_{bin,min} \leq \chi^2_{bin}$.

5.9.2 Expected sensitivity results

In fig. 5.21 the Run 1-9 data result for δ versus mass ordering is compared to the 1σ and 2σ uncertainties on the $\Delta\chi^2$ distributions corresponding to $\delta = -1.885$. It can be seen that the data contour is contained within the one-sided 2σ band for inverted ordering and approximately contained within the 2σ band for normal ordering. Thus, while the data contour appears stronger than the sensitivity given by Asimov A fits, approximately 5% of simulated data toys yield contours more extreme than that observed in the data.

Furthermore, it is possible to consider the probability to exclude the CP conserving points in the simulated data. Table 5.9 shows the probability to exclude the CP conserving points (separately and jointly) at the 2σ confidence level, with a substantial fraction of the toys ($\sim 25\%$) excluding CP conservation.

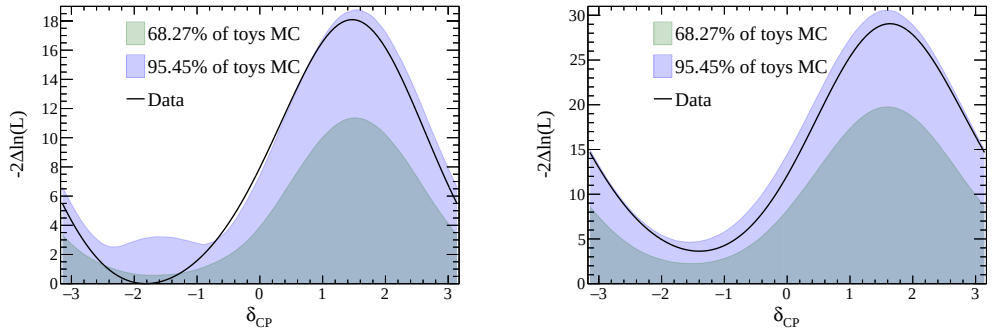

(a) Normal hierarchy

(b) Inverted hierarchy

Figure 5.21: The one-sided distribution of $\Delta\chi^2$ vs δ obtained with 2×10^4 toy experiments generated with $\delta = -1.885$ and normal ordering is shown. The $\Delta\chi^2$ distributions obtained by fixing the mass ordering to normal (a) and inverted (b) are shown, along with the $\Delta\chi^2$ values corresponding to 68.27% and 95.45% of the toy experiments.

δ	Mass ordering	2σ
0	NH	0.344
π	NH	0.320
0	IH	0.742
π	IH	0.734
0 and π	NH	0.249
0 and π	IH	0.688

Table 5.9: The fraction of toy experiments for which $\delta = 0, \pi$ in normal and inverted ordering are excluded at 2σ CL is shown.

5.10 Summary

The T2K Run 1-9 dataset corresponds to an integrated J-PARC neutrino beam exposure of 1.4938×10^{21} POT in neutrino mode and 1.6346×10^{21} POT in antineutrino mode. This dataset has been used to provide a measurement of the neutrino CP phase, δ.

This analysis predicts 272.4 $\pm$ 21.6 (stat + syst) for neutrino 1-ring ν_μ-like, 139.5 $\pm$ 13.4 (stat + syst) for 1-ring $\bar{\nu}_\mu$-like, 72.8 $\pm$ 10.8 (stat + syst) for neutrino 1-ring ν_e-like, and 16.8 $\pm$ 4.3 (stat + syst) for 1-ring $\bar{\nu}_e$-like single-ring events in Super-K and 6.9 $\pm$ 2.9 (stat + syst) 1-ring ν_e CC1π^+-like events, given the oscillation parameters of the Asimov data set A in 5.1. The observed event rates are respectively 243 for 1-ring ν_μ-like, 140 for 1-ring $\bar{\nu}_\mu$-like, 75 for 1-ring ν_e-like, 15 1-ring $\bar{\nu}_e$-like and 15 for 1-ring ν_e CC1π^+-like.

A joint $\nu/\bar{\nu}$ analysis in a 3-flavour framework with matter effects due to

constant density matter was performed to measure δ. The observed spectra were fitted for both normal and inverted mass ordering hypotheses, with δ allowed to float, whilst all other oscillation (and systematic) parameters were eliminated through marginalisation.

The global best-fit with the reactor constraint applied is for the case of normal ordering, yielding a best-fit value of $\delta = -1.885$, with a 1σ confidence interval given by the Feldman-Cousins method of $[-2.509, -1.260]$. The 2σ confidence level is $([-2.966, -0.628])$ and thus this result provides a hint of CP violation in the lepton sector. For the case of inverted ordering with the reactor constraint applied, the 1σ confidence interval is empty, but the 2σ confidence interval given by the Feldman-Cousins method is $[-1.799, -0.979]$ containing a local best-fit of $\delta = -1.382$.

The corresponding Jarlskog invariant is found to be $J = -3.15 \times 10^{-2}$, approximately 11% of the maximum allowed value and three orders of magnitude larger than the value in the quark sector.

The global best-fit without the reactor constraint applied is for the case of normal ordering, yielding a best-fit value of $\delta = -2.136$, with a 1σ confidence interval given by the constant-$\Delta\chi^2$ method of $[-2.827, -1.234]$. For the case of inverted ordering without the reactor constraint applied, the 1σ confidence interval is empty.

Chapter 6

Mass ordering measurement

6.1 Introduction

As discussed in section 2.2.3, the neutrino mass ordering is a discrete, non-nested parameter and while one might assume that the mass ordering would naturally follow the particle generations to adopt a normal ordering, as is the case in the quark sector, the inverted mass ordering is not excluded by currently available data. This chapter describes the measurement of the neutrino mass ordering. The data set used for this measurement is the same as that used for the CP phase measurement. Two approaches are taken to the measurement of the mass ordering. The first approach is the calculation of the posterior probability of the mass ordering in section 6.2, with the method described in section 6.2.1, the frequentist properties of the posterior probability distribution are discussed in section 6.2.2 and the result presented in section 6.2.3. The second approach involves the calculation of a $\Delta\chi^2$ statistic (section 6.3), the method for which is described in section 6.3.1, the sensitivity of T2K to this measurement of the mass ordering, along with a goodness of fit, is discussed in section 6.3.2 and the result is presented in section 6.3.3.

6.2 Mass ordering posterior probability

The Bayesian posterior probability for the mass ordering can be considered from a frequentist perspective by looking at the distribution of mass ordering posterior probabilities for given true values of the mass ordering and δ. The posterior probability for the (arbitrarily chosen) normal mass ordering is defined as

$$\mathrm{P(NO|E)} = \frac{\mathrm{P(E|NO)P(NO)}}{\mathrm{P(E|NO)P(NO)} + \mathrm{P(E|IO)P(IO)}} \tag{6.1}$$

where P(NO|E) is the probability of the normal mass ordering given the evidence, E, P(E|NO) is the probability of observing the evidence given a true normal mass ordering (P(E|IO) for the corresponding true inverted mass ordering), P(NO) is the prior probability of a true normal mass ordering and P(IO) is the prior probability of a true inverted mass ordering. For this analysis, the a priori assumption is that each mass ordering is equally likely and the thresholds to be considered for the posterior probability are 68.27% and 90%, higher thresholds being computationally impractical.

Given a distribution of posterior probabilities it is possible to understand, for a particular threshold, the rate of Type-I errors, α, (the fraction of toys for which the false mass ordering has a posterior probability exceeding the threshold) and the rate of Type-II errors, β, (the fraction of toys for which the true mass ordering has a posterior probability below the threshold) for a given true mass ordering and true value of δ, given the current T2K exposure. These values can, in turn, be used to provide a check that the distribution of posterior probabilities corresponds to the interpretation of posterior probability. It is expected, for example, that if a 90% posterior probability is observed, then, given equal prior probability, $\sim 90\%$ of the toys should prefer the correct mass ordering. This means that for a posterior probability threshold of 68.27%, the ratio of the rate at which the false mass ordering is accepted, α, to the rate at which the true mass ordering is accepted, $1-\beta$, should be 46.4% and for a threshold of 90%, this ratio should be 11.1%.

6.2.1 Method

The approach taken makes use of the Feldman-Cousins toys generated to determine critical $\Delta\chi^2$ values for the CP phase measurement (section 5.6). Recall that for the Feldman-Cousins toys a large number of simulated data sets are generated for a given true value of δ and the mass ordering, with χ^2 values for each toy computed relative to the marginalisation toys. This results in a χ^2 distribution in terms of δ for each of the two fitted mass orderings. The goal however, is to compute a posterior probability for the normal mass ordering for each toy. It's therefore necessary to move from a χ^2 distribution to a likelihood distribution and also to eliminate δ to produce a likelihood purely in terms of the mass ordering. The likelihood is retrieved as $e^{-\chi^2/2}$ and δ is eliminated by averaging the likelihoods over each bin of δ in the distribution for each fitted mass ordering, rather like the marginalisation procedure applied to the other parameters. The posterior probability then has the property that for inverted ordering it is simply P(IO|E) = 1−P(NO|E). For a given true value of δ, this procedure is followed to find the distributions of P(NO|E) and P(IO|E) for

each of the true mass orderings. To summarise, substituting $L_{\mathrm{NO}} = \mathrm{P}(\mathrm{E}|\mathrm{NO})$ and $L_{\mathrm{IO}} = \mathrm{P}(\mathrm{E}|\mathrm{IO})$:

1. For each true mass ordering, at least 2×10^4 simulated data sets are produced for a true value of δ taking into account both statistical and systematic uncertainties (i.e. systematic parameters, including the remaining oscillation parameters, are thrown from the standard analysis priors)

2. For each simulated data set:

   (a) χ^2 values are obtained for 101 bins of δ by fitting with respect to the marginalisation toys produced for the CP phase measurement in each mass ordering.

   (b) The χ^2 values are converted to likelihood values via $L = e^{-\chi^2/2}$

   (c) The likelihood values are averaged over the bins of δ in each fitted mass ordering to produce likelihood values L_{NO} and L_{IO} in terms of the fitted mass ordering only

   (d) The posterior probability is calculated as

$$\mathrm{P}(\mathrm{NO}|\mathrm{E}) = \frac{L_{\mathrm{NO}}}{L_{\mathrm{NO}} + L_{\mathrm{IO}}}$$

3. This results in a distribution of posterior probabilities for each true mass ordering

Having obtained distributions of posterior probabilities in each true mass ordering for a given value of δ, threshold values of 68.27% and 90% can be used to determine the rate of type-I and type-II errors at these threshold values and the ratio $\alpha/(1-\beta)$.

6.2.2 Frequentist properties of the posterior probability distribution

This section presents the posterior probability distributions determined from the Feldman-Cousins toys for a variety of true values of δ and the mass ordering. Throughout this section, thresholds will be specified to only two significant figures.

Posterior probability distributions for $\delta_{true} = \pm\pi$

In fig. 6.1 the posterior probability distributions for the mass ordering are shown with $\delta_{true} = \pm\pi$ in the case of each true mass ordering, while table 6.1 shows the probability of rejecting each mass ordering for a given true mass ordering at a given

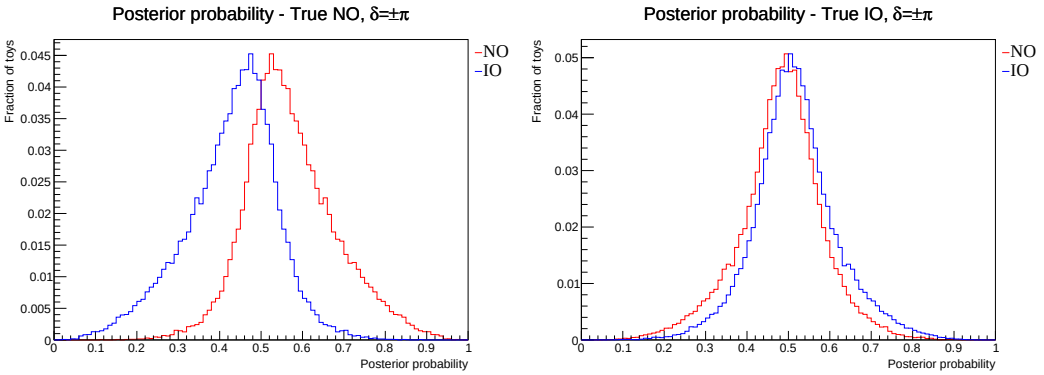

(a) True normal ordering (b) True inverted ordering

Figure 6.1: Posterior probability distributions of the two mass orderings given $\delta = \pm\pi$ and the true mass ordering.

Threshold	True ordering	Reject false ordering	Reject true ordering
68%	Normal	0.16295	0.00855
	Inverted	0.06505	0.02712
90%	Normal	0.00405	0.00000
	Inverted	0.00047	0.00015

Table 6.1: The probability to reject the false and true mass orderings at 68% and 90% thresholds for the given true mass ordering.

threshold. It can be seen from table 6.1 that at the 68% threshold the extent of the overlap between the distributions results in toys that can reject both mass orderings, irrespective of which is true. The ratio for rejecting the true ordering to rejecting the false ordering, $\alpha/(1-\beta)$, is $\sim 17\%$, considerably less than the $\sim 46\%$ expected. At the 90% threshold the true normal ordering is not rejected by any of the toys, whilst $\alpha/(1-\beta)$ is $\sim 4\%$, which, again, is much less than the $\sim 11\%$ expected. Clearly, the power to distinguish the mass ordering for a true value of δ near zero is extremely limited and furthermore, quoting posterior probability for the mass ordering appears inappropriate given the deviation between the observed and expected value of $\alpha/(1-\beta)$.

Posterior probability distributions for $\delta_{true} = -3\pi/4$

In fig. 6.2 the posterior probability distributions for the mass ordering are shown with $\delta_{true} = -3\pi/4$ in the case of each true mass ordering, while table 6.2 shows the probability of rejecting each mass ordering for a given true mass ordering at a given threshold. Table 6.2 shows that at the 68% threshold it is possible to reject

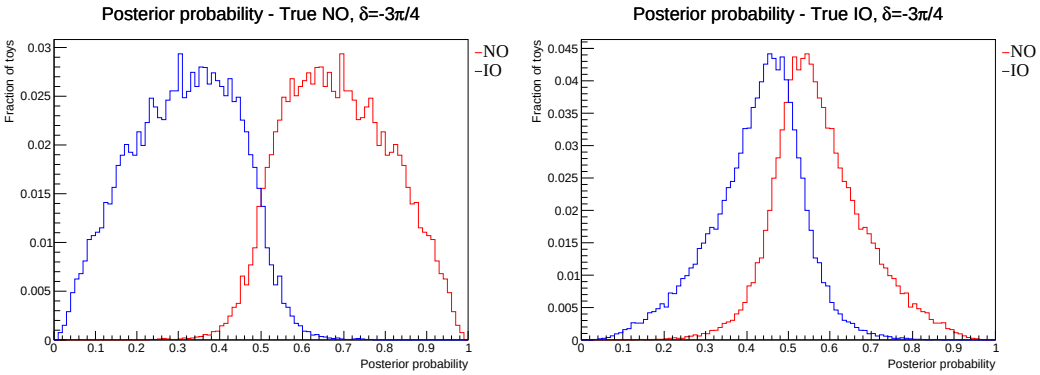

(a) True normal ordering

(b) True inverted ordering

Figure 6.2: Posterior probability distributions of the two mass orderings given $\delta = -3\pi/4$ and the true mass ordering.

Threshold	True ordering	Reject false ordering	Reject true ordering
68%	Normal	0.50110	0.00085
	Inverted	0.00768	0.16972
90%	Normal	0.05215	0.00000
	Inverted	0.00005	0.00359

Table 6.2: The probability to reject the false and true mass orderings at 68% and 90% thresholds for the given true mass ordering.

both the true and false mass orderings. The ratio $\alpha/(1-\beta)$ is $\sim 34\%$, closer to the expected value than for $\delta_{true} = \pm\pi$, but nonetheless smaller than expected. At the 90% threshold the normal ordering cannot be rejected for either true ordering, whilst $\alpha/(1-\beta)$ is $\sim 7\%$, also somewhat less than expected. Thus, for a true value of δ near $-3\pi/4$ the power to distinguish the mass orderings remains rather limited and the posterior probability distribution still deviates from the expected behaviour to a degree that makes its use questionable. Also of note is that the type-I error rate is very high; the variations in δ assuming normal ordering cover a larger fraction of the statistical fluctuations in the inverted ordering toys than do the variations in δ assuming inverted ordering as one approaches $\delta_{true} = -\pi/2$, as discussed in section 5.8.3. As a result, for true inverted ordering the true mass ordering is more likely to be rejected than the false mass ordering.

Posterior probability distributions for $\delta_{true} = -\pi/2$

In fig. 6.3 the posterior probability distributions for the mass ordering are shown with $\delta_{true} = -\pi/2$ in the case of each true mass ordering, while table 6.3 shows

the probability of rejecting each mass ordering for a given true mass ordering at a given threshold. From table 6.3 we can see that at the 90% threshold, normal

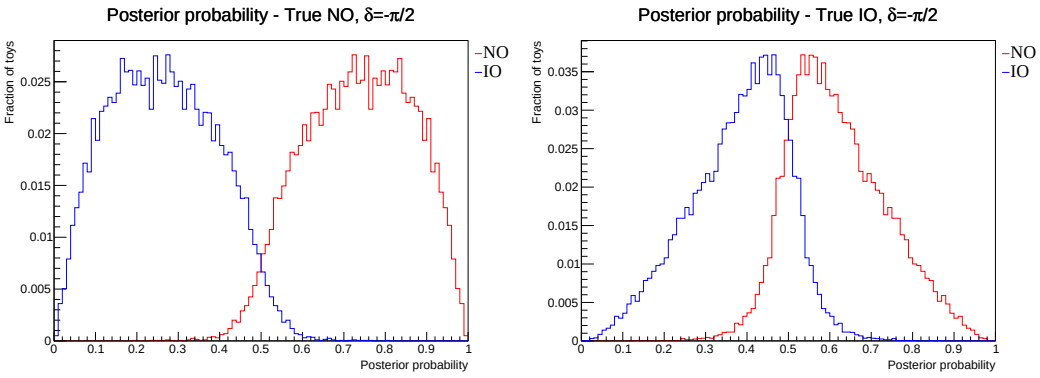

(a) True normal ordering (b) True inverted ordering

Figure 6.3: Posterior probability distributions of the two mass orderings given $\delta = -\pi/2$ and the true mass ordering.

Threshold	True ordering	Reject false ordering	Reject true ordering
68%	Normal	0.65025	0.00045
	Inverted	0.00265	0.28885
90%	Normal	0.11030	0.00000
	Inverted	0.00000	0.01285

Table 6.3: The probability to reject the false and true mass orderings at 68% and 90% thresholds for the given true mass ordering.

ordering is not rejected by any of the toys, irrespective of the true mass ordering, as we again observe lower posterior probabilities for the inverted ordering hypothesis even for true inverted ordering. At the 68% threshold the ratio $\alpha/(1-\beta)$ is $\sim 44\%$. If we considered the 90% threshold, the ratio $\alpha/(1-\beta)$ becomes $\sim 12\%$. For each threshold this is approximately the expected value.

Posterior probability distributions for $\delta_{true} = -\pi/4$

In fig. 6.4 the posterior probability distributions for the mass ordering are shown with $\delta_{true} = -\pi/4$ in the case of each true mass ordering, while table 6.4 shows the probability of rejecting each mass ordering for a given true mass ordering at a given threshold. Table 6.4 shows that, once again, the normal ordering is not rejected for either true mass ordering at the 90% threshold. We can also see that for the 68% threshold the ratio $\alpha/(1-\beta)$ is $\sim 36\%$, and at the 90% threshold it is $\sim 11\%$,

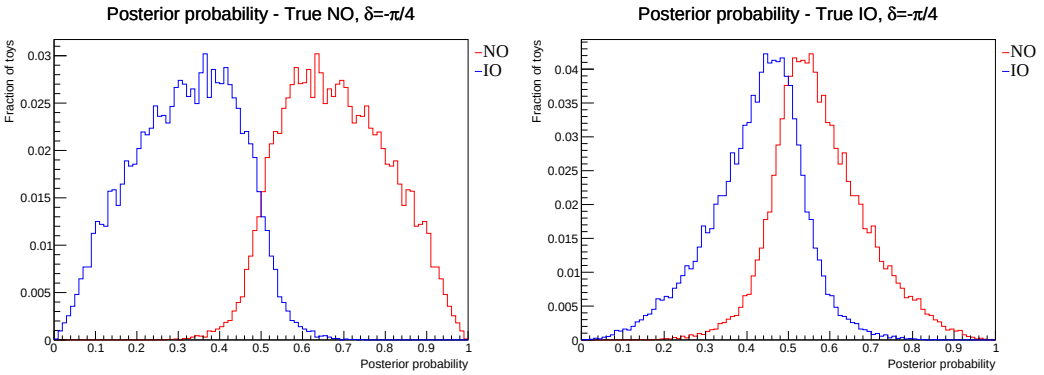

(a) True normal ordering

(b) True inverted ordering

Figure 6.4: Posterior probability distributions of the two mass orderings given $\delta = -\pi/4$ and the true mass ordering.

Threshold	True ordering	Reject false ordering	Reject true ordering
68%	Normal	0.48830	0.00040
	Inverted	0.00789	0.17362
90%	Normal	0.04685	0.00000
	Inverted	0.00000	0.00492

Table 6.4: The probability to reject the false and true mass orderings at 68% and 90% thresholds for the given true mass ordering.

thus we see a similar behaviour as for $\delta_{true} = -3\pi/4$ for the 68% threshold, though at 90% the ratio is quite close to the expected value.

Posterior probability distributions for $\delta_{true} = 0$

In fig. 6.5 the posterior probability distributions for the mass ordering are shown with $\delta_{true} = 0$ in the case of each true mass ordering, while table 6.5 shows the probability of rejecting each mass ordering for a given true mass ordering at a given threshold. For $\delta_{true} = 0$ we see a shift in the behaviour of the posterior probability

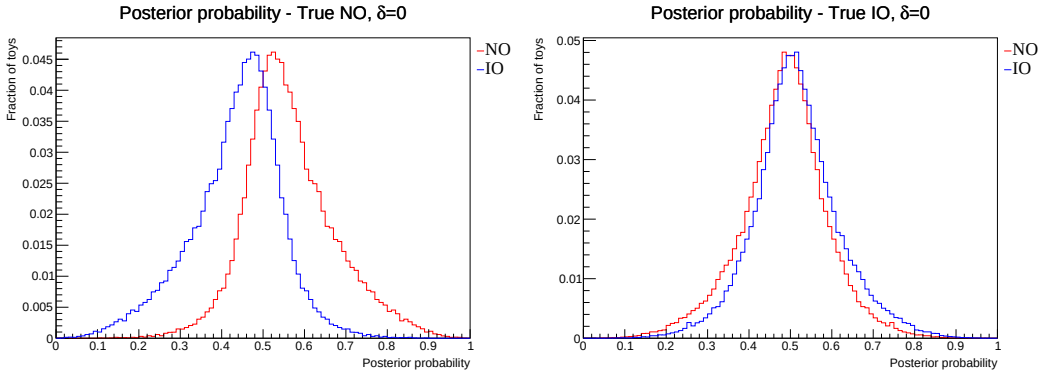

(a) True normal ordering (b) True inverted ordering

Figure 6.5: Posterior probability distributions of the two mass orderings given $\delta = 0$ and the true mass ordering.

Threshold	True ordering	Reject false ordering	Reject true ordering
68%	Normal	0.14665	0.01042
	Inverted	0.06377	0.03139
90%	Normal	0.00360	0.00000
	Inverted	0.00060	0.00020

Table 6.5: The probability to reject the false and true mass orderings at 68% and 90% thresholds for the given true mass ordering.

distributions, in line with that observed for $\delta_{true} = \pm\pi$. In particular, we observe that the true mass ordering is generally preferred (even if rather weakly) for both true mass orderings, rather than finding a preference for normal ordering even when the true mass ordering is the inverted ordering. Table 6.5 shows that at the 68% threshold the ratio $\alpha/(1-\beta)$ is $\sim 21\%$, and at the 90% threshold it is $\sim 6\%$. As with true $\delta = \pm\pi$, these values are clearly different from the expected values.

Posterior probability distributions for $\delta_{true} = +\pi/4$

In fig. 6.6 the posterior probability distributions for the mass ordering are shown with true $\delta_{true} = +\pi/4$ in the case of each true mass ordering, while table 6.6 shows

the probability of rejecting each mass ordering for a given true mass ordering at a given threshold. For $\delta_{true} = +\pi/4$ we again begin to see the preference for a

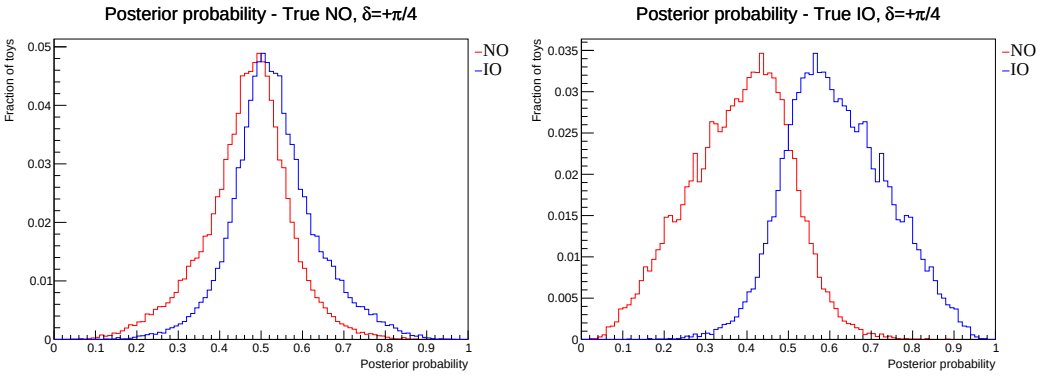

(a) True normal ordering

(b) True inverted ordering

Figure 6.6: Posterior probability distributions of the two mass orderings given $\delta = +\pi/4$ and the true mass ordering.

Threshold	True ordering	Reject false ordering	Reject true ordering
68%	Normal	0.01942	0.08623
	Inverted	0.30929	0.00455
90%	Normal	0.00013	0.00063
	Inverted	0.01000	0.00000

Table 6.6: The probability to reject the false and true mass orderings at 68% and 90% thresholds for the given true mass ordering.

single mass ordering, irrespective of the true mass ordering. However, for $\delta_{true} > 0$, the preferred mass ordering is the inverted ordering. The behaviour has the same origin as for the case of $\delta_{true} < 0$, but now we are in the upper-left region of the bi-event plot (fig. 5.14), where variations in δ assuming the inverted ordering cover a larger fraction of the statistical fluctuations in the normal ordering toys than do the variations in δ assuming normal ordering. Table 6.6 shows that at the 68% threshold the ratio $\alpha/(1-\beta)$ is $\sim 28\%$, while at the 90% threshold it is $\sim 6\%$, both much less than the expected value.

Posterior probability distributions for $\delta_{true} = +\pi/2$

In fig. 6.7 the posterior probability distributions for the mass ordering are shown with $\delta_{true} = +\pi/2$ in the case of each true mass ordering, while table 6.7 shows the probability of rejecting each mass ordering for a given true mass ordering at a given threshold. In table 6.7 we can see that at the 90% threshold, inverted

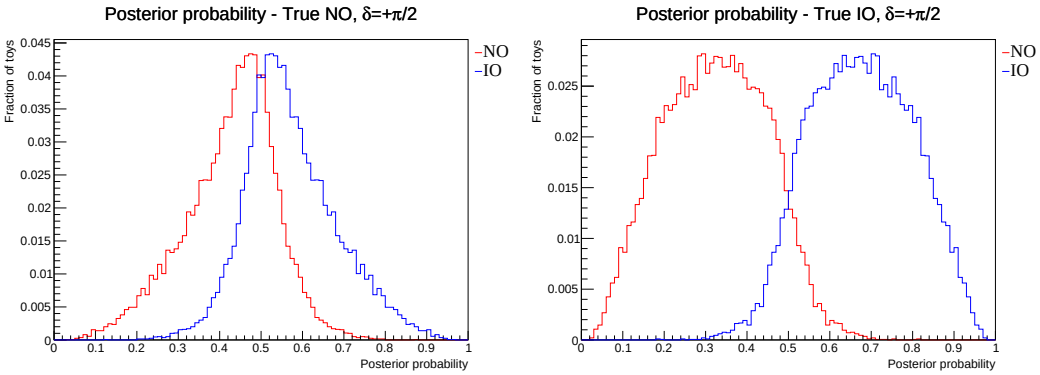

(a) True normal ordering (b) True inverted ordering

Figure 6.7: Posterior probability distributions of the two mass orderings given $\delta = +\pi/2$ and the true mass ordering.

Threshold	True ordering	Reject false ordering	Reject true ordering
68%	Normal	0.00775	0.16785
	Inverted	0.48732	0.00106
90%	Normal	0.00000	0.00360
	Inverted	0.03051	0.00000

Table 6.7: The probability to reject the false and true mass orderings at 68% and 90% thresholds for the given true mass ordering.

ordering is not rejected by any of the toys, irrespective of the true mass ordering, as we again observe lower posterior probabilities for the normal ordering hypothesis even for true normal ordering. At the 68% threshold the ratio $\alpha/(1-\beta)$ is $\sim 34\%$, while at 90% this ratio becomes $\sim 12\%$, and therefore we see a deficit relative to the expected value at 68%, while at 90% the behaviour is inline with expectation.

Posterior probability distributions for $\delta_{true} = +3\pi/4$

In fig. 6.8 the posterior probability distributions for the mass ordering are shown with $\delta_{true} = +3\pi/4$ in the case of each true mass ordering, while table 6.8 shows the probability of rejecting each mass ordering for a given true mass ordering at a given threshold. Finally, we can see that at the 90% threshold, inverted ordering is not rejected by any of the toys, irrespective of the true mass ordering. From table 6.8 we observe ratios $\alpha/(1-\beta)$ at the 68% threshold of $\sim 26\%$ and at the 90% threshold of $\sim 5\%$, again, rather less than expected.

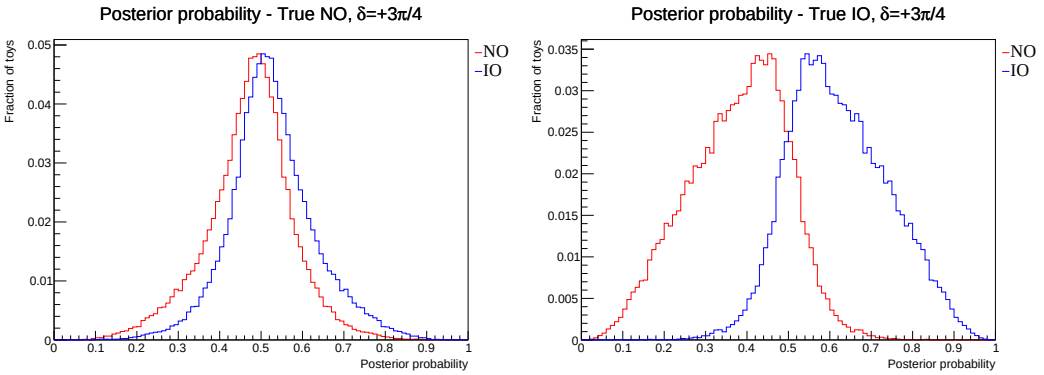

(a) True normal ordering

(b) True inverted ordering

Figure 6.8: Posterior probability distributions of the two mass orderings given $\delta = +3\pi/4$ and the true mass ordering.

Threshold	True ordering	Reject false ordering	Reject true ordering
68%	Normal	0.02328	0.08138
	Inverted	0.31132	0.00334
90%	Normal	0.00008	0.00048
	Inverted	0.00968	0.00005

Table 6.8: The probability to reject the false and true mass orderings at 68% and 90% thresholds for the given true mass ordering.

Summary

Considering the posterior probability distributions from the toy studies it is clear that T2K's power to distinguish the mass ordering is limited; indeed power exceeds 0.5 in only two cases at the 68% threshold, peaking at 0.65, while power peaks at $\sim$ 0.1 at the 90% threshold. However, it is noteworthy that power is dependent upon the particular true value of δ. There is almost no power to distinguish the mass orderings in the event that δ_{true} conserves CP even for a low threshold of 68%. The power increases as the CP violating values are approached, peaking for $\delta = -\pi/2$ in true normal ordering, which is close to the best-fit found in section 5.8. True inverted ordering generally results in lower power, driven by a reduction in the expected ν_e event rate relative to true normal ordering.

The type-I error rate depends upon the true mass ordering and the sign of δ_{true} (see fig. 6.9). In particular, for true normal ordering and $\delta_{true} < 0$ the type-I error rate is very low, but transitioning to $\delta_{true} > 0$ sees the type-I error rapidly increase, peaking for $\delta_{true} = +\pi/2$ because the wrong mass ordering is preferred due to greater coverage of the statistical fluctuations in inverted ordering in this region

of δ_{true}. For true inverted ordering the picture is reversed, with low type-I errors for $\delta_{true} > 0$ and very high type-I error rates for $\delta_{true} < 0$. The corresponding type-II

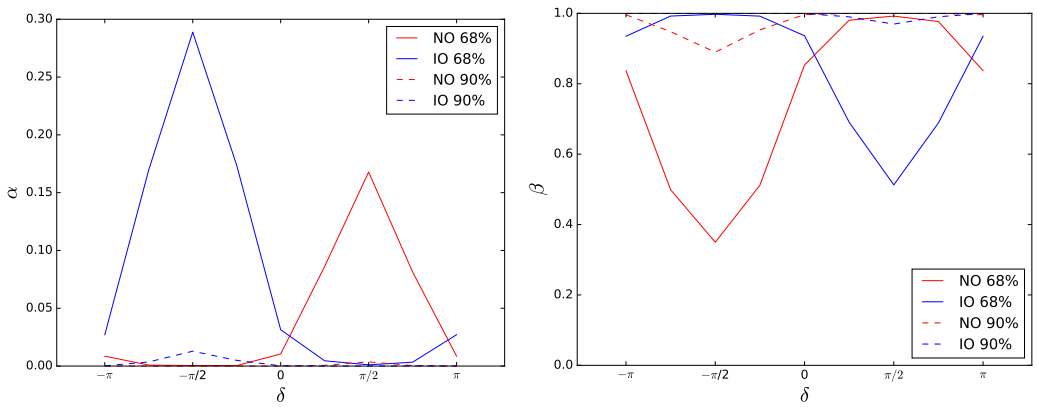

(a) Type-I error

(b) Type-II error

Figure 6.9: The type-I and type-II error rates for each true mass ordering at the 68% and 90% posterior probability thresholds.

error rate (fig. 6.9) is also dependent upon the true mass ordering and sign of δ_{true}. For true normal ordering and $\delta_{true} > 0$ the type-II error rate is very high, such that one cannot expect to reject the inverted ordering for positive values of δ_{true}, but transitioning to $\delta_{true} < 0$ sees the type-II error rate fall to a minimum (though still rather high) value at $\delta_{true} = -\pi/2$. For true inverted ordering the picture is again reversed, with high type-II error rates for $\delta_{true} < 0$ and falling type-II error rates for $\delta_{true} > 0$, reaching a minimum at $\delta_{true} = +\pi/2$.

A key feature of the posterior probability distributions is the extent to which they fail to correspond to the interpretation of the posterior probability. That is, the ratio $\alpha/(1-\beta)$ is largely not the value that one would expect (see fig. 6.10). In fact, the ratio only approaches its expected value for the case of $\delta_{true} = -\pi/2$. At all other values there is some deviation, which peaks at the CP conserving values. This result calls into question the reliability of the posterior probability away from the maximally CP violating region of δ_{true}. It is plausible that this effect is driven by the features of the mass ordering degeneracy observable in the bi-event plot (fig. 5.14). As described in section 5.8.3, degeneracy in the event rates for different values of δ and the mass ordering leads to a lowering of the χ^2 values for the incorrect mass ordering. The region around $\delta_{true} = -\pi/2$ and true normal ordering, for example, has relatively low compatibility with the inverted ordering because statistical fluctuations in the event rates need to be quite large to move to a region compatible with inverted ordering. However, as we move towards $\delta_{true} = 0$ the predicted event rates

start to become compatible with those for the inverted mass ordering and as a result the likelihood for inverted ordering increases, the posterior probability for normal ordering decreases and the type-II error rate increases. However, if we consider the same scenario for true inverted mass ordering we start in a region where upward (downward) statistical fluctuations in the ν_e ($\bar{\nu}_e$) event rate are highly compatible with the wrong mass ordering, increasing the likelihood and posterior probability for normal ordering and thereby increasing the type-I error rate. As we move towards $\delta_{true} = 0$ in this case, upward statistical fluctuations permit fits of both mass orderings, reducing the type-I error rate relative to its high starting point. The net effect of this is a gradual increase in type-II error rate for the true normal ordering along with a more rapid decrease in the type-I error rate in true inverted ordering as δ_{true} moves away from the maximally CP violating values, leading to lower values of the ratio $\alpha/(1-\beta)$.

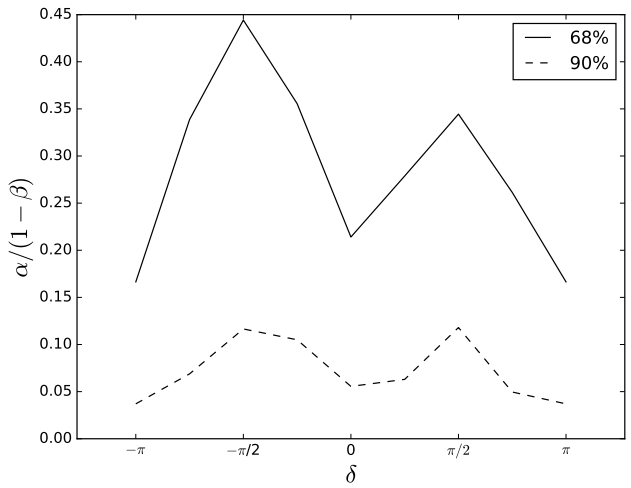

Figure 6.10: The rate at which the true mass ordering is rejected relative to the rate at which the false mass ordering is rejected ($\alpha/(1-\beta)$) at the 68% and 90% posterior probability thresholds.

6.2.3 Result

T2K's best-fit finds $\delta = -1.885$ and normal ordering, which is in the region for which T2K's power to distinguish the mass ordering is greatest and the posterior probability distribution from toy studies behaves in the way expected. As a result, Feldman-Cousins toys were generated for this best-fit and the posterior probability distribution calculated. The result can be seen in fig. 6.11. The posterior probability for the normal mass ordering is found to be 87.7% from data. Such a result should

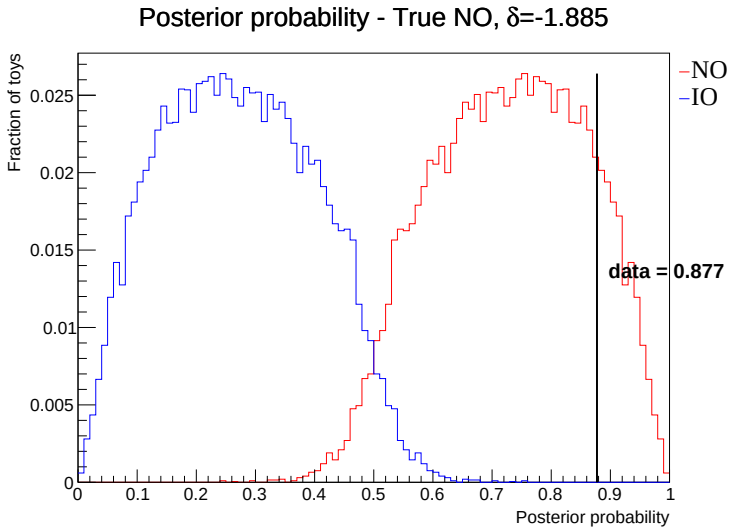

Figure 6.11: Posterior probability distributions of the two mass orderings given true $\delta = -1.885$ and true normal ordering.

not be considered particularly surprising given the findings from the toy studies in the previous section, with 14% of the toys finding a posterior probability more extreme than this value.

6.3 Mass ordering $\Delta\chi^2$

An alternative approach to the determination of the mass ordering is to consider the $\Delta\chi^2$ statistic directly. Rather than computing a posterior probability for the mass ordering we instead look at the distribution of $\Delta\chi^2$ values for given true values of the mass ordering and δ for a $\Delta\chi^2$ definition

$$\Delta\chi^2 = \chi^2_{NO} - \chi^2_{IO} \tag{6.2}$$

where χ^2_{NO} is the χ^2 value computed for a given simulated data set assuming normal mass ordering and χ^2_{IO} is the χ^2 value computed for the same simulated data set assuming inverted mass ordering. This allows the assessment of T2K's ability to distinguish the two mass orderings for the current exposure. The $\Delta\chi^2$ definition above is naturally two-sided, with the 68.27% and 90% intervals to be considered in this analysis.

6.3.1 Method

The approach taken again makes use of the Feldman-Cousins simulated data sets generated to determine critical $\Delta\chi^2$ values for the CP phase measurement (section 5.6). As was the case for posterior probability, it is necessary to eliminate δ to achieve a χ^2 value only in terms of the mass ordering. This follows the same procedure as described in section 6.2.1, with the additional step to move from the average likelihood, L, to the corresponding χ^2; $\chi^2 = -2\log(L)$. To summarise:

1. For each true mass ordering, at least 2×10^4 simulated data sets are produced for a true value of δ taking into account both statistical and systematic uncertainties

2. For each simulated data set:

   (a) χ^2 values are obtained for 101 bins of δ by fitting with respect to the marginalisation toys produced for the CP phase measurement in both mass orderings.

   (b) The χ^2 values are converted to likelihood values via $L = e^{-\chi^2/2}$.

   (c) The likelihood values are averaged over the bins of δ in each fitted mass ordering to produce likelihood values L_{NO} and L_{IO} only in terms of the fitted mass ordering.

   (d) Each average likelihood is then converted to a χ^2 value as $\chi^2 = -2\log(L)$.

   (e) The mass ordering statistic is then calculated as:

$$\Delta\chi^2 = \chi^2_{NO} - \chi^2_{IO}$$

3. This results in a distribution of $\Delta\chi^2$ values for each true mass ordering.

Having obtained distributions of $\Delta\chi^2$ in each true mass ordering for a given true value of δ, T2K's power to reject a given mass ordering for different true values of δ and mass ordering can be determined and can also act as a goodness of fit for the different δ-mass ordering hypotheses.

6.3.2 Mass ordering sensitivity and goodness of fit

Figure 6.12 shows the $\Delta\chi^2$ distributions for the case of $\delta_{true} = 0$. In this plot, the red lines demarcate the two-sided 90% $\Delta\chi^2$ interval for true normal ordering, while the blue lines cover the corresponding interval for the true inverted ordering. It is these intervals (and the equivalent 1σ intervals) that are shown on the following plots,

which present these intervals for all true values of δ in both true mass orderings simultaneously. T2K's sensitivity is neatly illustrated in fig. 6.13. It can be seen

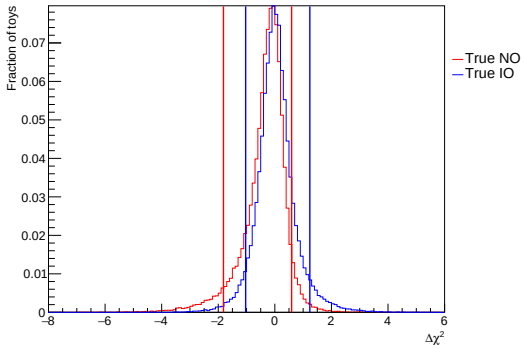

Figure 6.12: $\Delta\chi^2$ distributions for each true mass ordering given $\delta_{true} = 0$.

that T2K has greatest sensitivity near the maximally CP violating values of δ, in particular the greatest potential to reject inverted ordering is seen for $\delta_{true} = -\pi/2$, while the greatest potential to reject normal ordering is seen for $\delta_{true} = +\pi/2$. There is little scope to reject the normal ordering for $\delta_{true} \in (-\pi, 0)$ and correspondingly little scope to reject inverted ordering for $\delta_{true} \in (0, +\pi)$.

In addition to determining the sensitivity to the different mass ordering hypotheses, the Feldman-Cousins toys can be used to check the level of agreement between the model and the data. Comparing the $\Delta\chi^2$ value for the data to the $\Delta\chi^2$ distribution from the toys provides a Goodness of Fit test. Figure 6.13 presents the two-sided intervals from the Feldman-Cousins toys at 1σ and 90% confidence levels.

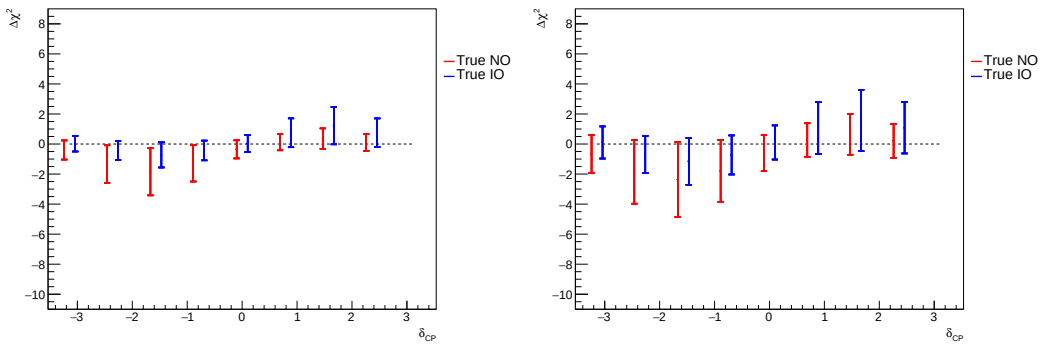

(a) 1σ interval

(b) 90% interval

Figure 6.13: Two-sided $\Delta\chi^2$ distributions for each true mass ordering at all true values of δ. Normal and inverted ordering intervals are separated to aid readability.

6.3.3 Result

Figure 6.14 overlays the data $\Delta\chi^2$ value (-3.51) on the distributions from the previous section. From this it can be seen that the inverted mass ordering is rejected at the 90% confidence level for all true values of δ, consistent with NOvA's latest reported result [153] rejecting the inverted mass ordering at the 1.8σ level. Furthermore, fig. 6.14 demonstrates that the model describes the data quite well for $\delta_{true} = -\pi/2$ and true normal ordering, with the data point falling narrowly outside of the range covered by 68% of the simulated data sets.

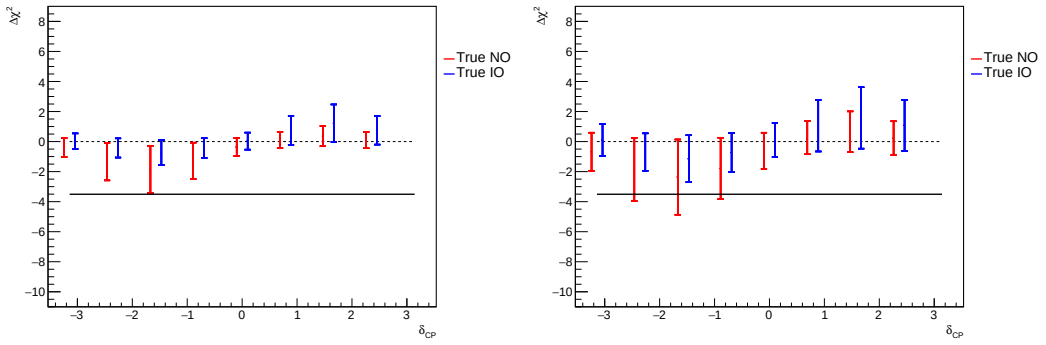

(a) 1σ interval (b) 90% interval

Figure 6.14: Two-sided $\Delta\chi^2$ distributions for each true mass ordering at all true values of δ. The $\Delta\chi^2$ value for the data is overlaid. The normal ordering and inverted ordering intervals have been separated to aid readability.

Summary

Considering the $\Delta\chi^2$ distributions from the toy studies we again confirm that T2K's sensitivity to the mass ordering is rather limited, with substantial overlap in the $\Delta\chi^2$ distributions of the two mass orderings for all true values of δ. The behaviour of the distributions is consistent with that exhibited by the posterior probability distributions, with almost no power to reject the inverted mass ordering for positive values of δ and correspondingly little power to reject normal mass ordering for negative values of δ. The data prefer the normal mass ordering with $\Delta\chi^2 = -3.51$ and reject the inverted mass ordering at the 90% confidence level for all values of δ. Furthermore, the data are in agreement with the toys for $\delta_{true} = -\pi/2$ and true normal ordering at approximately the 1σ confidence level.

Chapter 7

Conclusion

This thesis presented two analyses of beam data gathered by the T2K experiment. Each analysis fits the same five SK samples, using an exposure of 1.4938×10^{21} POT in neutrino-mode running and 1.6346×10^{21} POT in antineutrino-mode running.

The expected event rate from the best-fit is shown in table 7.1 along with T2K's observation. From these data, using the constant-$\Delta\chi^2$ method without

Sample	Asimov BF	Observed
FHC ν_μ	276.7	243
FHC ν_e	73.7	75
RHC ν_μ	141.9	140
RHC ν_e	17.2	15
FHC ν_e CC1π^+	6.9	15

Table 7.1: The observed and expected best-fit number of events in Run 1-9 data set for an FHC exposure of 1.4938×10^{21} POT and an RHC exposure of 1.6346×10^{21}.

the constraint on $\sin^2(\theta_{13})$ from reactor experiments, δ is measured to be -2.136 ($[-2.827, -1.234]$), in normal mass ordering. With the Feldman-Cousins method and applying the constraint from reactor experiments δ is measured to be -1.885 ($[-2.509, -1.260]$), in normal mass ordering and CP conservation is rejected at 2σ, a world-leading measurement.

The second analysis used similar techniques to measure the mass ordering. The posterior probability for the normal mass ordering is found to be 87.7%. Measuring the difference in χ^2 values between the two mass orderings, $\Delta\chi^2$ is found to be -3.51, rejecting the inverted mass ordering at the 90% confidence level. Neither result represents strong evidence against the inverted mass ordering.

T2K will continue to collect data toward a final goal of 7.8×10^{21} POT, with the methods and software developed for this analysis used to further constrain δ and

the mass ordering. The next generation of neutrino experiments, including DUNE and T2K's planned successor T2HK, are currently in development and will provide an order of magnitude more data to help resolve these open questions.

Appendices

Appendix A

Flux and cross-section systematic parameters

Tables A.1 to A.3 present the central values and corresponding pre- and post-fit errors for parameters in the BANFF fit. Note that the cross-section parameters listed below include parameters for the axial and vector second class currents, which are fixed at 1 for the analyses in this thesis. As such, they have no effect on the analyses and are not included in the covariance matrix in fig. 4.18.

Index	Parameter	Description	Best fit	1σ pre/postfit fractional error
0	$f^{banff}_{0;t,r}$	FHC ν_μ flux normalisation, E = 0.0 - 0.4 GeV	0.998	0.106 / 0.059
1	$f^{banff}_{1;t,r}$	FHC ν_μ flux normalisation, E = 0.4 - 0.5 GeV	1.019	0.105 / 0.054
2	$f^{banff}_{2;t,r}$	FHC ν_μ flux normalisation, E = 0.5 - 0.6 GeV	1.002	0.096 / 0.047
3	$f^{banff}_{3;t,r}$	FHC ν_μ flux normalisation, E = 0.6 - 0.7 GeV	0.962	0.088 / 0.044
4	$f^{banff}_{4;t,r}$	FHC ν_μ flux normalisation, E = 0.7 - 1.0 GeV	0.913	0.105 / 0.056
5	$f^{banff}_{5;t,r}$	FHC ν_μ flux normalisation, E = 1.0 - 1.5 GeV	0.937	0.088 / 0.051
6	$f^{banff}_{6;t,r}$	FHC ν_μ flux normalisation, E = 1.5 - 2.5 GeV	1.012	0.072 / 0.044
7	$f^{banff}_{7;t,r}$	FHC ν_μ flux normalisation, E = 2.5 - 3.5 GeV	1.025	0.077 / 0.046
8	$f^{banff}_{8;t,r}$	FHC ν_μ flux normalisation, E = 3.5 - 5.0 GeV	1.011	0.089 / 0.044
9	$f^{banff}_{9;t,r}$	FHC ν_μ flux normalisation, E = 5.0 - 7.0 GeV	0.967	0.099 / 0.044
10	$f^{banff}_{10;t,r}$	FHC ν_μ flux normalisation, E = 7.0 - 30.0 GeV	0.947	0.116 / 0.054
11	$f^{banff}_{11;t,r}$	FHC $\bar{\nu_\mu}$ flux normalisation, E = 0.0 - 0.7 GeV	0.970	0.108 / 0.076
12	$f^{banff}_{12;t,r}$	FHC $\bar{\nu_\mu}$ flux normalisation, E = 0.7 - 1.0 GeV	0.961	0.083 / 0.050
13	$f^{banff}_{13;t,r}$	FHC $\bar{\nu_\mu}$ flux normalisation, E = 1.0 - 1.5 GeV	0.977	0.085 / 0.058
14	$f^{banff}_{14;t,r}$	FHC $\bar{\nu_\mu}$ flux normalisation, E = 1.5 - 2.5 GeV	1.033	0.086 / 0.064
15	$f^{banff}_{15;t,r}$	FHC $\bar{\nu_\mu}$ flux normalisation, E = 2.5 - 30.0 GeV	1.099	0.087 / 0.066
16	$f^{banff}_{16;t,r}$	FHC ν_e flux normalisation, E = 0.0 - 0.5 GeV	1.002	0.095 / 0.049
17	$f^{banff}_{17;t,r}$	FHC ν_e flux normalisation, E = 0.5 - 0.7 GeV	1.004	0.091 / 0.045
18	$f^{banff}_{18;t,r}$	FHC ν_e flux normalisation, E = 0.7 - 0.8 GeV	1.002	0.087 / 0.044
19	$f^{banff}_{19;t,r}$	FHC ν_e flux normalisation, E = 0.8 - 1.5 GeV	0.993	0.081 / 0.042
20	$f^{banff}_{20;t,r}$	FHC ν_e flux normalisation, E = 1.5 - 2.5 GeV	1.010	0.080 / 0.043
21	$f^{banff}_{21;t,r}$	FHC ν_e flux normalisation, E = 2.5 - 4.0 GeV	1.009	0.086 / 0.045
22	$f^{banff}_{22;t,r}$	FHC ν_e flux normalisation, E = 4.0 - 30.0 GeV	1.023	0.096 / 0.061
23	$f^{banff}_{23;t,r}$	FHC $\bar{\nu_e}$ flux normalisation, E = 0.0 - 2.5 GeV	1.037	0.077 / 0.056
24	$f^{banff}_{24;t,r}$	FHC $\bar{\nu_e}$ flux normalisation, E = 2.5 - 30.0 GeV	1.088	0.131 / 0.116

Table A.1: Summary of neutrino mode flux systematics.

Index	Parameter	Description	Best fit	1σ pre/postfit fractional error
25	$f^{banff}_{0;t,r}RHC$	RHC ν_μ flux normalisation, E = 0.0 - 0.7 GeV	0.972	0.100 / 0.069
26	$f^{banff}_{1;t,r}RHC$	RHC ν_μ flux normalisation, E = 0.7 - 1.0 GeV	0.982	0.083 / 0.054
27	$f^{banff}_{2;t,r}RHC$	RHC ν_μ flux normalisation, E = 1.0 - 1.5 GeV	0.997	0.080 / 0.050
28	$f^{banff}_{3;t,r}RHC$	RHC ν_μ flux normalisation, E = 1.5 - 2.5 GeV	1.047	0.082 / 0.053
29	$f^{banff}_{4;t,r}RHC$	RHC ν_μ flux normalisation, E = 2.5 - 30.0 GeV	1.038	0.082 / 0.049
30	$f^{banff}_{5;t,r}RHC$	RHC $\bar{\nu_\mu}$ flux normalisation, E = 0.0 - 0.4 GeV	0.984	0.112 / 0.067
31	$f^{banff}_{6;t,r}RHC$	RHC $\bar{\nu_\mu}$ flux normalisation, E = 0.4 - 0.5 GeV	0.999	0.105 / 0.055
32	$f^{banff}_{7;t,r}RHC$	RHC $\bar{\nu_\mu}$ flux normalisation, E = 0.5 - 0.6 GeV	0.980	0.097 / 0.048
33	$f^{banff}_{8;t,r}RHC$	RHC $\bar{\nu_\mu}$ flux normalisation, E = 0.6 - 0.7 GeV	0.960	0.087 / 0.044
34	$f^{banff}_{9;t,r}RHC$	RHC $\bar{\nu_\mu}$ flux normalisation, E = 0.7 - 1.0 GeV	0.956	0.108 / 0.066
35	$f^{banff}_{10;t,r}RHC$	RHC $\bar{\nu_\mu}$ flux normalisation, E = 1.0 - 1.5 GeV	0.973	0.092 / 0.056
36	$f^{banff}_{11;t,r}RHC$	RHC $\bar{\nu_\mu}$ flux normalisation, E = 1.5 - 2.5 GeV	1.022	0.073 / 0.046
37	$f^{banff}_{12;t,r}RHC$	RHC $\bar{\nu_\mu}$ flux normalisation, E = 2.5 - 3.5 GeV	1.052	0.076 / 0.052
38	$f^{banff}_{13;t,r}RHC$	RHC $\bar{\nu_\mu}$ flux normalisation, E = 3.5 - 5.0 GeV	1.056	0.094 / 0.066
39	$f^{banff}_{14;t,r}RHC$	RHC $\bar{\nu_\mu}$ flux normalisation, E = 5.0 - 7.0 GeV	1.029	0.088 / 0.060
40	$f^{banff}_{15;t,r}RHC$	RHC $\bar{\nu_\mu}$ flux normalisation, E = 7.0 - 30.0 GeV	0.985	0.117 / 0.094
41	$f^{banff}_{16;t,r}RHC$	RHC ν_e flux normalisation, E = 0.0 - 2.5 GeV	1.036	0.072 / 0.050
42	$f^{banff}_{17;t,r}RHC$	RHC ν_e flux normalisation, E = 2.5 - 30.0 GeV	1.032	0.087 / 0.068
43	$f^{banff}_{18;t,r}RHC$	RHC $\bar{\nu_e}$ flux normalisation, E = 0.0 - 0.5 GeV	0.991	0.100 / 0.054
44	$f^{banff}_{19;t,r}RHC$	RHC $\bar{\nu_e}$ flux normalisation, E = 0.5 - 0.7 GeV	0.990	0.093 / 0.046
45	$f^{banff}_{20;t,r}RHC$	RHC $\bar{\nu_e}$ flux normalisation, E = 0.7 - 0.8 GeV	0.987	0.093 / 0.054
46	$f^{banff}_{21;t,r}RHC$	RHC $\bar{\nu_e}$ flux normalisation, E = 0.8 - 1.5 GeV	0.993	0.083 / 0.044
47	$f^{banff}_{22;t,r}RHC$	RHC $\bar{\nu_e}$ flux normalisation, E = 1.5 - 2.5 GeV	1.025	0.079 / 0.054
48	$f^{banff}_{23;t,r}RHC$	RHC $\bar{\nu_e}$ flux normalisation, E = 2.5 - 4.0 GeV	1.030	0.090 / 0.066
49	$f^{banff}_{24;t,r}RHC$	RHC $\bar{\nu_e}$ flux normalisation, E = 4.0 - 30.0 GeV	1.081	0.154 / 0.134

Table A.2: Summary of antineutrino mode flux systematics.

Index	Parameter	Description	Best fit	1σ pre/postfit fractional error
50	$f^{banff}_{Norm_{2p2h}}$	Two particle two hole normalisation for ^{16}O	1.477	1.000 / 0.196
51	$f^{banff}_{C_5^A}$	C_5^A nucleon to Δ transition axial form factor	0.964	0.149 / 0.063
52	$f^{banff}_{Bg_{RES}}$	Scale of isospin 1/2 nonresonant background	1.017	0.308 / 0.194
53	$f^{banff}_{M_A^{QE}}$	CCQE axial-mass scaling factor	0.940	0.025 / 0.066
54	$f^{banff}_{M_A^{RES}}$	Resonance-production axial-mass scaling factor	0.846	0.158 / 0.047
55	f^{banff}_{SCCA}	BANFF; Second current class axial	1.000	1.000 / 1.000
56	f^{banff}_{SCCV}	BANFF; Second current class vector	1.000	1.000 / 1.000
57	$f^{banff}_{p_f}$	Fermi momentum for ^{16}O	0.911	0.058 / 0.067
58	$f^{banff}_{Shape_{CCoth}}$	CC other shape	0.351	0.400 / 0.199
59	$f^{banff}_{Norm_{CCcoh}}$	CC coherent for ^{16}O normalisation	0.866	0.300 / 0.282
60	$f^{banff}_{Norm_{NCcoh}}$	NC coherent normalisation	0.937	0.300 / 0.297
61	$f^{banff}_{Norm_{NCother}}$	NC other normalisation	1.000	0.300 / 0.300
62	$f^{banff}_{Norm_{\nu_e\to\nu_\mu}}$	CC ν_e normalisation	1.000	0.028 / 0.028
63	$f^{banff}_{Norm_{NC1\gamma}}$	NC 1γ normalisation	1.000	1.000 / 1.000
64	$f^{banff}_{Norm_{\bar{\nu}_e\to\bar{\nu}_\mu}}$	CC $\bar{\nu}_e$ normalisation	1.000	0.028 / 0.028
65	$f^{banff}_{Norm_{2p2hBar}}$	Antineutrino two particle two hole normalisation for ^{16}O	0.731	1.000 / 0.231
66	$f^{banff}_{Shape_{BeRPA_A}}$	Bernstein Polynomial coefficient A	0.684	0.118 / 0.057
67	$f^{banff}_{Shape_{BeRPA_B}}$	Bernstein Polynomial coefficient B	1.599	0.210 / 0.118
68	$f^{banff}_{Shape_{BeRPA_D}}$	Bernstein Polynomial coefficient D	0.961	0.170 / 0.135
69	$f^{banff}_{Shape_{BeRPA_E}}$	Bernstein Polynomial coefficient E	0.875	0.352 / 0.353
70	$f^{banff}_{Shape_{BeRPA_U}}$	Bernstein Polynomial coefficient U	1.200	0.100 / 0.100
71	$f^{banff}_{Shape_{2p2h\nu}}$	Neutrino two particle two hole ^{16}O shape	0.987	3.000 / 0.362
72	$f^{banff}_{Norm_{2p2hCtoO}}$	Two particle two hole ^{12}C to ^{16}O normalisation	0.963	0.200 / 0.167
73	$f^{banff}_{Shape_{Eb}}$	Binding energy shape	0.000	2.000 / 2.000

Table A.3: Summary of cross section systematics. Parameters with no prefit error were unconstrained.

Appendix B

Detector, FSI, SI and PN systematic parameters

Table B.1 present the errors for the SK detector, final state and secondary interactions and photo nuclear parameters.

Index	Parameter	Description	1σ fractional error
0	$f^{SK+FSI}_{0;t,r}$	SKDet + FSI/SI 0; Ereco range 0.00 - 0.40 GeV; numu/numubar CCQE (1Rmu)	0.008
1	$f^{SK+FSI}_{1;t,r}$	SKDet + FSI/SI 1; Ereco range 0.40 - 1.10 GeV; numu/numubar CCQE (1Rmu)	0.013
2	$f^{SK+FSI}_{2;t,r}$	SKDet + FSI/SI 2; Ereco range 1.10 - 30.00 GeV; numu/numubar CCQE (1Rmu)	0.015
3	$f^{SK+FSI}_{3;t,r}$	SKDet + FSI/SI 3; Ereco range 0.00 - 30.00 GeV; numu/numubar CCnQE (1Rmu)	0.176
4	$f^{SK+FSI}_{4;t,r}$	SKDet + FSI/SI 4; Ereco range 0.00 - 30.00 GeV; nue/nuebar/signue CC (1Rmu)	1.006
5	$f^{SK+FSI}_{5;t,r}$	SKDet + FSI/SI 5; Ereco range 0.00 - 30.00 GeV; all NC (1Rmu)	0.660
6	$f^{SK+FSI}_{6;t,r}$	SKDet + FSI/SI 6; Ereco range 0.00 - 0.35 GeV; oscillated nue CC (1Re)	0.124
7	$f^{SK+FSI}_{7;t,r}$	SKDet + FSI/SI 7; Ereco range 0.35 - 0.80 GeV; oscillated nue CC (1Re)	0.032
8	$f^{SK+FSI}_{8;t,r}$	SKDet + FSI/SI 8; Ereco range 0.80 - 1.25 GeV; oscillated nue CC (1Re)	0.041
9	$f^{SK+FSI}_{9;t,r}$	SKDet + FSI/SI 9; Ereco range 0.00 - 0.35 GeV; numu/numubar CC (1Re)	0.271
10	$f^{SK+FSI}_{10;t,r}$	SKDet + FSI/SI 10; Ereco range 0.35 - 0.80 GeV; numu/numubar CC (1Re)	0.320
11	$f^{SK+FSI}_{11;t,r}$	SKDet + FSI/SI 11; Ereco range 0.80 - 1.25 GeV; numu/numubar CC (1Re)	0.393
12	$f^{SK+FSI}_{12;t,r}$	SKDet + FSI/SI 12; Ereco range 0.00 - 0.35 GeV; nue/nuebar CC (1Re)	0.089
13	$f^{SK+FSI}_{13;t,r}$	SKDet + FSI/SI 13; Ereco range 0.35 - 0.80 GeV; nue/nuebar CC (1Re)	0.050
14	$f^{SK+FSI}_{14;t,r}$	SKDet + FSI/SI 14; Ereco range 0.80 - 1.25 GeV; nue/nuebar CC (1Re)	0.063
15	$f^{SK+FSI}_{15;t,r}$	SKDet + FSI/SI 15; Ereco range 0.00 - 0.35 GeV; all NC (1Re)	0.307
16	$f^{SK+FSI}_{16;t,r}$	SKDet + FSI/SI 16; Ereco range 0.35 - 0.80 GeV; all NC (1Re)	0.195
17	$f^{SK+FSI}_{17;t,r}$	SKDet + FSI/SI 17; Ereco range 0.80 - 1.25 GeV; all NC (1Re)	0.473
18	$f^{SK+FSI}_{0;t,r}RHC$	SKDet + FSI/SI 0; Ereco range 0.00 - 0.40 GeV; numu/numubar CCQE (1Rmu); RHC	0.008
19	$f^{SK+FSI}_{1;t,r}RHC$	SKDet + FSI/SI 1; Ereco range 0.40 - 1.10 GeV; numu/numubar CCQE (1Rmu); RHC	0.009
20	$f^{SK+FSI}_{2;t,r}RHC$	SKDet + FSI/SI 2; Ereco range 1.10 - 30.00 GeV; numu/numubar CCQE (1Rmu); RHC	0.010
21	$f^{SK+FSI}_{3;t,r}RHC$	SKDet + FSI/SI 3; Ereco range 0.00 - 30.00 GeV; numu/numubar CCnQE (1Rmu); RHC	0.140
22	$f^{SK+FSI}_{4;t,r}RHC$	SKDet + FSI/SI 4; Ereco range 0.00 - 30.00 GeV; nue/nuebar/signue CC (1Rmu); RHC	1.005
23	$f^{SK+FSI}_{5;t,r}RHC$	SKDet + FSI/SI 5; Ereco range 0.00 - 30.00 GeV; all NC (1Rmu); RHC	0.659
24	$f^{SK+FSI}_{6;t,r}RHC$	SKDet + FSI/SI 6; Ereco range 0.00 - 0.35 GeV; oscillated nue CC (1Re); RHC	0.076
25	$f^{SK+FSI}_{7;t,r}RHC$	SKDet + FSI/SI 7; Ereco range 0.35 - 0.80 GeV; oscillated nue CC (1Re); RHC	0.033
26	$f^{SK+FSI}_{8;t,r}RHC$	SKDet + FSI/SI 8; Ereco range 0.80 - 1.25 GeV; oscillated nue CC (1Re); RHC	0.055
27	$f^{SK+FSI}_{9;t,r}RHC$	SKDet + FSI/SI 9; Ereco range 0.00 - 0.35 GeV; numu/numubar CC (1Re); RHC	0.317
28	$f^{SK+FSI}_{10;t,r}RHC$	SKDet + FSI/SI 10; Ereco range 0.35 - 0.80 GeV; numu/numubar CC (1Re); RHC	0.337
29	$f^{SK+FSI}_{11;t,r}RHC$	SKDet + FSI/SI 11; Ereco range 0.80 - 1.25 GeV; numu/numubar CC (1Re); RHC	0.417
30	$f^{SK+FSI}_{12;t,r}RHC$	SKDet + FSI/SI 12; Ereco range 0.00 - 0.35 GeV; nue/nuebar CC (1Re); RHC	0.060
31	$f^{SK+FSI}_{13;t,r}RHC$	SKDet + FSI/SI 13; Ereco range 0.35 - 0.80 GeV; nue/nuebar CC (1Re); RHC	0.043
32	$f^{SK+FSI}_{14;t,r}RHC$	SKDet + FSI/SI 14; Ereco range 0.80 - 1.25 GeV; nue/nuebar CC (1Re); RHC	0.065
33	$f^{SK+FSI}_{15;t,r}RHC$	SKDet + FSI/SI 15; Ereco range 0.00 - 0.35 GeV; all NC (1Re); RHC	0.329
34	$f^{SK+FSI}_{16;t,r}RHC$	SKDet + FSI/SI 16; Ereco range 0.35 - 0.80 GeV; all NC (1Re); RHC	0.198
35	$f^{SK+FSI}_{17;t,r}RHC$	SKDet + FSI/SI 17; Ereco range 0.80 - 1.25 GeV; all NC (1Re); RHC	0.465
36	$f^{SK+FSI}_{0;t,r}MultiRing$	SKDet + FSI/SI 0; Ereco range 0.30 - 0.80 GeV; oscillated nue CC (MultiRe); MultiRing	0.197
37	$f^{SK+FSI}_{1;t,r}MultiRing$	SKDet + FSI/SI 1; Ereco range 0.80 - 1.25 GeV; oscillated nue CC (MultiRe); MultiRing	0.165
38	$f^{SK+FSI}_{2;t,r}MultiRing$	SKDet + FSI/SI 2; Ereco range 0.30 - 0.80 GeV; numu/numubar CC (MultiRe); MultiRing	0.502
39	$f^{SK+FSI}_{3;t,r}MultiRing$	SKDet + FSI/SI 3; Ereco range 0.80 - 1.25 GeV; numu/numubar CC (MultiRe); MultiRing	0.236
40	$f^{SK+FSI}_{4;t,r}MultiRing$	SKDet + FSI/SI 4; Ereco range 0.30 - 0.80 GeV; nue/nuebar CC (MultiRe); MultiRing	0.192
41	$f^{SK+FSI}_{5;t,r}MultiRing$	SKDet + FSI/SI 5; Ereco range 0.80 - 1.25 GeV; nue/nuebar CC (MultiRe); MultiRing	0.189
42	$f^{SK+FSI}_{6;t,r}MultiRing$	SKDet + FSI/SI 6; Ereco range 0.30 - 0.80 GeV; all NC (MultiRe); MultiRing	0.983
43	$f^{SK+FSI}_{7;t,r}MultiRing$	SKDet + FSI/SI 7; Ereco range 0.80 - 1.25 GeV; all NC (MultiRe); MultiRing	0.523
44	$f^{SK}_{E;r}$	SK energy scale	0.024

Table B.1: Summary of SK detector + FSI + SI + PN systematics included in the VALOR joint fit analysis.

Appendix C

Effect of the BANFF fit

The effect of each category of systematic parameter on the expected event rate for each SK sample is given in tables C.1 to C.5. The mean and RMS of 10 000 throws of the respective systematics, with all correlations taken into account using Cholesky decomposition is computed for each sample, both without and with the near detector constraint applied.

	Pre-BANFF			**Post-BANFF**		
Group	Mean	1σ	%	Mean	1σ	%
SK Detector	-	-	-	273.06	6.56	2.40
SK FSI+SI+PN	-	-	-	272.36	6.01	2.21
Flux+Xsec constrained	259.08	36.84	14.22	270.71	8.86	3.27
$\sigma(\nu_e)/\sigma(\bar{\nu}_e)$	-	-	-	272.40	0.00	0.00
NC1γ	-	-	-	272.40	0.00	0.00
NC Other	-	-	-	272.40	0.69	0.25
E_b	-	-	-	272.31	6.48	2.38
Osc	-	-	-	272.44	0.07	0.03
All	258.96	37.96	14.66	271.33	13.88	5.12
All with osc	258.99	37.97	14.66	271.36	13.89	5.12

Table C.1: Average event rate and RMS error broken down by systematic parameter group for μ-like Super-K events with Run 1-9 POT for neutrino mode.

	Pre-BANFF			**Post-BANFF**		
Group	Mean	1σ	%	Mean	1σ	%
SK Detector	-	-	-	139.77	2.80	2.01
SK FSI+SI+PN	-	-	-	139.50	2.76	1.98
Flux+Xsec constrained	136.49	16.07	11.77	138.90	4.09	2.94
$\sigma(\nu_e)/\sigma(\bar{\nu}_e)$	-	-	-	139.51	0.00	0.00
NC1γ	-	-	-	139.51	0.00	0.00
NC Other	-	-	-	139.52	0.35	0.25
E_b	-	-	-	136.92	2.36	1.72
Osc	-	-	-	139.52	0.04	0.03
All	134.46	16.84	12.52	136.58	6.07	4.45
All with osc	134.46	16.84	12.52	136.58	6.07	4.45

Table C.2: Average event rate and RMS error broken down by systematic parameter group for μ-like Super-K events with Run 1-9 POT for antineutrino mode.

	Pre-BANFF			**Post-BANFF**		
Group	Mean	1σ	%	Mean	1σ	%
SK Detector	-	-	-	74.58	2.11	2.83
SK FSI+SI+PN	-	-	-	74.41	2.23	3.00
Flux+Xsec constrained	67.71	10.23	15.10	73.52	2.39	3.24
$\sigma(\nu_e)/\sigma(\bar{\nu}_e)$	-	-	-	74.41	1.96	2.63
NC1γ	-	-	-	74.71	0.81	1.09
NC Other	-	-	-	74.42	0.11	0.15
E_b	-	-	-	75.96	5.42	7.13
Osc	-	-	-	72.82	1.96	2.69
All	68.98	11.62	16.85	75.35	6.63	8.81
All with osc	67.52	11.50	17.04	73.74	6.78	9.19

Table C.3: Average event rate and RMS error broken down by systematic parameter group for e-like Super-K events with Run 1-9 POT for neutrino mode.

	Pre-BANFF			**Post-BANFF**		
Group	Mean	1σ	%	Mean	1σ	%
SK Detector	-	-	-	17.20	0.65	3.80
SK FSI+SI+PN	-	-	-	17.13	0.40	2.31
Flux+Xsec constrained	16.78	2.07	12.34	16.98	0.53	3.10
$\sigma(\nu_e)/\sigma(\bar{\nu}_e)$	-	-	-	17.13	0.25	1.46
NC1γ	-	-	-	17.29	0.45	2.60
NC Other	-	-	-	17.13	0.06	0.33
E_b	-	-	-	17.10	0.63	3.66
Osc	-	-	-	16.78	0.42	2.49
All	17.01	2.45	14.41	17.17	1.22	7.13
All with osc	16.67	2.44	14.64	16.82	1.27	7.57

Table C.4: Average event rate and RMS error broken down by systematic parameter group for e-like Super-K events with Run 1-9 POT for antineutrino mode.

	Pre-BANFF			**Post-BANFF**		
Group	Mean	1σ	%	Mean	1σ	%
SK Detector	-	-	-	7.13	0.94	13.15
SK FSI+SI+PN	-	-	-	7.03	0.80	11.43
Flux+Xsec constrained	7.99	0.98	12.21	7.01	0.29	4.09
$\sigma(\nu_e)/\sigma(\bar{\nu}_e)$	-	-	-	7.02	0.18	2.61
NC1γ	-	-	-	7.03	0.02	0.33
NC Other	-	-	-	7.03	0.07	0.99
E_b	-	-	-	7.02	0.21	2.95
Osc	-	-	-	6.88	0.18	2.63
All	8.07	1.75	21.75	7.10	1.30	18.38
All with osc	7.90	1.73	21.94	6.95	1.29	18.51

Table C.5: Average event rate and RMS error broken down by systematic parameter group for ν_e CC1π^+-like Super-K events with Run 1-9 POT for neutrino mode.

Bibliography

1. Jensen, C. & Aaserud, F. *Controversy and consensus : nuclear beta decay 1911-1934* 217. ISBN: 9783034895699 (Birkhäuser Verlag, 2000).
2. ELLIS, C. D. & WOOSTER, W. A. The Continuous Spectrum of β-Rays. *Nature* **119,** 563–564 (1927).
3. Pauli, W. Dear radioactive ladies and gentlemen. *Phys. Today* **31N9,** 27 (1978).
4. Cowan, C. L., Reines, F, Harrison, F. B., Kruse, H. W. & McGuire, A. D. Detection of the Free Neutrino: a Confirmation. *Science (New York, N.Y.)* **124,** 103–4 (1956).
5. Danby, G. *et al.* Observation of High-Energy Neutrino Reactions and the Existence of Two Kinds of Neutrinos. *Physical Review Letters* **9,** 36–44 (1962).
6. Perl, M. L. *et al.* Evidence for Anomalous Lepton Production in $e^+ - e^-$ Annihilation. *Physical Review Letters* **35,** 1489–1492 (1975).
7. Acciarri, M. *et al.* Determination of the number of light neutrino species from single photon production at LEP. *Physics Letters B* **431,** 199–208 (1998).
8. Kodama, K. *et al.* Observation of tau neutrino interactions. *Physics Letters B* **504,** 218–224 (2001).
9. Bahcall, J. N., Fowler, W. A., Iben I., J. & Sears, R. L. Solar Neutrino Flux. *The Astrophysical Journal* **137,** 344 (1963).
10. Cleveland, B. T. *et al.* Measurement of the Solar Electron Neutrino Flux with the Homestake Chlorine Detector. *The Astrophysical Journal* **496,** 505–526 (1998).
11. Kuz'min, V. A. Detection of Solar Neutrinos by Means of the ^{71}Ga $(\nu,e^-)^{71}$Ge Reaction. *Journal of Experimental and Theoretical Physics Letters* **22,** 1532–1534 (1966).

12. Bahcall, J. N., Serenelli, A. M. & Basu, S. New Solar Opacities, Abundances, Helioseismology, and Neutrino Fluxes. *The Astrophysical Journal* **621,** L85–L88 (2005).

13. Hampel, W. *et al.* GALLEX solar neutrino observations: results for GALLEX IV. *Physics Letters B* **447,** 127–133 (1999).

14. Altmann, M. *et al.* Complete results for five years of GNO solar neutrino observations. *Physics Letters B* **616,** 174–190 (2005).

15. Abdurashitov, J. *et al.* The BNO–LNGS joint measurement of the solar neutrino capture rate in ^{71}Ga. *Astroparticle Physics* **25,** 349–354 (2006).

16. Achar, C. *et al.* Detection of muons produced by cosmic ray neutrinos deep underground. *Physics Letters* **18,** 196–199 (1965).

17. Reines, F. *et al.* Evidence for High-Energy Cosmic-Ray Neutrino Interactions. *Physical Review Letters* **15,** 429–433 (1965).

18. Hirata, K. *et al.* Experimental study of the atmospheric neutrino flux. *Physics Letters B* **205,** 416–420 (1988).

19. Hirata, K. *et al.* Observation of a small atmospheric ν_μ/ν_e ratio in Kamiokande. *Physics Letters B* **280,** 146–152 (1992).

20. Becker-Szendy, R. *et al.* Electron- and muon-neutrino content of the atmospheric flux. *Physical Review D* **46,** 3720–3724 (1992).

21. Pontecorvo, B. Mesonium and antimesonium. *Journal of Experimental and Theoretical Physics* **6,** 429 (1957).

22. Pontecorvo, B. Inverse Beta Processes and Nonconservation of Lepton Charge. *Journal of Experimental and Theoretical Physics* **7,** 172–173 (1958).

23. Maki, Z., Nakagawa, M. & Sakata, S. Remarks on the Unified Model of Elementary Particles. *Progress of Theoretical Physics* **28,** 870–880 (1962).

24. Pontecorvo, B. Neutrino Experiments and the Problem of Conservation of Leptonic Charge. *Journal of Experimental and Theoretical Physics* **26,** 986–988 (1968).

25. Gribov, V. & Pontecorvo, B. Neutrino astronomy and lepton charge. *Physics Letters B* **28,** 493–496 (1969).

26. Ahmad, Q. R. *et al.* Direct Evidence for Neutrino Flavor Transformation from Neutral-Current Interactions in the Sudbury Neutrino Observatory. *Physical Review Letters* **89,** 011301 (2002).

27. Ahmed, S. N. *et al.* Measurement of the Total Active ^{8}B Solar Neutrino Flux at the Sudbury Neutrino Observatory with Enhanced Neutral Current Sensitivity. *Physical Review Letters* **92,** 181301 (2004).

28. Prior, G. Results from the Sudbury Neutrino Observatory Phase III. *Nuclear Physics B - Proceedings Supplements* **188,** 96–100 (2009).

29. Fukuda, Y. *et al.* Evidence for Oscillation of Atmospheric Neutrinos. *Physical Review Letters* **81,** 1562–1567 (1998).

30. Tanabashi, M. *et al.* Review of Particle Physics. *Physical Review D* **98,** 030001 (2018).

31. Griffiths, D. J.D. J. *Introduction to elementary particles* 454. ISBN: 9783527406012 (John Wiley & Sons, 2008).

32. Goldhaber, M., Grodzins, L. & Sunyar, A. W. Helicity of Neutrinos. *Physical Review* **109,** 1015–1017 (1958).

33. Giunti, C. & Kim, C. *Fundamentals of Neutrino Physics and Astrophysics* (Oxford University Press, Oxford, UK, 2007).

34. Thomson, M. *Modern particle physics* 554. ISBN: 9781107034266 (Cambridge University Press, Cambridge, 2013).

35. Kayser, B. *Neutrino Physics* tech. rep. (Fermilab, 2005), 21. arXiv: `hep-ph/0506165 [hep-ph]`.

36. Wolfenstein, L. Neutrino oscillations in matter. *Physical Review D* **17,** 2369–2374 (1978).

37. Abe, K. *et al.* Search for CP Violation in Neutrino and Antineutrino Oscillations by the T2K Experiment with 2.2×10^{21} Protons on Target. *Physical Review Letters* **121,** 171802 (2018).

38. Sakharov, A. D. Violation of CP in variance, C asymmetry, and baryon asymmetry of the universe. *Soviet Physics Uspekhi* **34,** 392–393 (1991).

39. Wu, C. S., Ambler, E., Hayward, R. W., Hoppes, D. D. & Hudson, R. P. Experimental Test of Parity Conservation in Beta Decay. *Physical Review* **105,** 1413–1415 (1957).

40. Christenson, J. H., Cronin, J. W., Fitch, V. L. & Turlay, R. Evidence for the 2π Decay of the K_2^0 Meson. *Physical Review Letters* **13,** 138–140 (1964).

41. Jarlskog, C. Commutator of the Quark Mass Matrices in the Standard Electroweak Model and a Measure of Maximal CP Nonconservation. *Physical Review Letters* **55,** 1039–1042 (1985).

42. Peskin, M. The matter with antimatter. *Nature* **419,** 25–27 (2002).

43. Adamson, P. *et al.* Combined Analysis of ν_μ Disappearance and $\nu_\mu \rightarrow \nu_e$ Appearance in MINOS Using Accelerator and Atmospheric Neutrinos. *Physical Review Letters* **112,** 191801 (2014).

44. Abe, K. *et al.* Atmospheric neutrino oscillation analysis with external constraints in Super-Kamiokande I-IV. *Physical Review D* **97,** 072001 (2018).

45. Acero, M. *et al.* New constraints on oscillation parameters from ν_e appearance and ν_μ disappearance in the NOvA experiment. *Physical Review D* **98,** 032012 (2018).

46. Aartsen, M. *et al.* Determining neutrino oscillation parameters from atmospheric muon neutrino disappearance with three years of IceCube DeepCore data. *Physical Review D* **91,** 072004 (2015).

47. Aartsen, M. *et al.* Measurement of Atmospheric Neutrino Oscillations at 6–56 GeV with IceCube DeepCore. *Physical Review Letters* **120,** 071801 (2018).

48. Abe, K. *et al.* Measurement of neutrino and antineutrino oscillations by the T2K experiment including a new additional sample of ν_e interactions at the far detector. *Physical Review D* **96,** 092006 (2017).

49. Abe, Y. *et al.* Improved measurements of the neutrino mixing angle θ_{13} with the Double Chooz detector. *Journal of High Energy Physics* **2014,** 86 (2014).

50. Ishitsuka, M. *New Results of Double Chooz* tech. rep. (2016), 1–30. `https://indico.in2p3.fr/event/12279/contributions/8840/attachments/7002/8602/7_DoubleChooz-Moriond2016.pdf`.

51. Seo, S.-H. New Results from RENO using 1500 Days of Data. arXiv: `1710.08204` (2017).

52. An, F. *et al.* Measurement of electron antineutrino oscillation based on 1230 days of operation of the Daya Bay experiment. *Physical Review D* **95,** 072006 (2017).

53. Andreopoulos, C. *et al.* T2K Neutrino and Anti-Neutrino 3-Flavour Joint Analysis of Run 1-8 Data Sets. *T2K Technical Note 327 v1.2* (2018).

54. Capozzi, F. *et al.* Global constraints on absolute neutrino masses and their ordering. *Physical Review D* **95,** 096014 (2017).

55. Collaboration, I.-P. Letter of Intent: The Precision IceCube Next Generation Upgrade (PINGU). arXiv: `1401.2046` (2014).

56. Katz, U. F. The ORCA Option for KM3NeT. arXiv: `1402.1022` (2014).

57. Kumar, A *et al.* Invited review: Physics potential of the ICAL detector at the India-based Neutrino Observatory (INO). *Pramana* **88,** 79 (2017).

58. Abe, K. *et al.* Hyper-Kamiokande Design Report. arXiv: 1805.04163 (2018).

59. Acciarri, R. *et al.* Long-Baseline Neutrino Facility (LBNF) and Deep Underground Neutrino Experiment (DUNE) Conceptual Design Report, Volume 4 The DUNE Detectors at LBNF. arXiv: 1601.02984 (2016).

60. DUNE Collaboration, D. *et al.* Long-Baseline Neutrino Facility (LBNF) and Deep Underground Neutrino Experiment (DUNE) Conceptual Design Report Volume 2: The Physics Program for DUNE at LBNF. arXiv: 1512.06148 (2015).

61. Abe, K. *et al.* Physics Potential of a Long Baseline Neutrino Oscillation Experiment Using J-PARC Neutrino Beam and Hyper-Kamiokande. arXiv: 1502.05199 (2015).

62. Li, Y.-F. Overview of the Jiangmen Underground Neutrino Observatory (JUNO). *International Journal of Modern Physics: Conference Series* **31,** 1460300 (2014).

63. Abe, K. *et al.* The T2K experiment. *Nuclear Instruments and Methods in Physics Research Section A: Accelerators, Spectrometers, Detectors and Associated Equipment* **659,** 106–135 (2011).

64. Abgrall, N. *et al.* Measurements of cross sections and charged pion spectra in proton-carbon interactions at 31 GeV/ c. *Physical Review C* **84,** 034604 (2011).

65. Para, A. & Szleper, M. Neutrino Oscillations Experiments using Off-axis NuMI Beam. arXiv: hep-ex/0110032 (2001).

66. Yoshii, M. *et al. Status of the J-PARC Ring RF Systems* in *Proc. 5th International Particle Accelerator Conference (IPAC'14)* (2014), 3376–3378.

67. Matsuoka, K. *et al.* Design and performance of the muon monitor for the T2K neutrino oscillation experiment. *Nuclear Instruments and Methods in Physics Research Section A: Accelerators, Spectrometers, Detectors and Associated Equipment* **624,** 591–600 (2010).

68. Galison, P. *Image and logic: a material culture of microphysics* ISBN: 0226279170 (University of Chicago Press, 1997).

69. Allan, D *et al.* The electromagnetic calorimeter for the T2K near detector ND280. *Journal of Instrumentation* **8,** 10019 (2013).

70. Assylbekov, S. *et al.* The T2K ND280 Off-Axis Pi-Zero Detector. *Nuclear Instruments and Methods in Physics Research Section A: Accelerators, Spectrometers, Detectors and Associated Equipment* **686,** 48–63 (2012).

71. Amaudruz, P.-A *et al.* The T2K Fine-Grained Detectors. *Nuclear Instruments and Methods in Physics Research Section A: Accelerators, Spectrometers, Detectors and Associated Equipment* **696,** 1–31 (2012).

72. T2K ND280 TPC collaboration. Time Projection Chambers for the T2K Near Detectors. arXiv: `1012.0865` (2010).

73. Abe, K *et al.* Measurement of the muon neutrino inclusive charged-current cross section in the energy range of 1–3 GeV with the T2K INGRID detector. *Physical Review D* **93,** 72002 (2016).

74. Hayato, Y. A Neutrino Interaction Simulation Program Library NEUT. *Acta Physica Polonica B* **40,** 2477 (2009).

75. Agostinelli, S. *et al.* Geant4—a simulation toolkit. *Nuclear Instruments and Methods in Physics Research Section A: Accelerators, Spectrometers, Detectors and Associated Equipment* **506,** 250–303 (2003).

76. Li, S. W. & Beacom, J. F. First calculation of cosmic-ray muon spallation backgrounds for MeV astrophysical neutrino signals in Super-Kamiokande. *Physical Review C* **89,** 045801 (2014).

77. Abe, K *et al.* Measurements of neutrino oscillation in appearance and disappearance channels by the T2K experiment with 6.6×10^{20} protons on target. *Physical Review D* **91,** 072010 (2015).

78. *Cherenkov radiation* `https://en.wikipedia.org/wiki/Cherenkov_radiation`.

79. Gonzalez, R. C. & Woods, R. E.R. E. *Digital image processing* 2nd edition, 793. ISBN: 0130946508 (2001).

80. Abe, K *et al.* Observation of Electron Neutrino Appearance in a Muon Neutrino Beam. *Physical Review Letters* **112,** 061802 (2014).

81. Abe, K *et al.* Measurement of the inclusive charged current cross section on carbon in the near detector of the T2K experiment. *Physical Review D* **87,** 92003 (2013).

82. Abe, K *et al.* Measurement of the Inclusive Electron Neutrino Charged Current Cross Section on Carbon with the T2K Near Detector. *Physical Review Letters* **113,** 241803 (2014).

83. Abe, K *et al.* Measurement of $\bar{\nu}_\mu$ and ν_μ charged current inclusive cross sections and their ratio with the T2K off-axis near detector. *Physical Review D* **96,** 52001 (2017).

84. Abe, K *et al.* Measurement of the inclusive ν_μ charged current cross section on iron and hydrocarbon in the T2K on-axis neutrino beam. *Physical Review D* **90,** 52010 (2014).

85. Abe, K *et al.* First measurement of the muon neutrino charged current single pion production cross section on water with the T2K near detector. *Physical Review D* **95,** 12010 (2017).

86. Abe, K *et al.* Measurement of the ν_μ charged-current quasielastic cross section on carbon with the ND280 detector at T2K. *Physical Review D* **92,** 112003 (2015).

87. Abe, K *et al.* Measurement of the ν_μ charged current quasielastic cross section on carbon with the T2K on-axis neutrino beam. *Physical Review D* **91,** 112002 (2015).

88. Abe, K *et al.* Measurement of double-differential muon neutrino charged-current interactions on C_8H_8 without pions in the final state using the T2K off-axis beam. *Physical Review D* **93,** 112012 (2016).

89. Abe, K. *et al.* Measurement of the ν_μ charged current quasi-elastic cross-section on carbon with the T2K on-axis neutrino beam, 112002 (2015).

90. Abe, K *et al.* First measurement of the ν_μ charged-current cross section on a water target without pions in the final state. *Physical Review D* **97,** 012001 (2018).

91. Abe, K *et al.* Measurement of Coherent π^+ Production in Low Energy Neutrino-Carbon Scattering. *Physical Review Letters* **117,** 192501 (2017).

92. Abe, K *et al.* Search for short baseline ν_e disappearance with the T2K near detector. *Physical Review D* **91,** 51102 (2015).

93. Abe, K *et al.* Search for Lorentz and CPT violation using sidereal time dependence of neutrino flavor transitions over a short baseline. *Physical Review D* **95,** 111101 (2017).

94. Abe, K *et al.* Upper bound on neutrino mass based on T2K neutrino timing measurements. *Physical Review D* **93,** 12006 (2016).

95. Battistoni, G. *et al.* Overview of the FLUKA code. *Annals of Nuclear Energy* **82,** 10–18 (2015).

96. Zeitnitz, C. & Gabriel, T. The GEANT-CALOR interface and benchmark calculations of ZEUS test calorimeters. *Nuclear Instruments and Methods in Physics Research Section A: Accelerators, Spectrometers, Detectors and Associated Equipment* **349,** 106–111 (1994).

97. Abgrall, N. *et al.* Neutrino Flux Prediction for the 2010a Analysis. *T2K Technical Note 38 v3.0.*

98. Abgrall, N. *et al.* Measurement of production properties of positively charged kaons in proton-carbon interactions at 31 GeV/ c. *Physical Review C* **85,** 035210 (2012).

99. Abgrall, N. *et al.* Measurements of production properties of K^0_S mesons and Λ hyperons in proton-carbon interactions at 31 GeV/ c. *Physical Review C* **89,** 025205 (2014).

100. Abgrall, N. *et al.* Pion emission from the T2K replica target: Method, results and application. *Nuclear Instruments and Methods in Physics Research Section A: Accelerators, Spectrometers, Detectors and Associated Equipment* **701,** 99–114 (2013).

101. Fiorentini, A. *et al.* Flux Prediction and Uncertainty Updates with NA61 2009 Thin Target Data and Negative Focussing Mode Predictions. *T2k Technical Note 217 - Full Run 1-9 Flux* (2018).

102. Hayato, Y., Cao, S. & Nguyen, V. The NEUT Neutrino Monte Carlo Generator: Physics and User Manual. *T2K Technical Note 351 v0.2.*

103. Bolognesi, S. *et al.* Updated recommendation of the 2017 NIWG parameters. *T2K Technical Note 315 v5.0.*

104. Aguilar-Arevalo, A. A. *et al.* First measurement of the muon neutrino charged current quasielastic double differential cross section. *Physical Review D* **81,** 092005 (2010).

105. Aguilar-Arevalo, A. A. *et al.* First measurement of the muon antineutrino double-differential charged-current quasielastic cross section. *Physical Review D* **88,** 032001 (2013).

106. Fields, L. *et al.* Measurement of Muon Antineutrino Quasielastic Scattering on a Hydrocarbon Target at $E_\nu \sim 3.5\,\mathrm{GeV}$. *Physical Review Letters* **111,** 022501 (2013).

107. Wilkinson, C *et al.* Testing charged current quasi-elastic and multinucleon interaction models in the NEUT neutrino interaction generator with published datasets from the MiniBooNE and MINERνA experiments. *Physical Review D* **93,** 72010 (2016).

108. Nieves, J., Simo, I. R. & Vacas, M. J. V. Inclusive charged-current neutrino-nucleus reactions. *Physical Review C* **83,** 045501 (2011).

109. Bercellie, A. *et al.* Cross section parameters for 2014 oscillation analysis. *T2K Technical Note 192 v2.2.*

110. Bercellie, A. *et al.* Implementation of additional NIWG cross section parameterizations for 2014 analyses. *T2K Technical Note 193 v1.1.*

111. Moniz, E. J. *et al.* Nuclear Fermi Momenta from Quasielastic Electron Scattering. *Physical Review Letters* **26,** 445–448 (1971).

112. Martini, M., Ericson, M., Chanfray, G. & Marteau, J. Unified approach for nucleon knock-out and coherent and incoherent pion production in neutrino interactions with nuclei. *Physical Review C* **80,** 065501 (2009).

113. De Perio, P., Hayato, Y. & Tacik, R. NEUT Nuclear Effects (FSI). *T2K Technical Note 33 v2.0* (2012).

114. Dulat, S. *et al.* New parton distribution functions from a global analysis of quantum chromodynamics. *Physical Review D* **93,** 033006 (2016).

115. Llewellyn Smith, C. Neutrino reactions at accelerator energies. *Physics Reports* **3,** 261–379 (1972).

116. Kuzmin, K. S., Lyubushkin, V. V. & Naumov, V. A. Quasielastic axial-vector mass from experiments on neutrino-nucleus scattering. *The European Physical Journal C* **54,** 517–538 (2008).

117. Bernard, V., Elouadrhiri, L. & Meißner, U.-G. Axial structure of the nucleon. *Journal of Physics G: Nuclear and Particle Physics* **28,** 1–35 (2002).

118. Rein, D. & Sehgal, L. M. Neutrino-excitation of baryon resonances and single pion production. *Annals of Physics* **133,** 79–153 (1981).

119. Benhar, O., Day, D. & Sick, I. Inclusive quasielastic electron-nucleus scattering. *Reviews of Modern Physics* **80,** 189–224 (2008).

120. Rein, D. & Sehgal, L. M. Coherent π^0 production in neutrino reactions. *Nuclear Physics B* **223,** 29–44 (1983).

121. Berger, C. & Sehgal, L. M. Partially conserved axial vector current and coherent pion production by low energy neutrinos. *Physical Review D* **79,** 053003 (2009).

122. Glück, M., Reya, E. & Vogt, A. Dynamical Parton Distributions Revisited. *The European Physical Journal C* **5,** 461–470 (1998).

123. Bodek, A & Yang, U. K. Modeling Neutrino and Electron Scattering Cross Sections in the Few GeV Region with Effective LOPDFs. arXiv: `hep-ex/0301036` (2003).

124. Jihn, E. K., Langacker, P., Levine, M & Williams, H. H. A theoretical and experimental review of the weak neutral current: a determination of its structure and limits on deviations from the minimal SU(2)xU(1) electroweak theory. *Review of Modern Physics* **53,** 211 (1981).

125. Musset, P. & Vialle, J.-P. Neutrino physics with gargamelle. *Physics Reports* **39,** 1–130 (1978).

126. Derrick, M *et al.* c resulting from $\bar{\nu}_\mu p$ interactions. *Physical Review D* **53,** 1 (1978).

127. Berkman, S., de Piero, P., Tanaka, H. & Tobayama, S. Pion Hadronic Secondary Interactions in SK. *T2K Technical Note 105 v1.1.*

128. De Jager, C., De Vries H. & De Vries, C. Nuclear charge- and magnetization-density-distribution parameters from elastic electron scattering. *Atomic Data and Nuclear Data Tables* **14,** 479–665 (1974).

129. Salcedo, L., Oset, E., Vicente-Vacas, M. & Garcia-Recio, C. Computer simulation of inclusive pion nuclear reactions. *Nuclear Physics A* **484,** 557–592. ISSN: 0375-9474 (1988).

130. Nakamura, K & Group, P. D. Review of Particle Physics. *Journal of Physics G: Nuclear and Particle Physics* **37,** 075021 (2010).

131. Tanaka, H. *Photonuclear interactions in skdetsim* 2012. `https://www.t2k.org/meet/collab/archive/201209/talks/thurpm/phonuc/view`.

132. Bienstock, S., Kaboth, A., Scott, M. & Wret, C. ND280 Analysis (BANFF) for 2017 Oscillation Analyses. *T2K Technical Note 324 v3.0.*

133. Hartz, M. *et al.* ND280 Flux and Cross Section Constraint (BANFF) for 2015/16. *T2K Technical Note 230 v3.0.*

134. Bartet, P. *et al.* ν_μ CC event selections in the ND280 tracker using Run 2+3+4. *T2K Technical Note 212 v2.0.*

135. Berardi, V. *et al.* CC $\bar{\nu}_\mu$ event selection in the ND280 tracker using Run 5c and Run 6 anti-neutrino beam data. *T2K Technical Note 246 v1.0.*

136. Berardi, V. *et al.* CC ν_μ background event selection in the ND280 tracker using Run 5c+Run 6 anti-neutrino beam data. *T2K Technical Note 248 v1.2.*

137. Hartz, M. *et al.* Constraining the Flux and Cross Section Models with Data from the ND280 Detector for the 2014/15 Oscillation Analysis. *T2K Technical Note 220 v4.0.*

138. Akutsu, R., Nakayama, S., Vilela, C., Wendell, R. & Yoshida, T. Super-Kamiokande Data Quality In T2K Runs 1-9. *T2K Technical Note 355 v1.1.*

139. Himmel, A. *et al.* Super-Kamiokande Events and Data Quality Studies for T2K Runs 5 and 6. *T2K Technical Note 219 v2.6.*

140. Hignight, J. *et al.* Super-Kamiokande Events and Data Quality Studies for T2K Run4. *T2K Technical Note 148 v4.0.*

141. Li, X. & Wilking, M. fiTQun event selection optimization. *T2K Technical Note 319 v1.1.*

142. Imber, J. *et al.* T2K-SK Systematic Error Summary for 2017 OA. *T2K Technical Note 326 v1.2.*

143. Missert, A. SK Atmospheric Neutrino Fit and Fiducial Volume Optimization. *T2K Technical Note 318 v2.2.*

144. Mueller, T. & Mine, S. SK π^0 systematic errors for nue analysis with T2K 6.4×10^{20} POT (RUN1-4) data. *T2K Technical Note 156 v2.0.*

145. Asimov, I. *Franchise* ISBN: 0886822327 (Creative Education, 1989).

146. Andreopoulos, C. *et al.* T2K Neutrino and Anti-Neutrino 3-Flavour Joint Analysis of Run 1-9 Data Sets. *T2K Technical Note 360 v1.2* (2018).

147. Andreopoulos, C., Dealtry, T., Escudero Sanchez, L., Grant, N. & Weber, A. T2K 3.010×10^{20}-POT 3-Flavour Muon-Neutrino Disappearance Analysis. *T2K Technical Note 141 v10.0.*

148. Reid, N. & Fraser, D. *Likelihood Inference in the Presence of Nuisance Parameters* in *Proceedings of the Conference on Statistical Problems in Particle Physics, Astrophysics and Cosmology* (SLAC, Stanford, 2003), 265–271.

149. Wilks, S. S. The Large-Sample Distribution of the Likelihood Ratio for Testing Composite Hypotheses. *The Annals of Mathematical Statistics* **9,** 60–62 (1938).

150. Press, W. H. *Numerical recipes : the art of scientific computing* 100–102. ISBN: 0521880688 (Cambridge University Press, 2007).

151. Feldman, G. J. & Cousins, R. D. A Unified Approach to the Classical Statistical Analysis of Small Signals. *Physical Review D* **57,** 3873 (1998).

152. Ciuffoli, E., Evslin, J. & Zhang, X. Confidence in a neutrino mass hierarchy determination. *Journal of High Energy Physics* **2014,** 95 (2014).

153. Warburton, T. K. *Latest Results from NOvA and future experimental prospects* 2018. `https://indico.ph.qmul.ac.uk/indico/getFile.py/access?contribId=23&resId=0&materialId=slides&confId=289`.